Innovative concept of multifunctional heat exchanger/reactor by passive dynamic control using flexible vortex generators

Samer Ali

Thèse de doctorat

Pour obtenir le grade de Docteur de l'Université de

VALENCIENNES ET DU HAINAUT-CAMBRESIS

et L'ÉCOLE DES MINES DE DOUAI

Spécialité :

Mécanique et Énergétique

Présentée et soutenue par

Samer ALI

Le 01/12/2015, à L'École des Mines de Douai

Ecole doctorale :

Sciences Pour l'Ingénieur (SPI - 072)

Equipe de recherche, Laboratoire :

Département Énergétique Industrielle (DEI), École des Mines de Douai

Concept innovant d'échangeur/réacteur multifonctionnel par contrôle dynamique passif par générateurs de vorticité flexibles

Rapporteurs

- GOURDON, Christophe. Professeur, INPT–ENSIACET, Toulouse
- TOPIN, Frédéric. Maître de Conférence HDR, IUSTI, Marseille

Examinateurs

- PEERHOSSAINI, Hassan. Professeur, Laboratoire Interdisciplinaire des Energies de Demain-LIED (CNRS-UMR 8236), Paris (**Président du jury**)
- SAURY, Didier. Professeur, Institut PPrime, Poitiers

Encadrants

- MENANTEAU, Sébastien. Maître-Assistant, Mines Douai-Energétique Industrielle
- HABCHI, Charbel. Assistant Professor, Department of Mechanical Engineering, Notre Dame University-Louaize

Codirecteurs de thèse

- HARION, Jean-Luc. Professeur, Mines Douai–Energétique Industrielle
- LEMENAND, Thierry. Maître de Conférence HDR, LARIS-EA7315, Angers

ACKNOWLEDGMENTS

First and foremost I would like to express my sincere gratitude to my advisors: Professor Jean-Luc Harion, Dr. Thierry Lemenand, Dr. Charbel Habchi and Dr. Sébastien Menanteau. I want to thank you for the continuous support of my Ph.D study and related research, for your patience, motivation and immense knowledge. Your guidance helped me in all the time of research and writing of this thesis.

I would like to thank my committee members, Professor Christophe Gourdon, Dr. Frédéric Topin, Professor Hassan Peerhossaini and Professor Didier Saury for serving as my committee members. I also want to thank you for letting my defense be an enjoyable moment, and for your brilliant comments and suggestions.

A special thanks to my family. Words can not express how grateful I am to my mother, my father and my two brothers for all the sacrifices that you've made on my behalf. Your prayers for me was what sustained me thus far. I would also like to thank my beloved wife Razane for supporting me for everything, and especially I can't thank you enough for encouraging me throughout this experience and its ups and downs.

Finally I thank my God for letting me through all the difficulties. You are the one who let me finish my degree. I will keep on trusting You for my future.

Science is what we understand well enough to explain to a computer. Art is everything else we do.

D.E KNUTH, 1996.

Contents

List of Figures

List of Tables

Nomenclature

c	scalar $(-)$
c_p	specific heat $(\mathrm{Jkg^{-1}K^{-1}})$
De	Dean number (-)
D_h	hydraulic diameter (m)
$\mathbf{d_s}$	solid displacement vector (m)
D_m	mass diffusivity $(\mathrm{kgm^{-1}s^{-1}})$
e	thickness of the elastic flap (m)
E	Young's modulus (Pa)
f	friction factor $(-)$
f_b	body force (N)
f_{comm}	synchronization frequency (N)
f_{ex}	structural excitation frequency (Hz)
f_N	structural natural frequency in a fluid medium (Hz)
f_{st}	Strouhal frequency (Hz)
f_v	vortex shedding frequency (Hz)
f_{vacc}	structural frequency in vacuum (Hz)
$\mathbf{F}$	deformation gradient tensor $(-)$
$\mathbf{G}$	Green lagrangian strain tensor $(-)$
H	height of the computational channel (m)
h	height of the flap (m)
h_g	grid size (m)
$\mathbf{I}$	unity tensor $(-)$
j	Colburn factor $(-)$
k	thermal conductivity $(\mathrm{Wm^{-1}K^{-1}})$
L	length of the computational domain (m)
l	cell distance to the nearest moving boundary (m)
$\dot{m}$	mass flow rate $(\mathrm{kgs^{-1}})$
m^*	mass ratio $(-)$
MA	mean displacement amplitude (m)
N	number of cells $(-)$
Nu	Nusselt number $(-)$
p	pressure (Pa)
p_c	apparent order of convergence $(-)$
Pr	Prandtl number $(-)$
q''	wall heat flux $(\mathrm{Wm^{-2}})$
r	grid refinement factor $(-)$
Re	Reynolds number $(-)$
St	Strouhal number $(-)$
T	temperature (K)
t	time (s)
$\mathbf{u}$	velocity vector $(u,\, v)$ $(\mathrm{ms^{-1}})$
$\overline{U}_f$	mean flow velocity $(\mathrm{ms^{-1}})$
V_r	reduced velocity (-)
$(x,\, y)$	Cartesian coordinate system (m)
$(\ )^*$	dimensionless position: $X^* = x/H$, $Y^* = y/H$ $(-)$

Greek symbols

α	field synergy angle $(^\circ)$
γ	mesh diffusion coefficient $(-)$
ϵ	relative kinetic energy $(-)$

η	thermal performance factor $(-)$
λ	eigenvalue $(-)$
ν_f	fluid kinematic viscosity $(\mathrm{m^2 s^{-1}})$
ν_s	Poisson's ratio $(-)$
ϕ	normalized basis function $(-)$
ρ	mass density $(\mathrm{kgm^{-3}})$
Σ	Piola-Krichhoff stress tensor $(-)$
τ_s	shear stress (Pa)
ζ	cumulative relative kinetic energy $(-)$
Σ	Piola-Krichhoff stress tensor $(-)$
ζ	damping ratio (-)

Abbreviations

ALE	arbitrary Lagrangian-Eulerian
CoV	coefficient of variation
CFD	computational fluid dynamics
CFL	Courant–Friedrichs–Lewy condition
CSD	computational structure dynamics
DWVG	delta winglet vortex generator
FEM	finite element method
FVG	flexible vortex generators
FVM	finite volume method
FSI	fluid-structure interaction
GCI	grid convergence index
HEV	high-efficiency vortex
LV	longitudinal vortex
LVG	longitudinal vortex generators
MI	mixing index
OSF	offset strip fins
PDF	probability density function
PSD	power spectra density
RVG	rigid vortex generators
RWVG	rectangular winglet vortex generator
STR	stirred tank reactor
TV	transverse vortex
VIV	vortex-induced vibrations

Subscripts

ave	spatial average
b	bulk
f	fluid
g	global
in	inlet
m	mesh
max	maximum value
s	solid
w	wall

General introduction

This thesis proposes an innovative way of increasing the performances of vortex generator type MHER (Multifunctional Heat Exchangers/Reactors) by using a passive and dynamic perturbation. Classically, the HEV (High Efficiency Vortex) mixer is a tubular heat exchanger in which rigid vortex generators are attached to its wall; these vortex generators produce coherent structures and vortices that intensify heat and mass transfer.

We propose to study a new concept of increasing the efficiency of HEV mixer by using flexible vortex generators which are dynamic and passively controlled, combining the knowledge from vortex-induced vibrations studies and applying them in the context of heat/mass transfer enhancements. In fact, the succession of several vortex generators can increase the degree of freedom of the system and the aim is to quantify the improvement of thermal transport by increasing the interactions between different vortex generators. This approach consists of finding solutions that stay passive but dynamic as opposed to the motionless inserts previously mentioned and without the use of an additional source of energy except the pumping power alone, thus eliminating the difficulty to provide external power and reducing the complexity from the use and design point of view. The free oscillations of flexible vortex generators can perturb the flow and modify the coherent structures system to intensify heat and mass transfer.

The objective of this thesis is to provide designs for self-sustained oscillations of flexible vortex generators and to analyze the effects of introducing several flexible vortex generators on oscillation behaviors, flow patterns, heat transfer and mixing performances.

This manuscript is organized as follows:

- The first chapter is dedicated to literature review in which we present a background about the types of multifunctional heat exchangers/reactors already available and then an overview of some of the passive methods used to intensify heat transfer and mixing such as vortex generators. On the other hand, active methods relying on either rigid or elastic structural oscillations and the effects of several parameters such as Young's modulus, flaps arrangement, amplitude and frequency of oscillation on heat transfer and mixing enhancement are highlighted. Finally, other disciplines of engineering are presented such as vortex-induced vibrations and flapping motion which are relevant to our study.

- The second chapter deals with the numerical procedures and strategies to solve the fluid-structure interaction (FSI) problem. The coupling between the computational fluid dynamics (CFD) solver, computational solid dynamics (CSD) solver and the mesh motion solver is presented and especially the strong coupling strategy used to best simulate the large displacement problem. Furthermore, in order to maintain a high quality mesh near the moving elastic flaps, reliable mesh rezoning techniques are applied and presented in this chapter. Moreover, the FSI algorithm is validated using a benchmark from the literature which consists of a large oscillatory motion of a flap confined in a two dimensional laminar flow.

The subsequent chapters are presented as either published or submitted papers as follows:

- Chapter 3 is the article "Heat transfer and mixing enhancement by free elastic flaps oscillation", published in *International Journal of Heat and Mass Transfer* in 2015.

- Chapter 4 is an article titled "Towards self-sustained oscillations of multiple flexible vortex generators", to be submitted to *Journal of Fluids and Structures*, (2015).

- Chapter 5 concerns "Heat transfer and mixing enhancement by using multiple freely oscillating flexible vortex generators", an article to be submitted to *Applied Thermal Engineering*, (2015).
- Chapter 6 is the article "Three-dimensional numerical study of heat transfer and mixing enhancement in a circular pipe using self-sustained oscillating flexible vorticity generators", to be submitted to *Physics of Fluids*, (2015).
- Chapter 7 is devoted to conclusions and perspectives. Since the present methods using self-sustained oscillations of flexible vortex generators are still in their early development stages as heat transfer and mixing enhancement, several future suggestions to further optimize the system are highlighted.

Appendix A presents the early on algorithm developments using OpenFOAM (C++ library) to model the fluid structure interaction problem published as part of the 2013 CFM conference added at the end of Appendix A. The OpenFOAM library was used first to upgrade an original fluid-structure interaction solver to use an updated Arbitrary Lagrangian Eulerian method. In addition, a PIMPLE algorithm for the fluid solver was implemented with heat coupling strategy at the fluid-structure interface. However, since the OpenFOAM library could not handle large displacement flapping motion due to high distortion of the mesh, we have used another strategy. In fact, the ANSYS Fluent solver which supports remeshing and rezoning capabilities is coupled with ANSYS Mechanical solid solver. This maintains good boundary layer resolution and allows for larger mesh deformations with a single mesh topology. This strategy is validated in Chapter 2 using a numerical FSI benchmark and furthermore applied in all the subsequent studies presented in this manuscript.

Finally, appendix B presents an international communication as part of the 2015 Colloque Interuniversitaire Franco-Québécois (CIFQ) conference. This paper deals with a part of the results of the two-dimensional simulations presented in Chapter 5.

Chapter 1

Literature review

1.1 Introduction

Over the years, many methods have been studied to enhance heat transfer in forced convection problems. A classification of single phase heat transfer enhancement as passive, active, or compound has been proposed by Webb [Webb, 1987]. Active methods require external power and involve electric, magnetic or acoustic fields. Passive methods involve surface modifications, fluid additives or introduction of protuberances in order to destabilize the flow. Compound methods involve the use of both active and passive techniques. Since active methods require external energy and thus an added cost, passive methods are more widely spread in several engineering applications such as intensification of secondary oil refining process, catalytic process, dust removal and calendering processes [Levinbuk and Kustov, 2001, Kiwi-Minsker and Renken, 2010, Panov et al., 2006, Kohlert et al., 1986].

To this end, researchers work on designing novel equipments and techniques that would lead to compact, safe, energy efficient and sustainable processes. One of the way to reach such objectives is to develop multifunctional devices such as multifunctional heat exchangers/reactors (MHER) for instance [Dautzenberg and Mukherjee, 2001].

Stankiewicz and Moulijn [Stankiewicz and Moulijn, 2000] provided the following definition for process intensification:
"*Process intensification consists of the development of novel apparatuses and techniques that, compared to those commonly used today, are expected to bring dramatic improvements in manufacturing and processing, substantially decreasing the equipment-size/production-capacity ratio, energy consumption, or waste production and ultimately resulting in cheaper, sustainable technologies.*"

In pharmaceutical fields, mixing and heat transfer requirements add an important flexibility criterion to be considered while designing and selecting a reactor. The solution to overcome such flexibility is to use a jacketed stirred tank reactor (STR) equipped with a variable speed drive mixing system and the facility to use different types of impellers. However STR fails to provide the molecular scale environment for fast, multiple exo/endo-thermic reactions, and also doesn't comply with environmental regulations, acceptable levels of safety and the poor heat removal ability [Shelat and Sharratt, 2004].

As a consequence, the heat removal from a reactor during an exothermic process is a crucial characteristic that has to be improved. The solution lies in the intensification of heat transfer between the utility and process streams in the apparatus. MHER have been developed to intensify chemical processes by synergistically combining chemical reaction with momentum, heat and mass transport in a single system [Dautzenberg and Mukherjee, 2001], which leads to a significant reduction in energy consumption, hence reducing the overall utility requirements of the process, and allows significant reductions in both investment and plant operating costs by optimizing the process. Results have shown that specific inserts such as vortex generators [Fiebig et al., 1991] can enhance heat transfer significantly, however with an added penalty of pressure drop and higher pumping power requirements. Since this type of vortex generators (VG) is usually fixed and offers limited control or system flexibility, actively controlled VGs at different amplitudes and frequencies of oscillations can solve this problem.

In the last decades, heat transfer enhancement with active flow control has been implemented due to the development of electro-mechanical systems. For example, Ma *et al.* [Ma et al., 2009] and Yu *et al.* [Yu et al., 2014] studied vibrating fins that are actuated with piezoelectric material to disrupt the growth of the thermal boundary layer, thus enhancing the convective heat transfer coefficient. On the other hand, vortex-induced vibrations (VIV) of structures have attracted so much attention due to its application in several engineering disciplines such as design of bridges, chimneys and marine vehicles. This phenomenon of VIV is the underlying cause in the collapse of the Tacoma bridge in 1940. The results of VIV have demonstrated that the vortex shedding frequency in some cases resonates with one of the structural natural frequencies. This is referred to as lock-in [Williamson and Govardhan, 2004] where the flow in this case supplies energy to the structure instead of damping it, resulting in large amplitude oscillations. However, the effects of this passive fluid structure interaction (FSI) on heat transfer and mixing have not been studied in theory or experiments. In this thesis, we investigate the effect of passive oscillations of elastic structures on mixing and heat transfer, without addition of any external force except that of the flow itself.

The objective of this chapter is to provide information about the followings:

- An overview of the main MHER from the open literature: classifications and applications.
- Methods of quantification for heat transfer and mixing.
- Heat and mass transfer enhancement using passive flow perturbations with emphasis on vortex generators.
- Active flow perturbations: review on heat and mass enhancement using structural oscillations.
- An overview of vortex-induced vibrations, with emphasis on free vibration which is relevant to our study.
- Energy harvesting potential from VIV/FSI configurations.

1.2 Multifunctional heat exchangers/reactors MHER

1.2.1 Static mixers

Static mixers consist of series of motionless inserts installed in pipes or transfer tubes. They have interesting applications in continuous industrial mixing processes as an alternative to mechanical agitators [Rauline et al., 2000], since similar or better performances can be achieved at lower cost. Motionless mixers typically have lower energy consumptions and reduced maintenance requirements because they have no moving parts.

Figure 1.1 shows two kinds of static mixers for example. The Kenics® HEV static mixer (Figure 1.1 (a)) consists of a circular pipe fitted with several rows of vortex generators. Each vortex generator produces a streamwise pair of counter-rotating vortices which enhances the radial mass and heat transfer [Habchi et al., 2012]. The SMX® static mixer (Figure 1.1 (b)) is designed to divide and redistribute the fluid streams sequentially until good mixing is achieved; the effectiveness of this redistribution is a function of the specific design and the number of elements [Liu et al., 2006].

In static mixers, products are mixed by the flow energy which is provided by the pumping power alone. The elements of the static mixer produce radial secondary flows toward the walls, the products are thus continuously intermixed and gradients of temperature, velocity and concentration are reduced.

Commercial static mixers have a wide variety of basic geometries and many adjustable parameters that can be optimized for specific applications. The number of elements in the streamwise direction can be adjusted and so the aspect ratio of the mixers is defined as the ratio of length to diameter of a single element.

Ghanem *et al.* [Ghanem et al., 2014] provided a review about the recent innovative concepts regarding passive static mixers by focusing on their mixing performances. In this paper, they highlighted that the laminar and turbulent regimes must be distinguished in order to choose a device for

(a) (b)

Figure 1.1: Motionless mixers: (a) Kenics® HEV static mixer [Chemineer, 2015] and (b) SMX® static mixer [Chemtech, 2015]

mixing, since the mixing mechanisms differ significantly between the two flow regimes. On one hand, when laminar regimes are considered, especially for applications dealing with high viscous fluids like in food, paint and detergent industries, the low levels of mixing are quite obvious and are reflected in the spatial non-homogeneities of the composition. A provided solution is thus to apply mixing techniques as in the split-and-recombine reactors (SAR). The concept is based on shortening the striation thickness by splitting the solute and the solvent into multiple streams and rejoining them through parallel lamination, thus achieving stretching/folding following the baker's transform. Figure 1.2 illustrates the SAR principle in action by increasing the interfacial area between the scalars of different concentrations and reducing the striation thickness size to the extent where the molecular diffusion can act efficiently and thus amplify its effect [Ghanem et al., 2013b].

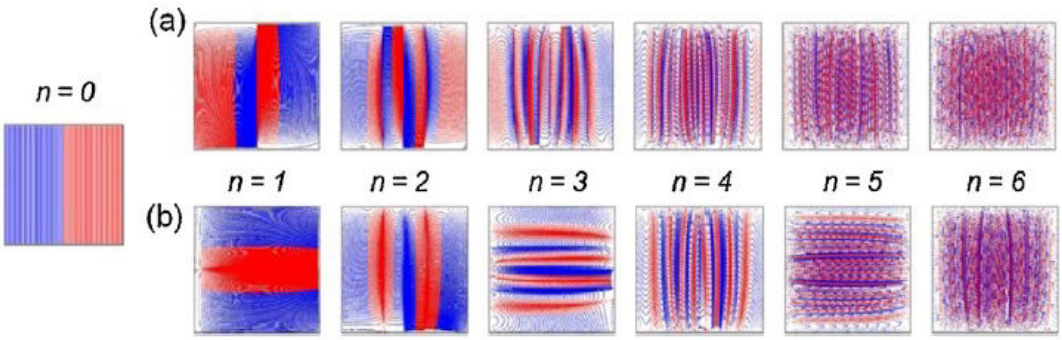

Figure 1.2: Laminar mixing in two SAR configurations: (a) SAR-1 and (b) SAR-2 with n the number of splitting and recombination steps [Ghanem et al., 2013b]

In the turbulent regimes however, the eddy diffusion generated by turbulence provides sufficient mixing for most industrial applications and the motionless mixers can generate intense radial mixing or increase heat transfer significantly when compared to a plain pipe. When comparing both laminar and turbulent regimes, Ghanem *et al.* [Ghanem et al., 2013a] pinpoints the fact that performance enhancement of mixing techniques is more efficient for laminar flows and tends to decrease in the turbulent regimes. Indeed, although static mixers can increase the level of turbulence by producing structures with larger scales without changing the pipe diameter and flow rate, it is yet achieved at the expenses of higher pressure drops. Specific types of inserts and perturbators are usually introduced in a static mixer device. Similar to the HEV and SMX static mixers, Figure 1.3 illustrates the different mixing mechanisms in a Komax Triple Action Mixer.

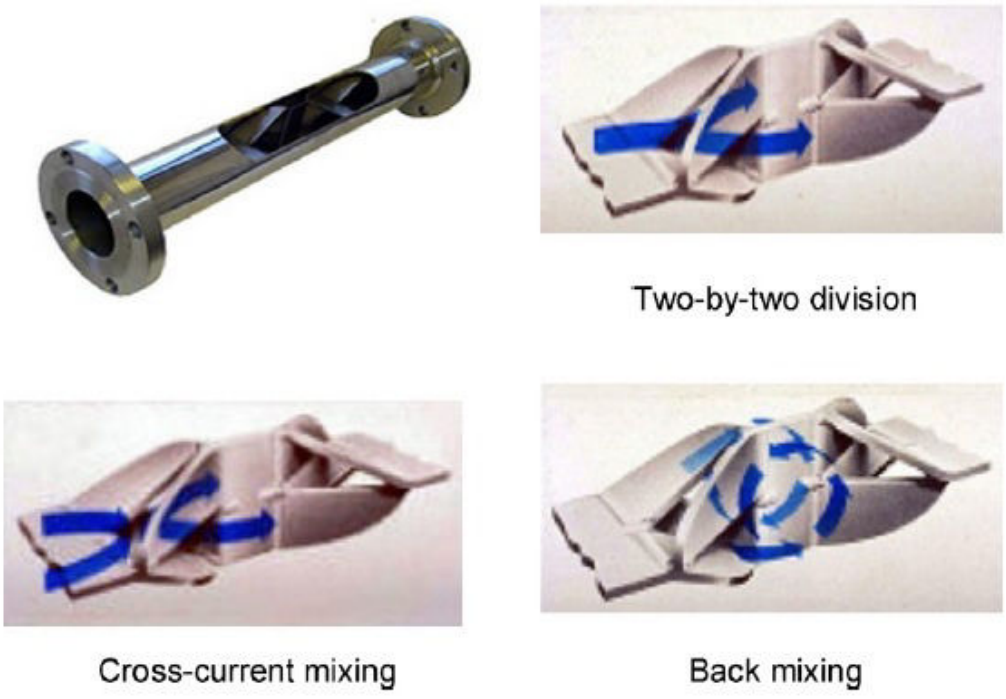

Figure 1.3: Triple Action Mixer and the associated mixing mechanisms [Ghanem et al., 2014]

1.2.2 Pulsatile flow reactors

An oscillatory or pulsatile flow reactor consists of baffled reactor tubes fitted to an oscillatory unit as shown in Figure 1.4 and allows providing variable intensity oscillation superimposed on a mean flow rate. By applying the right intensity to the flow rate ratio, it is then possible to control the residence time with the flow rate whereas mixing is controlled only by the oscillation intensity.

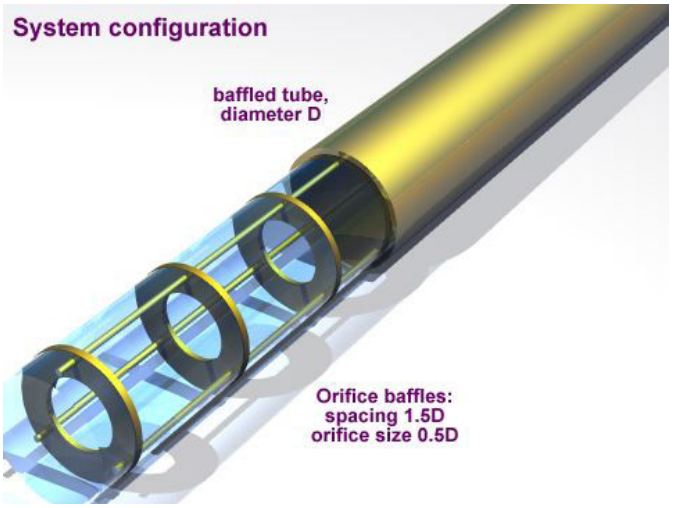

Figure 1.4: A 3-D schematic diagram of an oscillatory flow baffled tube [OFM Research Group, 2015]

Mackley and Stonestreet [Mackley and Stonestreet, 1995] showed that oscillatory flow leads to a substantial enhancement in tube-side heat transfer in a shell-and-tube heat exchanger. While the presence of baffles in a tube results in heat transfer enhancement, the greatest enhancement is obtained when both baffles and oscillations are present.

For a broad range of oscillatory conditions tested, it was found that the heat transfer rate was strongly dependent on the product of frequency and amplitude of oscillations. As a consequence, precise control of heat transfer enhancement can be achieved by choosing a specific set of frequency

and amplitude.

The greatest advantage of oscillatory flow appears to be found at low Reynolds number. It was seen that a 30-fold improvement in Nusselt number could be obtained under certain conditions [Mackley and Stonestreet, 1995].

Timité *et al.* [Timité et al., 2011] presented experimental and numerical studies of three-dimensional pulsatile flow in a twisted pipe in order to show the effects of chaotic advection on mixing in this flow configuration. The secondary flow being generated by centrifugal force, the pulsating velocity field and the change in curvature plane lead to irregular fluid particle trajectories. The studies revealed modifications in the trajectories evolution due to pulsation. The number of regular zones, that disappear with an increase in the number of bends, decreases with pulsation frequency and velocity-amplitude ratio as in Figure 1.5 where both these phenomena contribute to the mixing and mass transfer enhancement.

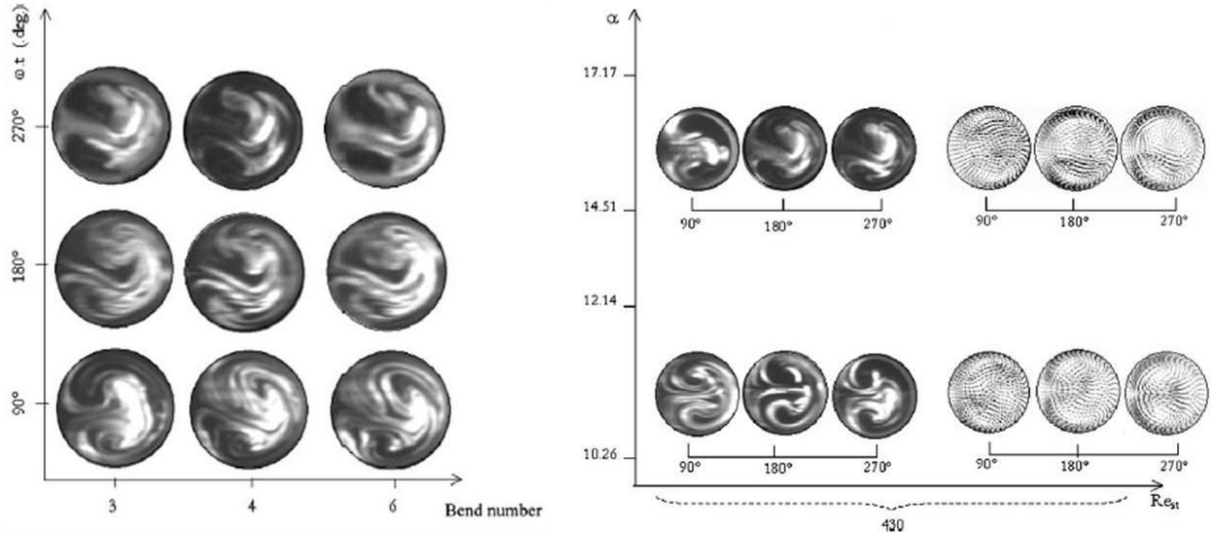

(a) (b)

Figure 1.5: Experimental and numerical visualization of secondary flows for various: (a) bend number; (b) dimensionless frequency parameter α [Timité et al., 2011]

1.3 Lagrangian mixing

Studies on laminar mixing began in the 80s as a formal approach, and they were at the beginning more an "art" rather than a fully developed scientific discipline [Kays and London, 1984]. The fundamentals evolved mainly from empiricism to a semi-qualitative level, and a unifying framework that describes the dynamics of laminar mixing processes has only begun to emerge in the past decade. From a fundamental viewpoint, one of the main motivations to study laminar mixing is that the underlying physics is amenable to direct analysis in a rigorous framework to develop meaningful theory. Additionally, mixing problems in laminar environments tend to be very difficult. In the context of pharmaceutical, food, polymer, and biotechnological processes, liquid mixing applications are frequently carried out at low speeds or involve high viscosity substances such as detergents, ointments, creams, suspensions, antibiotic fermentations or food emulsions. During the past few years there has been growing awareness of problems related to incomplete or inefficient mixing at various stages of these manufacturing processes.

In other instances, the concern for mechanical damages on the fluid itself constrains mixing operations at low-speed regime. Biological processes using shear-sensitive cell cultures are prime examples where adequate mixing must be accomplished at low speeds to avoid compromising the metabolic and physical integrity of shear-sensitive cells and molecules. Increases in batch viscosity are also a common characteristic of these applications. As the biomass concentration increases at

continued shearing, the fluid properties often become highly complex and strongly non-Newtonian, imposing thus new challenges on effective mixing.

1.3.1 Molecular diffusion

The one dimensional molecular diffusion for a passive scalar $c(x,t)$ with a diffusion coefficient D_m is governed by the following equation [Chaté et al., 2012]:

$$\frac{\partial c}{\partial t} = D_m \frac{\partial^2 c}{\partial x^2} \tag{1.1}$$

The well-known solution for this equation for initial conditions as $c = 0$ in $x < 0$ and $c = 1$ in $x > 0$ is:

$$c(x,t) = \frac{1}{2} + \frac{1}{2} erf\left(\frac{x}{\sqrt{D_m t}}\right) \tag{1.2}$$

where $erf()$ is a standard error function.

From this solution, a distance over which the substance has diffused is known which is equal to $\delta(t) = \sqrt{D_m t}$. Consequently, the concentration will have a value of $c = 0.5 \pm 0.3$ at $x = \pm\delta(t)$ and a value of $c = 0.5 \pm 0.45$ at $x = \pm 3\delta(t)$. For the diffusion of heat in air, this diffusion distance is 0.14 mm after 1 ms, 4 mm in 1 s and 300 mm in 1 hr. For the diffusion of salt in water, $\delta = 1$ μm in 1 ms, 30 μm in 1 s, 2 mm in 1 hr and 200 mm in 1 day. From these examples, one can learn that molecular diffusion becomes very slow as time increases, where this slowness is the heart of the mixing problem.

The volume of the mixed fluid at the interface is:

$$V = A\sqrt{D_m t} \tag{1.3}$$

where A is the interfacial area between the species being mixed. Since the diffusion distance $\sqrt{D_m t}$ is increasing slowly with time, the only way here to improve the mixing process is to increase the interfacial area A. In fact, this results in reducing the thickness between layers of unmixed fluid compared to distances over which diffusion can act, i.e. to $V/A = \sqrt{D_m t}$.

1.3.2 Taylor dispersion

Taylor dispersion is an effective mechanism for mixing of a solute in a distributed velocity field, such as pressure-driven flow in a microchannel. This axial effect arises from a coupling between molecular diffusion in the transverse direction and transverse distribution of the flow velocity. Figure 1.6 illustrates the difference between molecular diffusion in a plug-like flow and Taylor dispersion in a distributed flow. In a uniform flow field, such as the plug-like electro osmotic flow, advection and diffusion are independent. Axial diffusion is the same as molecular diffusion, as in Figure 1.6 (a).

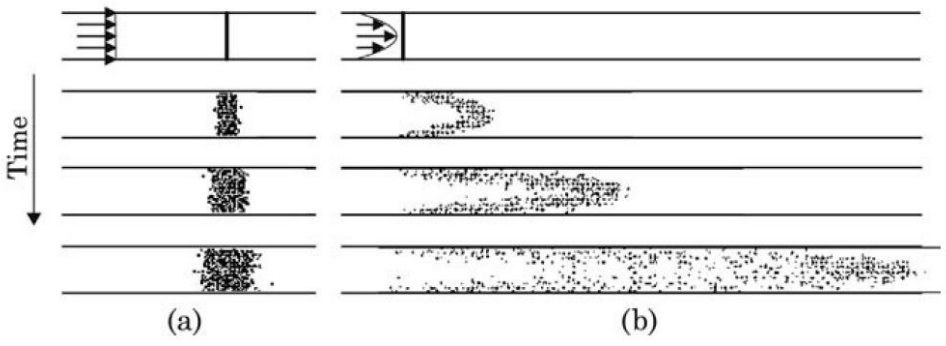

Figure 1.6: Particle distribution in a microchannel: (a) uniform velocity profile; (b) parabolic velocity profile [Nguyen, 2011]

In a distributed flow field, such as the pressure-driven flow with a parabolic velocity distribution, the solvent is stretched more in the middle of the channel than near the wall due to axial convective transport. The resulting concentration gradient between the different fluid layers is then blurred by diffusion in the transverse direction, as in Figure 1.6 (b). As a result, the solute appears to be diffusing in the axial direction at a rate that is much faster than what would be predicted by ordinary molecular diffusion.

1.3.3 Chaotic advection

The term chaotic advection refers to the phenomenon where a simple Eulerian velocity field leads to a chaotic response in the distribution of a Lagrangian marker such as a tracing particle. Advection refers to species transport by the flow. A flow field can be chaotic even in the laminar flow regime. Chaotic advection can be created in a simple two-dimensional flow with time-dependent disturbance or in a three-dimensional flow even without time-dependent disturbance. It is important to note that chaotic advection is not turbulence. For a flow system without disturbance, the velocity components of chaotic advection at a point in space remain constant over time, while the velocity components of turbulent flows are random. The streamlines of steady chaotic advection flow across each other, causing the particles to change their paths. Under chaotic advection, the particles diverge exponentially and enhance mixing between the solvent and solute flows. In a time-periodic system, the condition for chaos is that streamlines must cross at two consecutive instants.

A very interesting step towards a realizable flow is the blinking pair of line vortices suggested by Aref [Aref, 1984]. Consider some dyed fluid which starts near one line vortex, and let that vortex turn while the other remains at rest. The dye will be sheared by the near vortex and after sufficient time will be spread around through its initial position. Now stop the first vortex and switch on the second. The shear flow from the second vortex will be perpendicular to the shear from the first at most locations. The dye will therefore be stretched efficiently for the first few strains. On then switches back to the first vortex and continues in a cyclic manner, hence the name "blinking pair of vortices".

While the dye remains near the first vortex, one can see the dye stretched out by the far vortex and then wrapped round by the near vortex. This stretching-and-folding is essential for good mixing in finite devices, the stretching of interfacial area being the good mixing and the folding being necessary to fit exponentially stretching material into a finite space.

1.4 Mixing and heat transfer quantification

1.4.1 Direct statistical methods to quantify mixing

There are several quantification methods to evaluate mixing. Because good mixing is understood as the homogeneity of the mixed results, the distribution of the scalar values c of an image or a cross section area in a computational domain can be used for evaluating the degree of mixing [Nguyen, 2011].

The normalized concentration (which also can be the temperature field or a passive scalar or any field of interest) in a cross sectional area of the domain is defined by:

$$c^* = \frac{c - c_{min}}{c_{max} - c_{min}} \tag{1.4}$$

The probability values can be obtained by normalizing the number of each scalar value by the total number of the scalar values in the evaluated region:

$$P(c^*) = P(c) = \frac{N(c)}{\sum_{c_{min}}^{c_{max}} N(c)} \tag{1.5}$$

Figure 1.7 shows the typical results of probability density functions (PDFs) of a micromixer. In a region such as the entrance region, where the two fluids are not mixed, there exist two predominant

concentration values of 0 and 1 resulting in two separate peaks as shown in Figure 1.7 (a). In a region of well-mixed fluids, the predominant concentration is 0.5 resulting in a single peak as shown in Figure 1.7 (b).

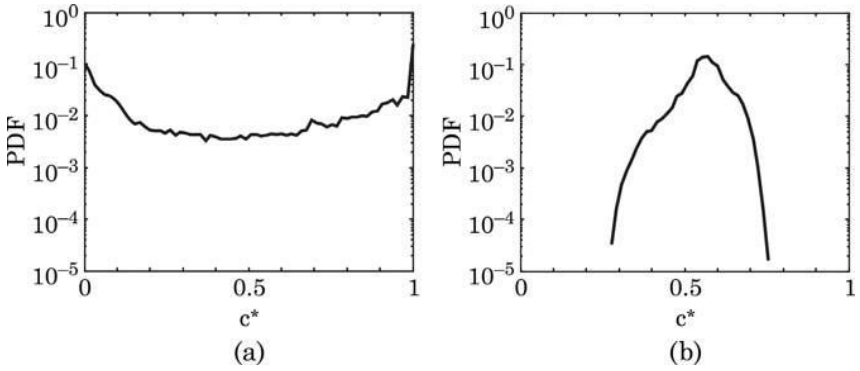

Figure 1.7: Probability density function of: (a) non mixed region; (b) well mixed region [Nguyen, 2011]

The homogeneity can be expressed as the standard deviation of the concentration values:

$$\sigma_{st} = \sqrt{\frac{1}{N}\sum_{i=1}^{N}\left(c_i^* - \overline{c^*}\right)^2} \tag{1.6}$$

where the normalized concentration c^* is calculated according to Eq.(1.4), and $\overline{c^*}$ is the mean normalized concentration. If the expected normalized is $\overline{c^*} = 0.5$, the standard deviations are 0.5 and 0 for the unmixed case and mixed case respectively.

The standard deviation can be normalized again by the mean concentration to get the coefficient of variation:

$$CoV(c^*) = \sqrt{\frac{1}{N}\sum_{i=1}^{N}\left(\frac{c_i^* - \overline{c^*}}{\overline{c^*}}\right)^2} \tag{1.7}$$

Therefore, the coefficient of variation (CoV) varies from 1 to 0. For convenience, the mixing index can also be defined based on the coefficient of variation:

$$MI(c^*) = 1 - CoV(c^*) = 1 - \sqrt{\frac{1}{N}\sum_{i=1}^{N}\left(\frac{c_i^* - \overline{c^*}}{\overline{c^*}}\right)^2} \tag{1.8}$$

The mixing index is 1 if the two fluids are fully mixed and 0 if they are fully unmixed.

1.4.2 Heat transfer quantification

1.4.2.1 Thermal performance

In order to quantify the heat transfer performance, the Nusselt number has to be calculated which is defined as the ratio of convective to conductive heat transfer across a boundary. Two notions of Nusselt number are usually used, local and global Nusselt numbers which are defined as follows:

$$\mathrm{Nu}_x = \frac{q"_x D_h}{k_{th}\left(T_w - T_b(x)\right)} \tag{1.9}$$

$$\mathrm{Nu}_{0-L} = \frac{q"_{0-L} D_h}{k_{th}\left(T_w - T_{mean}\right)} \tag{1.10}$$

where $q"_x$ is the local wall heat flux, $q"_{0-L}$ is the heat flux averaged from $x = 0$ to the overall heat exchanger length L, D_h is the hydraulic diameter of the studied configuration, k_{th} is the thermal conductivity of the working fluid, T_w is the wall temperature or the heated surface temperature,

$T_{mean} = (T_{b,outlet} + T_{b,inlet})/2$ is the mean temperature, and $T_{b,inlet}$ and $T_{b,outlet}$ are the bulk temperatures respectively at the heat exchanger inlet and outlet where the bulk temperature T_b is defined on a cross section A by:

$$T_b = \frac{\int_A U(x)T(x,y,z)dA}{\int_A U(x,y,z)dA} \tag{1.11}$$

where U and T are the velocity magnitude and temperature at a specific location (x, y, z) in the heat exchanger.

In addition to the calculations of the Nusselt number, the friction factor is computed in order to account for the pressure drop in a given MHER design and is defined by:

$$f = \frac{2D_h}{4L}\frac{\Delta P}{\rho_f \overline{U}^2_{f,inlet}} \tag{1.12}$$

where ρ_f is the density of the working fluid, $\overline{U}_{f,inlet}$ is the average flow velocity at the inlet and ΔP is the pressure drop between the heat exchanger inlet and outlet. Moreover, to evaluate the thermal efficiency at constant pumping power, usually the thermal performance factor η is to be calculated:

$$\eta = \left(\frac{\mathrm{Nu}_{0-\mathrm{L}}}{\mathrm{Nu}_0}\right)\left(\frac{f}{f_0}\right)^{-\frac{1}{3}} \tag{1.13}$$

where the subscript 0 refers to the results of empty pipe or channel simulations. Values of η higher than unity are considered an increase in the thermal performance of the heat exchanger.

Another factor allowing to compare the energy efficiency of the heat exchanger is the Colburn factor defined by:

$$j = \frac{\mathrm{Nu}_{0-\mathrm{L}}}{\mathrm{Re}_{D_h}\mathrm{Pr}^{\frac{1}{3}}} \tag{1.14}$$

with Pr and Re_{D_h} respectively the Prandtl number and Reynolds number calculated based on the hydraulic diameter of the studied configuration. The Colburn factor quantifies the ratio of the thermal power transferred to the mechanical power consumed. For a given fluid, and a specific Reynolds number, a higher Colburn factor means a higher efficiency of heat transfer.

1.4.2.2 Field synergy principle

Guo *et al.* [Guo et al., 1998] proposed a novel concept to enhance convective heat transfer: the reduction of the angle between the velocity and temperature gradient. This can briefly be demonstrated starting from the energy equation:

$$\rho_f C_p(\boldsymbol{U} \cdot \boldsymbol{\nabla} T_f) = k_{th}\boldsymbol{\nabla^2} T_f \tag{1.15}$$

where $\boldsymbol{U}$ and T_f are respectively the local velocity field and fluid temperature distribution in Cartesian coordinates. By integrating over the whole domain of interest using Gaussian integration and neglecting the axial conduction since the Péclet number is greater than 100 in most engineering applications, the energy equation becomes:

$$\rho_f C_p \iiint_{Vol}(\boldsymbol{U} \cdot \boldsymbol{\nabla} T_f)dxdydz = q''_w \propto \mathrm{Nu} \tag{1.16}$$

with the total heat flux q''_w proportional to the Nusselt number Nu. In fact, the Nusselt number depends on the dot product $\boldsymbol{U} \cdot \boldsymbol{\nabla} T_f = \| \boldsymbol{U} \| \times \| \boldsymbol{\nabla} T_f \| \times \cos(\alpha)$, where α is the angle between the velocity vector and the temperature gradient. It is obvious that for a fixed flow rate and temperature difference, the smaller the angle between the velocity and temperature gradient, the larger the heat

transfer rate [He and Tao, 2014, Wu and Tao, 2007, Zhang et al., 2009, Li et al., 2014]. Thus, α can be obtained by the following expression:

$$\alpha = \arccos\left(\frac{U\frac{\partial T_f}{\partial x} + V\frac{\partial T_f}{\partial y} + W\frac{\partial T_f}{\partial z}}{M}\right) \tag{1.17}$$

where M is the local module production and is defined as:

$$M = \sqrt{U^2+V^2+W^2}\sqrt{\left(\frac{\partial T_f}{\partial x}\right)^2 + \left(\frac{\partial T_f}{\partial y}\right)^2 + \left(\frac{\partial T_f}{\partial z}\right)^2} \tag{1.18}$$

It is important to note that optimizing a synergy angle in a part of the domain where the module production M has a relatively small value has very little influence on enhancing heat transfer and consequently is out of interest.

Local analysis of the field synergy principle is as important as a global analysis. From the local intersection angle, the average intersection angle of the computational domain can be obtained by using numerical integration:

$$\alpha_{ave} = \frac{\sum \alpha_{i,j,k}\mathrm{d}v_{i,j,k}}{\sum \mathrm{d}v_{i,j,k}} \tag{1.19}$$

where $\mathrm{d}v_{i,j,k}$ is the volume element of the control volume (i,j,k). In addition to the average angle α_{ave}, the module production parameter is usually introduced in the analysis of heat transfer using the field synergy principle and is defined as:

$$M_{ave} = \frac{\sum \parallel \boldsymbol{U} \parallel \times \parallel \boldsymbol{\nabla} T_f \parallel}{N} \tag{1.20}$$

where N is the number of control volumes covering the entire grid.

Nevertheless, it has to be noted that the field synergy angle is not always reliable to assess heat transfer enhancement because higher synergy angles don't necessarily mean a deterioration of heat transfer. For example, Tao *et al.* [Tao et al., 2007] displayed the effect of Reynolds number in a fin and tube heat exchangers on Nusselt number, synergy angle and module production. Figure 1.8 (a) shows that as the Reynolds number increases, the Nusselt number increases and thus the convective heat transfer. Moreover, Figure 1.8 (b) displays the variation of the average angle between velocity and temperature gradient and Figure 1.8 (c) provides the relation between M_{ave} and Re. It can be seen that the synergy angle increases with increasing Re implying then a deterioration of the synergy between velocity and temperature gradient, although Nusselt number gets increasing values. This is actually explained by the fact that the values of M_{ave} are proportional with Re and this term has also to be taken into consideration for heat transfer analyses.

Habchi *et al.* [Habchi et al., 2011] furthermore used the field synergy method in order to compare the heat transfer performances of vortex generators inserted in a round tube and proposed another more appropriate formulation. Three configurations were studied: in the first, the vortex generators were aligned and inclined in the flow direction (aligned geometry); in the second, a periodic rotation of $45°$ has been applied to the tab arrays (alternating geometry) and in the third, the vortex generators were reversed in the direction opposite to the flow (reversed geometry). For global analysis, Habchi *et al.* [Habchi et al., 2011] indeed concluded that the average synergy angle α_{ave} did not properly reflect the heat transfer enhancement, since in Figure 1.9 (b), α_{ave} remains constant with Reynolds number even though the heat transfer is increased as observed in Figure 1.9 (a). In this case, the increase in $\parallel \boldsymbol{U} \parallel$ and $\parallel \boldsymbol{\nabla} T_f \parallel$ is the reason behind the heat transfer enhancement. Then, for local analysis, they instead used the dot product of $\boldsymbol{U} \cdot \boldsymbol{\nabla} T_f$ to observe the regions of high heat transfer (see Figure 1.10) since the synergy angle alone was demonstrated not to be sufficient for local heat transfer analysis.

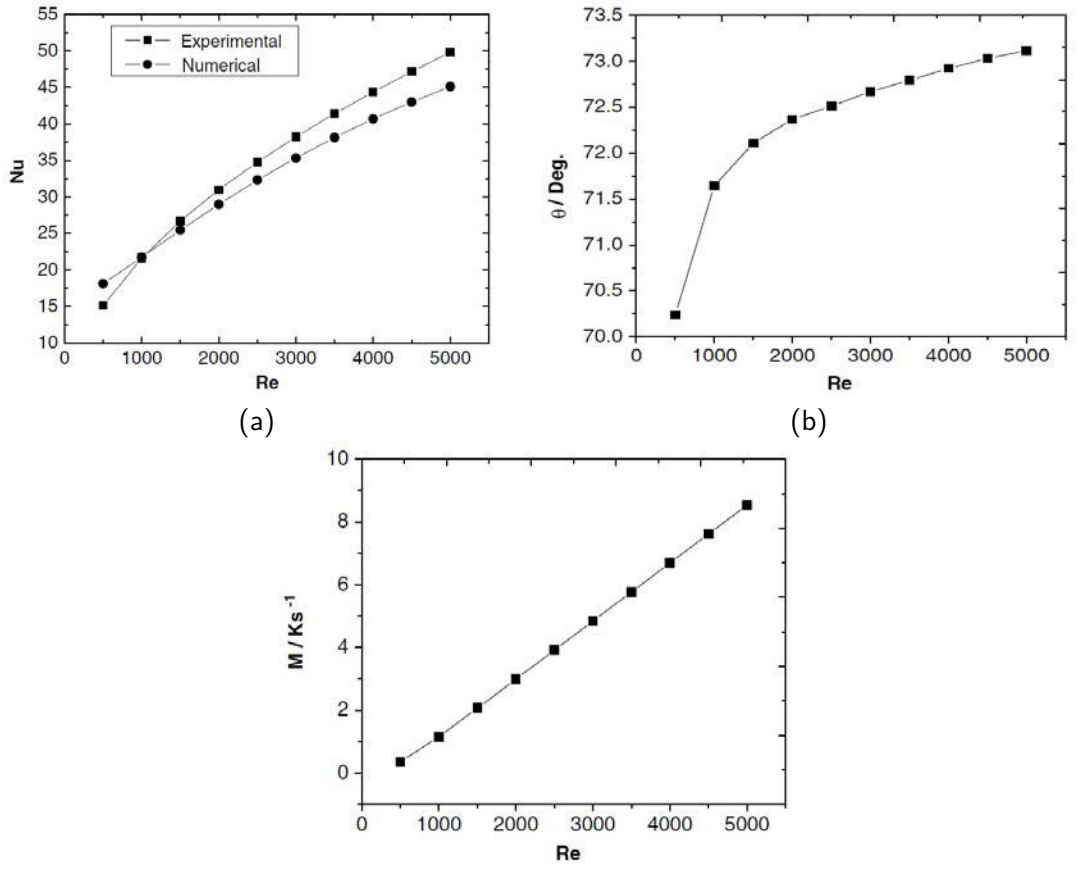

Figure 1.8: Variation of heat transfer parameters in fin and tube heat exchangers: (a) effect of Reynolds number on Nusselt number; (b) Variation of intersection angle; (c) Variation of module production [Tao et al., 2007]

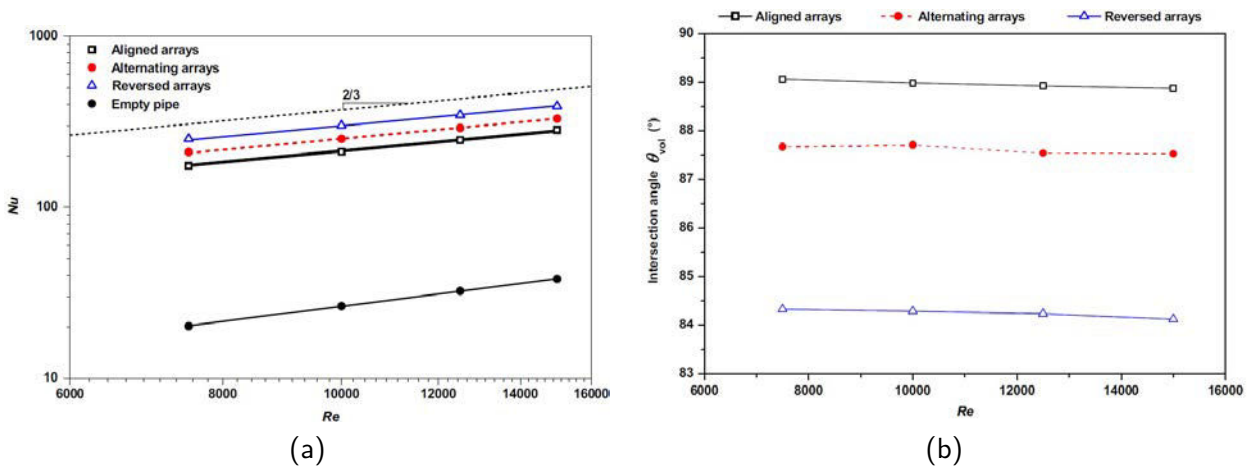

Figure 1.9: (a) Nusselt number versus Reynolds number and (b) average intersection angle versus Reynolds number for aligned, alternating and reversed geometries [Habchi et al., 2011]

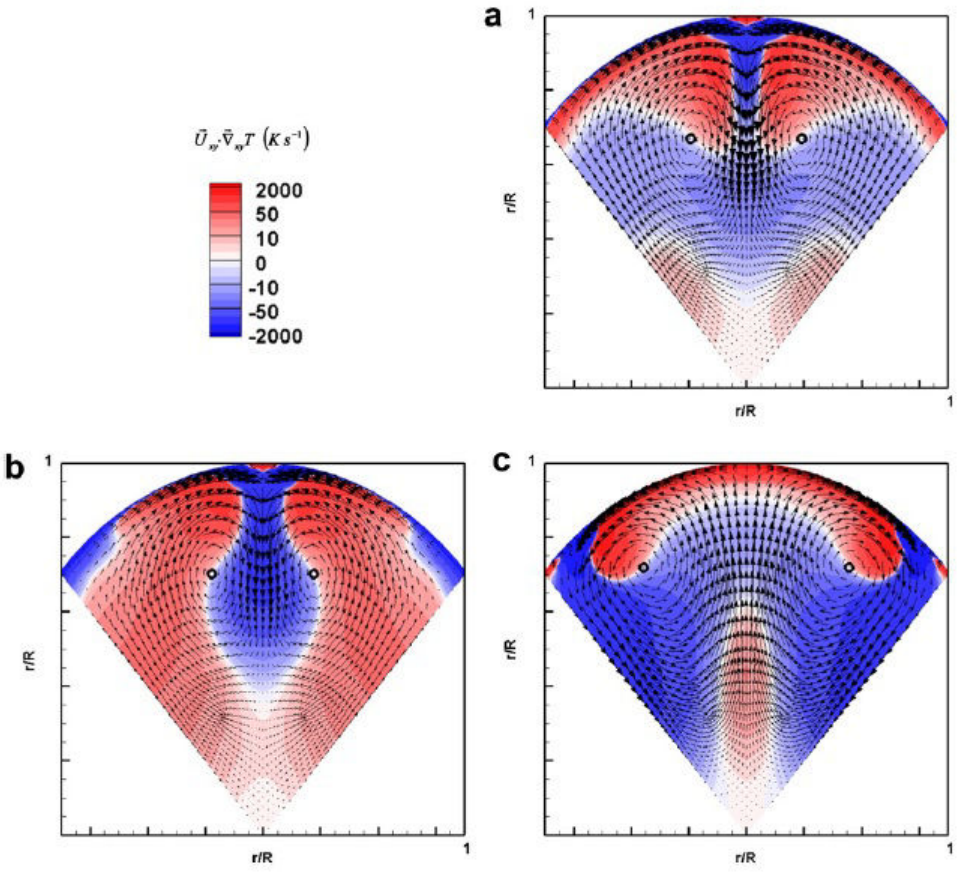

Figure 1.10: Distribution of the field synergy in a cross sectional view for (a) aligned; (b) alternating and (c) reversed arrays at Re=15,000 [Habchi et al., 2011]

1.5 Mixing and heat transfer enhancement by passive methods

Compact heat exchangers offer many opportunities in terms of heat transfer. However, to be used as reactors in the chemical processing industry, they must be characterized in terms of mixing efficiency and residence time distributions. Indeed, mixing has an important influence on product quality in industrial reactions such as polymerization or precipitation and it may be a limiting parameter for instantaneous reactions.

An efficient way to enhance mixing performance would be to work in the turbulent flow regimes. Nevertheless, this approach is not suitable in some applications and furthermore involves a significant increase of pressure drops and a reduced residence time. As a consequence, the challenge of adding inserts in compact heat exchangers is important to enhance both heat and mass transfer while staying in a laminar regime. In the literature, different geometries have been tested and are presented below.

1.5.1 Offset strip fins

The offset strip fin is one of the widely used finned surfaces, particularly in high effectiveness heat exchangers employed in cryogenic and aircraft applications. These fins are created by cutting a set of plain rectangular fins periodically along the flow direction, and shifting each strip thus generated by half the fin spacing alternating leftward and rightward.

The flow is thus periodically interrupted, leading to formation of new boundary layers and consequent heat transfer improvement. Interruption of flow also leads to greater viscous pressure drop manifested by a higher value of effective friction factor. In addition of wall shear, resistance to flow increases due to both drag force over the leading edges of the fin sections facing the flow and trailing edges vortices. The increase in the effective heat transfer coefficient and friction factor is a consequence of these mechanisms. Figure 1.11 shows a schematic view of the rectangular offset strip fin surface and defines the geometric parameters i.e. b, s, h and ℓ.

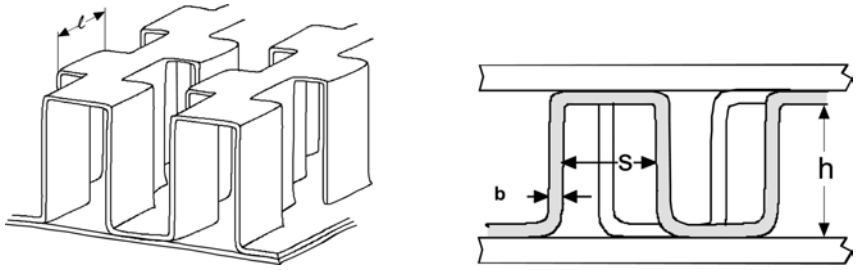

Figure 1.11: Offset strip fin geometry [Ferrouillat et al., 2006]

Many experiments have been carried out in order to quantify the mixing level of an apparatus filled with offset strip fins, to characterize it and to compare its properties with an empty duct channel so as to implement chemical reactions [Ferrouillat et al., 2006]. First of all, to evaluate and then compare the mixing level of offset strip fins with an empty duct channel, Ferrouillat *et al.* [Ferrouillat et al., 2006] used a chemical engineering method developed by Villermaux and co-workers [Fournier et al., 1996]. Three geometries of offset strip fins (OSF 1, OSF 2 and OSF 3 described in Table 1.1), inserted into the same duct channel, were tested and compared with an empty duct channel.

Table 1.1: Offset strip fins characteristics [Ferrouillat et al., 2006]

Fin type	OSF 1	OSF 2	OSF 3
b (mm)	0.1	0.3	0.3
s (mm)	1.4	3.0	1.2
ℓ (mm)	3.2	1.6	3.2
h (mm)	6.25	6.05	6.05

They showed that turbulence, micromixing and pressure drops depend on the geometry, the size and the number of fins. For instance, whatever the geometry, the micromixing time decreases

with flow rate. Moreover, for a given flow rate, the empty duct channel is the worst in micromixing performance as shown in Figure 1.12, then for a given micromixing time, the empty duct channel must work at too high velocities, implying an increase in the volume of multifunctional heat exchanger. For a given micromixing level, insert geometries allows to reduce the volume of the reactor but leads to a pumping power increase. In process design it is thus necessary to take into account the pumping power required for the system, the process compactness, and the micromixing level required.

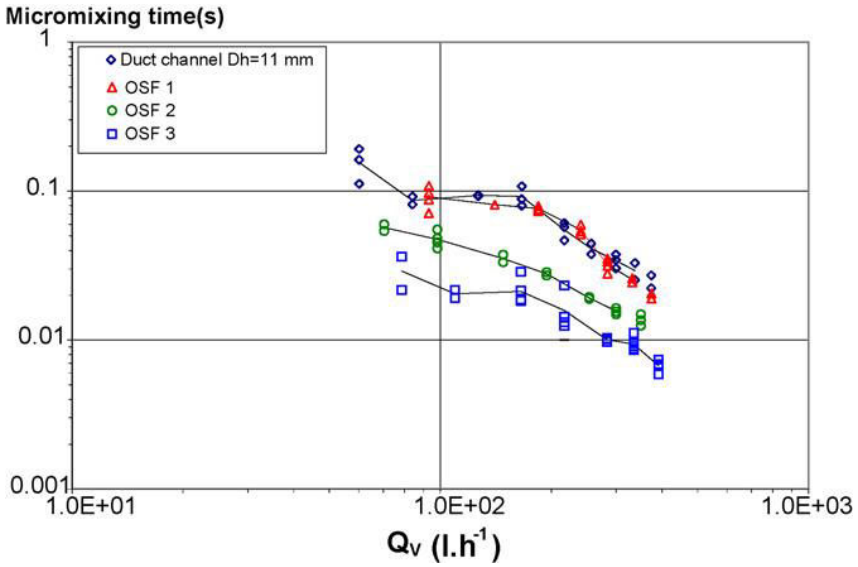

Figure 1.12: Micromixing time versus flow rate for three different offset strip fins (OSF) and a duct channel [Ferrouillat et al., 2006]

1.5.2 T-mixers

Figure 1.13 illustrates the entrance region of a T-mixer. Due to the sharp 90° turn at the entrance, vortices are formed due to the large inertia force which will result in chaotic advection. In fact, the laminar regime can be divided into three subregimes: stratefied, vortex and engulfment [Bothe et al., 2006]. In the stratefied regime (Re<50), the two inlet streams flow side by side and the only transport phenomena available is molecular diffusion. In the vortex regime (50<Re<150), Dean vortices are present but they are symmetrical between the two streams. In the engulfment regime, (Re>150), the Dean vortices become asymmetrical and chaotic advection takes place and is particularly suitable for mixing.

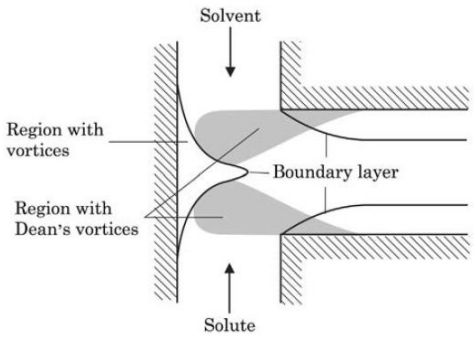

Figure 1.13: Mixing regions and boundary layers at the entrance of a T-mixer [Nguyen, 2011]

Figure 1.14 shows the trajectory of fluid particles at the entrance of a T-mixer [Bothe et al., 2006]. At the Reynolds numbers on the order of units, the flow is stable as shown in Figure 1.14 (a). At higher Reynolds number depicted in Figures 1.14 (b) and (c), the trajectories clearly show the appearance of vortices due to secondary flow caused by the centrifugal force at the 90° turn. However

no mixing will occur at Re=119 as in Figure 1.14 (b) since the vortices are symmetric, thus the solute and the solvent will remain in their particular half. As the Reynolds number increases to Re=146, the symmetry of the vortices is destroyed as illustrated in Figure 1.14 (c). Hence, the inertia force in this case is strong enough to make the fluid streams cross each other halves in the mixing channel.

Consequently, the transport process at high Reynolds (Re>100) is mostly due to chaotic advection here but not turbulence. Figure 1.15 illustrates the stretching and folding of the scalar at higher Reynolds numbers. The reduction in the striation thickness and the increase in the interfacial area between the different concentrations will lead eventually to better mixing.

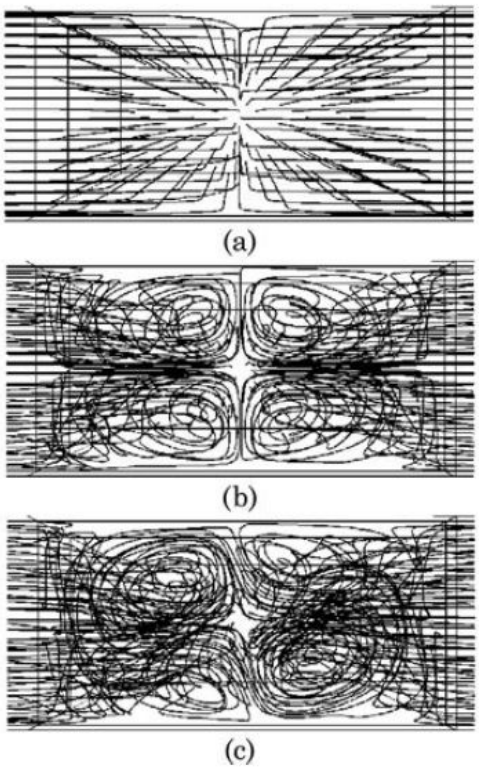

Figure 1.14: Trajectory of flow near the entrance of a T-mixer at different Reynolds numbers: (a) Re=1.32; (b) Re=119; (c) Re=146 [Bothe et al., 2006]

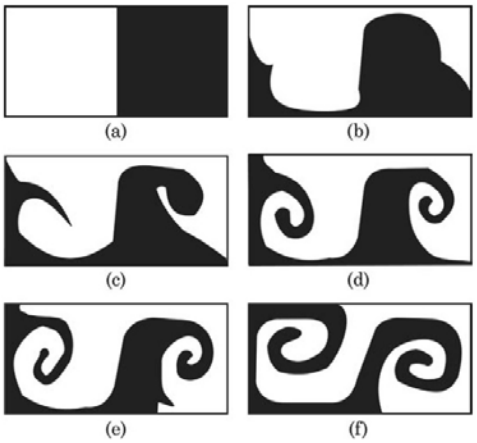

Figure 1.15: Concentration distribution at different Reynolds number: (a) Re=119; (b) Re=139;(c) Re=146; (d) Re=153; (e) Re=159; (f) Re=186 [Bothe et al., 2006]

1.5.3 Dean flow in curved pipes

The flow field inside a curved pipe was first described and analyzed by Dean *et al.* [Dean and Hurst, 1959] and has also been studied through various works as reported in Berger *et al.* [Berger et al., 1983]. The flow in this case is characterized by the Dean number:

$$\mathrm{De} = \mathrm{Re}\sqrt{\frac{D}{R}} \tag{1.21}$$

where D is the diameter of the pipe and R is the radius of curvature of the path of the pipe. As previously stated, Dean vortices at the 90° turn in a T-mixer are the reason behind chaotic advection at high Reynolds number. Thus, repeating the turns will involve an intensification of the effect of Dean's secondary flows. Figure 1.16 illustrates the concept of Dean vortices in a closed circular channel with a rectangular cross section. At high Dean number De>150 [Jiang et al., 2004], two pairs of vortices appear.

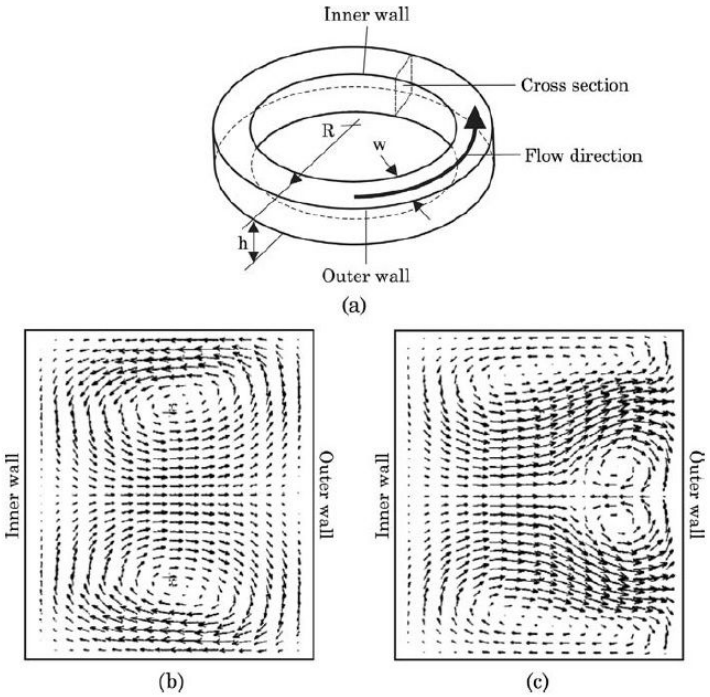

Figure 1.16: Dean vortices at different Dean numbers: (a) channel geometry; (b) flow patterns at De<150; (c) flow patterns at De>150 [Jiang et al., 2004]

Dean vortices can also be obtained by repeating the turns in curved sections as illustrated in Figure 1.17 (a) [Jiang et al., 2004]. By alternating the signs of the radius of curvature, the two Dean vortices appear at low Dean numbers as in Figure 1.16 (a). Folding and stretching of the fluid occurs because of this effect but efficient mixing is not present. At higher Dean number, above the critical value De>150, a secondary vortex pair is obtained. As the small vortices sweep from one side to the other, the flow become asymmetric and makes the chaotic advection possible in the channel. Experimental results of Jiang *et al.* [Jiang et al., 2004] show that the mixing time is inversely proportional to Dean number.

Moreover, sharp 90° turns as proposed in Figure 1.17 (b) are also studied by Mengeaud *et al.* [Mengeaud et al., 2002] where spatially periodic flows can occur at high Reynolds number. They used the ratio between the period s and the channel width w as the optimization parameter. Chaotic advection occurs above a critical Reynolds number of 80. For a given Reynolds, an optimal value of the ratio between s and w based on the mixing efficiency is observed. For example, the numerical results show an optimal geometry ratio of 4 for a Reynolds number of 267, for which the mixing efficiency increases up to 98.6%.

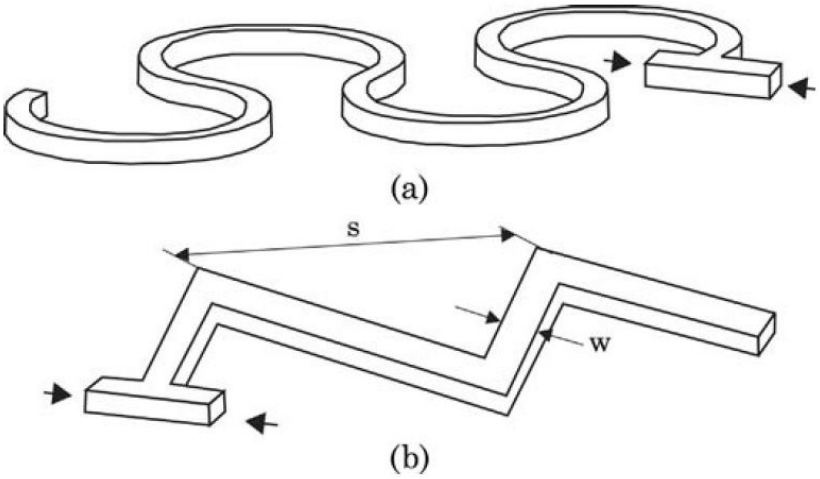

Figure 1.17: Designs based on Dean flow: (a) curved channels [Jiang et al., 2004] and (b) 90° turns [Mengeaud et al., 2002]

Lemenand *et al.* [Lemenand et al., 2014] compared the droplet sizes obtained in helical (regular) and alternating (chaotic) static mixers of the same cross section and the same tube length. The coils of the static mixer are assembled from 90° bends, and the chaotic configuration is obtained by turning each bend by $\pm$ 90° with respect to the previous one as shown in Figure 1.18. The results from the liquid/liquid dispersion achieved in the twisted pipes are more efficient from that in the helically coiled pipe. In fact, the droplet size distribution for a flow with pure water and oil are obtained as shown in Figure 1.19. It can be seen that the standard deviation for the drop-size distribution is about 20% lower for the twisted pipe than for the helically coiled pipe with similar Dean number. This effect is reflected in creating more effective drop break-up than in the helical configuration because lower droplet diameters are observed.

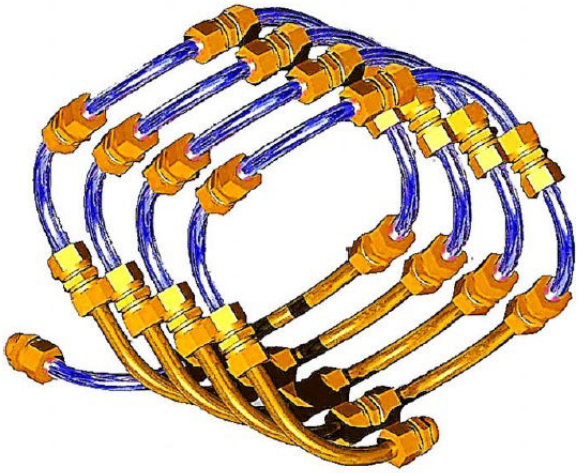

Figure 1.18: Twisted pipe design [Habchi et al., 2009]

Moreover, Habchi *et al.* [Habchi et al., 2009] interpreted the dispersive performance of the twisted pipe configuration when compared to a helically coiled pipe. The dispersive performance is provided by the Lagrangian trajectories of particles injected at a given initial position. Figure 1.20 shows the Poincaré section for the helically coiled and chaotic twisted pipe configurations. It is observed that in the helically coiled configuration, the particles remain in the roll-cell while in the chaotic case, the particles spread over the whole tube section.

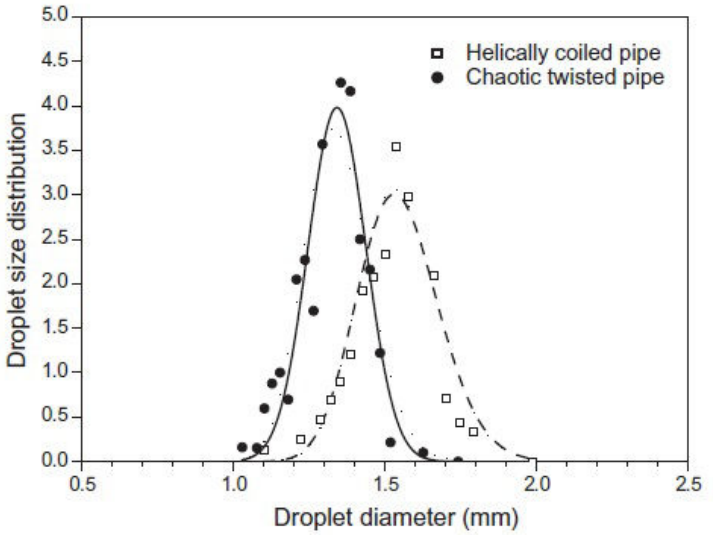

Figure 1.19: Droplet size distribution for helically coiled and chaotic twisted pipe flows with pure oil and water emulsification for De=50 [Lemenand et al., 2014]

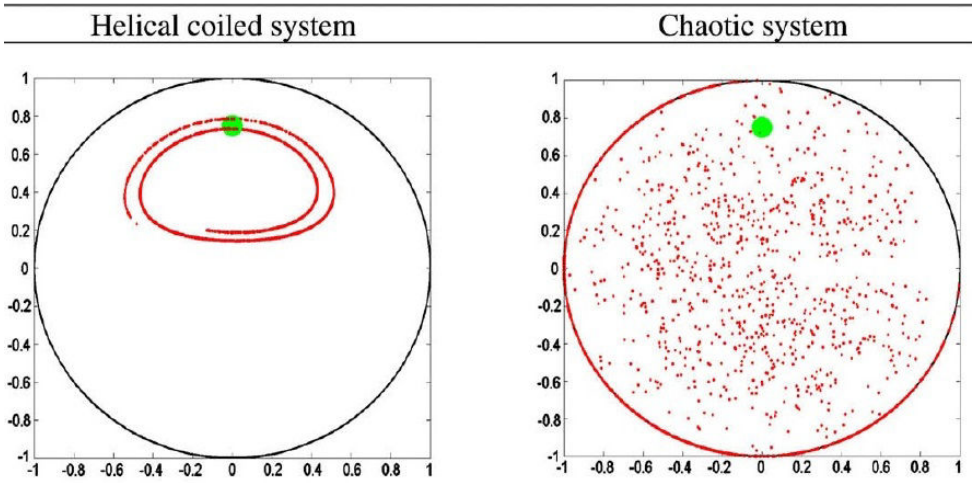

Figure 1.20: Poincaré section ($\mathrm{De} = 150$, $\mathrm{Re} = 81$) [Habchi et al., 2009]

1.5.4 Vortex generators

One of the effective ways to increase the heat transfer coefficient is to decrease the thermal resistance of the sublayer adjacent to the wall immediately where the viscous effects of the sublayer are dominant. This can be achieved by increasing the turbulence of the fluid flow in the main stream so that the quasi-streamwise wall eddies will be closer to the wall and so more efficient. The thermal resistance can also be reduced and heat transfer can be augmented by using vortex generators (VGs) that allow disrupting the growth of the boundary layer and also make fluid swirling. This swirl effect causes exchange between the core and wall fluid, leading to the enhancement of heat transfer between the flowing fluid and the channel walls. The VGs may be categorized whether they produce transverse vortices (TV) or longitudinal vortices (LV). The rotation axis of longitudinal vortices is parallel to the main flow direction whereas the axis of the transverse vortices is normal to the flow direction. In general, the LVs have been reported to be more effective than TVs on heat transfer enhancement [Wu and Tao, 2008b] and longitudinal vortex generators (LVGs) are actually one of the most widely used passive methods. They can be mounted on channel surfaces to generate longitudinal vortices which create secondary flows and disrupt the growth of the boundary layer. LVGs have been extensively studied due to their high heat transfer performances.

The heat transfer enhancement by using LVGs depends on many parameters such as their shape,

their geometries, their position from the leading edge of the test duct, and angles of attack. As shown in the review of heat transfer enhancement techniques of Jacobi *et al.* [Jacobi and Shah, 1995], four basic configurations of LVGs are delta wings, rectangular wings, delta-winglets and rectangular winglets (see Figure 1.21).

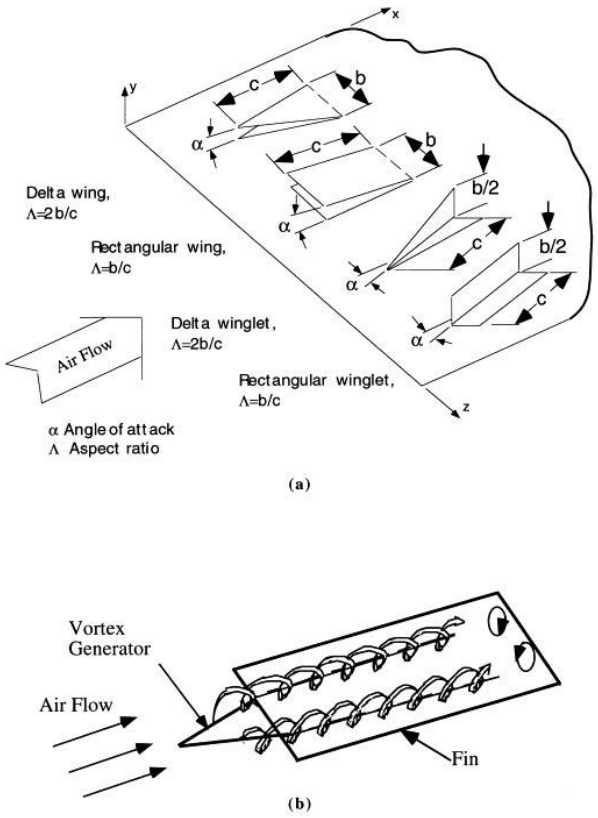

Figure 1.21: (a) Common vortex generator types; (b) longitudinal vortices that are generated passively [Jacobi and Shah, 1995]

Winglets have been successfully used in order to improve the convective heat transfer rate of modern thermal systems because they can generate intensive longitudinal vortices with low pressure drop penalties [Allison and Dally, 2007].

Yakut *et al.* [Yakut et al., 2005a] analyzed various kinds of design parameters on heat transfer and flow characteristics of the tapes with delta-winglet vortex generators. They pointed out that most effective parameter affecting the heat transfer is the Reynolds number. Heat transfer can be successfully improved by increasing the Reynolds number, also it has the most important influence on the amplitude of pressure fluctuations, while the most effective parameter with respect to the friction factor is the winglet height.

Min *et al.* [Min et al., 2010] studied the effect of modifying the rectangular vortex generator by cutting off the four corners of a rectangular wing as shown in Figure 1.22. Fluid flow and heat transfer characteristics of this vortex generator mounted in a rectangular channel were experimentally investigated and compared with those of original rectangular vortex generator. Results showed that the modified rectangular wing pairs have better flow and heat transfer characteristics, and also lower friction factors than those of rectangular wing pair, the average Nusselt number Nu increases with the attack angle and 55° angle shows that highest average Nusselt number which was 46-55% higher compared to plain channel in the range of their operating conditions.

Numerically, Habchi *et al.* [Habchi et al., 2012] performed 3D simulations to study the heat transfer in turbulent vortical flows. Vorticity is generated by inclined vortex generators in a turbulent circular pipe flow with different configurations that fall into three categories which are, rows of trapezoidal vortex generators in different arrangements; vortex generators fixed at certain distance from the tube wall, and vortex generators rows between which a row of small protrusions are inserted on the tube wall. They pointed out that the longitudinal variation of local Nusselt number computed

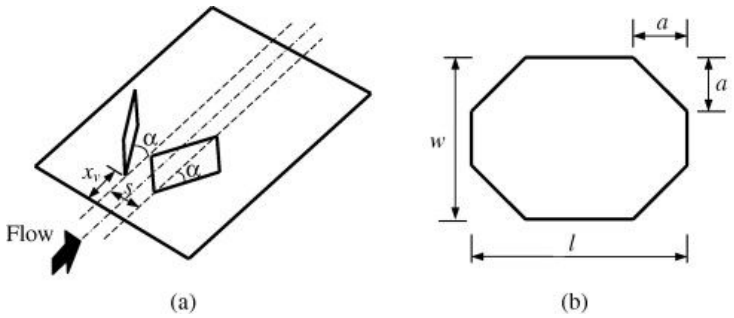

Figure 1.22: Schematic view of modified vortex generator: (a) common flow down (CFD) wing; (b) modified rectangular wing [Min et al., 2010]

in different high-frequency vortex mixer cross sections shows the advantage of using protrusions between successive vortex generator rows in which they increase the local heat transfer by increasing the temperature gradients and vorticity very close to the heated wall as shown in Figure 1.23.

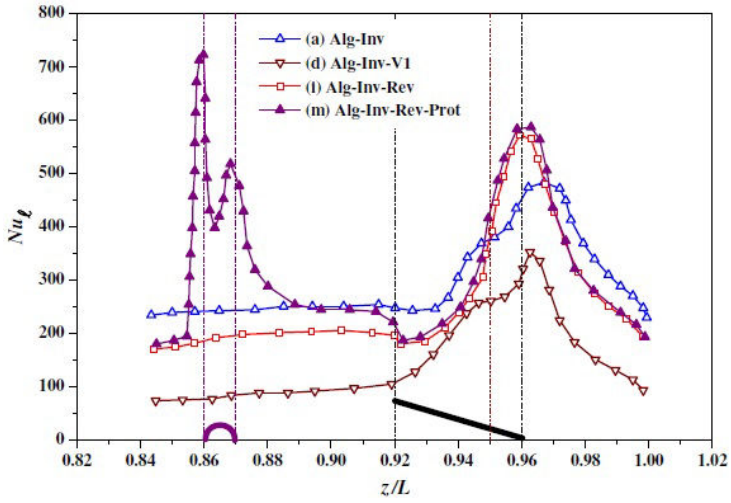

Figure 1.23: Longitudinal variation of the Nusselt number for Re=15000 [Habchi et al., 2012]

Wu and Tao [Wu and Tao, 2008b,Wu and Tao, 2008a] investigated the heat transfer characteristic in a rectangular channel with a pair of rectangular wing vortex generators mounted on the lower wall of the channel. Reynolds number was ranged from 800 to 3000. They remarked that the thickness of the rectangular winglet vortex generator (RWVG) can cause less heat transfer enhancement in the region near the VG. They found that the pressure drop in the rectangular channel with RWVG increases rapidly with the increase of the angle of the LVG. They observed that the thickness of LVG has little influence on the average friction factor of the channel. The LVGs can improve the synergy between the velocity and temperature fields not only in the region near LVG but also in the large downstream region of the LVG. LVs enable to enhance the global heat transfer of the channel, whereas TVs can only enhance the local heat transfer of the channel. The attack angle of 45° of VG always provides the better effectiveness of heat transfer enhancement. They found that Nusselt number decreases with the LVG's location away from the inlet of the channel and decreases too when the space between the LVG pair decreases. They observed also that the heat transfer was improved better with the increasing length of RWVG and decreasing height of RWVG when the area of LVG was fixed. They found that the delta winglet vortex generator (DWVG) is more effective than RWVG on Nusselt number at the same area of LVG.

Sanders and Thole [Sanders and Thole, 2006] tested the effect of attack angle, aspect ratio, direction, and shape of winglet in a laminar regime. They highlighted that the best heat transfer improvement is found with rectangular winglets pair of VG and is around 3%, 36%, and 38% at Reynolds numbers of 230, 615, and 1016, respectively. There were three primary winglet orientations

and directions tested as shown in Figure 1.24: winglets all aimed toward the wall VG-F, winglets with alternating direction and orientation (VG-F/B) and winglet only in the backward orientation but alternating in direction (VG-B) . In the configuration where all of the winglets were aimed towards the wall in the VG-F (Forward orientation) configuration, the average heat transfer augmentations were typically very low. When the winglet direction and orientation were alternated on every other louver, results were significantly improved with a maximum increase of 25%. When all the winglets were placed in VG-B (Backward orientation) with alternating direction, results improved yielding augmentations of up to 33%.

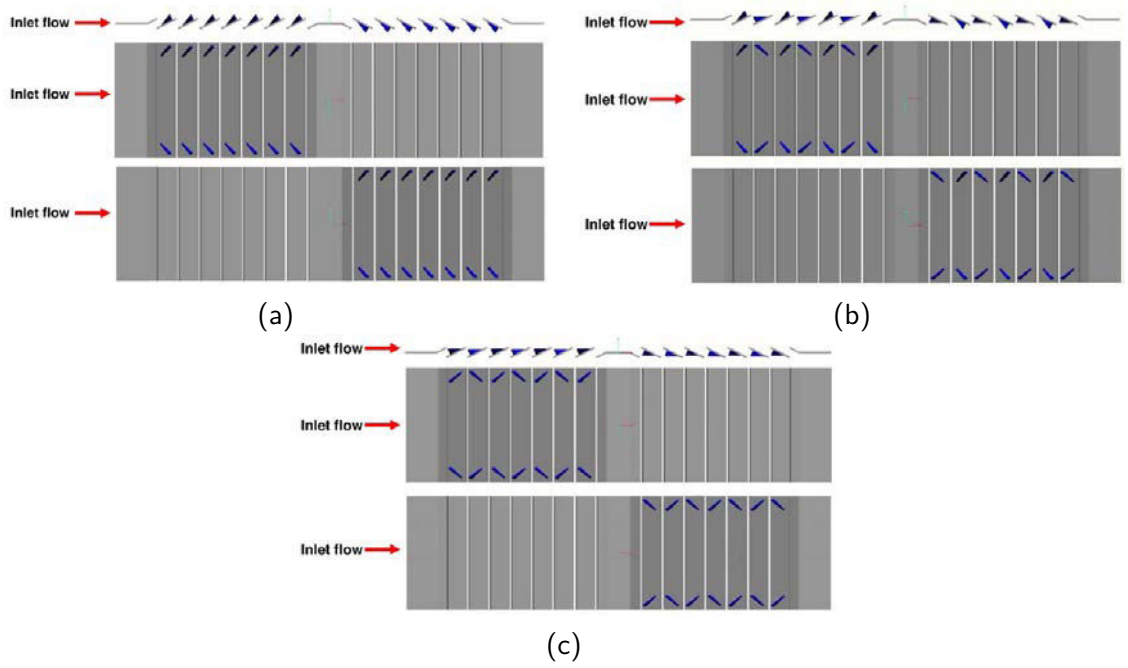

Figure 1.24: Side, top, bottom view of VG: (a) VG-F winglets all aimed toward the wall; (b) VG-F/B alternating winglets; (c) VG-B winglets with alternating direction [Sanders and Thole, 2006]

1.6 Mixing and heat transfer enhancement by rigid structural oscillations

Vortices which are naturally formed in the internal and external flows induce a flow towards the heat transfer surface. This flow may enhance the local heat transfer appreciably. Thus, heat transfer rate can be enhanced by modifying the geometric surfaces or flow structures. It seems the main purposes of the vortex generators is to increase transverse fluid mixing and to reduce the thermal boundary layer thickness by vortices. However, most of the vortex generators mentioned above are fixed and classified as passive means to generate vortices. The number of vortices generated by these methods is limited.

The literature on enhancing heat and mass transfer using oscillating structures is relatively scarce and most of them use active methods to control the frequency, velocity, amplitude of oscillations of the produced structures. In this section some of the work previously done will be presented followed by our proposed method which will be the main discussion of this thesis work and which will be based on vortex-induced vibration (VIV) of structures, a subject of practical interest to many fields of engineering.

Yang [Yang, 2003] performed two dimensional numerical simulation to study the unsteady flow and heat transfer in a channel with an oscillating bar as shown in Figure 1.25, which is called an oscillating vortex generator. The effects of Reynolds number based on the channel height ($\mathrm{Re} = 100 - 800$), maximum oscillating speed, oscillating amplitude and oscillating frequency of the bar on

the flow and heat transfer were examined in details.

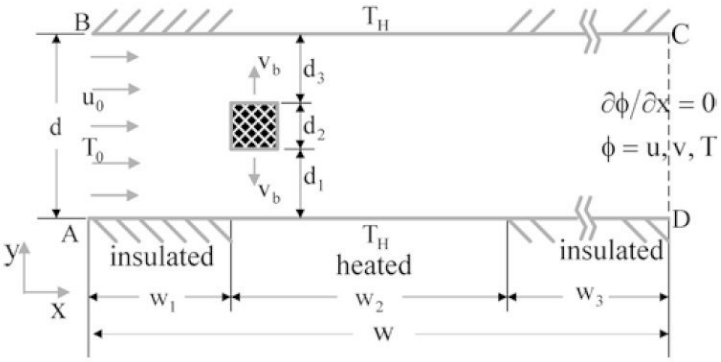

Figure 1.25: Oscillating vortex generator in a channel flow [Yang, 2003]

Some conclusions about these numerical simulations can be summarized as follows:

- The transverse vortices are formed actively and largely behind the bar because of its oscillation in the channel. The high temperature wall flow is carried away from the heated regions to mix with the low temperature core flow by the transverse vortices, thus enhancing the heat transfer remarkably.
- The heat transfer rate is strongly dependent on the oscillating amplitude of the bar because the transverse vortices behind the bar could be more drastic as the bar oscillates with larger amplitudes.
- For the same oscillating amplitude of the bar, the heat transfer augmentation is significantly decreased when the maximum oscillating speed or the oscillating frequency of the bar is larger.
- The heat transfer is greatly augmented with increasing Reynolds number.
- The oscillating vortex generator is efficient to enhance the heat transfer in the channel flow but also to produce a significant pressure drop increase. Based upon the fixed heat transfer area, the efficiency index defined as the ratio $(\mathrm{Nu}/\mathrm{Nu}_0)/(f/f_0)$, where the 0 subscript represents the stationary bar, is greater than 1.0 for almost all cases.

In recent years, many researchers have studied the flow around a single oscillating circular cylinder (forced or vortex-induced) using experimental measurements and numerical simulations, such as Patnaik *et al.* [Patnaik et al., 1999], Ongoren and Rockwell [Ongoren and Rockwell, 1988], Cetiner and Rockwell [Cetiner and Rockwell, 2001], Al-Mdallala *et al.* [Al-Mdallal et al., 2007]. It is a very active problem since this nonlinear system is mainly controlled by some dimensionless factors, such as the frequency f_{ex}, the amplitude of the forced/free oscillations A, and the Reynolds number based on the cylinder diameter Re_D. An interesting phenomenon that is studied is the lock-in effect, where the frequency of oscillation f_{ex} synchronizes with the vortex formation frequency f_v and the natural frequency of the body in motion f_N, resulting in large amplitude oscillations. In the literature, several authors studied the flow around a heated transversely oscillating cylinder both numerically and experimentally. Cheng *et al.* [Cheng et al., 1997] simulated heat transfer characteristics and the flow behavior of cross flow over a transversely oscillating cylinder, the dominant parameters were $\mathrm{Re}_D = 0 - 300$, $f_{ex}/f_{st} = 0 - 0.3$, $A = 0 - 0.7D$ where f_{st} is the natural Stokes frequency of a stationary cylinder. They drew some conclusions which show that an appreciable heat transfer increase caused by the oscillation is observed in the lock-in regimes. While the flow is outside these regimes, the heat transfer from the cylinder is almost unaffected by the oscillations. With the Arbitrary Lagrangian-Eulerian (ALE) method, Fu and Tong [Fu and Tong, 2002] also simulated the heat transfer from a heated transversely oscillating cylinder in a cross flow at $\mathrm{Re_D} = 200$. Their numerical results confirmed that the heat transfer rate would be enhanced remarkably as the oscillating frequency of the

cylinder approaches the natural shedding frequency (lock-in regime). When $\mathrm{Re_D}$ increases to [800-8000], the results from Yang and Chen [Yang and Chen, 2008] indicated that the heat transfer from heated blocks is enhanced as the oscillating frequency of the cylinder is in lock-in regimes. Moreover, a detailed experimental investigation of the effects of transverse oscillations on the heat transfer from a circular cylinder in cross-flow was carried out by Pottebaum and Gharib [Pottebaum and Gharib, 2006] in which the dominant parameters were $\mathrm{Re}_D = 687$, $f_{ex}/f_{st} = 0 - 0.3$, $A = 0 - 0.7D$. The ratio of Nusselt number in an oscillating cylinder configuration to its relative non oscillating cylinder is calculated. They concluded that the heat transfer enhancement in the lock-in regimes is limited to ratios less than 0.5 because of the shortening of formation length in the wake under these conditions. For the flow around a pair of vertically aligned horizontal heated cylinders, the plume from the lower cylinder oscillates out of phase with the flow around the upper cylinder, and it increases the mixing, which results in enhanced heat transfer [Reymond et al., 2008]. When these two heated cylinders were in tandem arrangement at $\mathrm{Re}_D = 100 - 200$, numerical results from Mahir and Altac [Mahír and Altaç, 2008] showed that the mean Nusselt number of the upstream cylinder approached to that of a single isothermal cylinder for $(L/D) > 4$ (where L is the center-to-center distance) and the mean Nusselt number of the downstream cylinder was about 80% of the upstream cylinder.

1.7 Mixing and heat transfer by elastic structural oscillations

The motion of slender flaps in a viscous fluid is a fundamental problem that has numerous applications in nature and in industry. The use of an actuated flap to generate micromixing has been proposed for applications in the biomedical industry. Solutions containing biological material such as DNA and proteins have low molecular diffusivities. Due to limitations of diffusion, adding convection to the flow field enhances the micro-fluidic process.

Lambert *et al.* [Lambert et al., 2008] performed numerical simulations to study the effect of introducing streamwise oscillating mechanical flap in a microchannel, located on the top or bottom walls of the channel. The period of oscillations is chosen to match the surface reaction time. The results show that the mechanical actuator behaves like a miniature pump that drives a favorable gradient of macromolecules towards the surface reaction sites within an initial lapse of time. In a stagnant fluid, the results show that the moving flap behaves like a stirring agent bringing fluid with a higher concentration in contact with the reaction site and enhancing the concentration surface. In this case, the effect of the moving flap increases as the reaction progresses. The moving flap has the largest beneficial effect on surface concentration in the presence of a background flow when the position of the moving flap is along the top wall above the reaction site as shown in Figure 1.26.

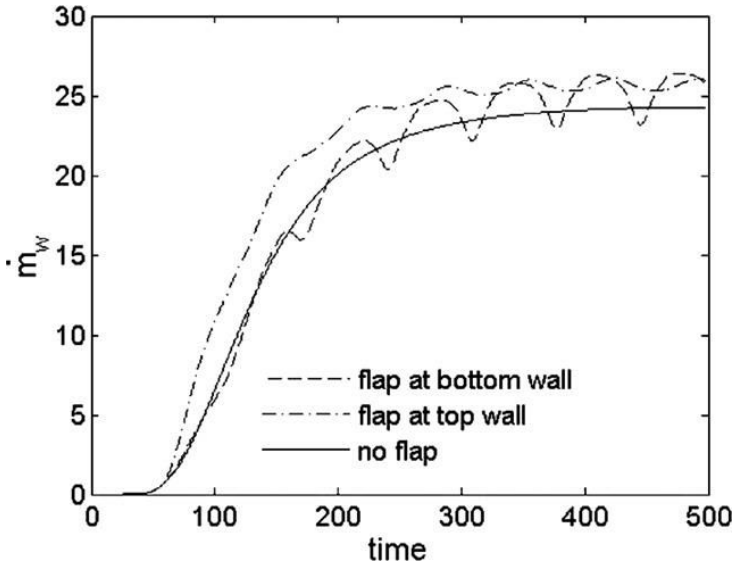

Figure 1.26: Total mass flow rate at the bottom channel surface with and without flap motion [Lambert et al., 2008]

In another paper, Lambert and Rangel [Lambert and Rangel, 2010] explored the capacity of a flexible flap to increase mixing in a microchannel for a flap Reynolds number Re_f (based on the flap length L) ranging from 0.3-80. The flap is actuated using a dimensionless follower force $\boldsymbol{b}$ normal to the direction of the beam midline and is represented by a sinusoidal function:

$$\boldsymbol{b} = \mathrm{B}\cos(2\pi \mathrm{St} T)\boldsymbol{e}_n \tag{1.22}$$

where B is the dimensionless magnitude, St is the dimensionless frequency or the Strouhal number ($\mathrm{St} = f_{ex}L/U_f$, where f_{ex} is the forcing frequency) and $\mathrm{T} = L/U_f$ is the dimensionless time. The results show that mixing is enhanced for larger flap displacements and for dimensionless frequencies or Strouhal number in the range [1-2] as shown in Figure 1.27. Optimal mixing occurs when the flap length is of the microchannel height. The influence of the hydrodynamic force on the beam bending motion enhances the mixing process. Under optimal conditions the flap behaves as a rapid mixing device where 80% of the long time mixing fraction (here defined as M and calculated according to Eq.(1.8)) is reached during an initial time interval of 3.8 s.

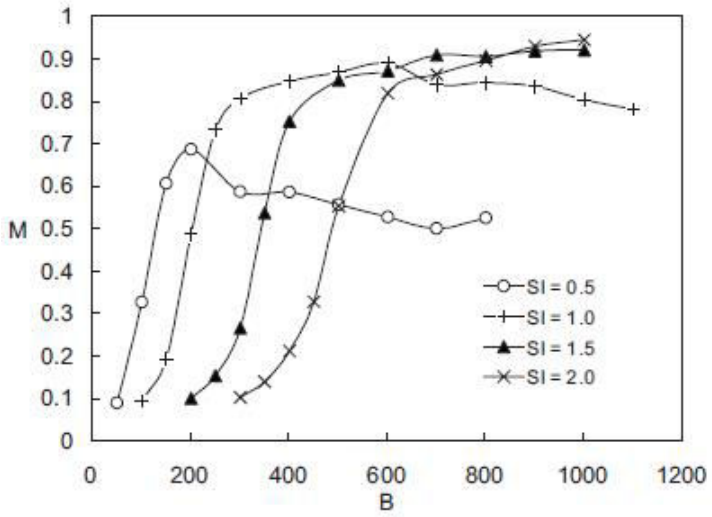

Figure 1.27: Effect of applied load (B) and frequency on the mixing fraction M [Lambert and Rangel, 2010]

Moreover, the results in Figure 1.28 show a difference in the flap motion and the concentration gradient patterns between flexible and rigid flaps. For this study, a dimensionless modulus of elasticity $\mathrm{D}_s = (\lambda + 2\mu)/(2\rho_f U_f^2)$ is varied. The differences illustrated in the figure can be attributed to the influence of the hydrodynamic force on the beam bending motion, also as shown in this figure, the beam curvature bends away from the direction of motion. The flap bending motion has an influence on the solute mixing patterns in the fluid as recirculation patterns appear in the concentration gradients in the fluid with flexible flap and are less apparent in those of the rigid flap, and with higher mixing fraction in the flexible case ($\mathrm{D_s} = 1\mathrm{E}+6$) than the rigid case ($\mathrm{D_s} = 1\mathrm{E}+8$) as shown in Figure 1.29 at dimensionless times $\mathrm{T} = 6$ and $\mathrm{T} = 36$.

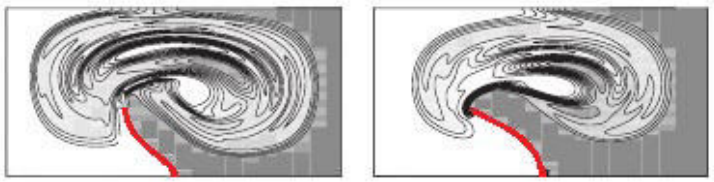

Figure 1.28: Concentration contours at time T for a flexible (left) and rigid (right) flap [Lambert and Rangel, 2010]

Khatavkar *et al.* [Khatavkar et al., 2007] numerically studied effects of active control cilia used as microactuators on the mixing of microchannel flows. They highlighted the major role played by

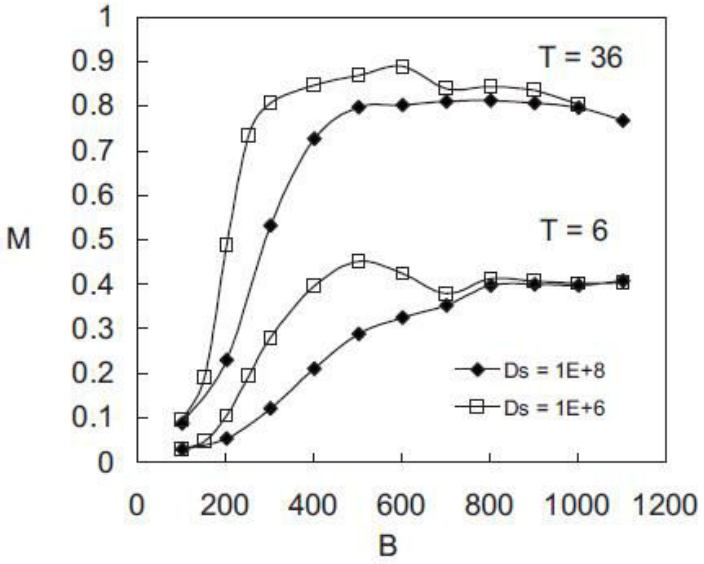

Figure 1.29: Mixing fraction between a flexible flap (open symbols) and a rigid flap (closed symbols) [Lambert and Rangel, 2010]

several parameters like the fluid viscosity, shear modulus and length of the microactuator. They furthermore investigated configurations with two microactuators located on the same channel wall or on opposite walls, with a phase-shifted frequency applied to their motions. They concluded that under given optimal conditions, the use of two actuated flaps mounted on the same wall or on opposite can induce chaotic advection in a microchannel flow. In such cases, they highlighted that a key factor for mixing enhancement is the phase shifting between the actuators motions. Moreover, recently Mirzae *et al.* [Mirzaee et al., 2012] carried out numerical simulations of a 2D channel flow with one oscillation controlled flap mounted on an inner wall. They compared heat transfer enhancement obtained from flexible or rigid flap as a function of laminar Reynolds numbers. They concluded that not only thermal performances were increased with the use of the oscillation-controlled flap whatever the laminar Reynolds number but this flexible flap induces also lower pressure drop.

Until recently, Shi *et al.* [Shi et al., 2014] performed numerical simulations on a benchmark for FSI problems already available in the literature and proposed by Turek and Hron [Turek and Hron, 2006], which consists of a two dimensional laminar flow around a flexible structure attached to a rigid cylinder. They included the effect of heat transfer to assess the thermal performance of the FSI benchmark and simulations were carried out at different Reynolds numbers calculated based on the rigid cylinder diameter ($\mathrm{Re}_D = 200 - 330$). They observed that the FSI problem strengthens the disruption of the thermal boundary layer by vortex interaction with the wall and improves the mixing process between the hot and cold fluid regions. Their results indicate that VIV could increase the Nusselt number of a maximum enhancement of about 90.1% with respect to an empty channel. Nevertheless, the heat transfer effect on the same Turek and Hron benchmark has also been investigated by Soti *et al.* [Soti et al., 2015] by varying the Prandtl number, the Reynolds number and the Young's modulus of the flap. The analyses suggest that larger Prandtl and Reynolds number tend to promote the thermal enhancement but with less efficiency. On the other hand, larger values of Young's modulus reduce the thermal enhancement and require much more pumping power.

1.8 Vortex-induced vibrations (VIV)

Vortex-induced vibration (VIV) of structures is of practical interest to many fields of engineering. For example, it can cause vibrations in heat exchanger tubes; it influences the dynamics of riser tubes bringing oil from the seabed to the surface; it is important to the design of civil engineering structures such as bridges, as well as to the design of marine and land vehicles; and it can cause large amplitude vibrations of tethered structures in the ocean.

As the flow velocity U_f shown in Figure 1.30 increases, a condition is reached when the vortex formation frequency f_v is close enough to the body's natural frequency f_N such that the unsteady pressures from the wake vortices induce body to respond. Certain wake patterns can be induced by body motion which are highlighted as 2S, 2P and P+S modes:

- 2S mode which indicates two single vortices within per cycle.
- 2P mode which means two pair of vortices formed per cycle.
- An asymmetric P+S mode, which comprises a pair of vortices and a single vortex per cycle.

In essence, a nominal periodic vibration results if the energy transfer or work done by the fluid on the body over a cycle is positive. This net energy transfer is significantly influenced by the phase of induced side force relative to body motion, which in turn is associated with the timing of vortex dynamics. The problem of VIV is therefore an interaction loop between body motion and vortex motion.

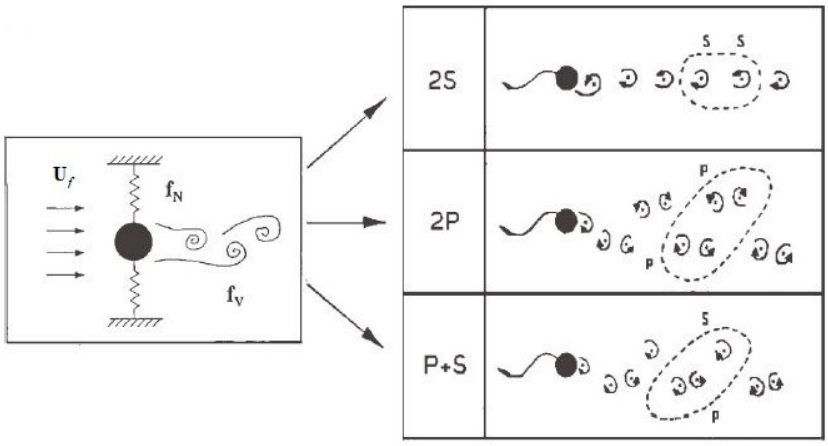

Figure 1.30: Vortex formation modes in the wake of an oscillating cylinder [Williamson and Roshko, 1988]

1.8.1 Definitions

The literature of VIV is large and introduces several specific frequencies. With these thoughts in mind, two or three letter subscripts were chosen to enhance the instant recognition of the most important symbols as in [Sarpkaya, 2004]:

- f_{vac}: the frequency measured in vacuum, as the only natural frequency calculated as:

$$f_{vac} = \frac{1}{2\pi}\sqrt{\frac{k}{m_s}} \tag{1.23}$$

  where k denotes the linear spring constant and m_s the mass of the oscillating body.

- f_{comm}: the common frequency at which synchronization or lock-in occurs at a given velocity, i.e. $f_{ex} = f_{comm}$.

- f_{ex}: the frequency of oscillation of a (forced or self-excited) body, meaning the excitation frequency whether there is lock-in or not. At lock-in:

$$f_{ex} = f_{comm} = \frac{1}{2\pi}\sqrt{\frac{k}{m_s + \Delta m}} \tag{1.24}$$

  where Δm is the added mass effect.

- f_{st}: the vortex shedding frequency (or the Strouhal frequency) of a body at rest. It is uniquely related to the velocity of the flow and the characteristic size of the body through the Strouhal number defined as:

$$\mathrm{St} = \frac{f_{st} L}{U_f} \tag{1.25}$$

where L is the characteristic length of the stationary body.

- f_v: the vortex shedding frequency of a body in motion (forced or self-excited). In the lock-in range, f_v becomes increasingly smaller than f_{st} until lock-out. If for example, the velocity of the fluid increases to a new value U, the body will start to respond with a defined amplitude. The diameter of the body (if we consider the body as a cylinder) seen by the flow will virtually increases as the body oscillates in a transverse direction. The apparent increases in D will be compensated by a reduction of the vortex shedding frequency to follow the oscillation frequency of the body f_{comm}, thus keeping the vortex shedding frequency nearly constant for a range of fluid velocity U, as opposed to a fixed body behavior at the new increased U.

- f_N: the natural frequency of the structure in the fluid medium.

Moreover some of the most important dimensionless parameters used in VIV are summarized in Table 1.2. These dimensionless groups are computed for a cylinder with a diameter D. One can note regarding these groups that:

- As f_N is the natural frequency in the fluid medium, correspondingly ζ is the ratio of (structural damping c)/(critical damping in the fluid medium). The frequency f_{ex} , used in f^*, is the actual body oscillation frequency during induced vibration.

- The added mass $\Delta m = \frac{\pi}{4}\rho_f D^2 L$, where ρ_f is the density of the fluid and L the length of the cylinder.

Table 1.2: Non dimensional groups in VIV

Mass ratio	m^*	$\frac{m}{\frac{\pi}{4}\rho_f D^2 L}$
Damping ratio	ζ	$\frac{c}{2\sqrt{k(m_s + \Delta m)}}$
Reduced velocity	V_r	$\frac{U_f}{f_N D}$
Amplitude ratio	A^*	$\frac{x}{D}$ or $\frac{y}{D}$
Frequency ratio	f^*	$\frac{f_{ex}}{f_N}$
Reynolds number	Re_D	$\frac{U_f D}{\nu_f}$

1.8.2 Modal analysis

The undamped free vibration of a bar of length L and thickness T is governed by the following differential equation [Rao, 2011]:

$$EI\frac{\partial^4 Y(x,t)}{\partial x^4} + m_{s'}\frac{\partial^2 Y(x,t)}{\partial t^2} = 0 \tag{1.26}$$

where E is the modulus of elasticity for the bar and $m_{s'}$ its mass per unit length, the rectangular cross sectional area of the bar is $A = WT$, where W is the width and T is the thickness. The moment of inertia of the cross section is given by $I = WT^3/12$. The fixed-free end bar has eigenmodes that vibrate with the following frequencies:

$$w_n = \frac{\alpha_n^2}{L^2}\sqrt{\frac{EI}{m_{s'}}} \tag{1.27}$$

where $\alpha_n = 1.875, 4.694, 7.855, ...$ [Rao, 2011].

However, the calculated frequency above is valid in vacuum and does not take into consideration the added mass effect where the mass per unit length of the bar becomes $m_B = m_{s'} + m_{f,n} = (1+\mu_{f,n})m_{s'}$. The mass of the fluid moved with the oscillating structure is $m_{f,n}$ and the dimensionless $\mu_{f,n}$ accounts for the mass of the fluid that has to be moved with the structure when vibrating at the n^{th} mode as shown in Figure 1.31 [Weigert et al., 1996].

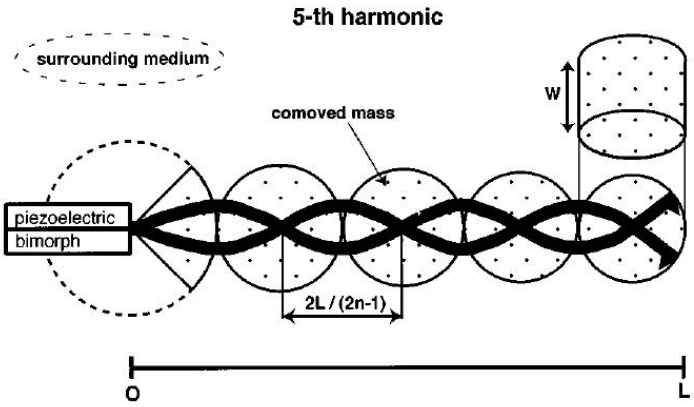

Figure 1.31: Scheme of a rectangular cantilever oscillating at its fifth harmonic in a fluid medium [Weigert et al., 1996]

An expression for $\mu_{f,n}$ for the n^{th} eigenmode is found to be:

$$\mu_{f,n} = \frac{L}{T}\frac{\rho_f}{\rho_s}\frac{\pi}{3}\frac{(n-1)+1/4}{(2n-1)^2} \tag{1.28}$$

where ρ_s is the density of the structure. Extensive details about Eq.(1.28) can be found in [Weigert et al., 1996]. As a result, the frequencies of the bar in a medium of density ρ_f are given by:

$$w_n^f = \frac{w_n^{vac}}{\sqrt{1+(\frac{L}{T})(\frac{\rho_f}{\rho_s})(\frac{\pi}{3}\frac{(n-1)+1/4}{(2n-1)^2})}} \tag{1.29}$$

Consequently the frequency of the structure immersed in the fluid medium depends on the ratio L/T, on the ratio ρ_s/ρ_f and on the mode under consideration.

1.8.3 Overview of free vortex-induced vibrations

VIV has been studied intensively in the past decades and the results and conclusions regarding this subject are vast. In this section, we present the main concepts regarding VIV based on the reviews of Williamson and Govardhan [Williamson and Govardhan, 2004] and Sarpkaya [Sarpkaya, 2004].

Figure 1.32 and 1.33 shows the maximum amplitude ratio and frequency response of a circular cylinder subjected to VIV. It can be seen from Figure 1.32 that the range of reduced velocity at which significant amplitudes are obtained is limited and the maximum amplitude depends on the mass ratio. Furthermore, Figure 1.33 shows that for the same range of reduced velocity ($5<V_r<8$), the body responds with a frequency of oscillation close to the natural frequency of the body. This range is referred to as lock-in or synchronization range at which the vortex shedding frequency lock-in matches

the oscillation frequency of the body. However, recent studies show a departure from this conclusion, bodies can vibrate at large amplitude with hundreds of times the natural frequency. For light bodies in water (low mass ratio $m^* = 2.4$), Khalak and Williamson [Khalak and Williamson, 1997], the body displayed high amplitude oscillation at frequency ratio distinctly higher ($f^* = 1.4$) than that obtained by Feng [Feng, 1968] at high mass ratio. Therefore, one might define synchronization as the matching of the frequency of the periodic wake vortex mode with the body oscillation frequency. It is also well known that a reduction in mass ratio leads to a wider synchronization regime and a significant increase in the lock-in range.

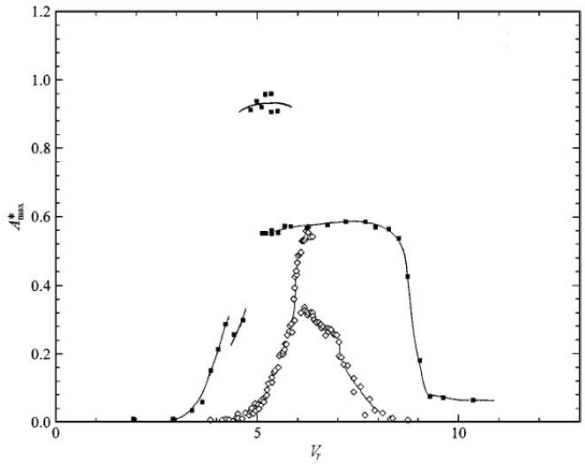

Figure 1.32: Amplitude of vibration in terms of cylinder diameter A^*_{max} as a function of reduced velocity V_r in VIV of cylinder with mass ratio $m^* = 10.1$, (■ Khalak and Williamson [Khalak and Williamson, 1999]), and $m^* = 248$, (◇ Feng [Feng, 1968])

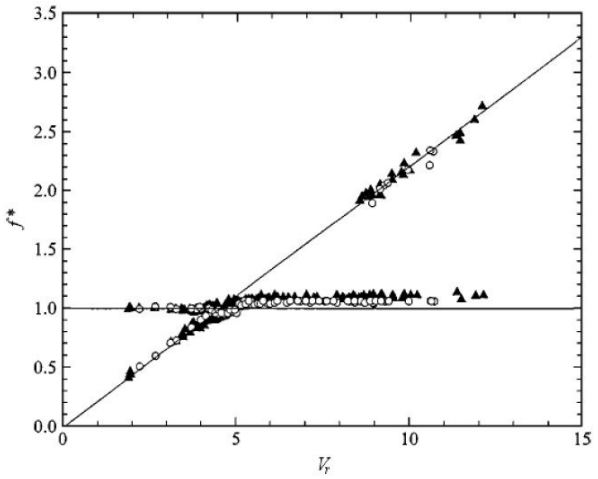

Figure 1.33: Frequency response $f^* = f_{ex}/f_N$ for circular cylinders in VIV of mass ratios (▲, $m^* = 10.1$) and (○, $m^* = 20.6$). The horizontal line corresponds to the natural frequency of the cylinder in VIV and the diagonal line corresponds to the vortex shedding frequency of a fixed cylinder (Khalak and Williamson [Khalak and Williamson, 1999])

Moreover, several publications studied the response of cylinders affected by the wake of an upstream cylinder. However, the parameters involving such studies are significantly larger than those associated with only one isolated cylinder. For example, one can vary the streamwise and the cross-stream separations of the cylinders, the number of cylinders and the ratio of diameters between the cylinders. Three main arrangements are studied: side by side, tandem and staggered arrangements as shown in Figure 1.34. King and Johns [King and Johns, 1976] studied the response of two flexible cylinders arranged in tandem, uncoupled and coupled with a rigid or flexible links. The center to center separation is in the range of $3.5 \leq L_x/D \leq 7$. They concluded that the vortex shedding

from the oscillating upstream cylinder strengthens the vortex shedding of the downstream cylinder, resulting in a large amplitude response and wide lock-in regime in which the high amplitude response is significant.

Bokaian and Geoola [Bokaian and Geoola, 1984] studied experimentally two cylinders in a water channel, that have the same diameter and placed in tandem and staggered arrangements. They concluded that for small separations ($L_x/D = 1.09$), the downstream cylinder exhibits wake-induced galloping. This is characterized by a continuous increase of the amplitude as the reduced velocity increases. This result differs from vortex-induced vibrations as the peak amplitude is well defined at resonance. For separation of $L_x/D = 1.5$, the wake-induced galloping happens before the vortex-resonance vibration reaches its zero amplitude. In the range $2 \leq L_x/D \leq 3$, the wake-induced galloping occurs at reduced velocity outside the lock-in range and after the vortex resonance reaches its zero amplitude position. Finally, for $L_x/D > 4$, only vortex-resonance is observed. Wake-induced galloping was observed for staggered geometry ($L_y/D \leq 1$) and not present in the range ($L_y/D \geq 2$).

Zdravkovich [Zdravkovich, 1985] studied two flexible cylinder and performed wind tunnel experiments. The results show the existence of two flow induced vibration regimes: the vortex-induced vibrations and fluid elastic response. Vortex-induced vibrations are considered when the vortex shedding frequency matches the natural frequency of the structure for a range of reduced velocities around 5. However, fluid elastic response occurs at higher reduced velocities, around 30, and is not subjected to a limited range of reduced velocity, persisting a significant amplitude of oscillation at increasing reduced velocity.

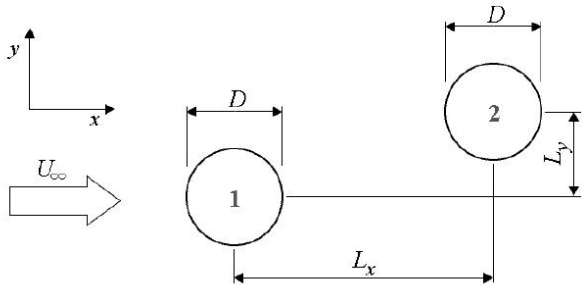

Figure 1.34: Two cylinders in staggered arrangement. If $L_y = 0$, they will be in tandem arrangement; if $L_x = 0$, they will be in side by side arrangement

Hover and Triantafyllou [Hover and Triantafyllou, 2001] performed experiments in a water channel for an oscillating rigid cylinder immersed in the wake of a fixed cylinder. Tandem arrangement with $L_x/D = 4.75$ and staggered arrangement with $L_x/D = 4.75$ and $L_y/D = 1$ are studied. The mass ratio was $m^* = 3$ and with a damping ratio of 0.04. The tandem and staggered arrangements displayed a high amplitude response for reduced velocities $V_r > 10$, reaching amplitudes of $1.9D$ for the tandem arrangement and $1.3D$ for the staggered arrangement. The high amplitude vibrations at the high reduced velocities were explained by the extension of the lock-in range for the two cylinders. Mittal and Kumar [Mittal and Kumar, 2001] carried numerical simulations of two cylinders with wake interference, using the finite element method with an Arbitrary Lagrangian Eulerian formulation. Tandem arrangements $L_x/D = 5.5$ and staggered arrangements with $L_x/D = 5.5$ and $L_y/D = 0.7$ were studied. The simulations were done so that the structural natural frequency is close to the vortex shedding frequency of the flow around two fixed cylinders in the same arrangements. In almost all the cases, the response of the upstream body is similar to that of an isolated cylinder, while the downstream cylinder vibrates with higher amplitudes. Furthermore, Assi *et al.* [Assi et al., 2006] presented experimentally results of a cylinder isolated and immersed in the wake of an identical fixed cylinder for a range of reduced velocity ($2 \leq V_r \leq 12$). The mass ratio of the downstream cylinder is $m^* = 2$. They tested a range of tandem separations ($2 \leq L_x/D \leq 5.6$) and found that the peak amplitude for the downstream cylinder was about 50% higher than that for the isolated cylinder.

Moreover, in terms of drag measurements, previous labs experiments conduced on tandem rigid bodies moving in viscous incompressible fluids found that a downstream body experiences less drag

than an upstream body. However, recently Ristroph and Zhang [Ristroph and Zhang, 2008] found an interesting phenomenon of inverted drafting that is apparent in the interactions between deformable bodies and absent between rigid bodies. In these experiments, the upstream body experiences less drag than the downstream one. The Reynolds number in the experiments were around $\mathrm{Re} = 10^4$. Nevertheless, to find out how this phenomenon depends on the Reynolds number, Zhu [Zhu, 2009] performed a series of numerical simulations on a pair of tandem flexible flags separated by a vertical distance of $(0 \leq L_y/D \leq 5.5)$ at lower Reynolds number in the range of $(40 \leq Re \leq 220)$. The results show that when the Reynolds number is high enough so that the oscillation of the flexible flags is self-sustained, the upstream flag had less drag than the downstream one. However, when the Reynolds number is small enough so that the flags are nearly static, the downstream flag has less drag than the upstream one.

1.8.4 Energy harvesting from VIV

As previously stated, when a fluid flow generates vibrations of a body and when the frequency of vortex shedding matches the natural frequency of the body, the latter will exhibit large amplitude vibrations. Energy harvesting from VIV caught the attention of several researchers [Li et al., 2011, Abdelkefi et al., 2012, Mehmood et al., 2013, Dai et al., 2014]. A research group from the University of Michigan has developed an energy extraction system called VIVACE (Vortex-Induced Vibration for Aquatic Clean Energy) [Bernitsas et al., 2008].

The converter of VIVACE system has been designed to extract clean and hydrokinetic energy by relying on VIV. This system consists of a smooth circular cylinder mounted on springs, where the vibrations of the cylinder are transmitted to drive a generator by a belt-gear system as shown in Figure 1.35. The VIVACE converter can extract energy from low speed ocean or river currents and tides as slow as 0.4 m/s unlike the traditional energy conversion devices (turbines, water-mill) which are efficient for flow velocities greater than 2 m/s [Chang, 2010].

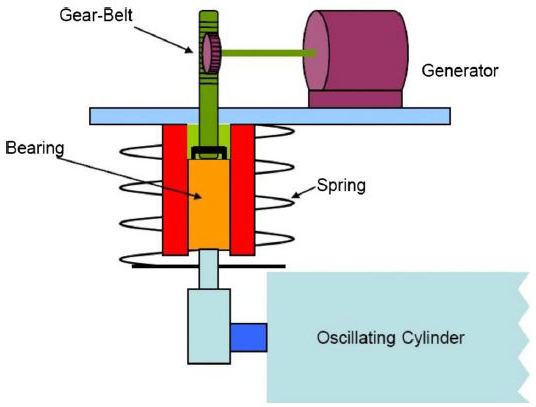

Figure 1.35: VIVACE system ([Bernitsas et al., 2008])

Erturk *et al.* [Erturk et al., 2010] studied piezoelectric beam to harvest the energy from airflow. They were able to produce a maximum power of 10.7 mW for an electrical load resistance of 100 $\mathrm{k}\Omega$ and at an airflow velocity of 9.30 m/s using the self-sustained oscillations resulting from VIV. Moreover, Akaydin *et al.* [Akaydın et al., 2010] placed a piezoelectric beam in the wake of a circular cylinder to evaluate its performance as energy generators. When the periodic forcing from the vortex shedding produced by the cylinder tuned to the resonant frequency of the beam, a maximum output power of 4 μW is generated. Tang *et al.* [Tang et al., 2009] designed a flutter-mill to generate electricity by extracting energy from the fluid flow. They introduced a cantilevered flexible plate that loses stability when operated above a critical velocity where the flow continuously pumps energy into the plate and induces self-sustained flutter motion. The flexible plate is placed between two parallel magnetic panels and generates an electric potential due to its motion.

1.9 Conclusion

In this chapter, we presented an overview of the different mechanisms used to enhance heat and mass transfer according to their classifications as passive or active systems. We conclude that active methods offer an additional flexibility on passive methods especially when using actively controlled vortex generators to produce coherent structures that reduce the thermal boundary layer and enhance fluid mixing between the fluid core and the wall boundaries. The oscillation frequency and amplitude of the vortex generator are usually modified to control the number and strength of the vortices generated. However, since active methods are more complex to implement and require a great amount of power to control the VGs, passively oscillating bodies present great interest and are already studied in other disciplines of engineering such as in Vortex-Induced Vibrations (VIV). An interesting phenomenon in VIV is the lock-in where the vortex shedding frequency matches the oscillation frequency of the structure, which produces large amplitude oscillations. Most of the studies in VIV are performed in order to suppress such oscillations due to their damaging effect. However, as mentioned previously in section 1.8.4 other studies intend to enhance VIV in order to harvest renewable energy from vibrations and transform it to electricity.

Nevertheless, in the domain of heat and mass transfer, the literature concerning enhancing the thermal performance of multifunctional heat exchangers/reactors by relying on VIV or passively vibrating structures is nearly absent. We intend in this study to start an investigation on new configuration designs that benefit from the phenomena of lock-in to cause large amplitude oscillations produced only by the pumping power, without any additional external forces. The effect of self-sustained oscillations of flexible VGs on heat and mass transfer will be studied and compared to geometries for which the VGs are completely rigid and non-deforming. The final proposal is to provide and highlight the potential of applying such technique to improve the efficiency of heat exchangers and reactors.

Chapter 2

FSI Numerical Methods

2.1 Introduction

Multiphysics problems such as fluid-structure interaction (FSI) give rise to more and more attention in the recent years. The coupling of fluid structure interaction can occur in many engineering systems and designs such as the stability and response of aircraft wings in aerospace engineering, flow of blood in arteries or hemodynamics in biomedical applications, response of bridges and tall structures when subjected to wind in civil engineering and heat exchangers vibrations in nuclear industry. Such problems are too difficult to solve analytically and they must be analyzed by means of numerical simulations. In exploratory approach, numerical simulations of coupled problems can replace experimental studies especially if they are expensive and time consuming. However, the maturity level achieved in the fields of computational fluid dynamics and computational solid dynamics is not yet reached to perfectly solve numerical simulations of fluid-structure interactions and there are still key questions regarding robustness, stability, and computational time that need to be resolved in a satisfactory way.

Several approaches have been investigated to model the fluid-structure interaction problems. For example, in order to reduce the number of degrees of freedom in the system and save computational time, the added mass technique can be used to model the FSI problems when small displacements and deformations of the structure are present. The dynamic behavior of the structure in this method is investigated without computing the fluid motion. Since solving the full Navier-Stokes equations to obtain the hydrodynamic forces on the structure are time consuming, the added mass technique can be used by designers to predict the small vibrations and fatigue damages of the structures when coupling occurs. However, for problems when large deformations are present, the full Navier-Stokes equations need to be solved in a moving mesh. The most common approach to solve the coupling problem is the ALE (Arbitrary-Lagrangian Eulerian) formulation [Donea et al., 1982] for the fluid domain and the Lagrangian formulation for the structural domain. The Lagrangian formulation where the mesh moves with the material is commonly used in solid mechanics. This choice resolves the material boundaries very accurately, however it suffers from a main limitation that the deformations must be limited, otherwise the mesh will be distorted and numerical inaccuracies and instabilities in the solution will occur. The Eulerian formulation where the mesh is fixed in space eliminates the concern for mesh distortion, but it introduces an additional complexity when dealing with the convective terms associated with the transport of the material throughout the mesh. The ALE formulation permits the transition of the mesh from being Eulerian for modeling the fluid flow to nearly Lagrangian that follows the solide structure deformations.

In this chapter, we present the different numerical schemes to solve the fluid-structure interaction problem, resulting in a weakly or more strongly coupled procedures. Finally, the coupling algorithm used in all the numerical simulations presented in this study, mainly by coupling ANSYS Fluent CFD solver with ANSYS Mechanical CSD solver, will be presented followed by a numerical validation of the FSI algorithm from the literature.

2.2 Governing equations

The governing equations for the fluid and solid domains are different in terms of their constitutive relationships. In this section, we present the general equations for continuum mechanics followed by the specifics for each fluid and solid domains. The equations presented will be cast in their ALE formulation which is a general framework for the Eulerian, Lagrangian or the arbitrary frame of work. We start by the the continuity equation defined by:

$$\frac{\partial \rho}{\partial t} + \nabla \cdot [\rho (\mathbf{u} - \mathbf{u_m})] = 0 \tag{2.1}$$

where ρ is the mass density, $\mathbf{u}$ is the (fluid or solid) particle velocity, and $\mathbf{u_m}$ is the mesh grid velocity which is required to deform the mesh due to the movement of the structure at the fluid-solid interface. For Lagrangian description, $\mathbf{u_m} = \mathbf{u}$ is set in Eq.(2.1) and for Eulerian description $\mathbf{u_m} = 0$. By performing the appropriate force balance and using the continuity equation, we obtain the following momentum equation:

$$\rho \frac{\partial \mathbf{u}}{\partial t} + \rho [(\mathbf{u} - \mathbf{u_m}) \cdot \nabla \mathbf{u}] = \nabla \cdot \boldsymbol{\sigma} + \rho \mathbf{b} \tag{2.2}$$

where $\boldsymbol{\sigma}$ is the Cauchy stress tensor and $\mathbf{b}$ is the body force. In order to satisfy the mesh conservation law [Thomas and Lombard, 1979], the mesh velocity has an additional constraint given by the following equation:

$$\frac{\partial V_{cv}}{\partial t} + \nabla \cdot \mathbf{u_m} = 0 \tag{2.3}$$

where V_{cv} is the volume of the control volume. The mesh conservation constraint imposes that the change in volume of each control volume between two time steps should be equal to the volume swept by the control volume faces during the time step.

Two main solution techniques are usually used to solve the above equations which are the finite element method (FEM) which subdivides the domain into simpler parts called finite elements and solves the equations by minimizing an associated error function, and the finite volume method (FVM). In this work, the structural solver ANSYS Mechanical uses the FEM and the fluid solver ANSYS Fluent uses the FVM method [ANSYS, 2015]. In the FVM method, the computational domain is divided into sets of discrete control volumes δV_i where the flow equations are then integrated over each finite volume δV_i. To convert the divergence terms in Eq.(2.1) and Eq.(2.2) into surface flux terms, the Gauss's theorem is used to discretize these terms and find the approximations of the fluxes at the surface of the control volume. The constitutive equations for the fluid and solid domains are provided in the next section, followed by the details on how to couple these two different domains at the fluid solid interface $\Gamma_{F/S}$.

2.3 Flow solver

The Cauchy stress tensor for a Newtonian incompressible fluid is approximated by the following equation:

$$\boldsymbol{\sigma} = -p\mathbf{I} + 2\mu_f \mathbf{S} \tag{2.4}$$

where p is the pressure, μ_f is the dynamic viscosity of the fluid and $\mathbf{S}$ is the strain rate tensor. By substituting Eq.(2.4) into the momentum equation Eq.(2.2) and using $2\nabla \cdot \mathbf{S} = \nabla^2 \mathbf{u}$, we obtain the Navier-Stokes equations:

$$\frac{\partial \mathbf{u_f}}{\partial t} + (\mathbf{u_f} - \mathbf{u_{m,f}}) \cdot \nabla \mathbf{u_f} = -\frac{\nabla p}{\rho_f} + \nu_f \nabla^2 \mathbf{u_f} \tag{2.5}$$

where the f subscript denotes the fluid domain and ν_f the kinematic viscosity of the fluid.

2.4 Structural solver

The structural solver is designed with a Lagrangian frame of reference, which means that the mesh velocity is equal to the material velocity $\mathbf{u_m} = \mathbf{u}$, thus the momentum equation Eq.(2.2) becomes:

$$\rho_s \frac{\partial \mathbf{d_s}^2}{\partial t^2} = \nabla \cdot \boldsymbol{\sigma} + \rho_s \mathbf{b} \tag{2.6}$$

where $\mathbf{d_s}$ is the structural displacement ($\partial \mathbf{d_s}/\partial t = \mathbf{u_s}$) and the s subscript denotes the structural domain.

Since all the work presented in this manuscript deals only with cases where the structure undergoes large deformation, only the formulations associated with large deformation will be presented in this section. When the material under consideration exceeds more than a few percents of strains, the changing geometry due to this deformation cannot be neglected and the equilibrium equations must be written for the deformed geometry. The applied force on a body will make it move from one position to another as shown in the "undeformed" and "deformed" positions in Figure 2.1. The position vectors of both the deformed and undeformed configurations is denoted by $\mathbf{d_x}$ and $\mathbf{d_X}$. Thus, the resulting displacement vector $\mathbf{d_s}$ is computed by:

$$\mathbf{d_s} = \mathbf{d_x} - \mathbf{d_X} \tag{2.7}$$

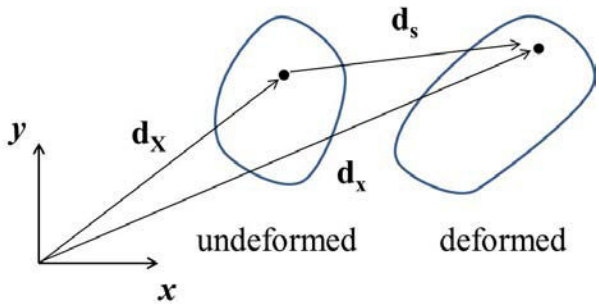

Figure 2.1: Motion of a deforming body

Consequently, the deformation gradient is defined as:

$$\mathbf{F} = \frac{\partial \mathbf{d_x}}{\partial \mathbf{d_X}} \tag{2.8}$$

which can be rewritten by using Eq.(2.7):

$$\mathbf{F} = \mathbf{I} + \frac{\partial \mathbf{d_s}}{\partial \mathbf{d_X}} \tag{2.9}$$

where $\mathbf{I}$ is the identity matrix.

The Green-Lagrange strain, referred usually as the Green strain, is defined as:

$$\mathbf{G} = \left(\mathbf{F}^T\mathbf{F} - \mathbf{I}\right) \tag{2.10}$$

which alternatively can be written as:

$$\mathbf{G} = \frac{1}{2}\left[\nabla \mathbf{d_s} + (\nabla \mathbf{d_s})^T + \nabla \mathbf{d_s} \cdot (\nabla \mathbf{d_s})^T\right] \tag{2.11}$$

To show the nonlinearity of the Green tensor we highlight its nonlinear form compared to its equivalent in small strain linear analysis:

$$\mathbf{G} \approx \frac{1}{2}\left[\nabla \mathbf{d_s} + (\nabla \mathbf{d_s})^T\right] \tag{2.12}$$

In order to measure the stress component in a suitable way for large deformation problems, it must be a conjugate of the strain measure. Thus, when interpreting the Cauchy stress $\boldsymbol{\sigma}$, it must be transformed in terms of the second *Piola-Kirchhoff* stress tensor Σ by:

$$\boldsymbol{\sigma} = J_F \mathbf{F} \Sigma \mathbf{F}^T \tag{2.13}$$

where J_F is the Jacobian of the deformation gradient:

$$J_F = \det(\mathbf{F}) \tag{2.14}$$

The finite element residual equation for large deformation formulation uses non-linear strain-displacement matrix $\mathbf{B}_{nl}$ and the second *Piola-Kirchhoff* stress tensor Σ as follows [Bathe, 2006]:

$$\mathbf{R}(\mathbf{d_s}) = \sum_V \left[\mathbf{B}_{nl}^T \Sigma - N^T \mathbf{b} \right] wJ - \sum_A N^T t^p wj \tag{2.15}$$

where $\mathbf{R}$ is the element force residual which represent the imbalance between the external applied loads and the internal element reaction forces, $\mathbf{B}_{nl}$ is the non-linear strain displacement matrix, t^p is the applied traction force, w is the Gauss-point weight for the Gaussian quadrature, J is the volume to volume Jacobian between the reference and physical volume elements, j is the face to face Jacobian and N is a shape function matrix that enables interpolation of the nodal values to a location within the element. The non-linear strain is composed of a linear and a non-linear component as:

$$\mathbf{B}_{nl} = \mathbf{B}_l + \mathbf{B}_n \tag{2.16}$$

where the Green tensor $\mathbf{G}$ can be rewritten in another form as:

$$\mathbf{G} = \mathbf{B}_l \mathbf{d_s} + \frac{1}{2} \mathbf{B}_n \mathbf{d_s} \tag{2.17}$$

Furthermore, the global residual *R* is determined by summing the force residual for all the elements using the direct stiffness method [Bathe, 2006]:

$$\mathbf{R}(\mathbf{D_s}) = \sum_{elements} \mathbf{R}(\mathbf{d_s}) \tag{2.18}$$

where $\mathbf{D_s}$ is the global displacement vector. In order to solve the system of equations, a Newton-Raphson method is employed by taking an initial guess of the solution vector $\mathbf{D_s}^i$ for $i = 0$ and a tangent to evaluate the next guess as:

$$\delta \mathbf{D_s} = - \left[\frac{\mathrm{d}\mathbf{R}}{\mathrm{d}\mathbf{D_s}} \Big|_{\mathbf{D_s}^i} \right]^{-1} \mathbf{R}(\mathbf{D_s}^i) \tag{2.19}$$

hence, the next guess of the solution will be of the form:

$$\mathbf{D_s}^{i+1} = \mathbf{D_s}^i + \delta \mathbf{D_s} \tag{2.20}$$

The iterative procedure continues until the global displacement residual is sufficiently small based on a convergence criteria for the norm of $\mathbf{R}$ to be less than 10^{-5} times the applied load magnitude as used in all the studied configurations.

2.5 Mesh motion solver

The purpose of a mesh motion solver is to enable the fluid mesh to track the motion of the flexible structure when it deforms due to the fluid stresses acting on its surface. The main role of any mesh motion approach is to accommodate the structural deformations while maintaining the quality of the mesh especially near the fluid-solid interface.

Three groups of mesh motion methods are available to update the volume mesh in the deforming regions and can be classified as Smoothing methods, Dynamic layering or Remeshing methods. An overview of these three mesh motion techniques is provided in the next sections.

In the next sections, we provide an overview of the three groups of mesh motion methods.

2.5.1 Smoothing methods

The smoothing methods moves interior nodes to absorb the motion of a moving/deforming boundary while the number of the nodes and their connectivity does not change. Two different methods known as Spring smoothing and Diffusion smoothing are available for interior zones.

2.5.1.1 Spring smoothing

Spring smoothing is the quickest method available in terms of computational time, however it only performs well when small deformations are present or when the boundary moves predominantly in its normal direction. In spring-based smoothing, the edges between any two nodes are idealized as a network of springs such as a displacement at a boundary node will generate a "spring force". Using Hooke's law, this force on a node, can be written as:

$$\mathbf{Fs}_i = \sum_j^{n_i} k_{ij} \left(\Delta \mathbf{x}_j - \Delta \mathbf{x}_i \right) \tag{2.21}$$

where $\Delta \mathbf{x}_i$, $\Delta \mathbf{x}_j$ are the displacement of node i and its neighbor j, n_i is the number of nodes connected to i and k_{ij} is the spring constant which is defined as:

$$k_{ij} = \frac{k_{\text{fac}}}{\sqrt{|\mathbf{x}_i - \mathbf{x}_j|}} \tag{2.22}$$

where k_{fac} is a predetermined value between 0 and 1. At equilibrium, the net force from all the springs connected to the node must be zero. This conditions results in an iterative equation such that:

$$\Delta \mathbf{x}_i^{m+1} = \frac{\sum_j^{n_i} k_{ij} \Delta \mathbf{x}_j^m}{\sum_j^{n_i} k_{ij}} \tag{2.23}$$

where m is the iteration index. The iterative solution stops when the above iterative equation reaches a predetermined convergence tolerance or a maximum number of iterations. At convergence, the positions of the nodes are updated such that:

$$\mathbf{x}_i^{n+1} = \mathbf{x}_i^n + \Delta \mathbf{x}_\mathbf{i}^{\text{converged}} \tag{2.24}$$

where n in this case is the current time step and $n+1$ is the next time step.

In Figure 2.2, we can see the effect of changing the value of the spring constant factor. A lower value will give a less "stiff" mesh where no damping will occur on the displacement of the interior nodes as in Figure 2.2 (a), while a higher value will mainly deforms the nodes adjacent to the moving wall as in Figure 2.2 (b).

2.5.1.2 Diffusion smoothing

For diffusion-based smoothing, the mesh motion is governed by the following equation:

$$\nabla \cdot (\gamma \nabla \mathbf{u_m}) = 0 \tag{2.25}$$

where γ is the mesh diffusion coefficient and $\mathbf{u_m}$ the mesh displacement velocity. The mesh diffusion coefficient is usually a function of the boundary distance:

$$\gamma = \frac{1}{\ell^\alpha} \tag{2.26}$$

where ℓ is a normalized boundary distance and α is the diffusion parameter.

The above vector equation is discretized using standard finite volume method and the resulting matrix is solved iteratively using the algebraic multigrid (AMG) solver. The cell centered solution for the displacement velocity is interpolated onto the nodes using inverse distance weighted averaging, and the nodes positions are updated according to the following equation:

$$\mathbf{x}_{\text{new}} = \mathbf{x}_{\text{old}} + \mathbf{u}_{\mathbf{m}}\Delta t \tag{2.27}$$

Diffusion-based smoothing is generally more computationally costly than spring-based smoothing but tends to generate better quality meshes and allows larger deformations than spring-based smoothing as shown in Figure 2.3.

The range of the diffusion parameter is usually between 0 and 2:

- $\alpha = 0$ gives $\gamma = 1$ and a uniform diffusion of the boundary motion into the interior of the mesh.
- higher values of α will preserve the mesh near the moving boundary better.
- A value of 1-1.5 often works well if one wish to let the "far field" mesh absorb the motion.

To illustrate the effect of the diffusion parameter α on the resulting mesh, a piston-type boundary motion is prescribed at an initially uniform meshed square domain which is deformed by compression effect by moving from the left boundary to the right boundary. Results are depicted in Figure 2.4 according to various given value for α.

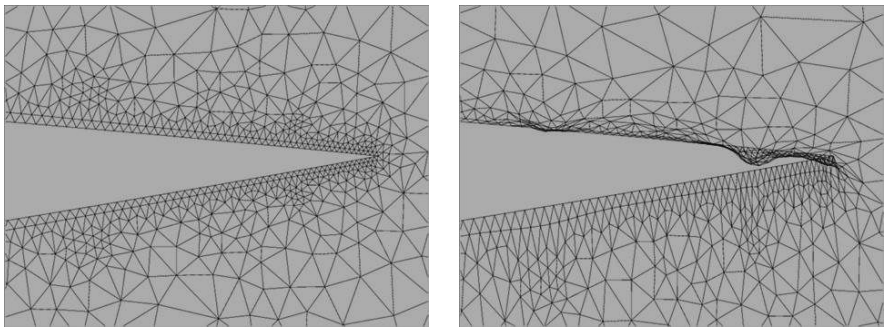

(a) (b)

Figure 2.2: Interior nodes movement: (a) spring constant factor=0; (b) spring constant factor=1 [ANSYS, 2015]

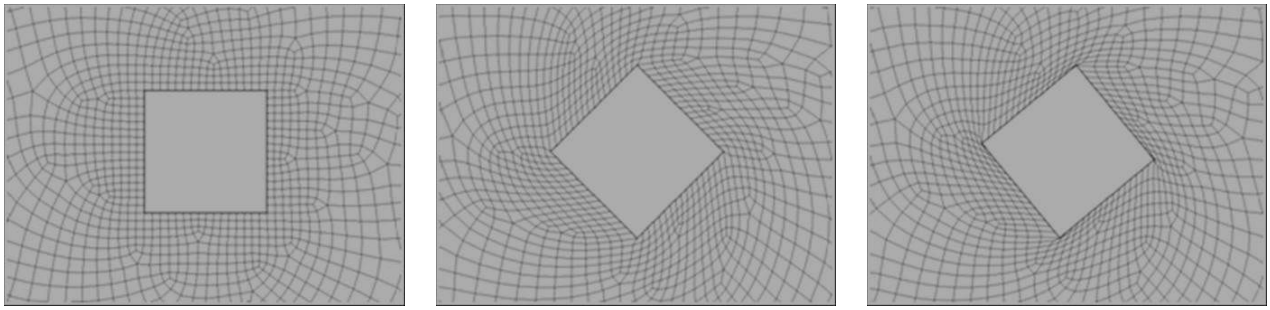

(a) (b) (c)

Figure 2.3: Comparison between spring-based and diffusion-based smoothing: (a) initial cube position; (b) cube rotated 45° using diffusion-based smoothing and (c) using spring-based smoothing [ANSYS, 2015]

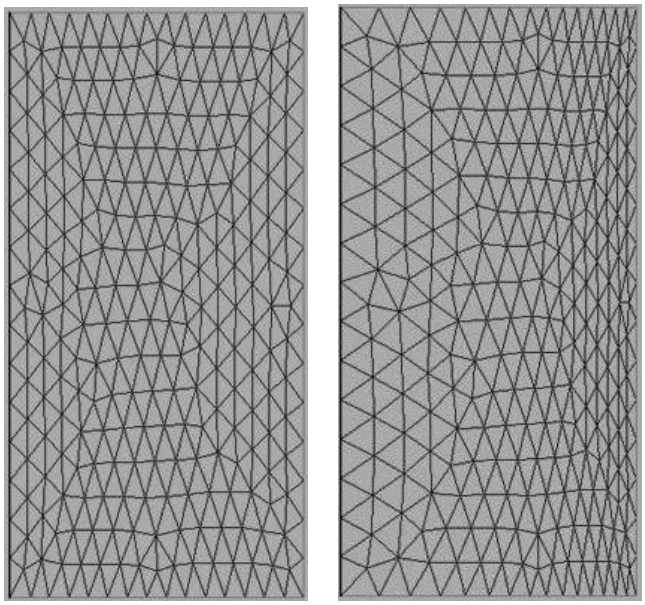

(a) (b)

Figure 2.4: Effect of diffusion parameter α on interior nodes movement: (a) $\alpha = 0$; (b) $\alpha = 1$ [ANSYS, 2015]

2.5.2 Dynamic layering

The dynamic layering method allows to add or remove layers of cells adjacent to a deforming zone. Cells are added or deleted as the zone grows or shrinks resulting in a connectivity change. The layering method is available for quad, hex and wedge mesh elements and is must useful for linear motion (e.g. moving piston) but can be used also for pure rotational motion as well. The layer cells adjacent to the moving boundaries (layer j) is split or merged with the layers of the cells next to it (layer i in Figure 2.5) based on the height of the cells in layer j.

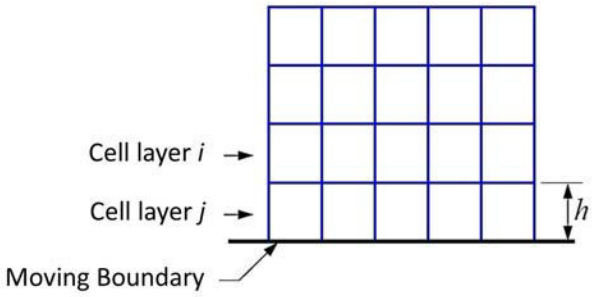

Figure 2.5: Dynamic layering applied to a domain moving at the bottom boundary [ANSYS, 2015]

Splitting and merging of the cell layers is dependent upon the split factor α_s and the collapse factor α_c. If the cells in layer j are expanding, splitting will occur if the following condition is satisfied:

$$h > (1 + \alpha_s)\, h_{\text{ideal}} \tag{2.28}$$

where h_{ideal} is the ideal height of the cell and generally is taken to be the same as the initial height in the layer near the moving boundary. When this condition is met, the cells are split to create a new cell layer of height equal to h_{ideal}. However, if the cells in layer j are being compressed, the cell heights are allowed to decrease until:

$$h < \alpha_c h_{\text{ideal}} \tag{2.29}$$

When the above condition is met, the cells in layer j are merged with those in layer i.

2.5.3 Remeshing methods

In order to avoid divergence problems especially caused by negative cell volumes when large deformations occur, the mesh solver supports several remeshing methods. Remeshing allows then simulating problems with large relative motion of boundaries where the cells and faces are remeshed when skewness or size exceeds specified limits as shown in Figure 2.6. The mesh solver can report negative volume cells if the mesh contains inacceptable elements (skewness in the range 0.98-1.00 as in Figure 2.6). The skewness of a cell is usually calculated by the equilateral deviation method [Thompson et al., 1998] as follows:

$$\text{Skewness} = \frac{\text{optimal cell size} - \text{actual cell size}}{\text{optimal cell size}} \tag{2.30}$$

If the new cells satisfy the skewness criterion (typically the skewness limit set in the simulations is less than 0.7 for acceptable mesh quality), the mesh is locally updated with the new cells (with the solution interpolated from the old cells). In these methods, the number of nodes and connectivity changes as cells/faces are added or deleted. Typically, remeshing and smoothing can be used together in order to produce high quality meshes and to allow larger time steps.

The available remeshing methods in ANSYS Fluent [ANSYS, 2015] are summarized below according to their supported mesh types:

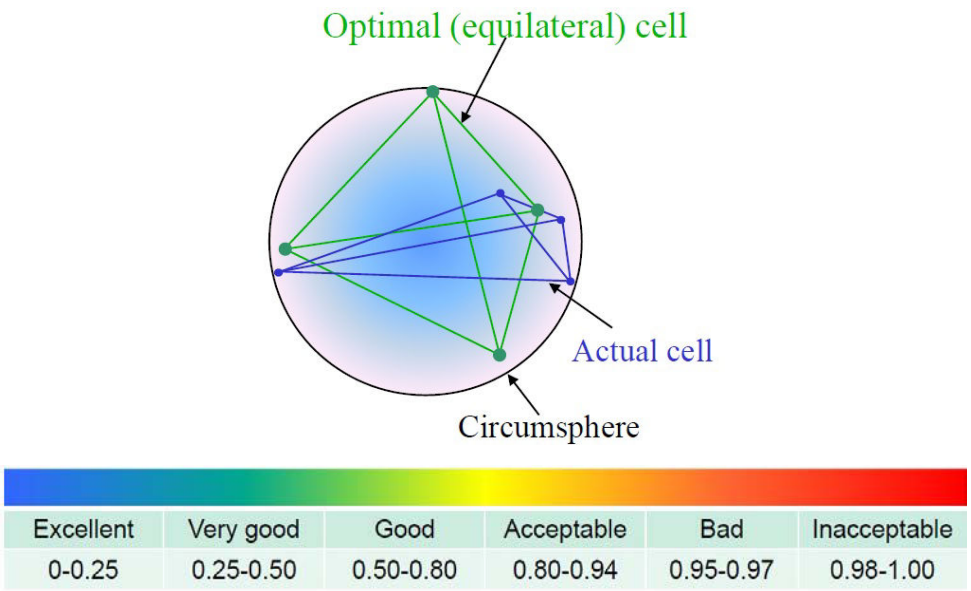

Figure 2.6: Skewness mesh metrics spectrum [Thompson et al., 1998]

- Local cell: remesh interior cells (2D and 3D). It only affects triangular and tetrahedral cell types in the mesh.
- Zone remeshing: remesh the complete cell zone if local cell remeshing fails. Usually, the zone remeshing type will be invoked if skewness>0.98 after local cell remeshing.
- Local face: remesh triangular faces on deforming boundaries (only in 3D).
- Region face: remesh faces adjacent to a moving boundary (2D and 3D). It is applied to triangular faces in 2D and tetrahedral faces in 3D and it remeshes the faces based on skewness only.
- 2.5D: remesh prism elements in 3D zones (prisms from extruded triangular elements).

Other remeshing criteria can be set based on the minimum and maximum cell length scale allowed. The edge length scale of a cell is calculated as the average of the edges of the cell. This length scale criterion combined with a skewness criterion and the smoothing method described in section 2.5.1 allows simulations of large deflections of flexible structures without deterioration of the mesh quality. The two snapshots below in Figure 2.7 are shown to illustrate zone remeshing where mesh quality is preserved in the highlighted areas in Figure 2.7 (b) even though large deformation occurs.

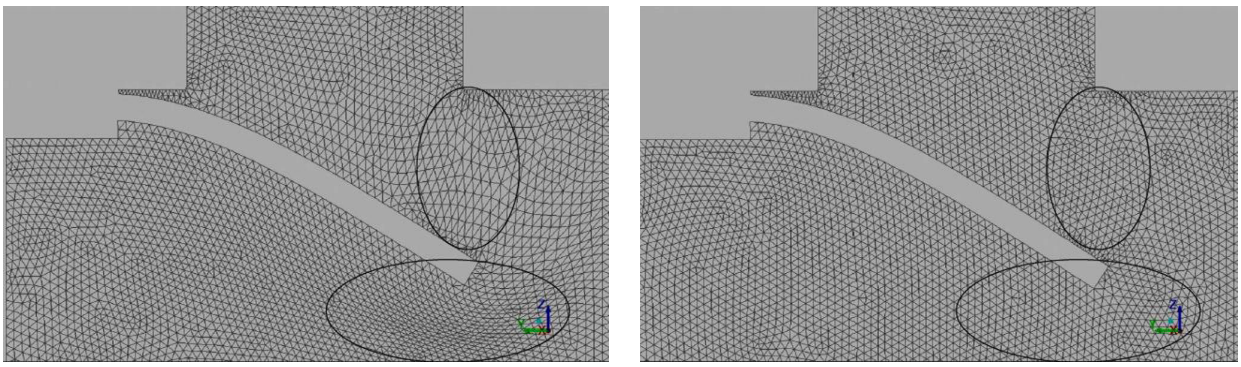

(a) (b)

Figure 2.7: (a) zone before remeshing; (b) zone after remeshing [ANSYS, 2015]

2.6 FSI coupling

Fluid-structure interaction problems can be modeled using different approaches mainly divided into *partitioned* and *monolithic* [Schäfer and Teschauer, 2001, Blom, 1998, Felippa and Park, 1980, Piperno, 1997, Wall et al., 2007]. Monolithic approaches are inherently considered as strongly coupled since the flow and structural equations are solved in the same matrix. However for partitioned approaches, the fluid and structural equations are solved separately and boundary conditions are exchanged between the two solvers at the fluid-solid interface. Partitioned approaches are divided into one-way (uncoupled) or two-way coupled methods. Depending on the degree of numerical coupling, the two-way coupled methods are further divided into weakly and strongly coupled as shown in Figure 2.8. The monolithic approach formulates the governing equations for both the fluid and the structure domains in terms of the same variables mainly pressure and velocity [Greenshields and Weller, 2005], and discretizes all the domain with the same numerical scheme. The main advantage of using a monolithic approach is that the algorithm is that perfect coupling between the fluid and solid domains is achieved, improving the stability of this numerical method. Nevertheless, monolithic approach suffers from several drawbacks:

- The system of algebraic equations obtained after discretization is non linear, thus this approach is not well suited for large scale problems and leads to complex software developments.
- The resulting system of equations requires a lot of CPU memory in order to store simultaneously the unknown variables for both the fluid and the solid domains.
- A common time step is used for all the domains, which may be inefficient especially when different time scales are present [Hübner et al., 2004].
- A single mesh is usually generated for both the fluid and solid domains which creates difficulties to provide a high quality mesh [Slone et al., 2004].

Regardless of whether the solution method is considered one-way or two-way, the partitioned approach involves separate solutions for the different physical equations. With this approach, each solver can be based on different discretization techniques such as the finite volume method for the fluid solver and the finite element method for the structural solver. Moreover, different time-integration schemes can be used and even different time steps. At the fluid-solid boundary, information is shared between the fluid solver and the structural solver and how this information is exchanged can determine the coupling method as either weakly or strongly coupled. For one-way coupling calculations, a converged solution is obtained for one field, then used as a boundary condition or external load for the second field. For example, if we consider a fluid-structure interaction domain, where the fluid domain consists of air and the structural domain consists mainly of a rigid moving body such as steel. This movement will set the fluid air in motion, however the air will not significantly causes

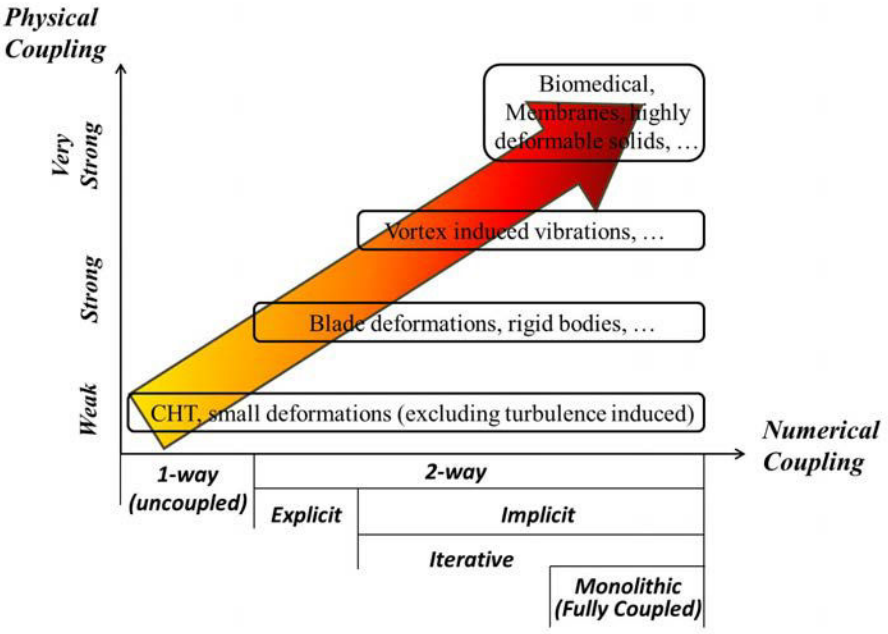

Figure 2.8: Modeling approaches for fluid-structure interaction problems

forces on the body in motion. This kind of problem can be solved using a one-way fluid-structure interaction problem. The movement of the structure controls the motion of the fluid but the fluid motion does not influence significantly the movement of the structure.

Figure 2.9 shows the solution procedure for one-way coupling. Initially, the structural field is solved until the convergence criterion is reached. The nodes displacement of the structure at the fluid-structure interface are transferred to the fluid side. Next the mesh motion solver will deform the mesh due to structural movement and the flow field is calculated until the convergence criterion is reached. Then, the structural movement for the next time step is calculated to convergence. The final solution is attained when the maximum number of time steps is reached. Unfortunately, fluid-structure interaction of our concern are mostly two-way coupled.

If we assume that the flow is driven by an inflow condition and that the structure is elastic, the flow will act on the structure and will produce a deformation. Due to the deformation of the structure, the flow domain is altered. Here, there is a real feedback between both systems and the coupling is said to be two-way. Figure 2.10 shows the solution algorithm for a two-way coupling strategy. During a time step of the two-way coupling method, the response of the structure to the acting loads represent a displacement of the structural grid nodes in ANSYS Mechanical. The displacement of the boundary at the fluid-solid interface is further interpolated to the fluid mesh which will cause its deformation where appropriate smoothing and remeshing algorithms are applied to ensure the high quality of the mesh. Finally, inner iterations of the flow solver ANSYS Fluent are performed until convergence criteria are reached where the convergence solution of the flow field is required to transfer the acting forces on the solid body. Figure 2.10 classify the two-way coupling algorithm into weakly (explicit) or strongly coupled (implicit) respectively in Figure 2.10 (a) and (b). A weakly coupled algorithm can be converted to a strongly coupled algorithm with the introduction of a fixed-point outer iteration loop as in Figure 2.10 (b). This outer loop will be repeatedly performed within a time step until changes in the flow forces and structural displacements fall below a defined tolerance. All the investigations presented in this manuscript are performed using a two-way strongly coupled partitioned approach since we only deal with large deformations of highly flexible structures. This implicit approach is more robust than the explicit one and allows the use of larger time steps and more stable converging solutions.

In order to establish the equilibrium on the fluid-structure interface $\Gamma_{F/S}$, some requirements must be respected. The boundary conditions for displacement $\mathbf{d}$, mesh velocity $\mathbf{u_m}$ and equilibrium

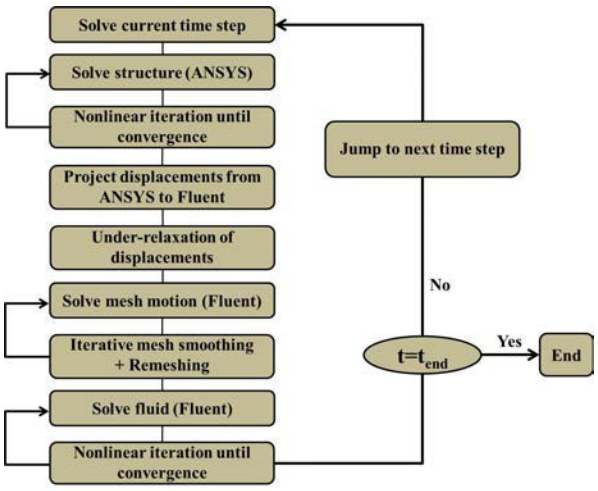

Figure 2.9: FSI solution algorithm for one-way coupling

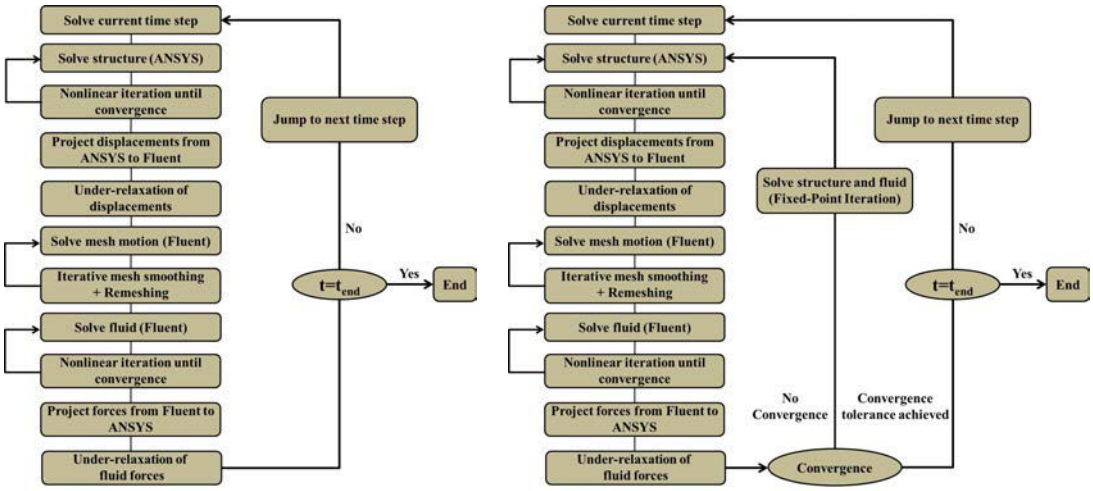

(a) (b)

Figure 2.10: FSI solution algorithm for two-way coupling: (a) weakly coupled and (b) strongly coupled

stress $\boldsymbol{\sigma}$ should satisfy the following relations:

$$\mathbf{d_s}^{\Gamma_{F/S}} = \mathbf{d_f}^{\Gamma_{F/S}} \tag{2.31}$$

$$\mathbf{u_s}^{\Gamma_{F/S}} = \mathbf{u_f}^{\Gamma_{F/S}} \tag{2.32}$$

$$\boldsymbol{\sigma_s}^{\Gamma_{F/S}} \cdot \mathbf{n} = \boldsymbol{\sigma_f}^{\Gamma_{F/S}} \cdot \mathbf{n} \tag{2.33}$$

where $\mathbf{n}$ is the unit normal on the fluid-solid interface. The flowchart defining the solution procedure in this study as in Figure 2.10 (b) involves the use of under-relaxation of displacements and forces when projecting them to the destination solver at the interface. The use of under-relaxation in these iterations is mainly to control the amount of the structure's displacement of fluid forces that is projected on either the fluid or solid domain with the aim of improving convergence. Thus, for each data transfer node on the fluid-solid interface, the following formula is applied in order to limit potentially large variations of the target-side data between two successive coupling iterations:

$$\phi_{\text{Relaxed}} = \phi_{\text{Reference}} + w\left(\phi_{\text{Raw}} - \phi_{\text{Reference}}\right) \tag{2.34}$$

where w is the under-relaxation factor, ϕ_{Relaxed} is the relaxed target-side value, $\phi_{\text{Reference}}$ is the reference target-side value which is the final value obtained from the last coupling iteration. ϕ_{Raw} is the raw value obtained from interpolation of the solution obtained at the current coupling iteration from the source grid node to the target grid node.

2.7 FSI numerical validation

The benchmark configuration proposed by Turek and Hron [Turek and Hron, 2006] has been chosen for the present FSI validation. The configuration consists of a laminar incompressible 2D channel flow around an elastic beam attached to a fixed cylinder. Under the unsteady effect of the hydrodynamic forces imposed by the flow around the cylinder, self-sustained oscillations are induced to the structure. A sketch of the computational domain is given in Figure 2.11. The domain has an inlet with a laminar parabolic velocity profile, a zero pressure condition at the outlet, and no slip boundary conditions at the walls. The 2D channel has a length of $2500\ \text{mm}$ and a height of $410\ \text{mm}$. The circular cylinder has a radius of $50\ \text{mm}$ and is slightly shifted from the horizontal middle line in order to produce a non symetrical flow. The flexible structure has a length of $350\ \text{mm}$ and a height of $20\ \text{mm}$. The axis origin is taken at the tip of the flap from its initial position.

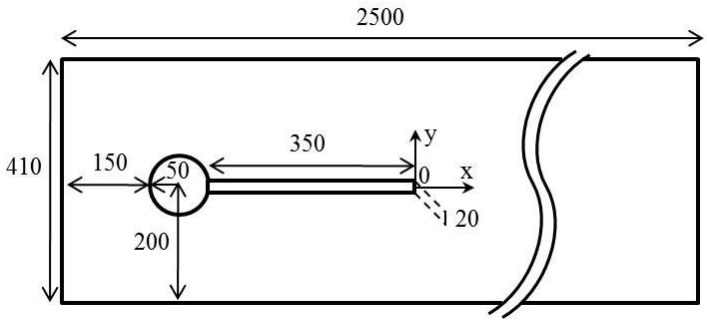

Figure 2.11: Schematic view of the computational domain used as benchmark (dimensions in mm)

Three different configurations are investigated and described in Turek and Hron [Turek and Hron, 2006] depending on the flow velocity, the shear modulus and density of the moving elastic beam. The second configuration case (cited as FSI2 in Table 12 in [Turek and Hron, 2006]) is retained for benchmark since the flap motion shows the largest displacements. The corresponding physical quantities are summarized in Table 2.1.

Table 2.1: Physical properties for FSI2 numerical benchmark

Parameter	$\rho_s\ [\text{kg/m}^3]$	ν_s	$E\ [\text{Pa}]$	$\rho_f\ [\text{kg/m}^3]$	$\nu_f\ [\text{m}^2/\text{s}]$	$U_{max}\ [\text{m/s}]$
FSI2	10,000	0.4	1.4×10^6	1,000	0.001	1.5

The fluid domain is discretized with 43,000 triangular cells and the mesh is refined at the walls and the fluid-structure interface, i.e. the elastic beam. The moving structural domain consists of 400 quadrilateral cells. In this simulation, a maximum number of 7 FSI outer iterations were needed to attain convergence criteria of 10^{-4} for both displacements and forces on the fluid-structure interface. To avoid divergence problems especially caused by negative cell volumes, the mesh solver uses in this numerical validation the $2.5D$ surface remeshing that applies on wedge/prism cells extruded from triangular surface elements. This method agglomerates cells that violate the skewness or size criteria and locally remeshes the agglomerated cells or faces. If the new cells or faces satisfy the skewness criterion, the mesh is locally updated with the new cells (with the solution interpolated from the old cells) [ANSYS, 2015]. Otherwise, the new cells are discarded and the old cells are retained. In the present numerical validation a maximum cell skewness of 0.7 has been used for remeshing with

cell size criterion depending on the minimum and maximum length scale of the mesh. The effect of remeshing especially at high deflections is shown in Figure 2.12 at the trailing edge of the elastic beam where the cells undergo cyclic expansion and compression, thus the remeshing algorithm always preserves a good quality of the mesh. An under-relaxation factor for both displacements and forces is set to unity and highlights a good stability and robustness of the model.

The pressure-velocity coupling is established using the coupled algorithm [ANSYS, 2015], which solves the momentum and pressure-based continuity equations together. The convergence criteria for pressure and velocity is set to 10^{-6}. The Laplace mesh smoothing convergence criteria is set to 10^{-4} using a diffusion-based smoothing with a diffusion coefficient $\alpha = 1.5$ (Eq.(2.26)) which causes the cells far from the fluid-solid interface to absorb much of the motion. Temporal discretization is performed using a first order implicit scheme and the time step is set to 10^{-4} sec. In an explicit time integration scheme, the time step is conditionally stable and limited by the courant number which is defined by:

$$\mathrm{CFL} = \frac{U_f \Delta t}{\Delta x} \leqslant \mathrm{CFL}_{\max} \tag{2.35}$$

where Δt is the time step, Δx is the size interval between two adjacent cells and $\mathrm{CFL}_{\max}$ is typically chosen to be equal to unity when using explicit time stepping in order to achieve numerical stability. However, the fully implicit first order scheme is unconditionally stable with respect to the time step value. Nevertheless, the CFL based on the time step size of 10^{-4} seconds and the minimum cell distance remains always less than unity.

The displacement at the tip of the elastic beam is shown in Figure 2.13 in y direction. After a 7 seconds transient state, the beam shows harmonic oscillations at constant frequency and amplitude. The vortex shedding from the upstream cylinder induces alternating forces on each side of the elastic beam that cause a periodic flapping motion as shown in Figure 2.14.

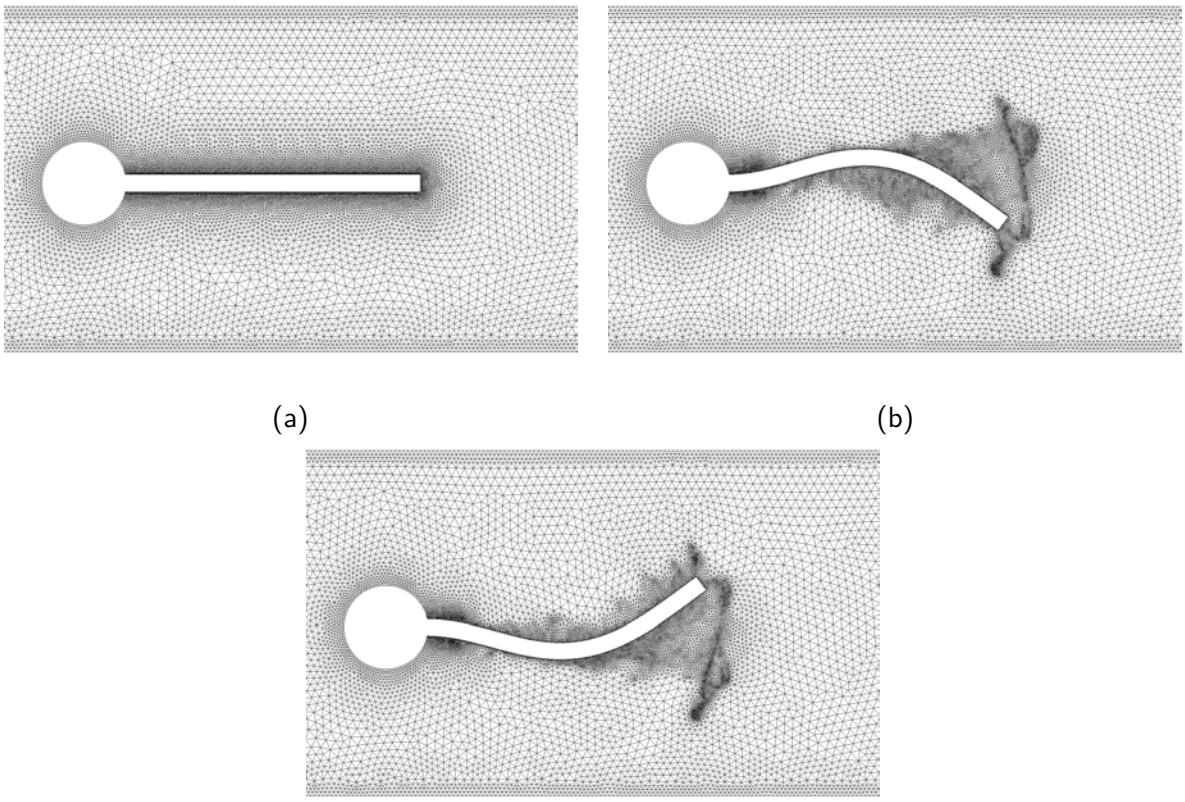

Figure 2.12: Snapshots of dynamic mesh motion with remeshing activated during three time steps: (a) t_0; (b) $t_0 + 11.0678$ s and (c) $t_0 + 11.3278$ s

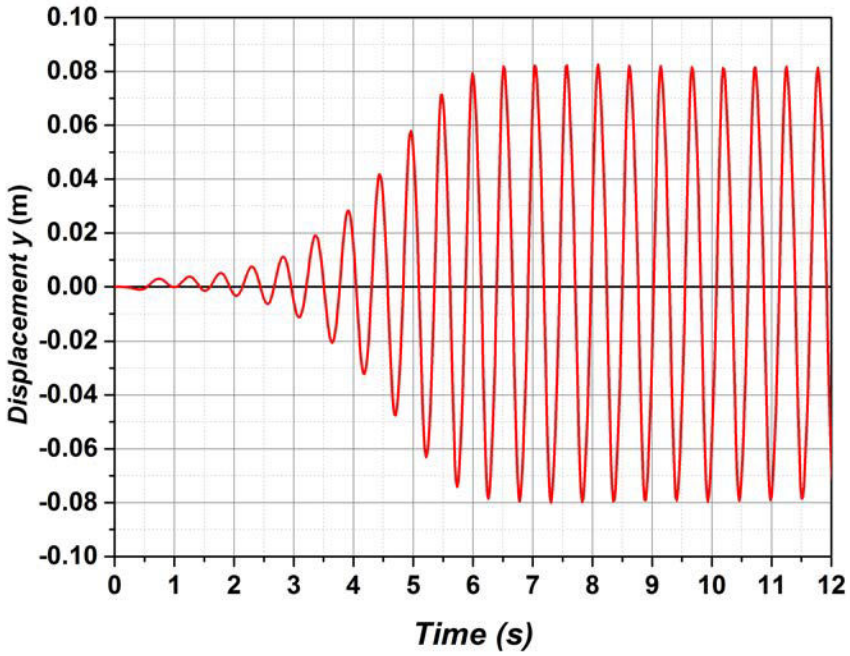

Figure 2.13: Displacement of the flap tip measured in the y direction for the numerical simulation proposed as a validation test case

For comparison with Turek and Hron [Turek and Hron, 2006], the mean and amplitude are computed from the last period of oscillations according to the following relations proposed in [Turek and Hron, 2006]:

$$mean = \frac{1}{2}\left(max + min\right) \tag{2.36}$$

$$amplitude = \frac{1}{2}\left(max - min\right) \tag{2.37}$$

The frequency of the oscillations is then computed by using a Fast Fourier Transformation on the displacement signal. Results are summarized in Table 2.2 and compared with the reference values [Turek and Hron, 2006]. One can observe that results are in very good agreement with the reference case and only exhibit small discrepancies in the x-direction (error is of 0.14% for the mean, 1.13% for the amplitude and 1.3% for the frequency) and y-direction (error is of 5.7% for the mean, 1.24% for the amplitude and 5.0% for the frequency).

Table 2.2: Results comparison between present simulation and Turek and Hron [Turek and Hron, 2006]

	x direction		y direction	
	Present results	reference [Turek and Hron, 2006]	Present results	reference [Turek and Hron, 2006]
Mean (mm)	-14.56	-14.58	1.30	1.23
Amplitude (mm)	12.58	12.44	81.05	80.06
Frequency (Hz)	3.75	3.80	1.90	2.00

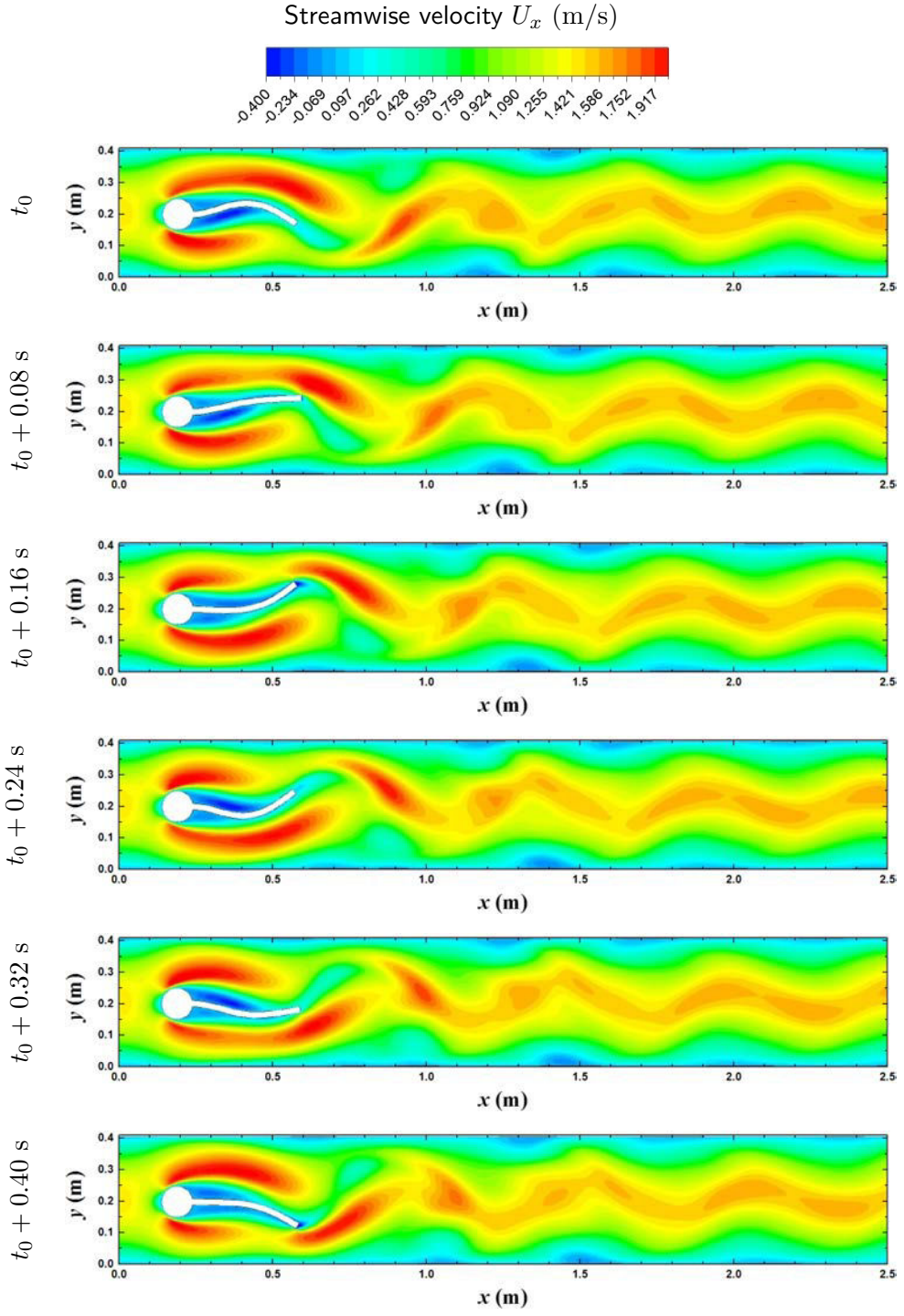

Figure 2.14: Instantaneous streamwise velocity fields U_x during one period of oscillation

2.8 Conclusion

In this chapter, we have presented the governing equations for the fluid, solid and mesh motion solvers. Smoothing capabilities were highlighted where the diffusion-based smoothing is favored in all the simulations present in this study since it performs and preserves the mesh quality much better when compared to other mesh smoothing methods. Remeshing is applied also in parallel with smoothing to avoid negative cell volumes when large displacement motions are present which is important to our subsequent studies since we deal with highly deformable elastic bodies. Moreover, the numerical coupling used in all the simulations is considered two-way with strong coupling at the fluid-structure interface which is necessary in order to resolve the feedback between the fluid flow and the structural deformations thus maintaining numerical stability. Finally, we validated the FSI solver with a challenging benchmark from the literature where the structure periodically undergoes high amplitude oscillations and the results show the robustness and reliability of applying the method suggested by coupling ANSYS Fluent to ANSYS Mechanical where minimal discrepancies are observed when comparing the results of our simulation and Turek and Hron [Turek and Hron, 2006] FSI2 reference test case.

Finally, in order to study the heat transfer and mixing performances of the oscillating elastic structures, one needs to compute the proper heat and mass equations in an ALE formulation. In the subsequent studies, the mass transport equation of a scalar c is considered to study the effect of the elastic flap deformations on fluid mixing:

$$\frac{\partial c}{\partial t} + (\mathbf{u_f} - \mathbf{u_{m.f}}) \cdot \nabla c = D_m \nabla^2 c \tag{2.38}$$

where D_m is the mass diffusivity of the scalar c. Usually, the convective scalar mixing is only considered so mass diffusion term will be set to 0.

The heat equation is also solved in the fluid domain to study the heat transfer performance and is given by:

$$\frac{\partial T_f}{\partial t} + (\mathbf{u_f} - \mathbf{u_{m.f}}) \cdot \nabla T_f = \frac{k_{th}}{\rho_f C_p} \nabla^2 T_f \tag{2.39}$$

where T_f is the fluid temperature and C_p is the specific heat.

Chapter 3

Heat transfer and mixing enhancement by free elastic flaps oscillation

In this chapter, a two-dimensional laminar study is investigated in a channel where four flexible vortex generators (FVGs) are attached to the opposite walls. Upstream of the channel, two co-planar FVG are inserted followed by two alternating FVGs downstream. Two cases are studied depending on the Reynolds number which is set to 1850 and 1000 (case 1 and case 2). Computationally expensive simulations are done in order to solve the fluid-structure interaction problems, which is estimated as a period of one to two months of simulation time per two-dimensional case. Two-way strongly coupled simulations are performed where the downstream FVG undergo periodically large free oscillations as they are excited by the vortices shed from the upstream co-planar FVGs. The FVGs oscillate at a frequency equal to their fundamental frequency and their vortex shedding frequency, reaching their lock-in state which is an essential criterion for large amplitude oscillations as seen previously in VIV studies.

Moreover, the FVG cases are compared to their relative rigid vortex generators case in terms of flow pattern and mixing and heat transfer performances. It is shown that flaps oscillations increase the velocity gradients and generate periodic vortices due to the shear layer instability generated at the tip of each flap. The mixing efficiency is quantified by the transport of a passive scalar where the scalar diffusivity is set to zero to avoid any mixing related to diffusion and highlight mainly the effect of flaps motion on mixing. The FVG cases show better mixture quality than the RVG cases with a 98% increase in mixture quality for case 1 and a 97% increase for case 2 when compared to their relative rigid cases. The mixture quality enhancement is mainly caused by the flaps high amplitude oscillations which act as a mechanical pump sequentially pumping scalar with different values and eventually improving the mixture quality. Furthermore, in order to analyze the heat transfer, parameters of local and global Nusselt numbers are evaluated. An increase of up to 97% in the local heat transfer and 134% in the overall heat transfer is observed when using elastic flaps instead of rigid ones. Another criterion is used to analyze the heat transfer which is the thermal performance factor η defined as the ratio of convective heat transfer in the elastic cases to that in the rigid case at constant pumping power. A value of thermal performance η greater than one is observed in both cases 1 and 2.

As a conclusion, this study shows an innovative concept to enhance heat transfer and mixing by relying on passive dynamic methods without addition of any external force except that of the fluid itself. To the author's opinion, this study can serve as a basic design to further analyze different parameters such as the flap length, thickness, angle with respect to wall, distance between the flaps, Young's modulus and could be performed in different fluid media such as water for instance. Another added value of these proposed configurations is that the free oscillating flaps are studied in a confined channel and attached to the channel walls with a steep angle relative to the flow direction. Usually, in the literature the studies of free flapping motion or VIV are very similar to the FSI numerical validation of Tureck previously shown in Chapter 2.

Note to the reader: the references related to the following article are included at the end of this chapter.

International Journal of Heat and Mass Transfer 85 (2015) 250–264

Contents lists available at ScienceDirect

International Journal of Heat and Mass Transfer

journal homepage: www.elsevier.com/locate/ijhmt

Heat transfer and mixing enhancement by free elastic flaps oscillation

Samer Ali [a,b,c,*], Charbel Habchi [a], Sébastien Menanteau [b,c], Thierry Lemenand [d], Jean-Luc Harion [b,c]

[a] Lebanese International University LIU, Mechanical Engineering Dept., P.O. Box 146404 Mazraa, Beirut, Lebanon
[b] Université Lille Nord de France, F-59000 Lille, France
[c] Mines Douai, EI, F-59500 Douai, France
[d] University of Angers – ISTIA, LARIS – EA 7315, Angers, France

ARTICLE INFO

Article history:
Received 12 March 2014
Received in revised form 22 January 2015
Accepted 26 January 2015
Available online 16 February 2015

Keywords:
Fluid–structure interaction
Thermal performance
Laminar mixing
Numerical simulation
Multifunctional heat exchangers/reactors

ABSTRACT

An original concept is proposed to enhance heat transfer and mixing quality performances by using flexible vortex generators (FVGs) for a static mixer configuration. The role of free elastic flaps oscillations on the mixing process and heat transfer in a two-dimensional laminar flow is numerically investigated. The computational domain consists of four distant FVGs mounted on two opposite walls. Two cases are studied depending on the Reynolds numbers (based on the bulk velocity and the channel height) set to 1000 and 1850. FVGs efficiencies are compared to the corresponding cases with rigid vortex generators (RVGs). In the flexible cases, flaps oscillations increase the velocity gradients and generate an unsteady laminar flow with complex coherent vortices detaching from the tip of the flaps. The mixing efficiency is quantified by the transport of a passive scalar through the channel. It is shown that oscillations in the elastic cases enhance the mixture quality up to 98% relative to that in the rigid cases. The heat transfer enhancement is also investigated showing up to a 96% increase in the Colburn factor, 56% increase in thermal performance factor and 134% increase in the overall heat transfer. As the FVGs oscillate freely without any additional external force other than that exerted by the flow itself, the implementation of such a technique shows a great potential for the performance enhancement of multifunctional heat exchangers/reactors.

1. Introduction

Rigid vortex generators (RVGs) are frequently used for mixing and heat transfer enhancement due to their ability to disrupt the boundary layers and generate complex coherent vortices that destabilize the flow, enhancing thus the convective heat transfer property [1,2]. Various domains of applications of this technique can be found such as in flow jets, chemical reactors, static mixers, heat exchangers and systems in which continuous process is needed [3,4].

Vortex generation methods can be classified into passive and active control techniques [5]. On one hand, passive RVGs are effective to enhance heat and mass transfer due to flow modification they induce. An overview of different RVG geometries is given by Fiebig [1]. Among them, trapezoidal shapes have successfully been used to enhance performances in the high efficiency vortex static mixer as described by Habchi et al. [6] in which a succession of 30° inclined trapezoidal RVGs arrays are mounted on the inner walls. For this configuration, performance enhancement can be achieved by optimizing RVGs shapes or locations in the pipe. Various studies have already been conducted to this aim. In the turbulent regime range, Habchi et al. [7] studied several configurations in which arrays of RVGs were aligned or set with a 45° offset angle and oriented in the main flow direction or in the opposite direction. They concluded that the RVGs orientation in the opposite direction of the main flow are the most efficient to increase heat transfer performance. In a more recent article, Habchi et al. [8] also studied tapped RVGs or coupled RVGs with downstream protrusions that could noticeably affect heat transfer performances. As far as laminar regimes are concerned, RVGs have also been proven to be efficient to destructurate the boundary layers in the wake and to increase by this way the heat transfer and mixing properties of the flow. Indeed, experimental and numerical studies conducted on a single tab or on one raw of tabs showed that developing counter-rotating vortex pair and hairpin-like vortices tend to enhance heat transfer in a laminar flow regime [6,9–11].

On the other hand, active control methods can be used to generate vorticity with oscillating tabs or flapping wings with their displacements amplitude and frequency controlled by an external

* Corresponding author at: Lebanese International University LIU, Mechanical Engineering Dept., P.O. Box 146404 Mazraa, Beirut, Lebanon. Tel.: +961 1 70 68 81; fax: +961 1 30 60 44.
E-mail address: samer.ali@liu.edu.lb (S. Ali).

http://dx.doi.org/10.1016/j.ijheatmasstransfer.2015.01.122
0017-9310/

Nomenclature

c	scalar (–)
c_p	specific heat (J kg^{-1} K^{-1})
CoV	coefficient of variation (–)
CFD	computational fluid dynamics
CSD	computational structure dynamics
$\mathbf{d_s}$	solid displacement vector (m)
D_m	mass diffusivity (kg m^{-1} s^{-1})
e	thickness of the elastic flap (m)
E	Young's modulus (Pa)
f	friction factor (–)
f_b	body force (N)
f_v	vortex shedding frequency (Hz)
$\mathbf{F}$	deformation gradient tensor (–)
FVG	flexible vortex generators
$\mathbf{G}$	Green lagrangian strain tensor (–)
GCI	grid convergence index (–)
H	height of the computational channel (m)
h	height of the flap (m)
h_g	grid size (m)
$\mathbf{I}$	unity tensor (–)
j	Colburn factor (–)
k	thermal conductivity (W m^{-1} K^{-1})
L	length of the computational domain (m)
l	cell distance to the nearest moving boundary (m)
$\dot{m}$	mass flow rate (kg s^{-1})
N	number of cells (–)
Nu	Nusselt number (–)
p	pressure (Pa)
p_c	apparent order of convergence (–)
Pr	Prandtl number (–)
q''	average heat flux between top and bottom walls (W m^{-2})
r	grid refinement factor (–)
Re	Reynolds number (–)
RVG	rigid vortex generators
St	Strouhal number (–)
T	temperature (K)
t	time (s)
$\mathbf{u}$	velocity vector (u, v) (m s^{-1})
$\bar{U}_f$	mean flow velocity (m s^{-1})
(x, y)	Cartesian coordinate system (m)
$()^*$	dimensionless position: $X^* = x/H,\ Y^* = y/H$ (–)

Greek symbols

γ	mesh diffusion coefficient (–)
η	thermal performance factor (–)
τ	dimensionless time (–)
ν_f	fluid kinematic viscosity (m^2 s^{-1})
ν_s	Poisson's ratio (–)
ϕ	mesh verification variable (–)
ρ	mass density (kg m^{-3})
σ	stress tensor (Pa)
τ_s	shear stress (Pa)
Σ	Piola–Kirchhoff stress tensor (–)

Subscripts

ave	spatial average
b	bulk
f	fluid
g	global
in	inlet
m	mesh
max	maximum value
s	solid
w	wall

power source to enhance the mixing process or heat transfer. These oscillations can be generated by mechanical or electromagnetic external forces acting on the moving structure for instance. Many studies dealing with forced oscillation of a heated cylinder in a laminar flow have been conducted. For example, Fu and Tong [12] numerically investigated convective heat transfer as a function of amplitude and frequency of the cylinder oscillations and Reynolds number. They concluded that best performances were achieved with increasing amplitude and Reynolds number and in the lock-in regime between the wake flow detachment and cylinder oscillations. Other interesting studies were carried out in microchannels where Reynolds numbers were very low and the flow was thus almost stagnant. Khatavkar et al. [13] numerically studied effects of active control cilia used as microactuators on the mixing of microchannel flows. They highlighted the major role played by several parameters like the fluid viscosity, shear modulus and length of the microactuator. They furthermore investigated configurations with two microactuators located on the same channel wall or on opposite walls, with a phase-shifted frequency applied to their motions. They concluded that under given optimal conditions, the use of two actuated flaps mounted on the same wall or on opposite can induce chaotic advection in a microchannel flow. In such cases, they highlighted that a key factor for mixing enhancement is the phase shifting between the actuators motions. Lambert and Rangel [14] numerically studied the effect of one elastic flap deformation on fluid mixing in a microchannel by using the fictitious-domain method to model the fluid–structure interaction. The mixing efficiency was analyzed by passive scalar patterns and surface reaction rates. They pointed out that deforming flap was found to accelerate the mixing process and suggested that mixing performances could be obtained with one single flap. At higher Reynolds numbers in the laminar flow regime (Reynolds numbers comprised between 100 and 500), Mirzae et al. [15] carried out numerical simulations of a 2D channel flow with one oscillation-controlled flap mounted on an inner wall. They compared heat transfer enhancement obtained from flexible or rigid flap as a function of laminar Reynolds numbers. They concluded that not only thermal performances were increased with the use of the oscillation-controlled flap whatever the laminar Reynolds number but this flexible flap induces also lower pressure drop. Although the dynamic techniques show promising results regarding performances enhancement, the practical implementation of active RVGs is complicated since it requires sophisticated techniques to control flaps motion and imply an external power to create and maintain the oscillations. Moreover, in all the above mentioned cases, no quantification of the required power to maintain the flaps oscillations are done.

In light of these observations, the main objective of the present study is to propose an original static mixer configuration that could benefit the advantages of both the passive and active control methods to increase heat transfer and mixing property. To this aim, we intend to take advantage of fluid–structure interaction (FSI) in order to produce self-sustained oscillations of flexible vortex generators (FVGs) from hydrodynamic forces induced by a laminar flow. Thus, making them oscillate is achieved without the need of external energy sources beside the hydrodynamic forces applied by the exist-

ing laminar flow itself, producing mixing and heat transfer in a passive but dynamic and self-sustained way. Noticeably, FSI of oscillating structures can naturally occur in fluid flows over elastic bodies and can be observed in many situations such as marine cables, petroleum production risers and airplane wings for example [16–18]. In these cases however, FSI studies are usually conducted in order to estimate loads applied to the structure in order to prevent damage risks. Thus, FSI problems are not often considered as a potential benefit for applications and to the authors knowledge, no previous studies have been performed to intentionally generate passive free vibrations of structures and investigate their effect on the heat and mass transfer enhancement.

In this paper, numerical coupled fluid–structure simulations are performed to investigate freely oscillating arrays of FVGs in a 2D channel flow and evaluate their potential in increasing mixing and heat transfer. The only acting forces are those exerted by the main laminar flow and vortices are thus produced in a passive-dynamic way in this case. The paper is organized as follows: first, the numerical procedure is presented in Section 2. Section 3 is then devoted to the numerical validation. The problem description is given in Section 4 and the associated results are discussed in Section 5. Finally, Section 6 is dedicated to concluding remarks.

2. Mathematical formulation and numerical procedure

Numerical fluid–structure interaction problems can be performed with either monolithic or partitioned approach. The latter method is the most commonly used for complex FSI problems. It involves one solver for fluid motion, another for the structure displacement and a third dedicated to remeshing procedure. If the solvers are called once per time step, loosely coupled solution is followed [19]. Loosely coupled solution procedures often work if a weak coupling is established between the fluid and the structure or if there is an important difference between the time scales of the fluid and the structure. However, for large structural displacements, for incompressible fluids fully enclosed by deformable bodies or when a significant amount of fluid mass is moving with the structure, a strongly coupled approach should be considered [20]. This is achieved by introducing an additional FSI outer loop where solutions of the fluid and structure are recalculated until reaching the convergence criteria set on forces and displacements [21]. In this paper, this method is used through the ANSYS Fluent CFD-solver and the ANSYS Mechanical CSD-solver [22].

Thus, the flow field is governed by the unsteady Navier–Stokes equations for an incompressible viscous laminar flow. These equations are solved in a computational domain which deforms in time due to the flexible structure deformations. Therefore, an Arbitrary Lagrangian–Eulerian (ALE) formulation is used to solve the flow equations on a deforming mesh [23]. The ALE formulation of the Navier–Stokes equations is written as:

$$\nabla \cdot \mathbf{u_f} = 0 \tag{1}$$

$$\frac{\partial \mathbf{u_f}}{\partial t} + (\mathbf{u_f} - \mathbf{u_{m,f}}) \cdot \nabla \mathbf{u_f} = -\frac{\nabla p}{\rho_f} + \nu_f \nabla^2 \mathbf{u_f} \tag{2}$$

where $(\mathbf{u_f} - \mathbf{u_{m,f}})$ is the convective term with $\mathbf{u_f}$ the fluid velocity and $\mathbf{u_{m,f}}$ the mesh motion velocity in the fluid domain. The pressure is denoted by p, the density of the fluid by ρ_f and the kinematic viscosity by ν_f. The Eulerian and Lagrangian descriptions are obtained by setting $\mathbf{u_{m,f}} = 0$ or $\mathbf{u_{m,f}} = \mathbf{u_f}$, respectively.

The mass transport equation of a scalar c is considered to study the effect of the elastic flap deformations on fluid mixing:

$$\frac{\partial c}{\partial t} + (\mathbf{u_f} - \mathbf{u_{m,f}}) \cdot \nabla c = D_m \nabla^2 c \tag{3}$$

where D_m is the mass diffusivity of the scalar c. Here, the convective scalar mixing is only considered so mass diffusion term is set 0.

The heat equation is also solved in the fluid domain and is given by:

$$\frac{\partial T_f}{\partial t} + (\mathbf{u_f} - \mathbf{u_{m,f}}) \cdot \nabla T_f = \frac{k}{\rho_f C_p} \nabla^2 T_f \tag{4}$$

where T_f is the fluid temperature, k is the thermal conductivity and C_p is the specific heat.

The equation of motion for an elastic isothermal solid structure can be described from a Lagrangian point of view, i.e. in terms of the initial configuration at $t = 0$, and it reads:

$$\rho_s \frac{\partial^2 \mathbf{d_s}}{\partial t^2} = \nabla \cdot \left(\Sigma \cdot \mathbf{F^T} \right) + \rho_s f_b \tag{5}$$

where $\mathbf{d_s}$ is the displacement of the structure, f_b is the resulting body force, ρ_s is the density of the structure and $\mathbf{F}$ is the deformation gradient tensor given by:

$$\mathbf{F} = \mathbf{I} + \nabla \mathbf{d_s^T} \tag{6}$$

where $\mathbf{I}$ is the identity.

The second Piola–Kirchhoff stress tensor Σ is related to the Green Lagrangian strain tensor $\mathbf{G}$ following [24,25]:

$$\Sigma = 2\mu_s \mathbf{G} + \lambda_s tr(\mathbf{G})\mathbf{I} \tag{7}$$

with $\mathbf{G}$ given by:

$$\mathbf{G} = \frac{1}{2}(\mathbf{F^T} \cdot \mathbf{F} - \mathbf{I}) \tag{8}$$

Here tr is the tensor trace, λ_s and μ_s are Lamé constants which are characteristics of the elastic material. They are linked to the Young modulus E and Poisson's coefficient ν_s by:

$$\lambda_s = \frac{\nu_s E}{(1 + \nu_s)(1 - 2\nu_s)} \tag{9}$$

$$\mu_s = \frac{E}{2(1 + \nu_s)} \tag{10}$$

Fluid–structure interaction problems with moving boundaries require a third coupled solver for an automatic internal mesh motion. The mesh motion solver in Fluent consequently deforms the internal fluid domain while maintaining the quality and validity of the deforming mesh. In this case, the displacement of the fluid–structure interface, which is the result of the structural solver, is then used as a boundary condition for the mesh motion solver. The present study employs the Laplace smoothing equation given by the following expression:

$$\nabla \cdot (\gamma \nabla \mathbf{u_m}) = 0 \tag{11}$$

where γ is the mesh diffusion coefficient and $\mathbf{u_m}$ the mesh displacement velocity. The mesh diffusion coefficient used in this study is a function of the boundary distance:

$$\gamma = \frac{1}{l^{\alpha}} \tag{12}$$

where l is a normalized boundary distance and α is the diffusion parameter. A diffusion parameter α of 1.5 has been used in the present study, which preserves larger regions of the mesh near the moving boundary, and cause the regions away from the moving boundary to absorb more of the motion.

To avoid divergence problems especially caused by negative cell volumes, the mesh solver supports several remeshing methods. The one used in this study is the 2.5D surface remeshing that applies on wedge/prism cells extruded from triangular surface elements. This method agglomerates cells that violate the skewness

or size criteria and locally remeshes the agglomerated cells or faces. If the new cells or faces satisfy the skewness criterion, the mesh is locally updated with the new cells (with the solution interpolated from the old cells) [22]. Otherwise, the new cells are discarded and the old cells are retained. In the present study a maximum cell skewness of 0.7 has been used for remeshing with cell size criterion depending on the minimum and maximum length scale of the mesh.

In order to perform the load and motion transfer between the different meshes for fluid and structure, the General Grid Interface (GGI) mapping algorithm is used [26]. At each time step, the FSI iteration loop sequentially calls the structural solver, the mesh motion algorithm and then the fluid solver until the convergence limits for displacements and forces are reached. An under-relaxation factor for both displacement and force is set to unity for all the simulations performed and convergence criteria set to 10^{-4} on force and displacement.

The pressure–velocity coupling is established using the coupled algorithm [22], which solves the momentum and pressure-based continuity equations together. The convergence criteria for pressure, velocity, energy, and scalar is set to 10^{-6}. The Laplace mesh smoothing convergence criteria is set to 10^{-4}. Temporal discretization is performed using a first order implicit scheme and the time step used for all the present simulations is set to 10^{-4} s. In an explicit time integration scheme, the time step is conditionally stable and limited by the CFL number. However, the fully implicit first order scheme is unconditionally stable with respect to the time step size. Nevertheless, the CFL based on the time step size of 10^{-4} s and the minimum cell distance is always less than unity.

Eventually, only the ANSYS Fluent CFD-solver is activated for the numerical simulations carried out with rigid vortex generators, with the above mentioned parameters kept identical.

3. Numerical validation

The benchmark configuration proposed by Turek and Hron [27] has been chosen for the present FSI validation. The configuration consists of a laminar incompressible 2D channel flow around an elastic beam attached to a fixed cylinder. Under the unsteady effect of the hydrodynamic forces imposed by the flow around the cylinder, self-sustained oscillations are induced to the structure. The domain has an inlet with a laminar parabolic velocity profile, a zero pressure condition at the outlet, and no slip boundary conditions at the walls. The 2D channel has a length of 2500 mm and a height of 410 mm. The circular cylinder has a radius of 50 mm and is slightly shifted from the horizontal middle line in order to produce a non symmetrical flow. The flexible structure has a length of 350 mm and a height of 20 mm. The axis origin is taken at the tip of the flap from its initial position. A sketch of the computational domain is given in Fig. 1.

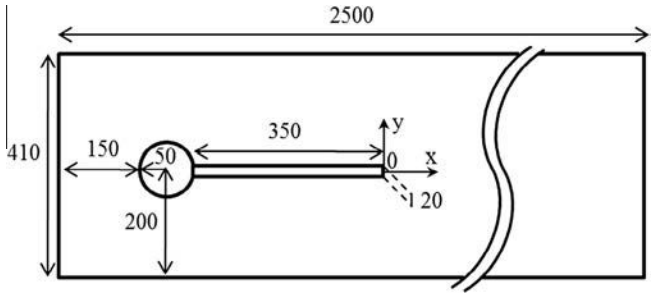

Fig. 1. Schematic view of the computational domain used as benchmark (dimensions in mm).

Three different configurations are investigated in [27], depending on the flow velocity, the shear modulus and density of the moving elastic beam. The second configuration case (cited as FSI2 in Table 12 in [27]) is retained for benchmark since the flap motion shows the largest displacements and the corresponding physical quantities are summarized in Table 1. A more detailed description is given in the original paper of Turek and Hron [27].

The fluid domain is discretized with 43,000 triangular cells and the mesh is refined at the walls and the fluid–structure interface, i.e. the elastic beam. The moving structural domain consists of 400 quadrilateral cells. In this simulation, a maximum number of 7 FSI outer iterations were needed to attain convergence criteria of 10^{-4} for both displacement and force on the fluid–structure interface.

The displacement at the tip of the elastic beam is shown in Fig. 2 in y direction. After a 7 s transient state, the beam shows harmonic oscillations at constant frequency and amplitude. For comparison with Turek and Hron [27], the mean and amplitude are computed from the last period of oscillations according to the following relations proposed in [27]:

$$mean = \frac{1}{2}(max + min) \tag{13}$$

$$amplitude = \frac{1}{2}(max - min) \tag{14}$$

The frequency of the oscillations is then computed by using a Fast Fourier Transformation on the displacement signal. Results are summarized in Table 2 and compared with the reference values [27]. One can observe that results are in very good agreement with the reference case and only exhibit small discrepancies in the x-direction (error is of 0.14% for the mean, 1.13% for the amplitude and 1.3% for the frequency) and y-direction (error is of 5.7% for the mean, 1.24% for the amplitude and 5.0% for the frequency).

Table 1
Physical properties for FSI2 numerical benchmark.

Parameter	ρ_s[kg/m^3]	ν_s	E[Pa]	ρ_f[kg/m^3]	ν_f[m^2/s]	U_{max}[m/s]
FSI2	10,000	0.4	1.4×10^6	1000	0.001	1.5

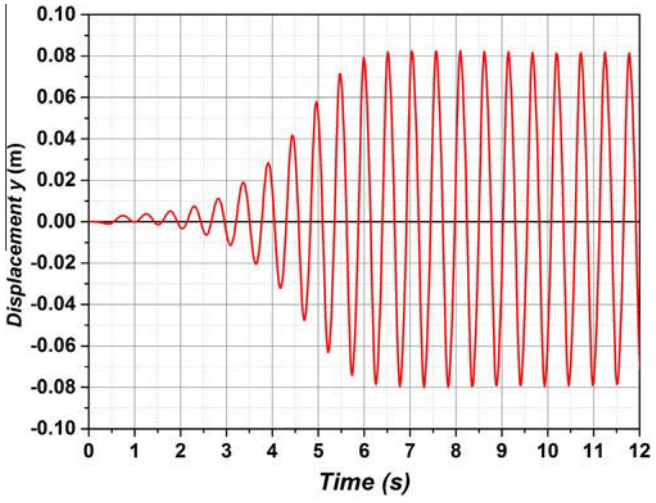

Fig. 2. Displacement of the flap tip measured in the y direction for the numerical simulation proposed as a validation test case.

Table 2
Results comparison between present simulation and Turek and Hron [27].

	x Direction		*y* Direction	
	Present results	Ref. [27]	Present results	Ref. [27]
Mean (mm)	−14.56	−14.58	1.30	1.23
Amplitude (mm)	12.58	12.44	81.05	80.06
Frequency (Hz)	3.75	3.80	1.90	2.00

Table 3
Physical parameters and flow conditions for all cases.

Parameters	RVG1	FVG1	RVG2	FVG2
ρ_s (kg/m^3)	–	1200	–	1200
ν_s	–	0.4	–	0.4
E (10^6 Pa)	–	10	–	10
e (mm)	1	1	0.6	0.6
$Re_H = (\bar{U}_{f,inlet} H)/\nu_f$	1850	1850	1000	1000

4. Problem description

In this section, the computational domains, flow initialization, boundary conditions and mesh validation are presented.

4.1. Computational domain, initial and boundary conditions

The computational domain is two-dimensional and consists of four elastic flaps mounted on opposite parallel walls and inclined at an angle of $\beta = 30^\circ$ to the wall, as shown in Fig. 3. As previously observed in [7], flaps are inclined in the opposite direction of the main flow to get better heat and mass transfer performances. Flaps A and B have the same length of 25 mm and Flaps C and D have the same length of 35 mm. Two different elastic flap cases are studied, namely FVG1 and FVG2, and differ by the Reynolds number Re_H based on the channel height H and the thickness of the flaps e as reported in Table 3. Their corresponding rigid cases RVG1 and RVG2 are also simulated in order to compare performances.

A parabolic laminar velocity profile corresponding to a fully developed laminar flow is set at the inlet:

$$U_{f,inlet} = \frac{3}{2}\bar{U}_{f,inlet}\left(\frac{4y}{H^2}\right)(H-y) \tag{15}$$

where $\bar{U}_{f,inlet}$ is the mean flow velocity at the inlet.

No slip boundary conditions are set at the top and bottom walls. The outlet is set to zero pressure and Neumann zero for velocity.

To characterize the mixing process within the channel, a passive scalar transport equation is solved (Eq. (3)). The inlet is initially divided in two equal parts; the scalar at the upper part ($y > H/2$) is $c = 0$ and at the lower part ($y \leqslant H/2$) is $c = 1$. The internal domain is initially set with uniform scalar $c = 1$. Zero flux boundary conditions are prescribed for the mass transport equation along the walls and the rigid/flexible flaps.

To characterize the heat transfer process, a uniform temperature of $T_w = 360$ K is imposed at the top and bottom walls of the channel. The laminar parabolic velocity profile is prescribed at the inlet with uniform temperature $T_{in} = 300$ K. The rigid/flexible flaps are treated as insulating material with zero heat flux along them. The thermophysical properties of the working fluid (air in our case) are assumed constants, with a thermal conductivity $k = 0.0242$ W/m.K and a specific heat $C_p = 1006.43$ J/kg.K.

Four probes (P1–P4) are inserted in the fluid domain downstream the flaps to be able to plot the transient streamwise velocity variation at these locations and characterize the power density spectra. The probes coordinates are illustrated in Fig. 3.

A grid size independence study for the FSI simulations is conducted on the case FVG1 having the highest Reynolds number. The fluid domain is thus discretized with three initial different mesh sizes using triangular cells, refined at the wall and at the fluid solid interface, i.e. at the four elastic flaps. During the FSI simulations, automatic mesh adaptation is performed to remesh the volume due to mesh distortion depending on the motion and behavior of the flaps. This aims to avoid negative cell volumes and allows to adapt cell sizes near the moving interfaces according to a size and skewness criteria set in the solver (see Section 2). The total cell number and the overall mean cell size were checked during the simulations and it was found that they did not change significantly from their initial values. The three mesh densities and their main characteristics are summarized in Table 4. where ΔA_i is the area of the ith cell.

To determine the appropriate mesh density for grid size independence, the simulations are performed on increasing mesh densities. The mesh validity verification is based on the method proposed by Celik et al. [28] where the grid convergence index (GCI) and the apparent order of convergence (p_c) can be obtained. Since the heat transfer strongly depends on the near-wall refinement and the flaps oscillation amplitude depends on the refinement near the fluid–solid interface, the Nusselt number and the

Table 4
Global meshes characteristics used for grid size independence study.

	Mesh 1	Mesh 2	Mesh 3
Initial number of cells (N)	4245	8234	16,140
Grid size $h = \left[\frac{1}{N}\sum_{i=1}^{N}(\Delta A_i)\right]^{\frac{1}{2}}$	0.00195	0.00140	0.00100
Grid refinement factor $r = h_i/h_j$	–	$h_2/h_1 = 1.39$	$h_3/h_2 = 1.40$

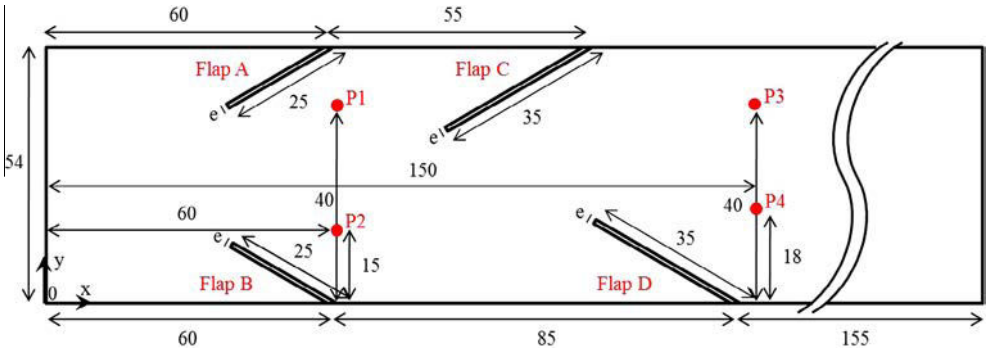

Fig. 3. Computational domain and boundary conditions for the studied cases (dimensions are in mm). For FVG1 and FVG2, this domain is set as an initial condition.

amplitude of oscillations of flap D are chosen for the mesh validity verification.

The dimensionless positions in the channel in the x and y directions are given as:

$$X^* = x/H \quad \text{and } Y^* = y/H \tag{16}$$

The time-averaged local Nusselt number $\overline{Nu}(x)$ at X^* in the channel is defined by:

$$\overline{Nu}(x) = \frac{1}{t_2 - t_1}\int_{t_1}^{t_2} \frac{q''_w(x,t)H}{k(T_w - T_b(x,t))}dt \tag{17}$$

where t_1 is the time step at which stable regime is reached ($t_1 = 2$ s) and t_2 is the final instant in seconds (about 18 oscillation periods have been averaged), q''_w is the average heat flux of the top and bottom walls, k is the thermal conductivity of the working fluid (air here) and T_w is the wall temperature (set to 360 K in these simulations). T_b is the bulk temperature of the fluid at position x and is calculated using the velocity and temperature distributions following the equation:

$$T_b(x,t) = \frac{\int_0^H U(x,y,t)T(x,y,t)dy}{\int_0^H U(x,y,t)dy} \tag{18}$$

For the validation of the scalar fields, we compute the local coefficient of variation $\overline{CoV}_c(x)$, defined as:

$$\overline{CoV}_c(x) = \frac{1}{t_2 - t_1}\int_{t_1}^{t_2} \frac{1}{c_{ave}(x,t)}\left[\frac{\sum_{j=1}^{n}\left(c_j(x,y,t) - c_{ave}(x,t)\right)^2}{n}\right]^{1/2} dt \tag{19}$$

where $c_j(x,y,t)$ is the local scalar value at a given (x,y) position and at a given time t, $c_{ave}(x,t)$ is the averaged value of c at location x and time t. n is the number of cells in direction y at the streamwise position x, i.e. the number of samples where the concentration value is extracted.

The results obtained from applying the method of Celik et al. [28] are reported in Table 5, where $\phi_{refined}$ is the variable calculated from the solution of the refined mesh, ϕ_{ext} is the extrapolated variable, e_a^{23} is the relative error between Mesh 3 and Mesh 2. Extensive information about the calculation of these parameters can be found in Celik et al. [28]. It can be concluded from Table 5 that the uncertainty in the fine-grid solution is about 0.95% for the integrated Nusselt number (along all the channel length, i.e. from X^*=0 to X^*=5.5); 0.82% for the integrated coefficient of variation and 0.06% for the displacement amplitude of Flap D. The refined Mesh 3 can thus be used as a reference mesh density for the other rigid and flexible vortex generators configurations.

Table 5
Estimated order of convergence p and GCI for refined Mesh 3.

	$\phi_{refined}$	ϕ_{ext}	e_a^{23} (%)	p_c	GCI (%)
Flap D amplitude (mm)	9.86	9.9	0.71	8.41	0.06
$\frac{1}{5.5}\int_0^{5.5}\overline{Nu}_x dX^*$	31.973	31.731	2.2	3.99	0.95
$\frac{1}{5.5}\int_0^{5.5}\overline{CoV}_c(x)dX^*$	0.3399	0.3421	4.68	6.21	0.82

5. Results and discussions

In this section, flow topologies induced by the RVGs and the corresponding FVGs cases are first studied. Then, the mixing quality of a passive scalar is compared between rigid and flexible flaps configurations. We also investigate their corresponding heat transfer performance through the study of the local and global Nusselt numbers, the Colburn factor and the thermal performance factor. Finally, a brief discussion is made about motions of the flaps and their potential risk to break.

5.1. Flow pattern

Fig. 4 shows a snapshot of the velocity streamlines in steady state regime for both the rigid cases RVG1 and RVG2. Eventhough rigid configurations were run taking into account the possible unsteadiness, however the flow remains stable. In this situation, the major part of the fluid flows in the central region between the flaps and no vortex shedding is observable downstream. The only vortices generated consist of recirculation regions up and downstream the flaps. Such a behavior is undesirable when mixing two or more components because it tends to decrease the homogeneity of the final product; the reagents located in the center region will exit the mixer faster than those in the wake regions and will not be mixed. Eventually, one can see that the main flow is deviated from the centerline downstream the flap D because the geometry is not symmetric.

Considering the FVGs cases, Fig. 5 shows the transient development of the velocity streamlines. For FVG1, a sequence of periodic vortices is shed from the tip edge of flaps A and B due to shear instability generated at the interface between the high momentum fluid in the bulk region and the low momentum fluid in the wake of the flap. One can note on Fig. 5(a) that even if flaps A and B are flexible, their motion is unsignificant compared to flaps C and D due to the upstream laminar flow at the inlet. Nevertheless, the vortices shed from flaps A and B induce periodically varying forces on flaps C and D, making them oscillate with larger amplitudes. Moreover, the base of flaps C and D are separated with a distance equal to 30 mm. Consequently, the hydrodynamic forces imposed to these flaps due to the vortex shedding of the upstream flow do not take the same time to impact flap C or D. This phenomenon, coupled with the mutual interaction of flaps C and D due to their free

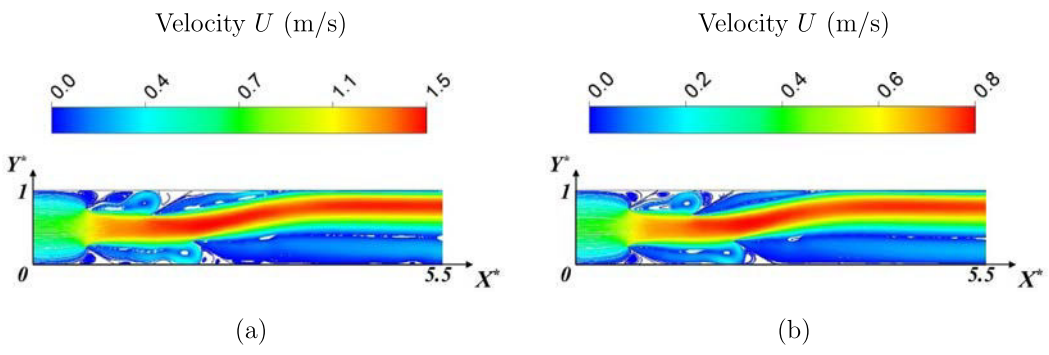

Fig. 4. Steady velocity field U observed for cases (a) RVG1 and (b) RVG2.

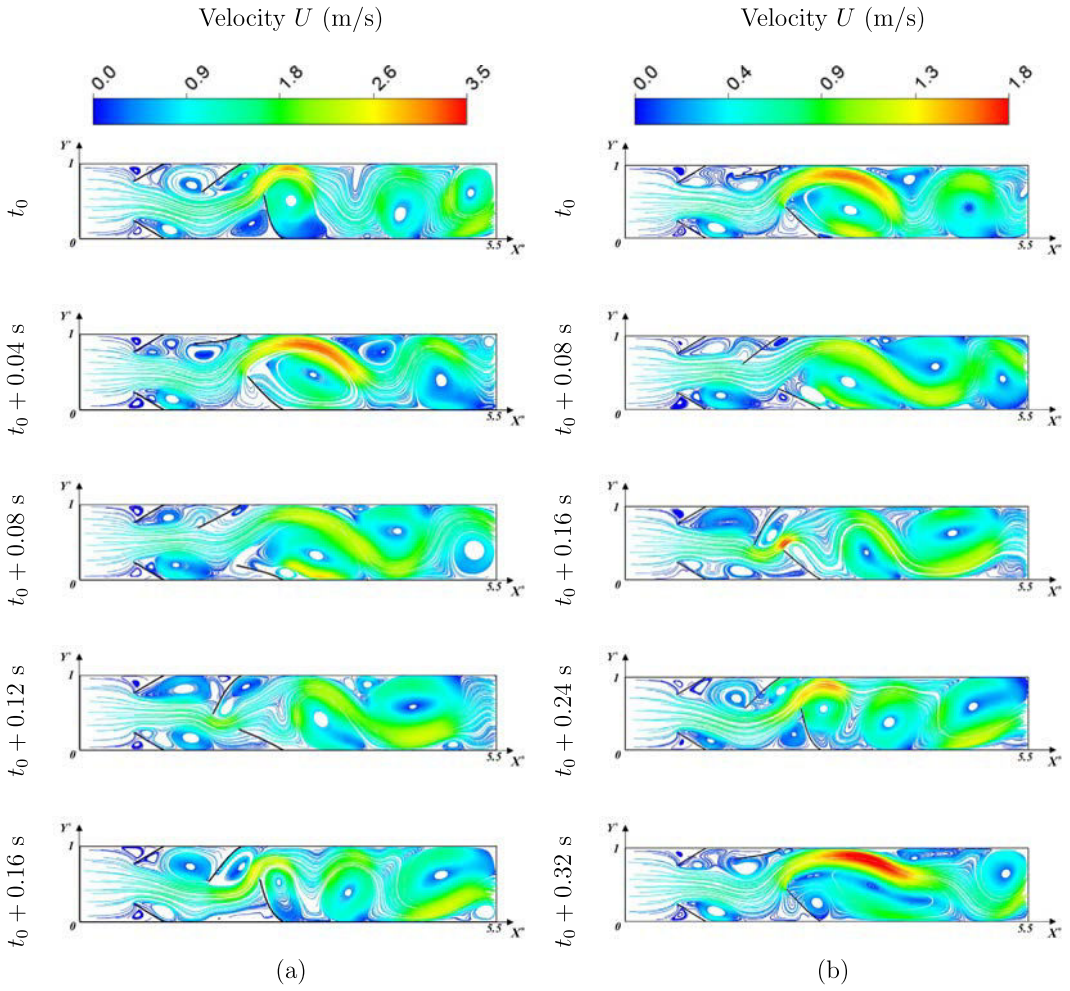

Fig. 5. Snapshots of velocity field U in cases (a) FVG1 and (b) FVG2 during one oscillation period (link to animations Video_Figure5_a.wmv and Video_Figure5_b.wmv).

motion leads to periodic oscillations with a phase difference between the two flaps. In Fig. 5(a), at the reference time t_0, flap D is at its higher displacement amplitude in the positive X^* direction, thus increasing the blockage ratio between the flap and the channel and generating higher velocity gradients at the tip of the flap. After reaching the highest amplitude, the stored energy in flap D will make it oscillate backward due to its springback property. The shear layer is then destabilized due to the backward motion of the flap where a vortex is formed and detaches downstream. At $t = t_0 + 0.08$ s and when flap D oscillates in the opposite direction of the flow, a recirculation zone is formed downstream. This is clearly observed at $t = t_0 + 0.12$ s, where the eddy gets larger until flap D reaches its minimum amplitude near the channel wall.

When flap D is at its minimum amplitude position near the channel wall, the negative pressure behind this flap and the decrease of the blockage ratio will decrease the velocity gradient and will allow the incoming fluid to exert forces on flap C that moves in the direction of the flow at $t = t_0 + 0.12$ s. This will increase the pressure upstream of flap D and will make it oscillate forward, whereas the energy stored in flap C will induce motion in the direction opposite of the flow after reaching its maximum amplitude in the positive X^* direction. This feedback interaction between flaps C and D combined with the periodic vortices shed from flaps A and B will self-sustain the oscillations in a passive way, without any external source of energy except the steady pumping power alone.

Power spectrum density (PSD) has been obtained at each probe location P1–P4 defined in Fig. 3, taking the instantaneous streamwise velocity after the flow reached its stable regime. Fast Fourier Transforms have been performed from 256 points, resulting in a resolution frequency of 0.19 Hz. For flaps A and B, the vortex shedding for the FVG1 case corresponds to a frequency of 5.6 Hz as shown in the PSD in Fig. 6(a) and a Strouhal number based on the flap height of about 0.28, defined as:

$$St_h = \frac{f_v h}{U_{f,inlet}} \tag{20}$$

where f_v is the vortex shedding frequency and h is the initial height of the flap.

This characteristic frequency is also observed at P3 and P4 locations in the flow downstream flaps C and D as illustrated in Fig. 6(b). Moreover, one can also notice that the fluid structure interaction between the flow and the flexible vortex generators that has been qualitatively described previously through Fig. 5 induces in the wake new frequency peaks in the PSD spectrum revealing an increase in the fluctuating momentum energy.

The same analyses also apply for FVG2 case through Fig. 5(b), with a vortex shedding frequency behind flap A and B of 3 Hz as shown in Fig. 6(c) (corresponding to a Strouhal number of $St_{h,FVG2} \approx 0.28$ similar to $St_{h,FVG1}$). Even at a lower Reynolds number of 1000, fluctuating part of the momentum energy of the power spectrum density is still increased by the induced motion of FSI

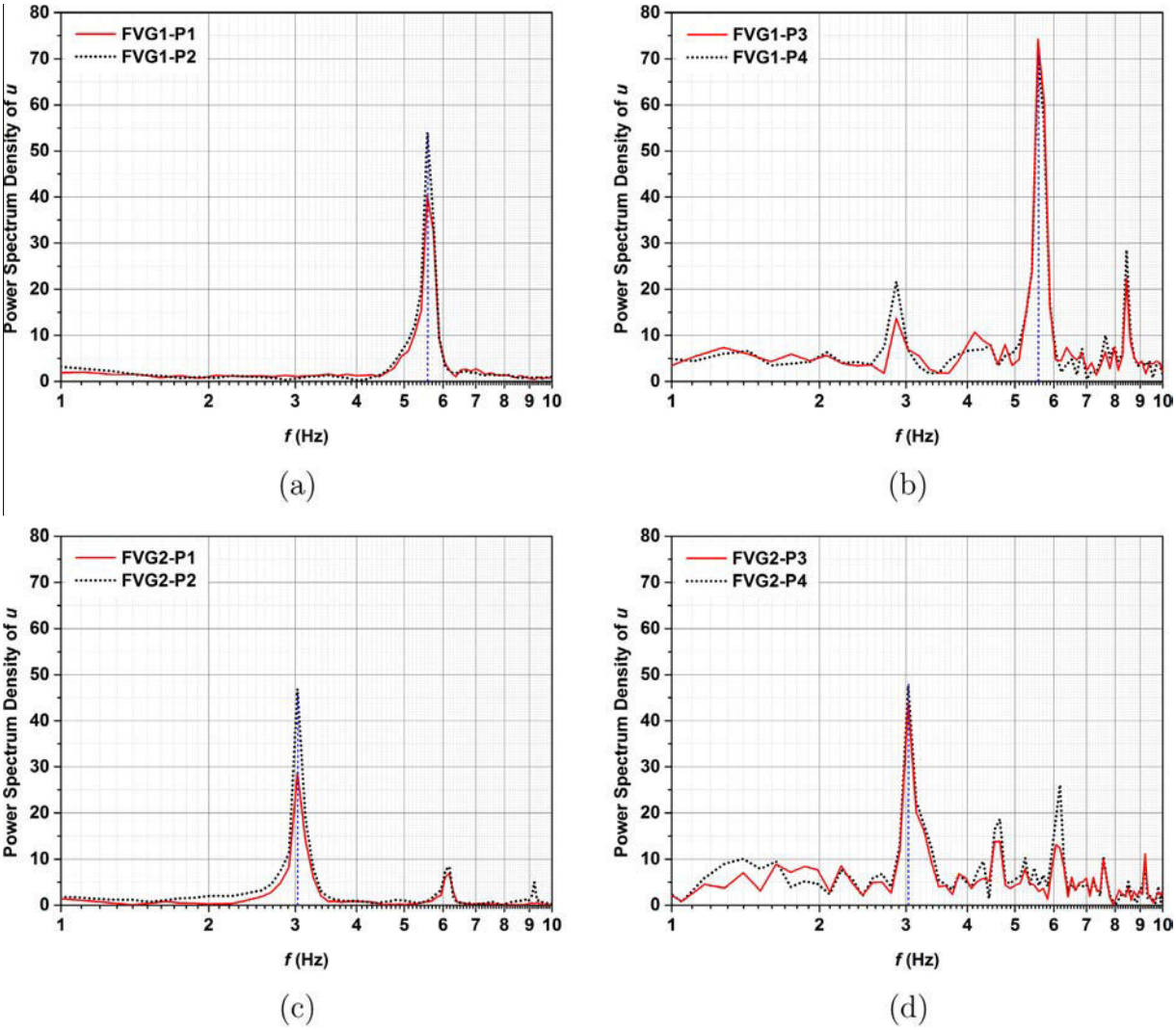

Fig. 6. Power spectrum density of the streamwise velocity u at probes location P1–P4 for (a), (b) case FVG1 and for (c), (d) case FVG2.

between the flow and the flaps, highlighting the potential capability of the FVGs at low Reynolds numbers.

5.2. Mixing performance

The mixing quality of a static mixer often refers to the reduction of inhomogeneity concerning a certain property like concentration, density, composition or temperature [29]. This section aims to compare the mixing performance of flexible vortex generators and their corresponding rigid version. As previously reported, the inlet boundary is divided into two equal parts with two different values of scalar c. Fig. 7 shows the distribution of scalar c in the computational domain after reaching a steady state condition for both RVG1 and RVG2 cases. It clearly shows that the fluid is not well mixed downstream the flaps. The two scalars introduced initially at the inlet, remain distinct with no mixing observed along the channel length. In fact, the scalar field 0 still occupies the upper part of the channel, and the scalar field 1 occupies the lower part of the channel. Only a small layer of mixed fluid is seen at the interface between the upper and bottom scalar fields 0 and 1. This layer is present due to the fact that an interpolation has to be done, so that the scalar field stays well conserved.

In Fig. 8, for both elastic cases FVG1 and FVG2, the scalar distribution is more homogeneous behind flaps C and D, with a value close to the mean value of c, i.e. 0.5. At $t = t_0 + 0.04$ s as shown in Fig. 8(a), flap C is at the minimum amplitude position near the wall allowing the fluid with $c = 0$ to flow past flap C. On the other hand, when flap C reaches its maximum amplitude at $t = t_0 + 0.12$ s and $t = t_0 + 0.16$ ls, it blocks the flow of the fluid with $c = 0$ and allows the fluid with $c = 1$ to flow past flap D to finally mix with the previously pumped scalar $c = 0$, thus leading to a sequential-like mixing procedure [30,31].

Mixing uniformity or mixedness can be quantified using the time-averaged local coefficient of variation (CoV) which is the ratio of the standard deviation to the mean value of the passive scalar c. It can either be thought in terms of duration needed to get a correct mixing at the outlet of the static mixer for instance, or in terms of mixing length performance. As it would be non sense to get a mixing time from the numerical simulations which started from quite unphysical initial conditions, we computed the local $CoV_c(x)$ at several streamwise positions along the channel. The lower the value of CoV_c, the better the mixture quality and a CoV_c of zero would indicate that there is no variation from the mean value c_{ave} and the mixture would be completely homogeneous.

Fig. 9 shows the time-averaged $\overline{CoV_c}(x)$ comparing the FVGs cases to their relative rigid cases, computed downstream flap D. One can notice that the mixture quality is widely improved in the elastic cases than in the rigid cases whatever the X^* location

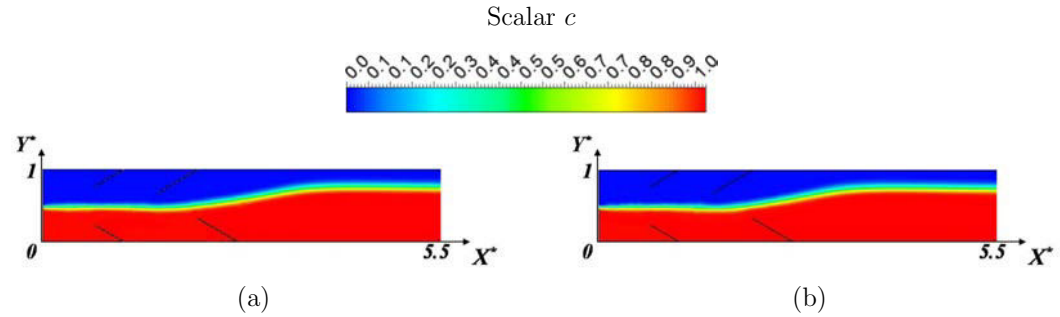

Fig. 7. Steady field of scalar c obtained in cases (a) RVG1 and (b) RVG2.

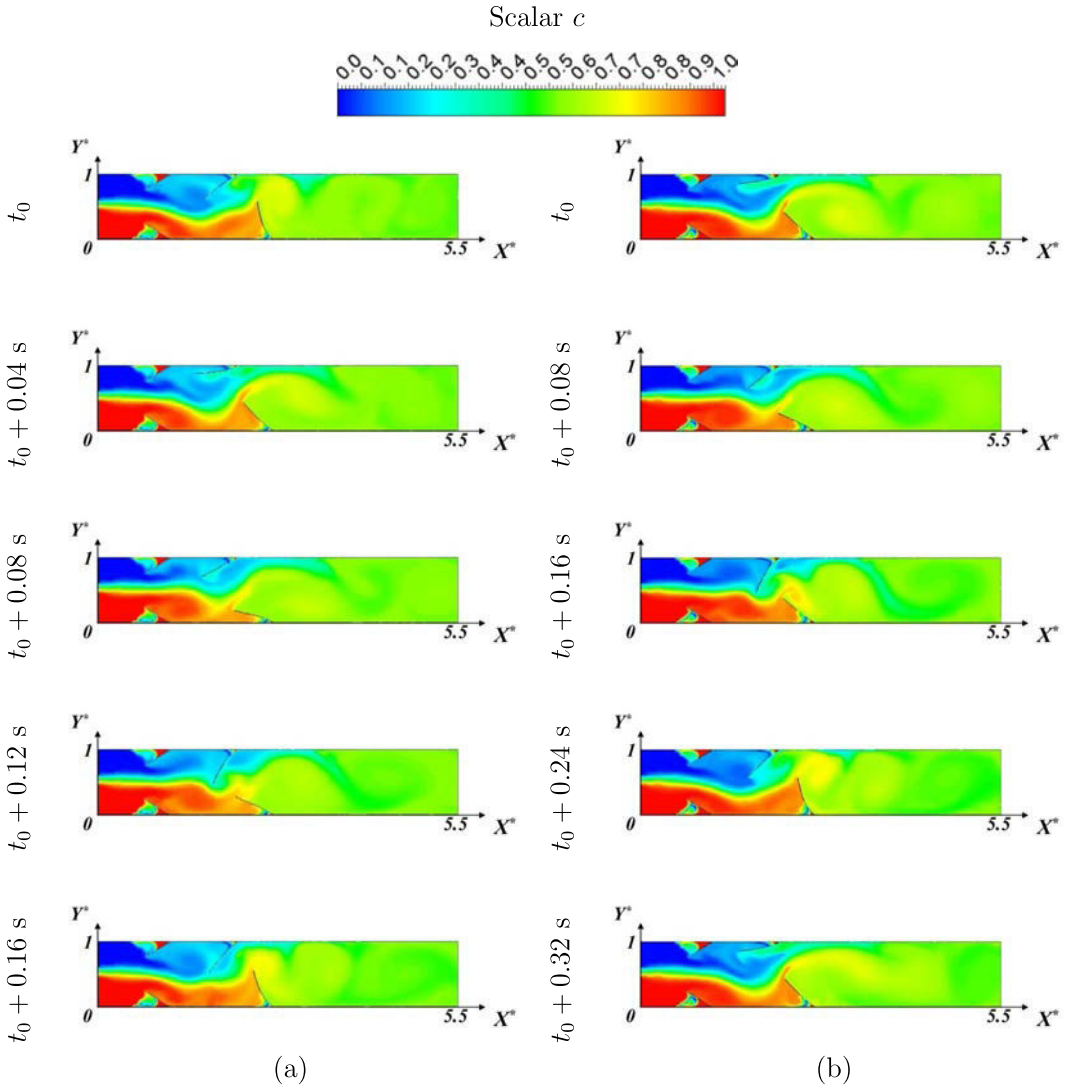

Fig. 8. Snapshots of scalar c in cases (a) FVG1 and (b) FVG2 during one period of oscillation (link to animations Video_Figure8_a.wmv and Video_Figure8_b.wmv).

considered. At the outlet, the rigid case RVG1 shows an average value of 0.7918, whereas the flexible case FVG1 shows an average value of 0.0166, which corresponds to an 98% increase in mixture quality when using elastic flaps instead of rigid ones. Similarly at the outlet, the value is also of 0.7918 for the rigid case RVG2, whereas it is of 0.025 for the flexible case FVG2, which corresponds to an 97% improvement in mixture quality when using elastic flaps. Usually a *CoV* value below 0.05 is said to be a reasonable target for most applications [4]. This value is reached at $X^* = 3.95$ for FVG1 case and $X^* = 4.05$ for FVG2 case whereas it has not been reached yet at the outlet for the two rigid cases. This analysis thus shows the real potential of performance of flexible vortex generators that can lead to shorter mixing lengths and more compact mixers.

5.3. Thermal exchange performance

In this section, numerical results are reported in terms of local Nusselt number Nu_x (Eq. (17)), global Nusselt number between

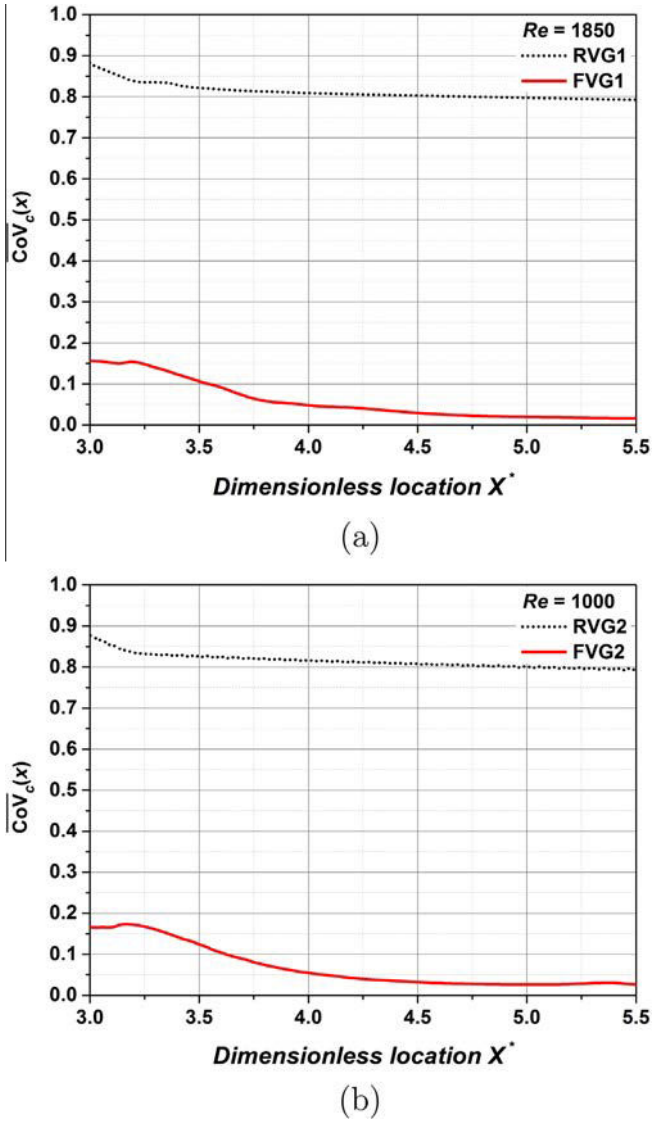

Fig. 9. Comparison of the time-averaged coefficient of variation of scalar c for (a) case 1 and (b) case 2.

the inlet and the outlet of the channel Nu_g (Eq. (21)), the Colburn factor j (Eq. (22)), the thermal performance factor η (Eq. (23)) and the time averaged local coefficient of variation for the temperature $\overline{CoV}_T(x)$ (Eq. (25)), where the elastic cases are compared to their relative rigid cases.

Fig. 10 shows the steady state solution for RVG1 (a) and RVG2 (b) cases. It clearly shows that the high wall temperature is not carried away to mix with the fluid at a lower temperature. The heat transfer is thus not improved that much as the main flow core still remains cold downstream the flaps.

Fig. 11 shows the temperature evolution as a function of time for cases FVG1 and FVG2, where the low-temperature and high-speed core fluid is transported toward the heated channel walls by the vortices generated downstream the oscillating flaps. Due to the presence of vortices, the high temperature wall flow is carried away to mix with the low-temperature core flow and the thermal boundary layers are destabilized in the elastic cases compared to the rigid cases, resulting in an increase of heat transfer.

Variation of the time-averaged local Nusselt number with respect to the dimensionless position X^* is presented in Fig. 12(a) for the case FVG1 compared to RVG1. For the elastic case, profile of $\overline{Nu}(x)$ clearly displays greater peaks at the positions of the flaps than the rigid case, especially where the flaps C and D undergo high amplitude oscillations. The averaged value of $\overline{Nu}(x)$ over the dimensionless position X^* (between X^*=0 and X^*=5.5) in the RVG1 case is 16.98 and is to be compared to 31.97 computed in the elastic case FVG1. It corresponds to 88% of heat transfer enhancement. Similarly, in Fig. 12(b), $\overline{Nu}(x)$ displays a higher peak value in the elastic case FVG2 and the averaged value of $\overline{Nu}(x)$ over X^* position in the RVG2 case is 11.24, compared to 22.12 obtained in the elastic case FVG2 and corresponding to 97% heat transfer enhancement.

The global Nusselt number Nu_g presented in Table 6 is computed using the following equation [8]:

$$Nu_g = \frac{\dot{m}c_pH}{2Lk}\frac{T_{b,outlet} - T_{b,inlet}}{T_w - T_{mean}} \tag{21}$$

where $\dot{m}$ is the mass flow rate, L the total channel length, $T_{b,outlet}$ and $T_{b,inlet}$ are the bulk temperatures respectively at the channel outlet and inlet and $T_{mean} = (T_{b,outlet} + T_{b,inlet})/2$.

Table 6 shows the statistical information about the global Nusselt number calculated as a function of time for the different cases. For rigid cases, only mean values are available as the flow is steady. The average global Nusselt number for case RVG1 is 15.94 and it increases to 31.26 in the elastic case FVG1, which represents a 96% increment in the overall heat transfer. Moreover, the average global Nusselt for case RVG2 is 9.3 and it increases up to 21.8 which corresponds to a 134% increment in the overall heat transfer.

In order to compare the energy efficiency between the rigid and elastic static mixers, the Colburn factor j is calculated using the following equation:

$$j = \frac{Nu_g}{\mathrm{Re}_H Pr^{\frac{1}{3}}} \tag{22}$$

where Pr is the Prandtl number, which is equal to 0.74 in all the cases studied.

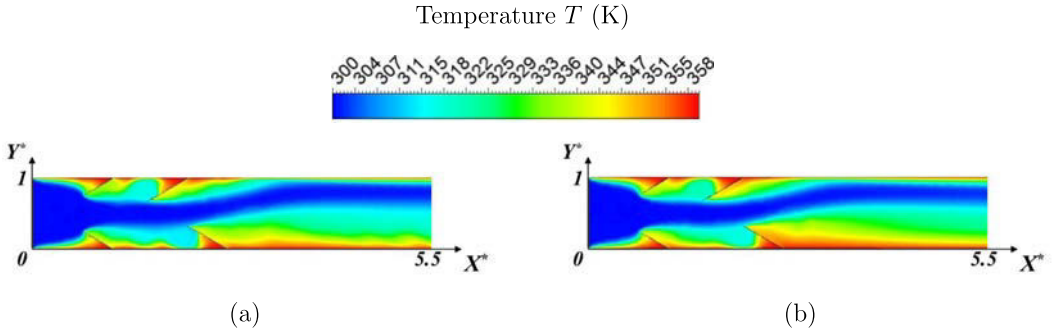

Fig. 10. Steady field of temperature T obtained in cases (a) RVG1 and (b) RVG2.

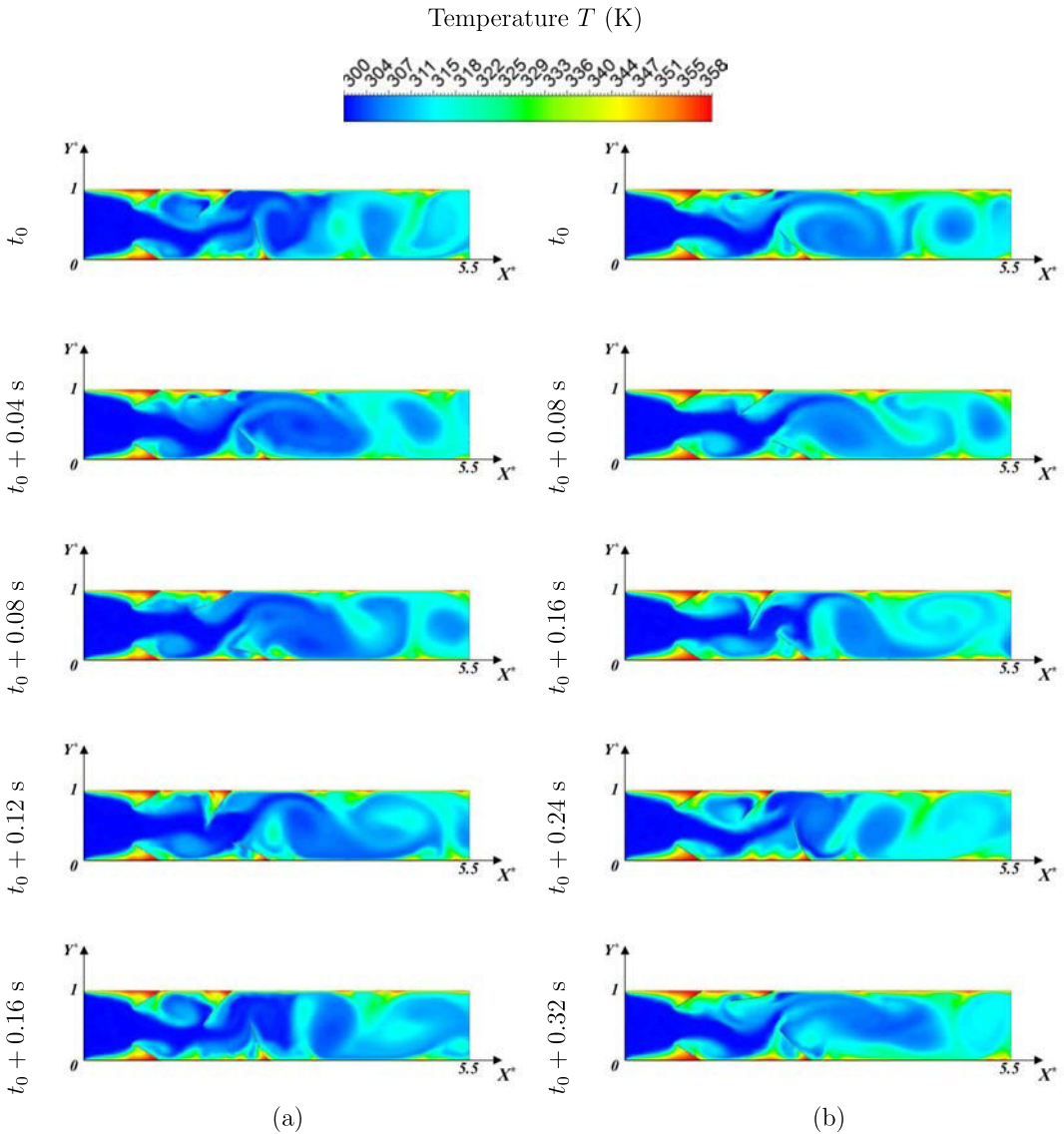

Fig. 11. Snapshots of temperature T in cases (a) FVG1 and (b) FVG2 during one period oscillation (link to animations Video_Figure11_a.wmv and Video_Figure11_b.wmv).

The Colburn factor quantifies the ratio of the thermal power transferred to the mechanical power consumed. For a given fluid and a specific Reynolds number, a higher Colburn factor indicates a higher efficiency of heat transfer. Table 7 details the statistical values of the Colburn factor (j), where it appears the average Colburn factor for case RVG1 is 0.0095 and it increases to 0.0187 for case FVG1, representing a 96% increase in Colburn factor. Besides, RVG2 shows an average Colburn factor of 0.0104 and it increases to 0.0198 in the FVG2 case, representing a 91% increase.

Another criterion, namely the thermal enhancement factor η, is computed to compare the heat transfer efficiency at constant pumping power. It is defined as the ratio of convective heat transfer in the elastic case to that in the rigid case according the relation [32,33]:

$$\eta = \left(\frac{Nu_{g,FVG}}{Nu_{g,RVG}}\right)\left(\frac{f_{FVG}}{f_{RVG}}\right)^{-\frac{1}{3}} \tag{23}$$

where $Nu_{g,FVG}$ and $Nu_{g,RVG}$ are the global Nusselt number in the elastic and rigid cases respectively and f_{FVG}, f_{RVG} are the corresponding friction factors, defined as:

$$f = \frac{2H}{L}\frac{\Delta p}{\rho \bar{U}^2_{f,inlet}} \tag{24}$$

where Δp is the computed pressure drop between the channel inlet and outlet.It is good to note that in the transient FVG cases, the Δp is computed as the time-averaged pressure drop.

The thermal enhancement factor shows averaged values of 1.51 for case 1 and 1.56 for case 2, meaning that the FVGs configurations enhance the heat transfer performance 51% and 56% relative to the rigid cases, respectively for the two values of Reynolds numbers.

In order to study the homogeneity of the temperature field in the fluid flow, the time-averaged local coefficient of variation for the temperature is determined as follow:

$$\overline{CoV_T}(x) = \frac{1}{t_2 - t_1}\int_{t_1}^{t_2} \frac{1}{T_{ave}(x,t)}\left[\frac{\sum_{j=1}^{n}\left(T_j(x,y,t) - T_{ave}(x,t)\right)^2}{n}\right]^{1/2} dt \tag{25}$$

where $T_j(x,y,t)$ is the local temperature at the position (x,y), $T_{ave}(x,t)$ is the averaged value of T on direction y at streamwise position x.

Fig. 13 presents the corresponding values of $\overline{CoV_T}$ comparing the elastic cases to their relative rigid cases computed downstream flap D. At the outlet, the rigid case RVG1 shows an average value of

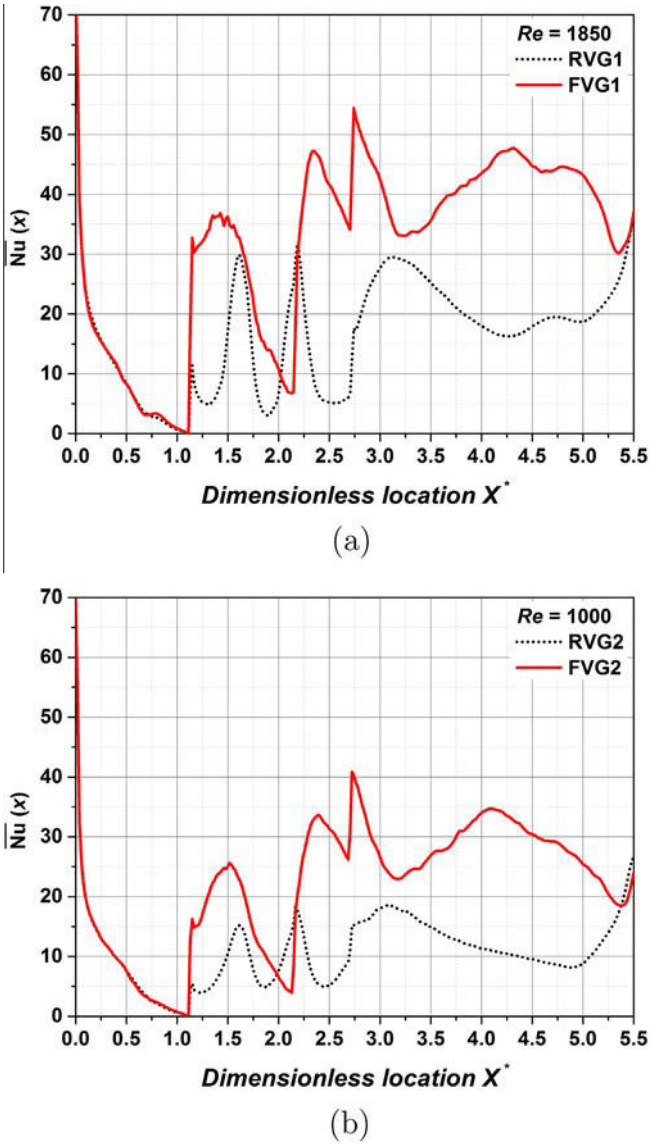

Fig. 12. Variation of the local Nusselt number in (a) case 1 and (b) case 2 comparing the rigid and flexible flaps.

0.0635 whereas the elastic case FVG1 shows an average value of 0.0466 (the time averaging is the same as used for $\overline{CoV_c}$), corresponding to a 27% increase in temperature uniformity and mixedness when using elastic flaps instead of rigid ones. Similarly at the outlet, the rigid case RVG2 shows an average value of 0.06007 against 0.04735 for case FVG2, resulting in 22% increase. Moreover, one can notice that the thermal uniformity is better in the elastic cases than in the rigid cases approximately for all X^*, leading to a shorter thermal length and more compact geometries. One particular region is to be noted when comparing FVG1 and RVG1 for $X^* < 3.5$. In this region, the $\overline{CoV_T}$ value for the rigid case is lower than for the flexible. It can be explained by the fact that the motion

Table 6
Statistical information about the global Nusselt number Nu_g computed at the outlet of the channel for the different cases.

Nu_g	RVG1	FVG1	RVG2	FVG2
Mean	15.94	31.26	9.30	21.80
Standard deviation	–	8.05	–	4.95

Table 7
Statistical information about the Colburn factor j computed at the outlet of the channel for different cases.

j	RVG1	FVG1	RVG2	FVG2
Mean	0.0095	0.0187	0.0104	0.0198
Standard deviation	–	0.0048	–	0.0055

of flap D gets the flow very unstable in this region, leading to high values of standard deviation and $\overline{CoV_T}$ of the temperature. Moreover, a small increase in $\overline{CoV_T}$ value can be observed for the rigid case at $3 < X^* < 3.5$ and can be explained by the fact that the growing boundary layer at the top wall is disturbed by the main flow core. Consequently, for $3 < X^* < 3.5$, the top wall thermal boundary layer grows, leading to increasing values of standard deviation and $\overline{CoV_T}$, and is then reduced by the blockage effect of the main flow resulting in a decrease in the standard deviation and $\overline{CoV_T}$ values. Ultimately, the $\overline{CoV_T}$ value of 0.0635 achieved at $X^* = 5.5$ in RVG1 configuration is obtained much earlier at $X^* = 3.8$ in FVG1 case as shown in Fig. 13(a); Similarly, the $\overline{CoV_T}$ value of 0.06007 achieved at $X^* = 5.5$ in RVG2 is obtained at $X^* = 3.9$ in FVG2 case, as shown in Fig. 13(b).

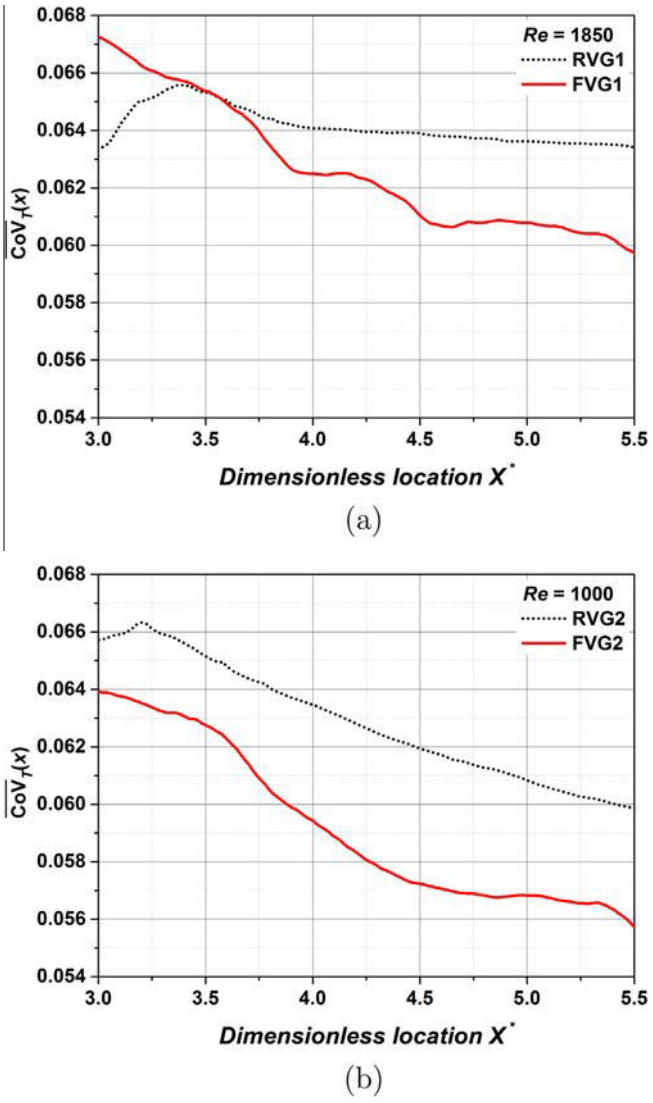

Fig. 13. Comparison of the time-averaged coefficient of variation of temperature T for (a) case 1 and (b) case 2.

5.4. Structural analysis

In this section, motion of the flexible flaps is investigated. Fig. 14(a) and (c) present the oscillation amplitudes of flaps C and D for FVG1 and FVG2 cases with respect to the dimensionless time τ defined as:

$$\tau = \frac{t\bar{U}_{f,inlet}}{H} \tag{26}$$

where t is the dimensional time in seconds.

The vortex shedding from upstream flaps A and B induces large amplitude vibrations of flap C and D with a frequency of oscillation equal to the frequency of vortex shedding reaching a lock-in state [34]. Indeed, in FVG1, both flaps C and D oscillate at the same frequency of about 5.6 Hz close to the fundamental frequency of 6.7 Hz (computed using the Block Lanczos mode extraction method available in ANSYS Mechanical [22]), and with a time delay of $\Delta\tau = 0.04$. In FVG2, flaps C and D oscillate at a frequency of 3 Hz also close to the fundamental frequency of 4 Hz and with a time delay of $\Delta\tau = 0.08$. This lock-in state vortex shedding actually forces flaps C and D to oscillate with large displacements as they are excited at their fundamental frequency, allowing their higher heat and mass transfer performances. Furthermore, looking at Fig. 14(a) and (c), one can note that flap D exhibits a higher displacement amplitude in the streamwise direction than flap C in both FVGs cases. This is explained by the fact that flap C motion is restricted in a narrower space than flap D, due to the presence of flap B upstream and flap D downstream.

Nevertheless, making a flexible material oscillate at its fundamental frequency may cause a break if forces applied on it get higher than the maximum yield strength allowable or may cause fatigue damage when using them for long-use cycles. As the primary goal of this study is to show the increase of mixing quality and heat transfer when using FVGs, only maxima of hydrodynamic forces are investigated here to show whether the rubber-like flaps could resist. Further investigations would still be necessary to study stress fatigue due to repeated cycles. The structural material used in these simulations has mechanical properties similar to that of silicone rubbers materials, which are characterized by a yield strength of approximately 4 MPa [35]. According to the maximum shearing stress theory, which is in widespread use because of its easy use and can offer a conservative result in design [36], yielding is expected to start when the maximum shearing stress of the material equals the maximum shear stress at yielding in a simple tension test. Failure will thus occur when:

$$\tau_{s,max} = \frac{\sigma_1 - \sigma_2}{2} \geqslant \tau_{yp} = \frac{\sigma_{yp}}{2} \tag{27}$$

where $\tau_{s,max}$ is the maximum shear stress, σ_1 and σ_2 are the principal stresses, τ_{yp} is the maximum shear stress at yielding and σ_{yp} is the yielding strength of the material.

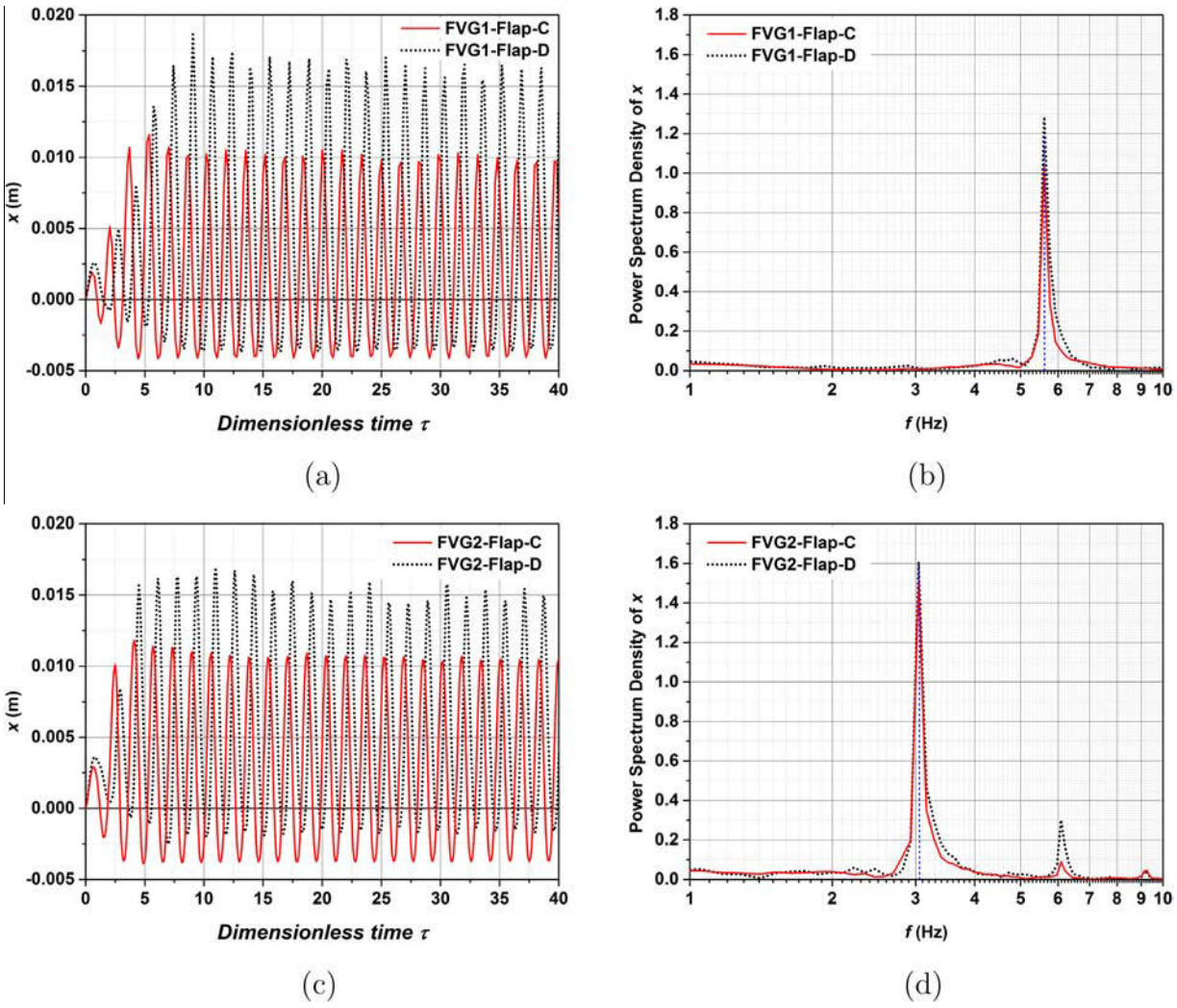

Fig. 14. Structure oscillations in x direction for cases (a) FVG1 and (c) FVG2 as a function of time and power spectra density for (b) FVG1 and (d) FVG2.

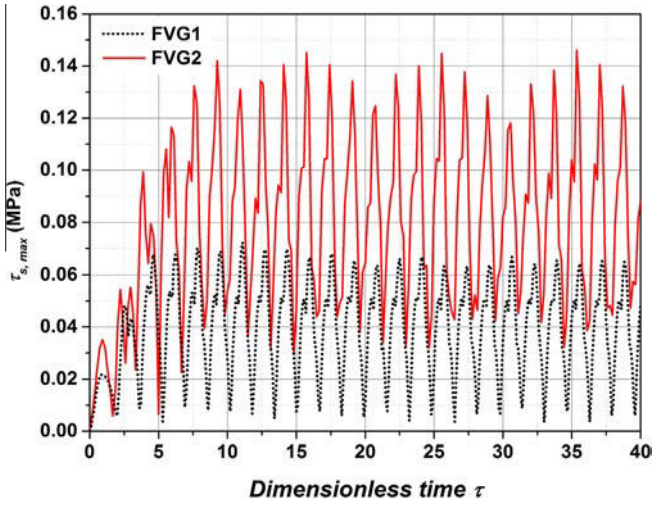

Fig. 15. Transient variation of the maximum shear stress in case FVG1 and FVG2.

Variations of maximum shear stress in the solid domain (i.e. the maximum on the four flaps at each time step) is plotted for both cases FVG1 and FVG2 with respect to time in Fig. 15. Maximum shear stresses are higher in FVG2 case than FVG1 case because the thickness of the flaps is reduced from 1 mm to 0.6 mm. The maximum shear stress value in FVG2 is 0.15 MPa, which is much less than 2 MPa i.e. $\sigma_{yp}/2$, leading to a safe design for both FVG1 and FVG2 cases according to the failure criterion given by Eq. (27).

6. Conclusions

Mixing and heat transfer enhancement is fundamental in many engineering applications and it is carried on by several methods based upon active or passive flow control. The present study focuses on an innovative way to enhance mixing and heat transfer by passive-dynamic flow manipulation in laminar flows. The method consists on using flexible vortex generators fixed at channel walls that can freely oscillate due to flow-induced forces. The flaps oscillations are induced by transient vortices shed from the upstream flaps tip edges which periodically change the external load on the flexible structures.

The computational domain in the present study consists of four flaps mounted on two opposite walls. The two downstream flaps are shifted in order to give the flow asymmetric. Two cases are studied depending on the Reynolds number (1000 and 1850) and thickness of the flaps. Their corresponding rigid vortex generators cases are also simulated in order to compare performances. The coupled fluid–structure numerical simulations are carried out by strong coupling method using ANSYS Fluent CFD-solver and Mechanical CSD-solver. The fluid flow is solved via an Arbitrary Lagrangian–Eulerian (ALE) formulation, solid deformations are computed by taking into account large structural deformation and strong coupling between the flow and the elastic solid solvers and mesh solver is used to perform automatic local remeshing depending on mesh distortion.

The observation of the flow pattern shows that the vortex shedding is mainly caused by shear instabilities, where the shear layer formed at the tip edge of the flaps detaches and forms a sequence of periodic vortices. This vortex shedding is intense in the FVGs cases, and plays an important role in mixing and heat transfer processes.

The mixing process is then quantified by investigating the transport of a passive scalar through the domain. The FVGs configurations show better mixture quality, with a 98% increase in mixture quality for case 1 and 97% increase for case 2 in comparison to their rigid cases. These performance enhancements are primarily caused by high oscillation amplitudes where the flaps act as a mechanical pump sequentially pumping scalar with different values and eventually improving the mixture quality.

Besides, heat transfer is analyzed by evaluating the local and global Nusselt numbers. An increase of up to 97% in the local heat transfer and 134% in the overall heat transfer is obtained when using elastic flaps instead of rigid flaps. In order to compare the energy efficiency between the rigid and elastic vortex generators, the Colburn factor j is calculated. It shows an increase of up to 96% in the elastic cases. In addition, a thermal performance factor allowing comparison between convective heat transfer for the elastic cases and rigid ones shows a value greater than one in both case 1 and 2, representing an increase of up to 56% in thermal performance. Eventually, temperature homogeneity of the fluid has been studied through the investigation of the coefficient of variation. It showed an increase of up to 27% in terms of temperature uniformity and mixedness at the outlet of the static mixer designed with FVGs.

Consequently, this study shows a new way of enhancing heat and mass transfer without relying on active methods but taking benefit of moving elastic flaps yet. Devices used to control the oscillation frequency and amplitude of the elastic flaps are not necessary in the present study, thus reducing the complexity of installation and increasing the overall efficiency by saving energy and relying only on the energy of the fluid itself.

Future studies will be performed on three dimensional flexible vortex generators using both experimental and numerical techniques.

Conflict of interest

None declared.

Appendix A. Supplementary data

Supplementary data associated with this article can be found, in the online version, at http://dx.doi.org/10.1016/j.ijheatmasstransfer.2015.01.122.

References

[1] M. Fiebig, Vortices, generators and heat transfer, Chem. Eng. Res. Des. 76 (2) (1998) 108–123.
[2] H.E. Ahmed, H.A. Mohammed, M.Z. Yusoff, An overview on heat transfer augmentation using vortex generators and nanofluids: approaches and applications, Renew. Sustain. Energy Rev. 16 (8) (2012) 5951–5993.
[3] H. Mohand Kaci, C. Habchi, T. Lemenand, D. Della Valle, H. Peerhossaini, Flow structure and heat transfer induced by embedded vorticity, Int. J. Heat Mass Transfer 53 (17–18) (2010) 3575–3584.
[4] R.K. Thakur, C. Vial, K.D.P. Nigam, E.B. Nauman, G. Djelveh, Static mixers in the process industries–a review, Chem. Eng. Res. Des. 81 (7) (2003) 787–826.
[5] R.L. Webb, Handbook of Single Phase Convective Heat Transfer, John Wiley & Sons Ltd, 1987.
[6] C. Habchi, T. Lemenand, D. Della Valle, H. Peerhossaini, Turbulence behavior of artificially generated vorticity, J. Turbul. 11 (36) (2010) 1–18.
[7] C. Habchi, T. Lemenand, D. Della Valle, H. Peerhossaini, Turbulent mixing and residence time distribution in novel multifunctional heat exchangers–reactors, Chem. Eng. Process. 49 (10) (2010) 1066–1075.
[8] C. Habchi, S. Russeil, D. Bougeard, J.-L. Harion, T. Lemenand, D. Della Valle, H. Peerhossaini, Enhancing heat transfer in vortex generator-type multifunctional heat exchangers, Appl. Therm. Eng. 38 (0) (2012) 14–25.
[9] W.J. Gretta, C.R. Smith, The flow structure and statistics of a passive mixing tab, J. Fluids Eng. 115 (2) (1993) 255–263.
[10] R. Elavarasan, H. Meng, Flow visualization study of role of coherent structures in a tab wake, Fluid Dyn. Res. 27 (3) (2000) 183–197.
[11] S. Dong, H.U.I. Meng, Flow past a trapezoidal tab, J. Fluid Mech. 510 (2004) 219–242.

[12] W. Fu, B. Tong, Numerical investigation of heat transfer from a heated oscillating cylinder in a cross flow, Int. J. Heat Mass Transfer 45 (2002) 3033–3043.
[13] V.V. Khatavkar, P.D. Anderson, J.M.J. den Toonder, H.E.H. Meijer, Active micromixer based on artificial cilia, Phys. Fluids 19 (8) (2007) 083605.
[14] R.A. Lambert, R.H. Rangel, The role of elastic flap deformation on fluid mixing in a microchannel, Phys. Fluids 22 (5) (2010) 1–12.
[15] H. Mirzaee, A. Dadvand, I. Mirzaee, R. Shabani, Heat transfer enhancement in microchannels using an elastic vortex generator, J. Enhanced Heat Transfer 19 (3) (2012) 199–211.
[16] M. Razzaq, H. Damanik, J. Hron, A. Ouazzi, S. Turek, FEM multigrid techniques for fluid-structure interaction with application to hemodynamics, Appl. Numer. Math. 62 (9) (2012) 1156–1170.
[17] D.J. Newman, G.E. Karnidakis, A direct numerical simulation study of flow past a freely vibrating cable, J. Fluid Mech. 344 (1997) 95–136.
[18] C. Evangelinos, G.E. Karnidakis, Dynamics and flow structures in the turbulent wake of rigid and flexible cylinders subject to vortex-induced vibrations, J. Fluid Mech. 400 (1999) 91–124.
[19] R. Loehner, C. Yang, J. Cebral, J.D. Baum, H. Luo, D. Pelessone, C. Charman, Fluid–structure–thermal interaction using a loose coupling algorithm and adaptive unstructured grids, in: Proc., 29th AIAA Fluid Dynamics Conference, 1998.
[20] C. Habchi, S. Russeil, D. Bougeard, J.-L. Harion, T. Lemenand, A. Ghanem, D. Della Valle, H. Peerhossaini, Partitioned solver for strongly coupled fluid–structure interaction, Comput. Fluids 71 (0) (2013) 306–319.
[21] P. Le Tallec, J. Mouro, Fluid structure interaction with large structural displacements, Comput. Methods Appl. Mech. Eng. 190 (2425) (2001) 3039–3067.
[22] ANSYS Academic Research, Release 15.0, Help system, Fluent theory user's guide, ANSYS Inc.
[23] J. Donea, A. Huerta, J.P. Ponthot, A. Rodriguez-Ferran, Arbitrary Lagrangian Eulerian Methods, John Wiley & Sons Ltd, 2004.
[24] Z. Tukovic, H. Jasak, Updated lagrangian finite volume solver for large deformation dynamic response of elastic body, Trans. FAMENA 31 (1) (2007) 1–16.
[25] F.M. Bos, Numerical simulations of flapping foil and wing aerodynamics (Ph.D.), Technical University of Delft, 2010.
[26] P.F. Galpin, R.B. Broberg, B.R. Hutchinson, Three-dimensional Navier Stokes predictions of steady-state rotor/stator interaction with pitch change, in: 3rd Annual Conference of the CFD, Society of Canada , Advanced Scientific Computing Ltd, Banff, Alberta, Canada, June 25–27, 1995.
[27] S. Turek, J. Hron, Proposal for Numerical Benchmarking of Fluid Structure Interaction Between an Elastic Object and Laminar Incompressible Flow, Ergebnisberichte angewandte Mathematik, Univ., 2006.
[28] I.B. Celik, U. Ghia, P.J. Roache, C.J. Freitas, H. Coleman, P.E. Raad, Procedure for estimation and reporting of uncertainty due to discretization in CFD applications, J. Fluids Eng. 130 (2008) 0780011–0780014.
[29] D. Bothe, Evaluating the Quality of a Mixture: Degree of Homogeneity and Scale of Segregation, Heat and Mass Transfer, Springer, Berlin Heidelberg, 2010 (Ch. 2).
[30] N.-T. Nguyen, X. Huang, Modelling, fabrication and characterization of a polymeric micromixer based on sequential segmentation, Biomed. Microdevices 8 (2) (2006) 133–139.
[31] C.K.L. Tan, M.C. Tracey, J.B. Davis, I.D. Johnston, Continuously variable mixing-ratio micromixer with elastomer valves, J. Micromech. Microeng. 15 (10) (2005) 1885.
[32] P. Promvonge, C. Thianpong, Thermal performance assessment of turbulent channel flows over different shaped ribs, Int. Commun. Heat Mass Transfer 35 (10) (2008) 1327–1334.
[33] S.R. Shabanian, M. Rahimi, M. Shahhosseini, A.A. Alsairafi, CFD and experimental studies on heat transfer enhancement in an air cooler equipped with different tube inserts, Int. Commun. Heat Mass Transfer 38 (3) (2011) 383–390.
[34] C.H.K. Williamson, R. Govardhan, Vortex-induced vibrations, Annu. Rev. Fluid Mech. 36 (1) (2004) 413–455.
[35] Silicone rubber, Website, <http://www.azom.com/properties.aspx?ArticleID=920>, 2014.
[36] A. Ugural, S. Fenster, Advanced Strength and Applied Elasticity, Prentice Hall PTR, 2003.

Chapter 4

Towards self-sustained oscillations of multiple flexible vortex generators

4.1 Introduction

Flow control is commonly used in industrial processes for a wide variety of automotive, aerospace, building or process engineering applications. Various objectives can be achieved such as drag and lift coefficients modifications, solid structure vibration reductions or heat and mass transfer enhancement among others. In order to stabilize a flow to prevent or reduce unsteadiness for example, fluttering and galloping phenomena have to be thoroughly understood before considering counter-balancing its effects. They can occur when the fluid surrounding a structure feeds back energy to it instead of absorbing it [Song et al., 2012, Ekici et al., 2013]. This instability can thus be analyzed as a competition between the fluid forces and the elasticity of the structure: when a structure experiences deflection, a destabilizing pressure jump occurs across the structure, while the bending stiffness of the structure tends to bring it back to its equilibrium position. The instability analysis can also be observed when several flapping structures interact with each other. Some remarkable insights from flags flapping in side-by-side or tandem arrangement can be found in the literature [Zhu, 2009, Farnell et al., 2004, Schouveiler and Eloy, 2009]. Ristroph and Zang [Ristroph and Zhang, 2008] showed that in tandem arrangement of flexible flags, the upstream flag experiences less drag than the downstream flag, which was highlighted as an inverted draft effect. They also pinpointed a resonance effect when the downstream flag oscillates at the same frequency of its oncoming fluid flow oscillations originally produced by the upstream flag. In the tandem arrangement, the upstream body strongly influences the downstream one through vortex shedding. Zhu [Zhu, 2009] also observed this inverted drafting phenomenon when investigating the interaction between two tandem flags, but he also showed that the opposite effect occurs when flags are in a static state at very low Reynolds number.

Dynamic response of elastic bodies produced by hydrodynamic forces has previously been studied and furthermore brought to light particular parameters such as the added mass effect, the critical velocity or the participative force applied to the structure. Particular attention has to be paid when operating at critical values of these parameters because the instability can lead to self-sustained and large amplitude flapping of the structure and can eventually irreversibly damage it. In consequence, most of the studies are performed in order to suppress instabilities of vortex-induced vibrations, galloping and fluttering either by adding weights, mass balancing methodologies or forcing operating conditions below the critical parameter values.

The understanding of flow unsteadiness production can however benefit other research fields such as electric energy production for example [Allen and Smits, 2001, Akcabay and Young, 2012]. Michelin

Note to reader: chapters 4, 5 and 6 were written in a format corresponding to the preparation of articles to be submitted in scientific journals. References are grouped at the end of thesis manuscript, however some repetitions may appear in these three chapters.

and Doaré [Michelin and Doaré, 2013] showed the potential of using flag fluttering instabilities when following flow motions using piezoelectric patches attached to it.

Khatavkar *et al.* [Khatavkar et al., 2007] numerically studied the effect of active control cilia as microactuators on the mixing in microchannel flows. They concluded that under optimal conditions, the use of two actuated flaps on the same wall or on opposite can induce chaotic advection in a microchannel flow. Furthermore, Fu and Tong [Fu and Tong, 2002] numerically investigated the effect of frequency and amplitude of a heated oscillating cylinder on the convective heat transfer. They concluded that the best performances were achieved with increasing amplitude and Reynolds number, and when a lock-in state is reached between the wake detachment and the cylinder oscillation. Lambert and Rangel [Lambert and Rangel, 2010] numerically studied the effect of introducing one elastic flap forced to oscillate in a fluid medium for mixing purposes. The results showed that mixing was enhanced for large flap displacements, the flap behaving as a rapid mixing device.

A need thus arises to implement self-sustained oscillating structures to enhance heat and mass transfer naturally forced (with no external control or energy) by taking advantage of the instability produced by phenomena of fluttering, galloping and vortex induced vibrations.

In a previous study, we considered Fluid-Structure Interaction (FSI) instabilities to validate the potential target to an energy efficient system for heat and mass transfer applications [Ali et al., 2015]. One of the passive methods commonly employed is the introduction of vortex generators, which were used as elastic bodies instead of rigid ones as frequently employed [Ahmed et al., 2012, Dong and Meng, 2004, Fiebig, 1998, Habchi et al., 2010a]. Our study were performed using validated CFD methodology and modeled laminar flows at two different Reynolds numbers (1000 and 1850 based on the hydraulic diameter) in a channel where flexible vortex generators were located at the walls. Results were compared to the corresponding cases with use of rigid vortex generators and showed increases up to 56% for a global thermal performance factor (determined as a ratio based on overall heat transfer and friction factor) and up to 27% enhancement of mixing quality (based on coefficient of variation criterion).

In the present study, we further investigate dynamics of such a proposal by arranging several flexible vortex generators (FVGs) confined in a two-dimensional laminar flow between two parallel plates, operating at a Reynolds number of 2000 based on the hydraulic diameter. The FVGs are placed on the same or opposite walls and fluid-structure oscillations and instabilities produced are analyzed accordingly with the aim to reach a self-sustained oscillating system. Details about mathematical formulation and numerical procedure are first presented. Then, numerical configurations are detailed and mesh-independency is considered. Eventually, increasing the FVG number and introducing two co-planar FVGs upstream are investigated through the analysis of flow pattern, structural oscillation amplitudes and drag of the FVGs.

4.2 Mathematical formulation and numerical procedure

The flow field is governed by the unsteady Navier-Stokes equations for an incompressible viscous laminar flow. These equations are discretized in a computational domain which deforms in time to perform simulations of the flexible structure deformation. Therefore, an Arbitrary Lagrangian-Eulerian (ALE) formulation [Donea et al., 2004] is used to solve the flow equations on a deforming mesh. The ALE formulation of the Navier-Stokes equations is thus:

$$\nabla \cdot \mathbf{u_f} = 0 \tag{4.1}$$

$$\frac{\partial \mathbf{u_f}}{\partial t} + (\mathbf{u_f} - \mathbf{u_{m,f}}) \cdot \nabla \mathbf{u_f} = -\frac{\nabla p}{\rho_f} + \nu_f \nabla^2 \mathbf{u_f} \tag{4.2}$$

where $(\mathbf{u_f} - \mathbf{u_{m,f}})$ is the convective term with $\mathbf{u_f}$ the fluid velocity and $\mathbf{u_{m,f}}$ the mesh velocity in the fluid domain. The pressure is denoted by p, the density of the fluid by ρ_f and the kinematic viscosity by ν_f. The Eulerian and Lagrangian descriptions are obtained respectively by setting $\mathbf{u_{m,f}} = 0$ away from the flaps or $\mathbf{u_{m,f}} = \mathbf{u_f}$ near the flaps.

The equation of motion for an elastic isothermal solid structure can be described from a Lagrangian point of view, i.e. in terms of the initial configuration at $t = 0$, and it reads:

$$\rho_s \frac{\partial^2 \mathbf{d_s}}{\partial t^2} = \nabla \cdot \left(\Sigma \cdot \mathbf{F^T} \right) \tag{4.3}$$

where $\mathbf{d_s}$ is the displacement of the structure, ρ_s is the density of the structure and **F** is the deformation gradient tensor given by:

$$\mathbf{F} = \mathbf{I} + \nabla \mathbf{d_s^T} \tag{4.4}$$

where **I** is the identity matrix.

The second Piola-Kirchhoff stress tensor Σ is related to the Green Lagrangian strain tensor **G** following [Tukovic and Jasak, 2007, Bos, 2010b]:

$$\Sigma = 2\mu_s \mathbf{G} + \lambda_s tr\left(\mathbf{G}\right) \mathbf{I} \tag{4.5}$$

with **G** given by:

$$\mathbf{G} = \frac{1}{2} \left(\mathbf{F^T} \cdot \mathbf{F} - \mathbf{I} \right) \tag{4.6}$$

Here *tr* is the tensor trace, λ_s and μ_s are Lamé constants which are characteristics of the elastic material. They are linked to the Young modulus *E* and Poisson's coefficient ν_s by:

$$\lambda_s = \frac{\nu_s E}{\left(1 + \nu_s\right)\left(1 - 2\nu_s\right)} \tag{4.7}$$

$$\mu_s = \frac{E}{2\left(1 + \nu_s\right)} \tag{4.8}$$

Analyses of fluid-structure interaction problems may be performed with partitioned approach, where different solvers for fluid and structure are called sequentially. As this paper deals with large structural displacements and incompressible fluid significantly moving with the structure, a strongly coupled approach with partitioned solutions is considered to solve the hydroelastic systems using the ANSYS-Fluent CFD-solver and the ANSYS-Mechanical CSD-solver [ANSYS, 2015].

Fluid-structure interaction problems with moving boundaries require a third coupled solver for automatic internal mesh motion. The mesh motion solver in Fluent consequently deforms the internal fluid domain while maintaining the quality and validity of the deforming mesh. In this case, the displacement of the fluid-structure interface, which is the result of the structural solver, is then used as a boundary condition for the mesh motion solver.

The present study employs the Laplace smoothing equation given by the following expression:

$$\nabla \cdot \left(\gamma \nabla \mathbf{u_m} \right) = 0 \tag{4.9}$$

where γ is the mesh diffusion coefficient and $\mathbf{u_m}$ the mesh displacement velocity. The mesh diffusion coefficient used in this study is a function of the boundary distance:

$$\gamma = \frac{1}{l^\alpha} \tag{4.10}$$

where *l* is a normalized boundary distance and α is the diffusion parameter. A diffusion parameter α of 1.5 has been used in the present study, which preserves larger regions of the mesh near the moving boundary, and cause the regions away from the moving boundary to absorb a bigger part of the motion.

To avoid divergence problems especially caused by negative cell volumes, the mesh motion solver supports several remeshing methods. The one used in this study is the 2.5*D* surface remeshing, which works on wedge/prism cells extruded from triangular surface elements. It agglomerates cells that violate the skewness or size criteria and locally remeshes the agglomerated cells or faces. If the new cells or faces satisfy the skewness criterion, the mesh is locally updated with the new cells (with

the solution interpolated from the old cells). Otherwise, the new cells are discarded and the old cells are retained. In the present study a maximum cell skewness of 0.7 has been used for remeshing with cell size criterion depending on the minimum and maximum length scale of the mesh.

In order to perform the load and motion transfer between different meshes for fluid and structure, the General Grid Interface (GGI) mapping algorithm is used [Galpin et al., 1995]. This algorithm generates weights that are well adapted to transfer conserved quantities such as mass, momentum and energy flows. At each time step, the FSI iteration loop continues to call sequentially the structural solver, the mesh motion algorithm and the fluid solver until the convergence limit for displacements and forces are reached. An under-relaxation factor for both displacement and force is set to unity for all the simulations performed in this study with a convergence criterion set on both force and displacement fixed to 10^{-4}.

Although temporal discretization is performed using a first order implicit scheme that is unconditionally stable, CFL based on the time step size set to 10^{-4} s and the minimum cell distance has been checked to be always less than unity.

The pressure-velocity coupling is established using the coupled algorithm [ANSYS, 2015] which solves the momentum and pressure-based continuity equations together. The full implicit coupling is achieved through an implicit discretization of pressure gradient terms in the momentum equations, and an implicit discretization of the face mass flux. The convergence criteria for pressure, momentum and conservation equations are set to 10^{-6}. The Laplace mesh smoothing convergence criterion is set to 10^{-4}. The global procedure and parameters setup have been validated on a benchmark test detailed in a previous work [Ali et al., 2015].

In the next section, the computational domain, boundary and initial conditions and mesh validation study are presented.

4.3 Problem description

The computational domain is two-dimensional and consists of several elastic flaps inclined with an angle $\beta = 30°$ to the walls as shown in Figure 6.1. Different designs are studied and specified through the name xCP-yFVG. Thus, 'y'FVG stands for the number of alternating successive FVG located in the domain whereas 'x'CP stands for the number of co-planar flaps that are located upstream. Based on this nomenclature, 0CP-2FVG, 0CP-3FVG, 0CP-4FVG are presented in Figure 6.1 (a), (b) and (c) respectively. Two co-planar flaps (2CP) are then introduced in 2CP-2FVG and 2CP-3FVG configurations, as shown in Figure 6.1 (d) and (e). For all cases, flaps C, D and E have the same length of 30 mm separated by a distance equal to their span and with a thickness e as reported in Table 6.1 whereas the co-planar flaps A and B have a length of 25 mm.

No slip boundary conditions are set on the top and bottom walls and on the flap surfaces. The outlet is set at zero pressure and Neumann zero for velocity. A parabolic laminar velocity profile corresponding to a fully developed laminar flow is set at the flow inlet. The Reynolds number for all the present simulations is fixed to 2000 based on a hydraulic diameter of $D_h = 2H$. Fluid considered here is air with a constant kinematic viscosity of $\nu_f = 1.46 \times 10^{-5}\, m^2/s$.

Table 4.1: Physical parameters and flow conditions for all cases

Cases	ρ_s (kg/m^3)	ν_s	E (10^6 Pa)	e (mm)	H (mm)	$Re_{D_h} = (\overline{U}_{f,inlet} D_h)/\nu_f$
FVG	1200	0.4	5	0.75	54	2000

A grid size independence study for the FSI simulations has been conducted on the case 2CP-3FVG where the elastic flaps undergo the highest displacement amplitudes. The fluid domain is thus discretized with three initial different mesh sizes using triangular cells, refined at the wall and at the fluid solid interface, i.e. at the elastic flaps. During the FSI simulations, automatic mesh adaptation is performed to remesh the volume due to mesh distortion depending on the motion and behaviour of the flaps as illustrated in Figure 5.2. This aims to avoid negative cell volumes and allows to adapt

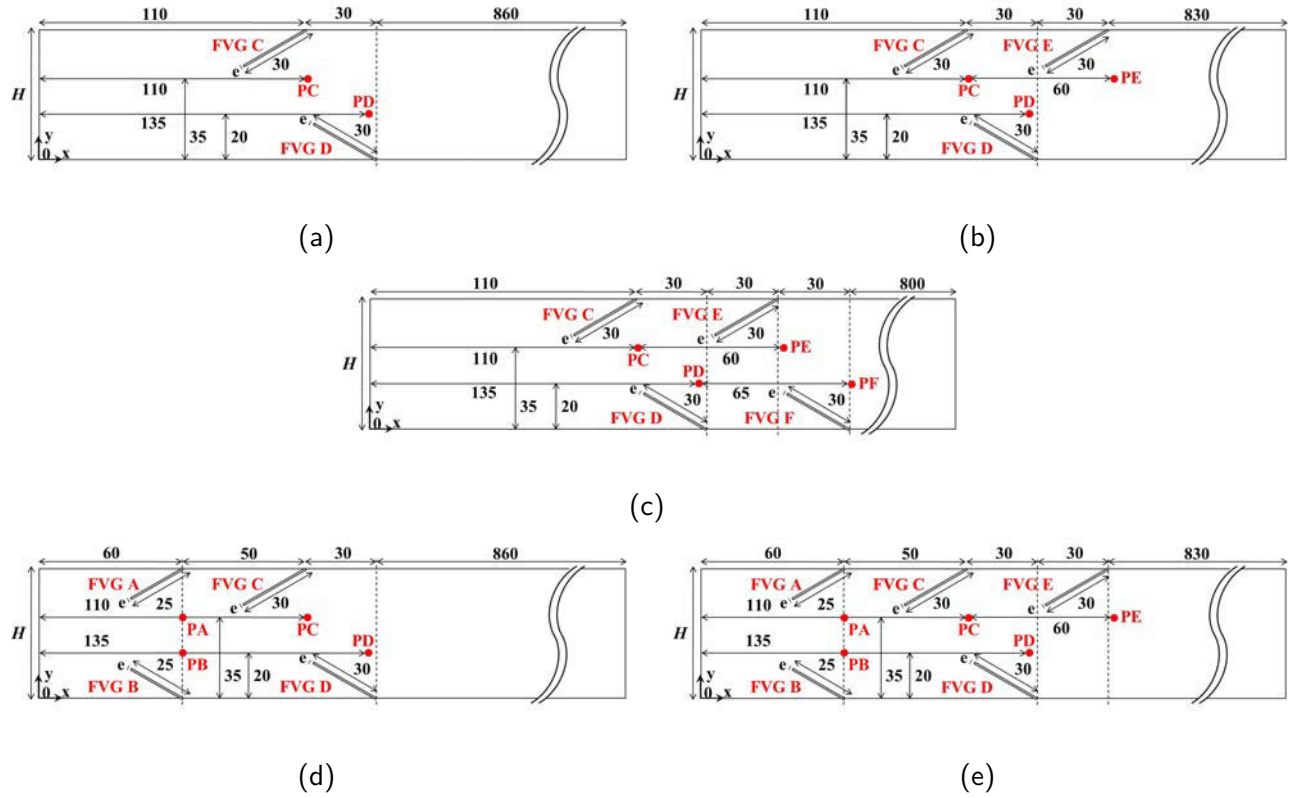

Figure 4.1: Computational domain and boundary conditions for the studied cases (dimensions are in mm, flow goes from left to right) as follows: (a) 0CP-2FVG, (b) 0CP-3FVG, (c) 0CP-4FVG, (d) 2CP-2FVG and (e) 2CP-3FVG

cell sizes near the moving interfaces according to a size and skewness criteria set in the solver (see Section 2). The total cell number and the overall mean cell size were checked during the simulations and no significant change from their initial value was found. The three mesh densities and their main characteristics are summarized in Table 6.2.

Table 4.2: Global meshes characteristics used for grid size independance study

▪	Mesh 1	Mesh 2	Mesh 3
Initial number of cells (N)	19437	47592	95360
Grid size $h = \left[\frac{1}{N}\sum_{i=1}^{N}(\Delta A_i)\right]^{\frac{1}{2}}$	0.001677	0.001065	0.000753
Grid refinement factor $r = h_i/h_j$	-	$h_2/h_1 = 1.56$	$h_3/h_2 = 1.42$

where ΔA_i is the area of the i^{th} cell.

To determine the appropriate mesh density for grid size independence, the simulations are performed on increasing mesh densities. The mesh validity verification is based on the method proposed by Celik *et al* [Celik et al., 2008] where the grid convergence index (GCI) and the apparent order of convergence (p_c) can be obtained. Since the flap oscillation amplitude strongly depends on the refinement near the fluid-solid interface and the precise estimation of the fluid forces, the amplitude of oscillations of flap E in the x-axis direction is chosen for the mesh validity verification.

Since the signal of the displacement is quasi-periodic, the mean amplitude MA of flap E is

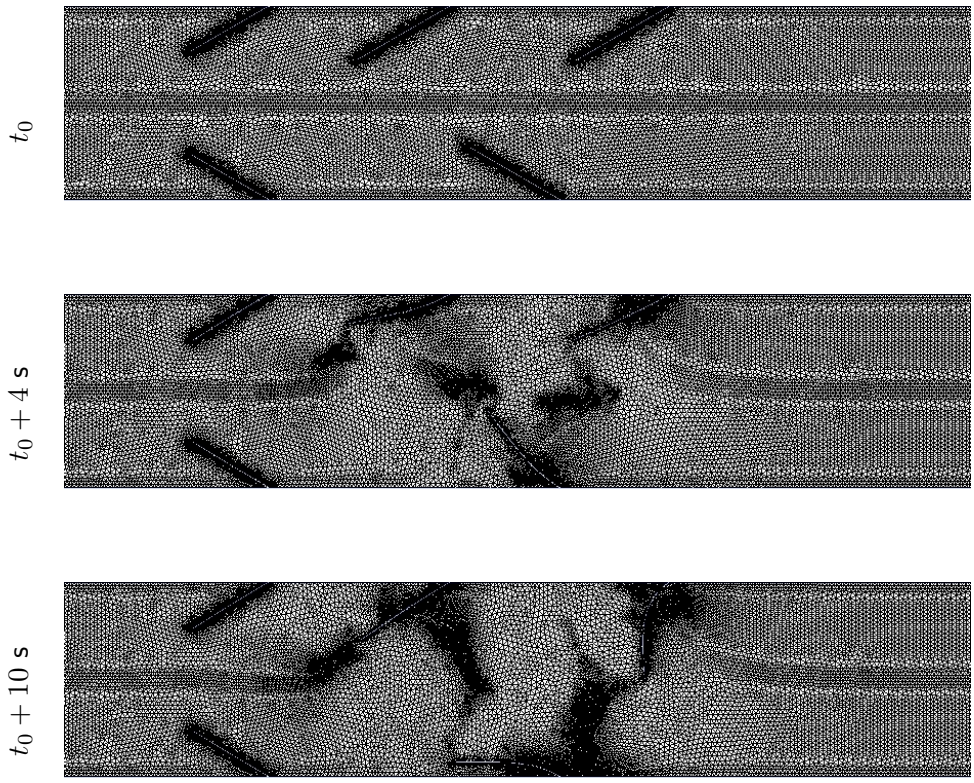

Figure 4.2: Snapshots of dynamic mesh at different time steps

calculated by:

$$MA = \frac{1}{n}\sum_{i=1}^{n} |x_{i_{peak}} - \overline{x}| \tag{4.11}$$

where n is the number of maximum and minimum peaks in the signal, $x_{i_{peak}}$ are the individual maximum and minimum values and $\overline{x}$ is the mean displacement. The amplitude calculation is performed from $t_1 = 4$ s to $t_2 = 10$ s in order to avoid taking into consideration the transitional time before reaching fully stabilized regime.

The results obtained by applying the method of Celik *et al* [Celik et al., 2008] are summarized in Table 6.3, where $\phi_{refined}$ is the variable calculated from the solution of the refined mesh, ϕ_{ext} is the extrapolated variable and e_a^{23} is the relative error between Mesh 3 and Mesh 2. Extensive information about the calculation of these parameters can be found in Celik *et al* [Celik et al., 2008]. It can be concluded from Table 6.3 that the uncertainty in the fine-grid solution is about 0.86% for the displacement amplitude of flap E. The refined Mesh 3 can thus be used as a reference mesh density for the flexible vortex generators configurations.

Table 4.3: Estimated order of convergence p and GCI for refined Mesh 3

Parameter	$\phi_{refined}$	ϕ_{ext}	e_a^{23} (%)	p_c	GCI (%)
Flap E amplitude (mm)	10.07	10.1	0.68	1.8	0.86

4.4 Results and discussion

In this section, we report the results of the two-dimensional numerical simulations and analyze the flow and structural patterns for the flexible flap configurations. We compare in this investigation all

the xCP-yFVG cases presented previously but for space reasons, we present snapshots of vorticity and pressure distribution for the 2CP-3FVG case only in Section 4.4.2 (other case studies can be found as supplementary materials on the website version). Finally, a brief discussion is made about the motions of the flaps, their potential risk to break and the relationship between drag and amplitude for the different cases studied.

4.4.1 Frequency lock-in between the flow and the flexible flaps

In order to investigate FSI local effect on flow pattern, Fast Fourier Transformations (FFT) have been processed on temporal signal of streamwise velocity u extracted downstream each flap of the studied configurations (numerical probes are depicted in Figure 6.1). Signals have been analyzed as power spectrum density plotted in Figure 4.3. When looking at Figure 4.3 (a) corresponding to the 0CP-2FVG case, a frequency peak is observed at 2.495 Hz representing the characteristic vortex shedding frequency f_v. Comparing this value to the fundamental frequency of the elastic flap in vacuum ($f_N = 4.8$ Hz, computed using the Block Lanczos mode extraction method [ANSYS, 2015]) leads to a frequency ratio of $f_v/f_N \approx 0.52$. No synchronization effect can thus be observed between vortex shedding and flap oscillation in such a configuration. At the contrary, when analyzing the other configurations vortex shedding frequency is shifted to the fundamental frequency of the flexible flaps, i.e. $f_v/f_N \approx 1$. This phenomenon is called the lock-in effect and has been subject to various studies in the literature. In order to predict whether lock-in effect could occur, a reduced velocity parameter can be determined based on the upstream velocity $\overline{U}_f$ (taken as the mean flow velocity upstream the flap), the length of the flap L and the fundamental frequency f_N as:

$$V_r = \frac{\overline{U}_f}{2\pi f_N L sin\beta} \tag{4.12}$$

Eventhough no data have been found in the literature for exact comparison with our case study (most of the values where available in vortex induced vibrations around a cylinder), we might refer to a previous work of Yang and Strganac [Yang and Strganac, 2013] that studied effect of a flow past a long flat plate attached to its tips but free to have torsional vibrations (those vibrations being similar to our flap bending oscillations). Lock-in effect was found to be observed for a range of reduced velocity $0.8 \leqslant V_r \leqslant 2$. In the 0CP-2FVG case, calculated value is approximately 0.6 which is not included in this range and explain the non lock-in observation between the flow and the structure. Bourguet *et al.* [Bourguet et al., 2011] numerically studied and modeled motion of a long elastic beam submitted to dynamic forces induced by a shear flow. In this particular situation of non lock-in state regime, they further observed that the flow tends to damp the structural oscillations, phenomenon that can also be observed here for the 0CP-2FVG case through Figure 4.5 (I) presented in section 4.4.3. Moreover, adding one more alternated flap to the 0CP-2FVG to become 0CP-3FVG, one can clearly notice the increase in the momentum fluctuating energy shown in the PSD diagram for this case. Here, flaps C and D behave as a section thinner thus locally increasing the reduced velocity in front of flap E (by increasing the streamwise velocity to keep constant flow rate). The fluid thus induces much higher forces on the added flap E and characteristic frequencies of fluid and structure synchronize to reach a lock-in state. Furthermore, all the PSD diagrams except for 0CP-2FVG exhibit two frequency peaks: one primary peak occurs at f_v=4.2 Hz and a secondary peak which appears to be a subharmonic peak that rises at twice the frequency f_v. On the other cases investigated, adding two co-planar flaps upstream (2CP-2FVG 4.3 (d) and 2CP-3FVG 4.3 (e)) increases the reduced velocity upstream the alternated flaps to 1.1. The flaps thus oscillate in their lock-in region where the vortex shedding frequency synchronizes with the structural frequency. Consequently, the fluid forces supply supplementary energy to the alternated FVGs downstream instead of damping it as it can be observed in the PSD diagrams. As a consequence, one can see that without modifying the incoming flow rate and Reynolds number and without additional energy source, self-sustained oscillations can be obtained by reaching a lock-in state between the flow and the immersed flexible structures. Three flaps are at least necessary to produce this excitation and this can be of particular interest when generation of vorticity and flow mixing is expected for mass or heat transfer enhancement for example.

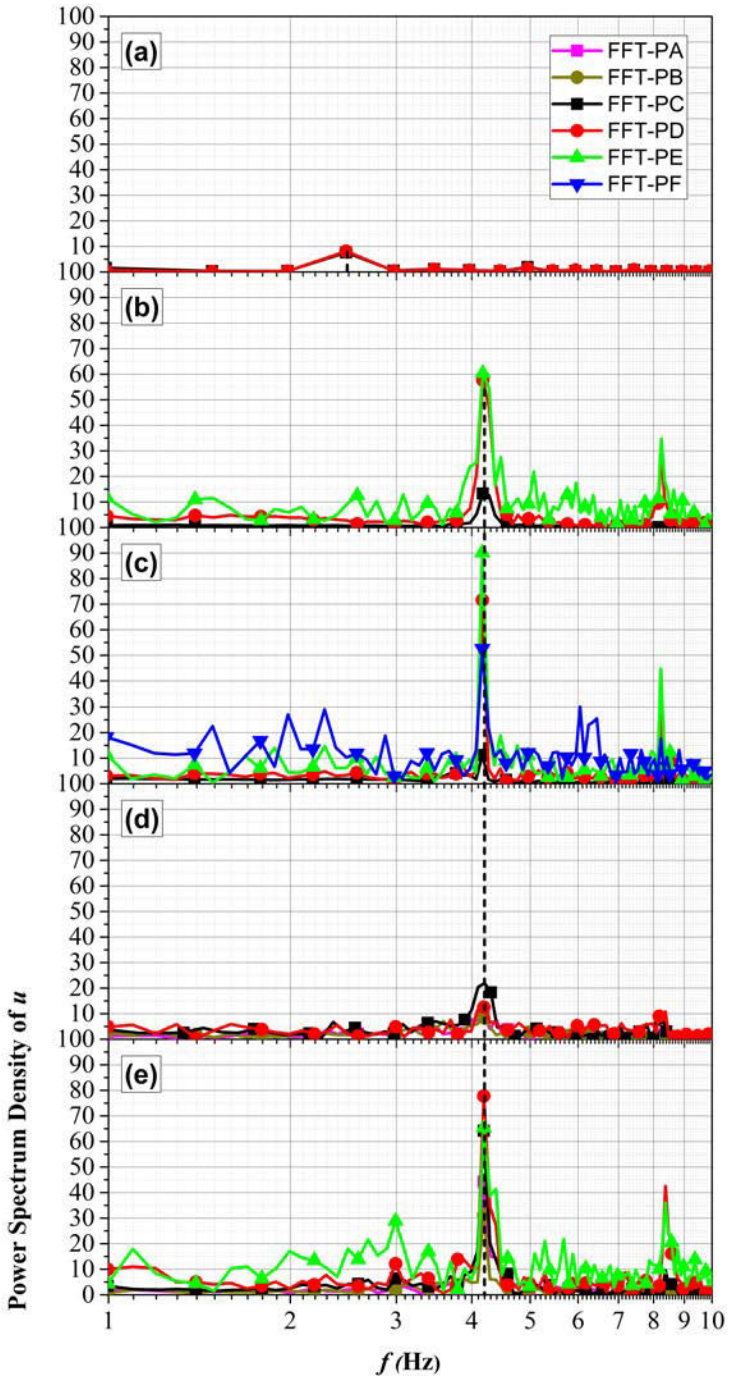

Figure 4.3: Power spectrum density of the streamwise velocity u at probe locations A,B,C,D and E when appropriate and for (a) case 0CP-2FVG, (b) case 0CP-3FVG, (c) case 0CP-4FVG, (d) case 2CP-2FVG and (e) case 2CP-3FVG

4.4.2 Vortex production and benefits on flap oscillations

To further investigate the FSI, one can also observe that not only adding flexible flaps upstream others produce area confinement and increase pressure forces applied to the downstream flaps but also large deformation amplitudes of the downstream flaps has a backward effect and changes drastically the pressure differences around the upstream flaps. To better understand this phenomenon, we illustrate the 2CP-3FVG configuration through its transient behavior as it shows the largest flap amplitudes and knowing that other case studies exhibit the same kind of flow interactions (supplementary materials being available on the website version). Figure 4.4 thus shows the instantaneous development of the vorticity field with the corresponding pressure distribution at given instants. First, looking at the co-planar flaps A and B, one can observe a sequence of periodic vortices shed from their tip edges due to the shear layer instability generated at the interface between the high momentum fluid in the bulk region and the low momentum fluid in the wake of the flaps. These co-planar flaps display insignificant motion (amplitude is in the order of 10^{-5} m) and can be considered negligible with respect to other flap oscillations. Their role is to increase the reduced velocity upstream of flaps C, D and E, thus increasing the dynamic forces applied and inducing high amplitude oscillations. Another interesting phenomenon is the interaction between vortices shed from flap A and flap C: the counter-clockwise vortex (CCW) shed from flap A at time t_0 deviates the flow stream marked by the high pressure region upstream of flap C as it reaches its tip edge (see instantaneous pressure field). Reducing the pressure and promoting flap C to accelerate downward to the negative x-axis direction allows a CCW vortex to detach from flap C tip edge, clearly shown at $t + 0.04$ s. Moreover, as vortex shedding period is the same as flap C oscillation and as the convective time between vortex detachment from flap A and interaction with flap C is small, the same periodic FSI is observed at the natural frequency of the flaps f_N, enhancing its motion. Interaction between vortices shed from flap B and flap D is the same as interaction between vortices shed from flap A and C previously described.

Alternated flaps C and D play then a major role in the interaction: as seen before, their downward oscillation allows forming new vortices at their tip that are convected downstream. As flap C gets to its minimum location near the channel wall, the vertical separation between flaps C and D becomes sufficiently large to expose flap D to the free stream velocity field. This leads to the formation of high stagnation pressure at flap D causing backward motion until its maximum amplitude level. From this maximum location, a clock-wise (CW) vortex forms at the tip of this flap which also merges with another co-rotating vortex shed from flap E (from $t_0 + 0.08$ s to $t_0 + 0.12$ s). The eddy of the merged pairs then gets larger until detachment at $t_0 + 0.12$ s. In addition, the potential energy stored in flap D at $t_0 + 0.08$ s and the CW vortex shed from flap B reaching flap D reduces the high pressure region and redirects the flow under it to flow in the gap region between flaps C and D. The CW vortex formed by flap D detaches and gets advected downstream away from the wall of flap D. These added effects consequently decrease the pressure difference between upstream and downstream of flap D and result in a restoring force opposite to the flow direction. The flap reaches its near wall minimum amplitude releasing two additional counter rotating vortices (seen at $t_0 + 0.20$ s). When flap D is in the process of reaching its minimum amplitude from $t_0 + 0.08$ s until approximately $t_0 + 0.20$ s, the flow passes through the gap region between flap C and D. Increasing forces apply thus on flap E due to the high pressure region upstream and forcing it reaching its maximum amplitude. A CCW vortex then forms and detaches from the tip of flap E and get merged with a previous vortex issued from the previous cycle of motion at $t_0 + 0.08$ s. Indeed, vortex previously shed from flap E at t_0 gets convected downstream. Because of the backward motion of flap D, this vortex is retained near flap E where a new one is in formation. From $t_0 + 0.16$ s to $t_0 + 0.24$ s, these two vortices formed on the same flap E then merge. As a result, a larger eddy forms at $t_0 + 0.20$ s which occupies a large area downstream flap E and being characterized by a negative pressure region.

Looking at motion of flap E, one can eventually observe that once reaching its maximum position, its starts to accelerate in the opposite direction leading to a significant negative-velocity region upstream, as seen by the velocity vectors plotted on the pressure field at $t_0 + 0.24$ s. This flow induces forces on the upstream flaps and participates to a backward interaction leading to an increase of amplitude of upstream flap C which is located on the same upper channel wall. This phenomenon

will also be highlighted in the next section: as studied configurations get increasing number of flaps (2, 3 or 4), the coupling between the fluid and the flexible structure gets stronger and leads to self-sustained motion of the ensemble.

These self-sustained and FSI motion can be hence thought as potential benefits for heat and mass transfer enhancement in situations where a laminar flow is confined and might be mixed up or thermally homogenized for industrial purposes like HEV-static mixer applications [Habchi et al., 2010a, Ghanem et al., 2013a]. Indeed, vortices shed by the flaps merge with co-rotating vortices produced by another structure or even by the same structure but from a previous oscillation cycle (see previous comments about vortex development on flap E). These vortex productions and pairings produce high-strength vortices which correspond to a constructive mode described by Gopalkrishnan *et al.* [Gopalkrishnan et al., 1994] and are known to improve heat and mass transfer.

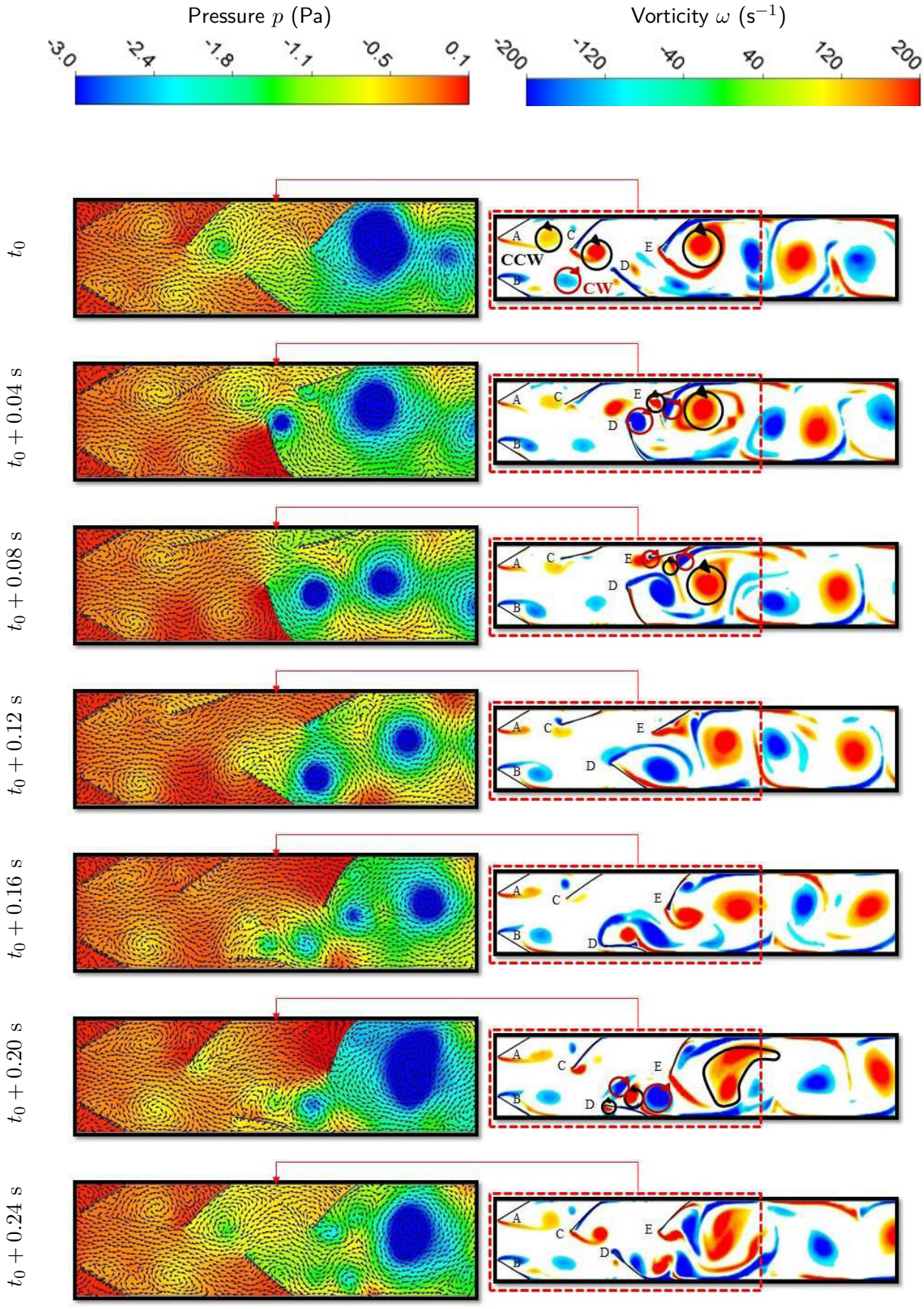

Figure 4.4: Snapshots of vorticity (right side) and pressure distributions (left side) in the 2CP-3FVG case. Velocity vectors are plotted on the pressure field

4.4.3 Structural analysis

In this section, the motion of the flexible flaps is investigated. Figure 4.5 (I) shows the flap oscillation amplitudes for the different cases studied with respect to the dimensionless time τ defined as:

$$\tau = \frac{t\overline{U}_{f,inlet}}{H} \tag{4.13}$$

where t is the dimensional time. The flaps in all the cases oscillate at their fundamental frequency ($f = f_N = 4.8$ Hz) as shown in the FFT of the x-displacement signal in Figure 4.5 (II).

An important feature of this system, is that when the number of alternating flaps increase, one can notice that the upstream flaps get affected by the added downstream ones. In fact, in the 0CP-2FVG and 0CP-3FVG cases (respectively Figure 4.5 (Ia) and (Ib)), adding a flap E increases drastically the amplitudes of the upstream flaps C and D. Flap C amplitude increases from 0.01 mm in the 0CP-2FVG case to 0.79 mm in the 0CP-3FVG case. Also, flap D amplitude increases from 0.05 mm in the 0CP-2FVG case to 3.94 mm in the 0CP-3FVG case. The same holds when adding a flap F and the effect produced on the upstream flaps when comparing the 0CP-4FVG and the 0CP-3FVG case. This effect was previously explained based on flow stream considerations in Section 4.4.2: flaps attached to the same wall induce a reversed flow effect when moving in the opposite streamwise direction that eventually produces additional forces on the upstream flaps and eventually increases amplitudes. Figure 4.5 (I) also shows that flaps located at the same channel wall oscillate in phase with each-others whereas they behave out of phase with the ones located at the opposite wall.

Introducing two co-planar flaps as in the 2CP-2FVG and 2CP-3FVG cases (respectively Figure 4.5 (IId) and (IIe)) also increases the amplitudes of flaps C, D and E in comparison to 0CP-2FVG and 0CP-3FVG cases. For example, flap C amplitude increases from 0.01 mm in the 0CP-2FVG case to 1.99 mm in the 2CP-2FVG case whereas flap E amplitude increases from 5.91 mm in the 0CP-3FVG case to 10.07 mm in the 2CP-3FVG case. Indeed, as the velocity of the fluid increases due to the more confined area between tips of flaps A and B, fluid forces become higher downstream. This makes flaps C and D reach the lock-in state, where the fluid forces supply energy to the structure as opposed to the case 0CP-2FVG where the structural oscillations are damped. It is also important to note that in all the simulations, the last flap in the channel exhibits the largest oscillation amplitude as the motion of this flap is not restricted by a narrower flap downstream.

To better highlight the correlation between the fluid forces and the flap motions, we present in Figure 4.6 the averaged normalized streamwise fluid forces D/D_0 where D_0 is the drag force computed by performing a steady-state simulation on a channel containing a single rigid flap C. The drag force D is then defined as:

$$D = \int_A (pcos\theta + \tau_D sin\theta)\, dA \tag{4.14}$$

where θ is the angle between the pressure force (normal to the flap wall) and the channel wall, dA is the elemental area of the flap and τ_D is the wall shear stress. For all the depicted cases in Figure 4.6, one can see the added downstream flaps experience higher drag forces than the upstream bodies because downstream flaps oscillate in the oscillating wake of the upstream ones.

This resonance effect drives the amplitude to increase, resulting in higher drag forces for the downstream bodies, similar to the inverted drafting phenomenon [Ristroph and Zhang, 2008]. Furthermore, considering the 0CP-2FVG compared to its relative co-planar case the 2CP-2FVG, we can observe in Figure 4.6 (a) a drop in the average drag on both flaps C and D for the co-planar case, although their amplitudes increase as illustrated in Figure 4.6 (b). This is explained by the fact, that in the 0CP-2FVG these flaps maintain the same frontal area, as their oscillations are negligible, however when adding two co-planar flaps, flaps C and D display larger amplitude and approximately half of their motion time they exhibit a reduced frontal area when they oscillate in negative x-axis direction and approach the channel wall and benefit from the drafting effect imposed by the upstream co planar flaps. This has a great effect on reducing their drag when compared to the approximately constant frontal area in the 0CP-2FVG case. Also adding flaps has a significant effect on increasing the amplitude of the upstream ones and the increase of drag also. The co-planar case 2CP-3FVG

shows the highest drag and amplitude values as the condition created by the co-planar flaps is to increase the fluid velocity in the restricted area upstream.

Finally, making a flexible material oscillate at its fundamental frequency may cause a break if forces applied on it get higher than the maximum yield strength allowable (static damage) or may cause fatigue damage when using them for long-use cycles, however. The study performed here only deals with static constraints applied on the structure by the hydrodynamic forces in order to show whether the rubber-like flaps can be damaged. Further investigations would still be necessary to study stress fatigue due to long time use cycles but it is not the aim of the present work since it attaches to analyze self-sustained oscillations produced by FSI in a laminar confined flow. The structural material used in these simulations has mechanical properties similar to silicone rubber materials' which are characterized by a yield strength of approximately 4 MPa. According to the maximum shearing stress theory, which is in widespread use because of its easy use and can offer a conservative result in design [Ugural and Fenster, 2003], yielding is expected to start when the maximum shearing stress of the material equals the maximum shear stress at yielding in a simple tension test. Failure thus occurs when:

$$\tau_{s,max} = \frac{\sigma_1 - \sigma_2}{2} \geqslant \tau_{yp} = \frac{\sigma_{yp}}{2} \tag{4.15}$$

where $\tau_{s,max}$ is the maximum shear stress, σ_1 and σ_2 are the principal stresses, τ_{yp} is the maximum shear stress at yielding and σ_{yp} is the yielding strength of the material.

Variations of the maximum shear stress in the solid domain (the maximum between all the flaps in a given case at a given instant) has thus been processed and shows an increase of the maximum shear stress in relation to the increase in the number of alternating flaps and introduction of co-planar ones. The bending moment at the base of each flap displays the highest values where the failure might occur. The maximum shear stress value of 0.074 MPa is found in the 2CP-3FVG case for which the flaps undergo the highest oscillation amplitudes and drag forces is much less than 2 MPa, i.e. $\sigma_{yp}/2$, leading to a safe static design with respect to all cases studied according to the failure criterion given by Eq. 4.15.

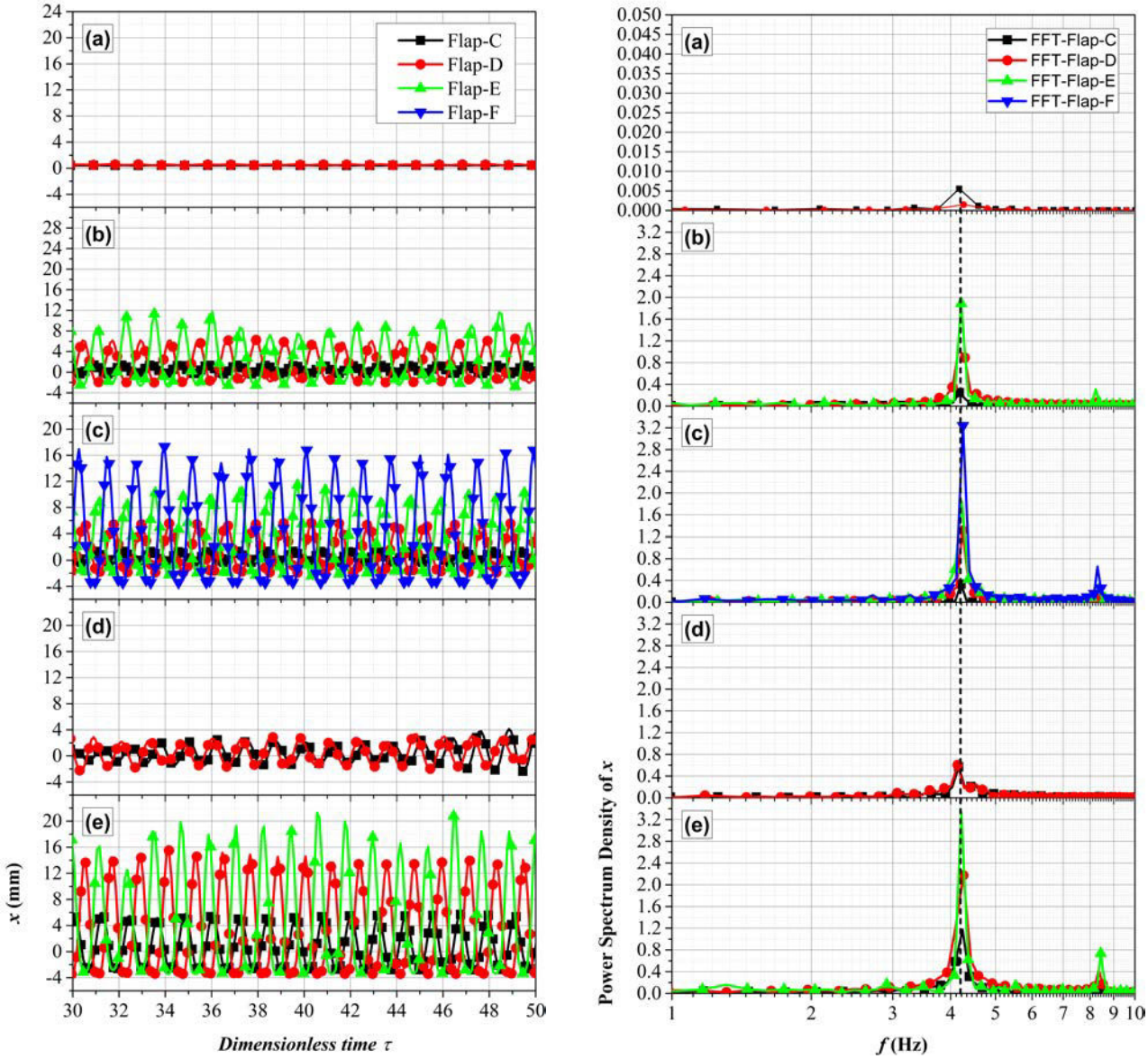

(I) (II)

Figure 4.5: (I) Structure oscillations in x direction for cases (a) 0CP-2FVG, (b) 0CP-3FVG, (c) 0CP-4FVG, (d) 2CP-2FVG and (e) 2CP-3FVG as a function of time. (II) Power spectra density of each flap displacement for cases (a) 0CP-2FVG, (b) 0CP-3FVG, (c) 0CP-4FVG, (d) 2CP-2FVG and (e) 2CP-3FVG

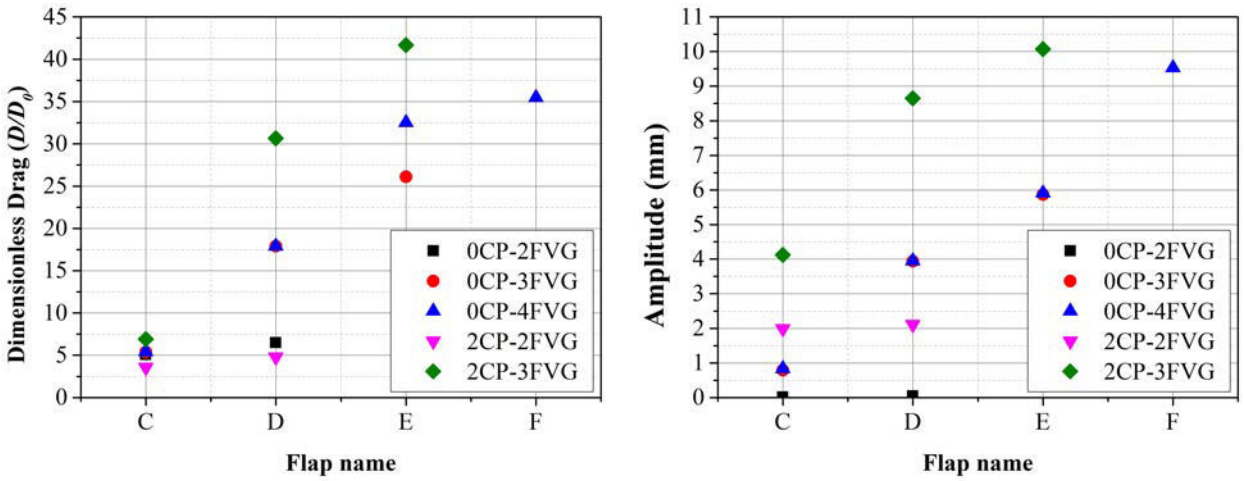

(a) (b)

Figure 4.6: (a) Average normalized streamwise fluid forces D/D_0 and (b) amplitude in mm of each flap for all the cases studied

4.5 Conclusion

This study aimed at analyzing possibility to produce self-sustain oscillations of flexible flaps located in a confined two dimensional channel in a passive way (without adding external energy use except hydroynamic forces). Flow pattern and structural analysis of multiple freely oscillating flaps have been investigated by simulating five cases of flexible flaps located in a two dimensional laminar flow. Three of these cases consist of alternating flaps separated by a distance equal to their length, the other two cases being similar with the introduction of two co-planar flaps upstream. All the cases shared the same Reynolds number of 2000 and were carried out by a strong coupling fluid structure interaction method by using ANSYS Mechanical (CSD solver) and ANSYS Fluent (CFD solver). The fluid flow was solved using an Arbitrary Lagrangian Eulerian (ALE) formulation by taking into account large deformation across the fluid-structure interface. An automatic local remeshing method was thus used to avoid distortion of the fluid mesh.

By analyzing the simulated flow pattern for the alternating flaps with the absence of co planar flaps, we noticed that a minimum of three alternating flaps is needed to produce self-sustained large amplitude oscillations in the channel. The addition of a downstream flap changed drastically the pressure distribution on the upstream ones. Indeed, the displaced fluid from the downstream flap oscillating in the opposite streamwise direction influences the upstream ones that undergo a reversed flow effect. It then induces higher forces altering motion behaviors and increasing FVG displacement amplitudes. As a result, various vortex-to-flap interactions are observed, where the vortices shed by a flexible structure merge with the vortices of the same rotational sense produced by another structure or even by the same structure (but from a previous cycle of oscillation). This act of merging produces vortices of high strength improving hydrodynamic forces applied on FVGs. Furthermore, when adding co-planar flaps upstream, the velocity is increased due to the stream area reduction. Fluid forces are thus increased and eventually lead in higher amplitude oscillations of the downstream flaps. Finally, an increase in the number of flaps allows reaching the lock-in state regime. This is of great interest when designing such process because the reduced velocity parameter does not have to be included within the lock-in region range because as the number of flaps increase, the interaction between flow and the structural oscillations leads eventually to lock-in for all the flaps in the channel. A failure study has been eventually conducted on all the cases and results show that the design is safe according to the maximum shear stress theory. Additional work might however be carried out to analyze potential fatigue damage due to long cycle use. Finally, such configurations, optimized in terms of flap shapes and locations in the channel can significantly improve vortex formation and might have significant applications in mixing and heat transfer enhancement using vortex generators.

Chapter 5

Heat transfer and mixing enhancement by using multiple freely oscillating flexible vortex generators

5.1 Introduction

Heat and mass transfers in chemical engineering processes are useful for various industrial applications and this enhancement have been widely studied through scientific works in order to assess the best performances through optimized system designed with more compact heat exchangers geometries, higher efficiency or lower weight [Anxionnaz et al., 2008]. In such applications, the thorough control of the flow allows destabilizing the stable shear layers, disrupting the growth of the boundary layer, increasing the turbulence intensity by generating a secondary flow, modifying the pipe geometry or introducing additives in the fluid for instance [Webb, 1994, Fiebig, 1998]. These actions eventually aim at enhancing heat transfer or mixing quality.

Rigid vortex generators (RVG) are one of the successful passive method used in this area as they can generate intense longitudinal vortices that can disrupt the flow with low penalty of pressure drop [Allison and Dally, 2007, Zeng et al., 2010, Habchi et al., 2012, Yakut et al., 2005b]. Fluid swirling causes convective exchanges of the wall fluid towards the core fluid and is deemed to increase the heat transfer between the flowing fluid and the pipe walls.

Intensive works investigated the influence of several parameters related to vortex generators in order to optimize the heat and mass transfer by varying their shapes, number of rows and relative distance from the duct or from each other. For example, Depaiwa *et al.* [Depaiwa et al., 2010] experimentally studied the effect of adding ten pairs of rectangular winglet vortex generators (WVG) in a solar air heating system, also taking into consideration the angle of attack by studying two different arrangements, by pointing upstream (PU) or downstream (PD) the flow with various angles ($30°$, $45°$, $60°$). They concluded that the largest angle of attack ($60°$) of the PD-WVGs yields the highest increase in Nusselt number and friction factor while the angle of $30°$ in the PU-WVGs showed the best thermal performance among all the cases. In addition, Habchi *et al.* [Habchi et al., 2010b] investigated configurations in which several tab arrays were aligned as in the conventional high efficiency vortex system (HEV), alternated from one another or reversed compared to the standard HEV geometry. The results showed that the reversed tab arrays give better efficiency in meso- and micro-mixing than the aligned and alternated arrays but show higher pressure drop. Nevertheless, Ma *et al.* [Ma et al., 2010] investigated the fluid flow and the convective heat transfer in a rectangular channel with either four longitudinal rigid vortex generators or not. They observed that the RVG could greatly improve the heat transfer rate by about 101% with an increase of pressure drop of

Note to reader: chapters 4, 5 and 6 were written in a format corresponding to the preparation of articles to be submitted in scientific journals. References are grouped at the end of thesis manuscript, however some repetitions may appear in these three chapters.

only 11% in the laminar flow regime. In the turbulent regime however, the RVG causes heat transfer enhancement of about 87% with an increase of pressure drop of about 100%.

In opposition to VG passive methods for flow control, active techniques can be used to promote high heat transfer and mixing properties. Indeed, active methods offer an additional flexibility by using an external force that can allow oscillations of the VGs at controlled frequencies and amplitudes. Lambert and Rangel [Lambert and Rangel, 2010] thus studied the role of thin elastic flaps to enhance fluid mixing in a microchannel where the flaps are actuated using an external surface load. The results show that the highest mixing fractions are obtained with larger flaps displacements and the addition of multiple flaps can further enhance mixing if the flaps oscillate out of phase with a phase angle of $\pi/2$. In addition, Yang [Yang, 2003] numerically investigated the unsteady flow and heat transfer in a channel with a squared bar placed in the middle and forced to oscillate normally to the inflow. The influence of Reynolds number, maximum oscillating speed, oscillating amplitude and oscillating frequency of the bar on flow and heat transfer were examined. The results reveal an efficiency index greater than 1 for all cases when compared to their relative stationary vortex generator. Furthermore, Yang and Chen [Yang and Chen, 2008] carried out numerical simulations to study the effect of a transversely oscillating cylinder on a transient flow with heated blocks located along one of the channel wall. They found that heat transfer is greatly enhanced when a resonance effect occurs between the flow and the oscillating cylinder that is to say when frequency oscillations get the same for both the cylinder and the vortex shedding. This phenomenon is called the lock-in regime. The same conclusions were also found by Fu and Tong [Fu and Tong, 2002] who performed numerical simulations and investigated the heat transfer from a heated oscillating cylinder in cross flow. Eventually, Mirzae *et al.* [Mirzaee et al., 2012] carried out numerical simulations of a 2D channel with one oscillation-controlled flap mounted on an inner wall, and compared the thermal performances between a flexible flap and a rigid one. Not only the thermal performances are increased in the flexible flap case, but also this flexible flap induces a lower pressure drop.

Based on the conclusions drawn by these previous works, we proposed a new concept to enhance heat transfer and mixing by using freely oscillating flexible vortex generators (FVGs) [Ali et al., 2015]. This system aims at taking both benefits from the simplicity of implementation of VGs (passive methods) and the structural oscillation that has been shown to improve heat and mass transfer (as in the active methods but without relying on an external source of energy). Here, FVG displacement is naturally controlled by the dynamic forces applied due to the pumping power of the fluid alone. The configurations studied previously consist of two co-planar FVGs followed by two alternating FVGs located at the opposite walls of a two dimensional channel. Flow regime was laminar with two investigated Reynolds number fixed at 1000 and 1850. The role of the co-planar FVGs is to destabilize the flow upstream and generate vortices that act as periodic forces on the alternating FVGs downstream. The results were then obtained comparing these flexible configurations to the corresponding cases with rigid vortex generators instead. An increase of the mixture quality up to 86% was observed and the heat transfer enhancement displayed an increase up to 56% using the thermal performance factor criterion with a 134% increase in the overall heat transfer. Hence, improving heat and mass transfer performances has been validated on the cases studied without controlling the flaps but allowing their motion based on the fluid forces in laminar flow regimes. This being said, numerical simulations were further carried out on FVG cases in a two dimensional laminar channel flow at Reynolds number of 2000 (based on the hydraulic diameter of the channel) in order to dynamically investigate the flow behavior and the fluid-structure interactions [Ali et al., 2016]. Increasing the degree of freedom of the whole system was thus performed by increasing the number of alternating FVGs and destabilizing the flow upstream by introducing two co-planar FVGs. The results showed that increasing the number of alternating FVGs in the channel has a reverse effect on the upstream FVG, increasing their motion amplitude. When inserting at least three FVGs, a lock-in state takes place between the flow and the flexible structures, and leads to higher amplitude oscillations as shown in other studies. As far as adding upstream co-planar FVGs is considered, the blocage effect of the flow stream and the vortices production upstream lead to higher oscillation amplitudes when compared to the cases whithout co-planar FVGs.

In the present study, we propose to analyze the influence of the FVGs number and positions on

heat transfer and mixing properties by using numerical coupled fluid-structure interaction simulations. To this aim, the numerical procedure already validated and used before is briefly presented first in section 6.2 with a specific focus on heat and mass equation resolutions. Section 6.4 depicts then the different configurations studied and the associated results are discussed in section 6.7. Finally, section 5.5 is dedicated to concluding remarks.

5.2 Mathematical formulation and numerical procedure

Fluid-structure interaction problem is numerically performed as we previously operated [Ali et al., 2015, Ali et al., 2016] using the ANSYS Fluent CFD-solver and the ANSYS Mechanical CSD-solver [ANSYS, 2015].

Briefly, the flow field is governed by the unsteady Navier-Stokes equations for an incompressible viscous laminar flow and are solved in an Arbitrary Lagrangian-Eulerian (ALE) formulation to take into account the deforming mesh [Donea et al., 2004]. The ALE formulation of the Navier-Stokes equations reads:

$$\nabla \cdot \mathbf{u_f} = 0 \tag{5.1}$$

$$\frac{\partial \mathbf{u_f}}{\partial t} + (\mathbf{u_f} - \mathbf{u_{m,f}}) \cdot \nabla \mathbf{u_f} = -\frac{\nabla p}{\rho_f} + \nu_f \nabla^2 \mathbf{u_f} \tag{5.2}$$

where $(\mathbf{u_f} - \mathbf{u_{m,f}})$ is the convective term with $\mathbf{u_f}$ the fluid velocity and $\mathbf{u_{m,f}}$ the mesh motion velocity in the fluid domain. The pressure is denoted by p, the density of the fluid by ρ_f and the kinematic viscosity by ν_f.

The mass transport equation of a scalar c is considered to study the effect of the elastic flap deformations on fluid mixing:

$$\frac{\partial c}{\partial t} + \nabla \cdot ((\mathbf{u_f} - \mathbf{u_{m,f}})\, c) = D_m \nabla^2 c \tag{5.3}$$

where D_m is the mass diffusivity of the scalar c. Here, the convective scalar mixing is only considered so mass diffusion term is set to 0.

The energy equation is also solved in the fluid domain and is given by:

$$\frac{\partial}{\partial t}(\rho_f E) + \nabla \cdot ((\mathbf{u_f} - \mathbf{u_{m,f}})(\rho_f E + p)) = \nabla \cdot (k \nabla T) \tag{5.4}$$

where E is the total energy and k is the thermal conductivity.

The equation of motion for an elastic isothermal solid structure can be described from a Lagrangian point of view, i.e. in terms of the initial configuration at time $t = 0$, and it reads:

$$\rho_s \frac{\partial^2 \mathbf{d_s}}{\partial t^2} = \nabla \cdot \left(\Sigma \cdot \mathbf{F^T}\right) + \rho_s f_b \tag{5.5}$$

where $\mathbf{d_s}$ is the displacement of the structure, f_b is the resulting body force, ρ_s is the density of the structure and **F** is the deformation gradient tensor given by:

$$\mathbf{F} = \mathbf{I} + \nabla \mathbf{d_s^T} \tag{5.6}$$

where **I** is the identity.

The second Piola-Kirchhoff stress tensor Σ is related to the Green Lagrangian strain tensor **G** following [Tukovic and Jasak, 2007, Bos, 2010b]:

$$\Sigma = 2\mu_s \mathbf{G} + \lambda_s tr(\mathbf{G})\, \mathbf{I} \tag{5.7}$$

with **G** given by:

$$\mathbf{G} = \frac{1}{2}\left(\mathbf{F^T} \cdot \mathbf{F} - \mathbf{I}\right) \tag{5.8}$$

Here *tr* is the tensor trace, λ_s and μ_s are Lamé constants which are characteristics of the elastic material. They are linked to the Young modulus E and Poisson's coefficient ν_s by:

$$\lambda_s = \frac{\nu_s E}{(1+\nu_s)(1-2\nu_s)} \tag{5.9}$$

$$\mu_s = \frac{E}{2(1+\nu_s)} \tag{5.10}$$

The present study employs the Laplace smoothing equation as third coupled solver for automatic internal remeshing, while maintaining the quality and validity of the resulting mesh. The remeshing method used in this study is the $2.5D$ surface remeshing. It agglomerates cells that violate the skewness or size criteria and locally remeshes bad quality cells. A maximum cell skewness of 0.7 has thus been fixed with cell size criterion depending on the minimum and maximum length scale of the mesh.

The global procedure can be described as follows: at each time step, the FSI iteration loop sequentially calls the structural solver, the mesh motion algorithm and then the fluid solver until the convergence limits for displacements and forces are reached. An under-relaxation factor for both displacement and force is set to unity for all the simulations performed and convergence criteria set to 10^{-4} on force and displacement. The pressure-velocity coupling is established using the Coupled algorithm [ANSYS, 2015]. The convergence criteria for pressure, velocity, energy and scalar are set to 10^{-6}. The Laplace mesh smoothing convergence criterion is set to 10^{-4}. Temporal discretization is performed using a first order implicit scheme and the time step used for all the present simulations is set to 10^{-4} sec.

The overall procedure has already been validated and more details can be found in Ali *et al.* [Ali et al., 2015].

Eventually, when simulating configurations with rigid vortex generators where FSI does not apply, only the ANSYS Fluent CFD-solver is activated with the above-mentioned parameters kept identical.

5.3 Problem description

In this section, the computational domain which consists of a two-dimensional flow in a channel and both the boundary and initial conditions are presented, followed by the mesh validation study.

5.3.1 Geometry, initial and boundary conditions

The computational domain is two-dimensional and consists of several elastic flaps inclined with an angle $\beta = 30°$ to the walls as shown in Figure 6.1. Two different designs are studied. The first ones named 0CP-xFVG with x varying from 2 to 4 and stands for the number of alternating successive flaps placed at the channel walls as shown in Figure 6.1 (a), (b) and (c). The second design is similar but 2 co-planar flaps are introduced upstream of the alternating ones and thus get the names 2CP-xFVG as depicted in Figure 6.1 (d) and (e). Flaps C, D, E and F in all the cases have the same length of 30 mm separated by a distance equal to their length and with a thickness e reported in Table 6.1 whereas the co-planar flaps have a length of 25 mm. The hydraulic diameter $D_h = 2H$ is the length taken for flow between two parallel plates [Bejan and Kraus, 2003] and $H = 54$ mm is the channel height. The flexible vortex generators cases (FVG) are compared to their relative rigid vortex generators (RVG) cases using rigid flaps instead of elastic ones.

No slip boundary conditions are set on the top and bottom walls. The outlet is set at zero pressure and Neumann zero for velocity. A parabolic laminar velocity profile corresponding to a fully developed channel flow is set at the flow inlet.

To characterize the mixing process within the channel, a passive scalar transport equation is solved (Eq. (6.3)). The fluid domain is initially divided in two equal parts: the scalar at the upper part $(y > H/2)$ is set to $c = 1$ whereas $c = 0$ at the lower part $(y \leq H/2)$. Zero flux boundary conditions are prescribed for the mass transport equation along the walls and the rigid/flexible flaps.

To characterize the heat transfer process, the same conditions are imposed for all the FVG and RVG cases with a uniform wall temperature $T_w = 360$ K at the top and bottom walls of the channel. The laminar parabolic velocity profile is prescribed at the inlet with uniform inlet temperature $T_{in} = 300$ K. Both the rigid and flexible flaps are treated as insulated material with zero heat flux along them.

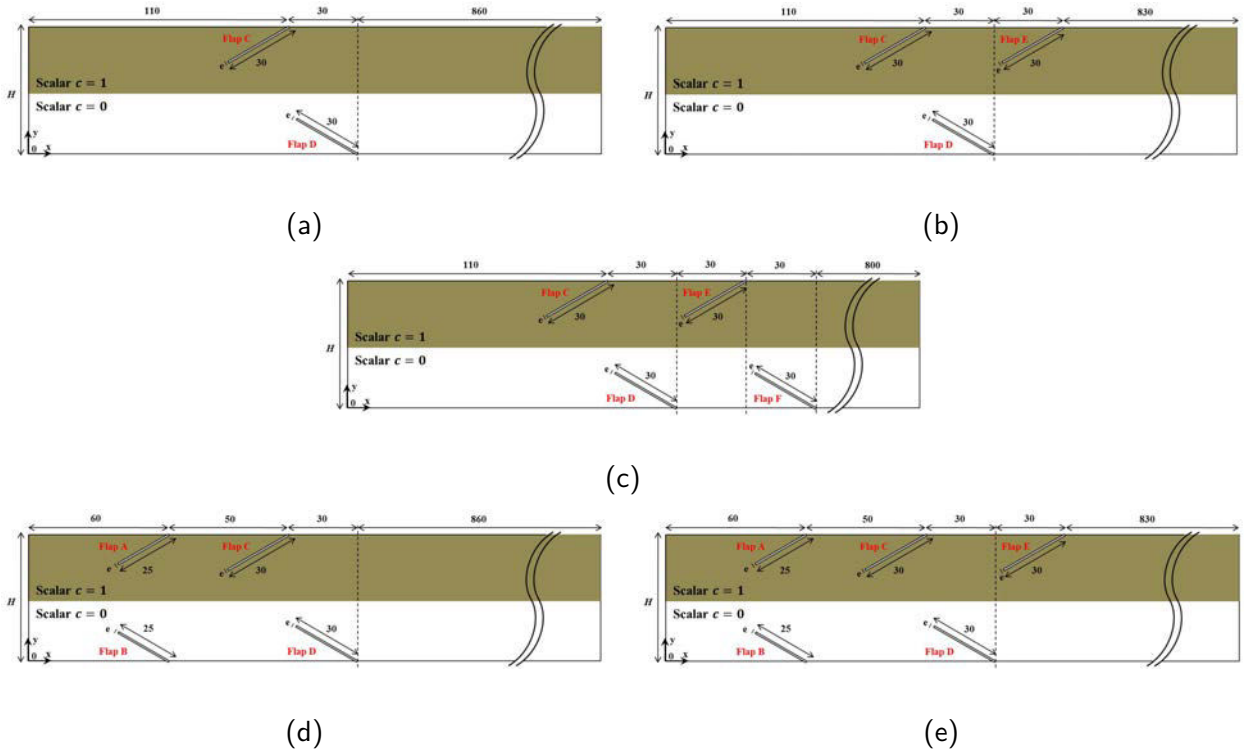

Figure 5.1: Computational domain and boundary conditions for the studied cases (dimensions are in mm, flow goes from left to right) as follows: (a) 0CP-2FVG, (b) 0CP-3FVG, (c) 0CP-4FVG, (d) 2CP-2FVG and (e) 2CP-3FVG

Table 5.1: Physical parameters and flow conditions for all cases

Cases	ρ_s (kg/m^3)	ν_s	E (Pa)	e (mm)	H (mm)	$Re_{D_h} = (\overline{U}_{f,inlet} D_h)/\nu_f$
FVG	1200	0.4	5×10^6	0.75	54	2000
RVG	1200	-	-	0.75	54	2000

5.3.2 Mesh validation

A grid size independence study for the FSI simulations is conducted on the case 2CP-3FVG for which the elastic flaps undergo the highest displacement amplitudes. The fluid domain is thus discretized with three initial different mesh sizes using triangular cells, refined at the wall and at the fluid-solid interfaces. During the FSI simulations, automatic mesh adaptation is performed to remesh the volume due to mesh distortion depending on the motion and behaviour of the flaps as shown in Figure 5.2. Moreover, the fluid mesh is refined at the centerline of the domain at a position $y = H/2$, where the two scalar fields ($c = 0$ and $c = 1$) are separated, in order to minimize the fake mixing due to numerical interpolation. The total cell number and the overall mean cell size were found to be almost constant during the simulations . The three mesh densities and their main characteristics are summarized in Table 6.2.

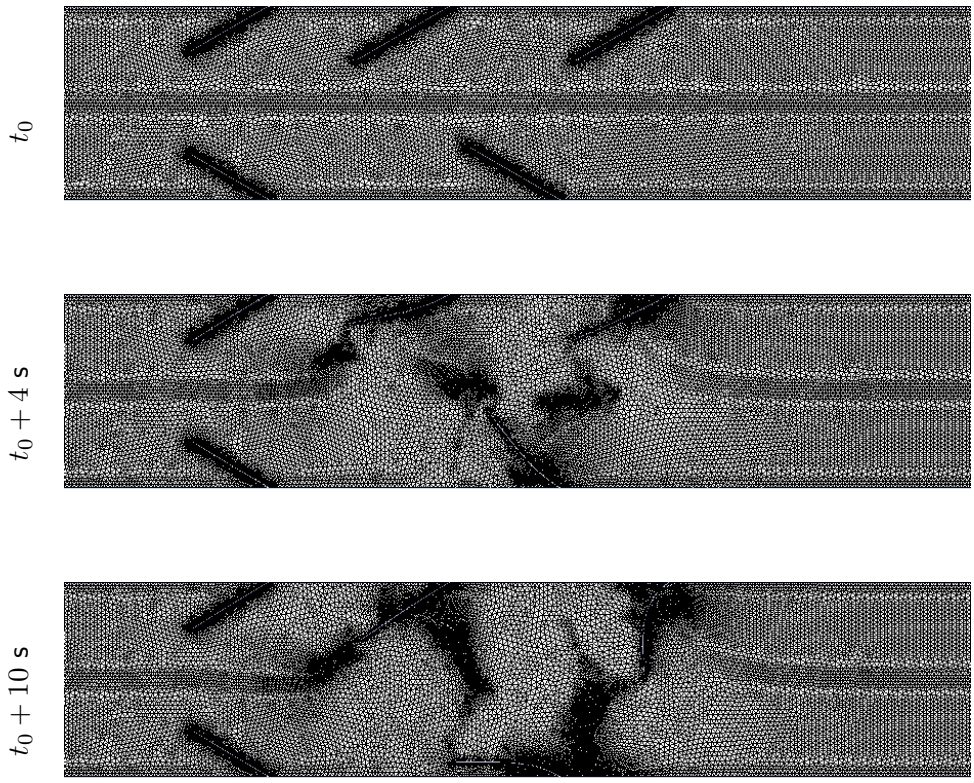

Figure 5.2: Snapshots of dynamic mesh at different time steps

Table 5.2: Global meshes characteristics used for grid size independance study

▪	Mesh 1	Mesh 2	Mesh 3
Initial number of cells (N)	19437	47592	95360
Grid size $h = \left[\frac{1}{N}\sum_{i=1}^{N}(\Delta A_i)\right]^{\frac{1}{2}}$	16.77×10^{-4}	10.65×10^{-4}	7.53×10^{-4}
Grid refinement factor $r = h_i/h_j$	-	$h_2/h_1 = 1.56$	$h_3/h_2 = 1.42$

where ΔA_i is the area of the i^{th} cell.

To determine the appropriate mesh density for grid size independence, the simulations are performed on increasing mesh densities. The mesh validity verification is based on the method proposed by Celik *et al.* [Celik et al., 2008] where the grid convergence index (GCI) and the apparent order of convergence (p_c) can be obtained. Since the heat transfer strongly depends on the near-wall refinement and the flaps oscillation amplitude depends on the refinement near the fluid-solid interface, the Nusselt number and the amplitude of oscillations of flap E are chosen for the mesh validity verification.

The signal of the displacement being quasi-periodic, the mean amplitude (MA) of flap E is calculated by:

$$\mathrm{MA} = \frac{1}{n}\sum_{i=1}^{n}|x_{i_{peak}} - x_{mean}| \tag{5.11}$$

where n is the number of maximum and minimum peaks in the signal, $x_{i_{peak}}$ are the individuals maximum and minimum values and x_{mean} is the mean displacement. The amplitude calculation is performed from $t_1 = 4$ seconds (the time step at which stable regime is reached) till $t_2 = 10$ seconds (the final instant) in order to avoid taking into consideration the transitional time before reaching

fully stabilized regime.

The time-averaged local Nusselt number $\overline{\mathrm{Nu}}(x)$ at $X^* = x/H$ in the channel is defined by:

$$\overline{\mathrm{Nu}}(x) = \frac{1}{t_2 - t_1} \int_{t_1}^{t_2} \frac{q''_w(x,t) D_h}{k\,(T_w - T_b(x,t))} dt \tag{5.12}$$

where q''_w is the average heat flux of the top and bottom walls, k is the thermal conductivity of air, T_b is the bulk temperature defined by:

$$T_b(x,t) = \frac{\int_0^H U(x,y,t) T(x,y,t) dy}{\int_0^H U(x,y,t) dy} \tag{5.13}$$

The results obtained from applying the method of Celik *et al.* [Celik et al., 2008] are summarized in Table 6.3, where $\phi_{refined}$ is the variable calculated from the solution of the refined mesh, ϕ_{ext} is the extrapolated variable and e_a^{23} is the relative error between Mesh 3 and Mesh 2. Extensive information about the calculation of these parameters can be found in Celik *et al.* [Celik et al., 2008]. It can be concluded from Table 6.3 that the uncertainty in the fine-grid solution is about 0.86% for the displacement amplitude of flap E and about 0.69% for the integrated Nusselt number (along all the channel length, i.e. from X^*=0 to X^*=18.5). The refined Mesh 3 can thus be used as a reference mesh density for the flexible vortex generator configurations.

Table 5.3: Estimated order of convergence p and GCI for refined Mesh 3

Parameter	$\phi_{refined}$	ϕ_{ext}	e_a^{23} (%)	p_c	GCI (%)
flap E amplitude (mm)	10.07	10.10	0.68	1.80	0.86
$\frac{1}{18.5}\int_0^{18.5} \overline{\mathrm{Nu}}_x dX^*$	45.49	45.70	0.55	1.76	0.69

5.4 Results and discussion

In this section, the flow topology is first depicted and the mixing quality of the passive scalar is then presented for the flexible and rigid flaps configurations. The effect of increasing the degree of freedom of the system by increasing the number of flexible alternating flaps, with the presence or absence of co-planar flaps placed upstream, on creating a higher displacement flapping motion and its impact on mixing performance is investigated. Furthermore, we investigate their corresponding heat transfer performance by studying the local and global Nusselt numbers and the thermal performance factors. For clarity and brevity of the article, exhaustive and full presentation of unsteady fields could not be reported here, but are more detailed in [Ali et al., 2016]. Supplementary materials can be found on the website version, however.

5.4.1 Flow pattern and vortex production

First, instantaneous fields of velocity magnitude are presented on Figure 5.3 for all the rigid cases. Unsteady behavior of the flow is almost unsignificant whatever the observed configuration, except in negligible small shear layer instability regions. For these rigid cases, velocity fields show that the major part of the fluid flows in the central part of the channel and is partly deviated due to the presence of the RVGs asymmetrically distributed along the channel walls. No vortex shedding is observed, only some recirculation zones upstream the rigid flaps, where a part of the main core flow is deviated by the presence of flaps and impacts the channel walls. Further downstream, momentum dissipation at the walls make the core flow go back to the channel center.

For the elastic cases, a previous work showed the potential of the unsteady dynamic flow produced by the fluid-structure interaction [Ali et al., 2016] as shown in Figure 5.4.

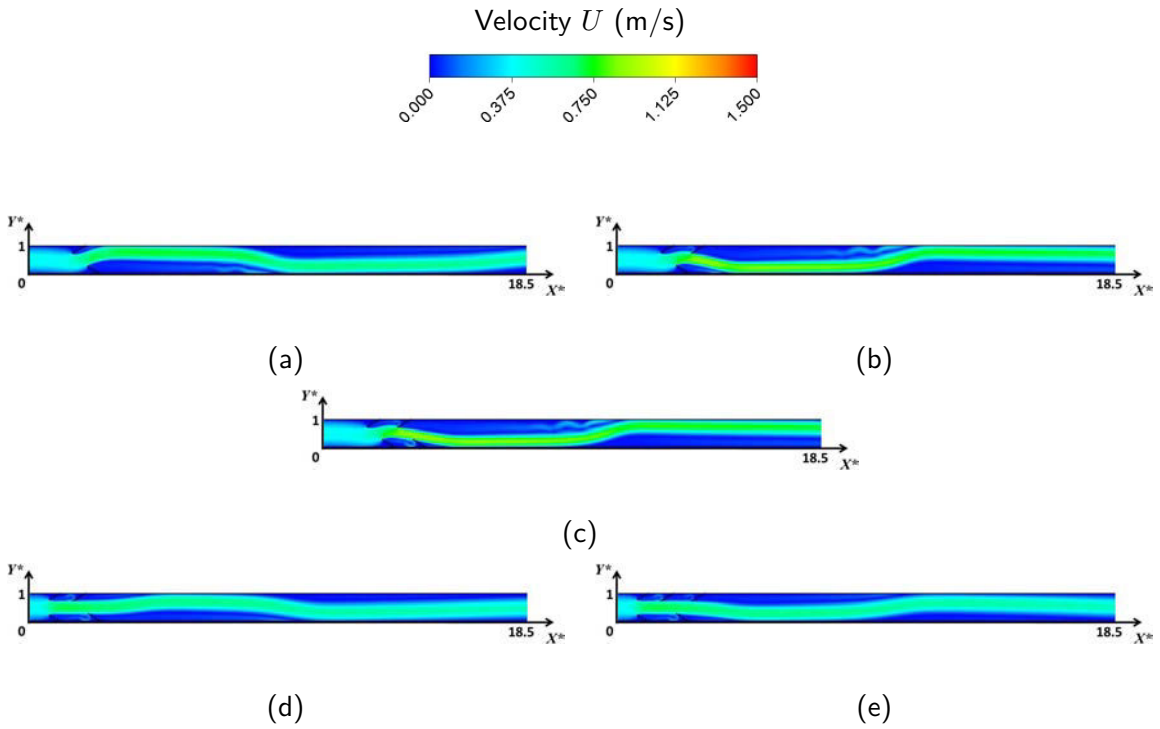

Figure 5.3: Steady fields of velocity magnitude U observed for rigid cases (a) 0CP-2RVG, (b) 0CP-3RVG, (c) 0CP-4RVG, (d) 2CP-2RVG and (e) 2CP-3RVG

From the first case 0CP-2FVG, one can observe that flap displacements are very limited due to a damping effect of the flow absorbing the energy instead of supplying it to the structure and eventually making the flaps oscillate with small amplitudes. Despite small oscillations, the flow becomes unsteady with vortex detachment phenomenon in the wake compared to the relative rigid VGs case. Hence, allowing the flap to oscillate, even in a limited way, has a big influence on flow behavior and can potentially benefit to heat and mass transfer performance. Furthermore, in order to achieve large amplitude oscillations of the FVGs, a minimum of three alternating flaps is needed when no co-planar flaps are placed upstream. The increase in the number of flaps actually produces a lock-in state between the flaps and the flow, and make them oscillate at their fundamental frequency, phenomenon known to greatly improve mixing and heat transfer properties due to the higher motion amplitudes [Lambert and Rangel, 2010, Fu and Tong, 2002, Khatavkar et al., 2007, Lambert et al., 2008]. Indeed, introducing successive alternated flap (cases 0CP-3FVG and 0CP-4FVG) changes drastically the pressure distribution on the upstream FVGs, especially when the downstream flap oscillates in the opposite streamwise direction and induces a reversed flow, leading to higher forces applied to the upstream FVGs. In addition, when introducing co-planar flaps in the upstream flow (cases 2CP-2FVG and 2CP-3FVG), velocity is increased due to the area restriction. It increases then the fluid forces which eventually results in higher amplitude oscillations of all the downstream flaps. As far as the flow is concerned, fluid-structure interaction strongly disturb the wake of the flaps with vortices shed by the flexible structures that merge with the vortices of the same rotational sense produced by an upstream FVG or even by the same FVG itself but from a previous cycle of oscillation. This act of merging, produces vortices of high strength. At each steamwise position normalized by the height of the channel $X^* = x/H$, both the mean absolute value and root mean square values of the time-averaged local vorticity $\overline{\omega}(x, y, t)$ normalized by $\overline{U}_{f,inlet}/H$ are plotted in Figure 5.5 (a) and (b) respectively. Indeed, looking at absolute values of mean vorticity allows analyzing the vortex strength and thus showing the intense heat transfer that can occur from the wall near the center of the channel and observing the fluctuating part of vorticity allows highlighting the mixing behavior within the channel.

Results globally show an increase in vorticity strength and fluctuating values when increasing

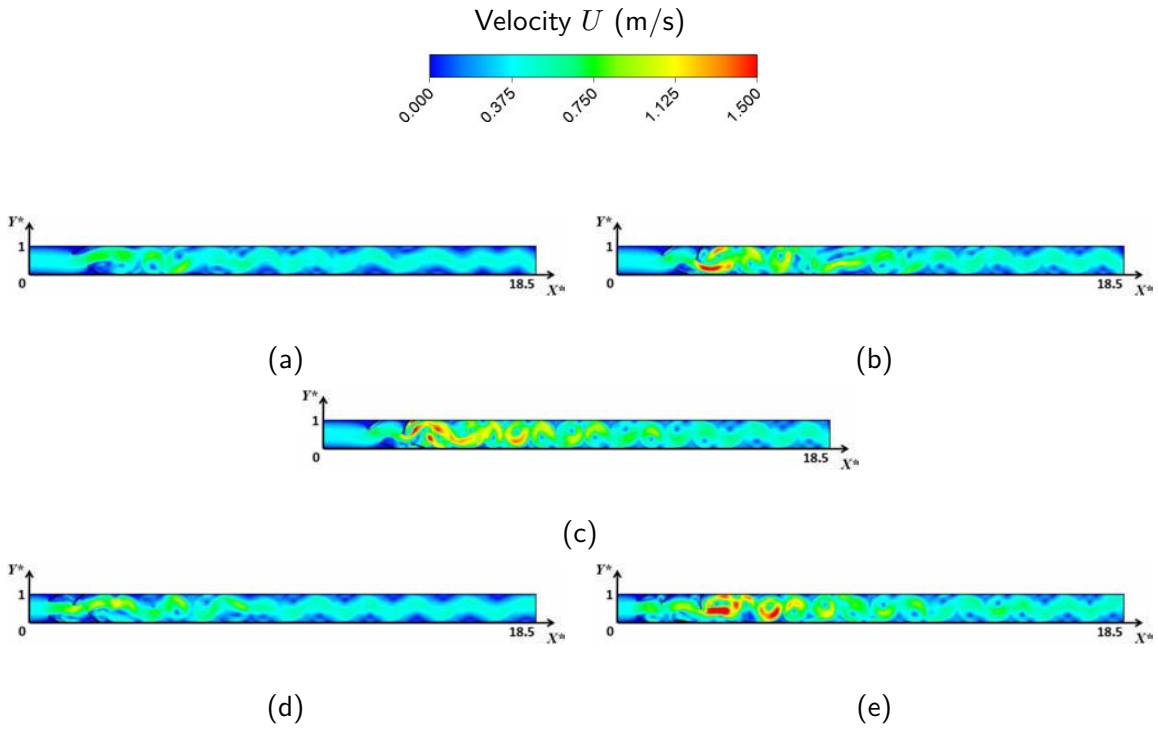

Figure 5.4: Snapshots of velocity magnitude U observed for flexible cases (a) 0CP-2FVG, (b) 0CP-3FVG, (c) 0CP-4FVG, (d) 2CP-2FVG and (e) 2CP-3FVG

the number of flaps in the channel as the amplitude of FVG oscillations increases and stronger vortices are formed downstream. Behind the last flaps, vortices are convected and then dissipate, making the mean and fluctuating values decreasing for all the cases. Hence, as the mass and energy transfers greatly depend on the vortex strength [Fiebig, 1998, Ahmed et al., 2012, Bejan and Kraus, 2003, Habchi et al., 2010a], the high vorticity produced in the laminar flow are thus expected to play an important role in mixing and heat transfer using the FVGs.

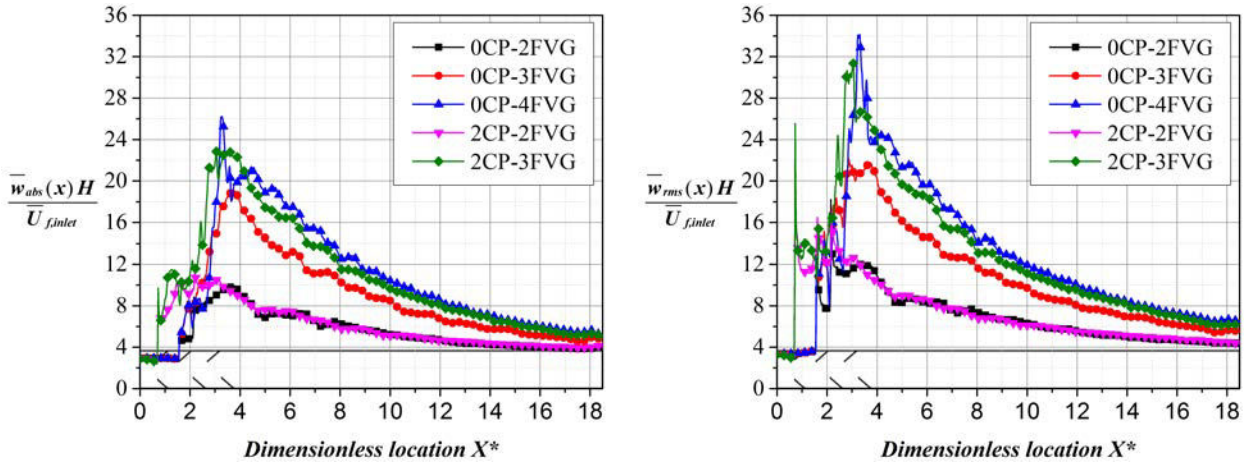

Figure 5.5: Streamwise variation of the time-averaged local vorticity for the FVG cases: (a) mean absolute and (b) root mean square (rms)

5.4.2 Mixing performance

This section relates to the mixing process analysis. First and as previously reported in section 6.4, the computational domain is initially divided into two equal spaces with two different values of scalar c as initial conditions that further mix together according to flow and flaps motions.

Section 5.4.1 presented the flow topology observed for the rigid cases. This kind of flow is particularly undesirable in the process of mixing: the reagents located in the high velocity regions are expected to exit the mixer faster and eventually will not be interacting. This is clearly demonstrated in Figure 5.6 as the two scalar values are deviated with the flow for the rigid cases but keep separated with the $c = 1$ in the upper part of the channel and $c = 0$ in the lower part similarly to their initial partition.

Figure 5.7 shows then instantaneous fields of the scalar c for the flexible cases. Qualitatively speaking, a sequence of periodic vortices is shed from the tip of each flap, due to the shear layer instability between the high momentum fluid in the bulk region and the low momentum fluid in the wake of the flaps. Figure 5.7 (a), for case 0CP-2FVG, shows a sinusoidal-like oscillatory motion that extends from the upper to the lower wall areas. The lobe-like structures formed in this case display areas of poor mixing. The addition of a third flexible flap downstream as shown in Figure 5.7 (b), has a drastic effect on oscillation behavior. For instance, the birth of a lock-in state in this situation forces the vortex shedding frequency to match the oscillation frequency, where in this case the vortices supply energy to the structure instead of damping it, hence seemingly improving its mixing efficiency.

When increasing FVG number, the induced large displacement of the flaps produces a massive separation downstream with formation and shedding of eddies that are transported and interact with each other. Generation of such type of coherent structures increases the surface contact area between the two passive scalars and are eventually beneficial to enhance the mixing process. The flow undergoes in this case severe stretching and folding and forms extremely periodic patterns of scattered clusters flowing along the channel length. One can also notice particularly bad mixed regions surrounded by well mixed ones in Figure 5.7 (b). They are due to the Kolmogorov-Arnold-Moser (KAM) boundaries that separate the chaotic and regular regions of the flow, preventing scalar transport (and to another extent particles) between both regions [Wiggins and Ottino, 2004]. The addition of more flexible flaps tends to minimize and destructurates these KAM islands, however. This is clearly observable when adding a fourth flexible flap in 0CP-4FVG case for example (Figure 5.7 (c)). KAM islands are almost missing in the 2CP-3FVG case as in Figure 5.7 (e), which represents a good indicator of efficient chaotic mixing and fast homogenization of passive scalar in the entire mixing domain.

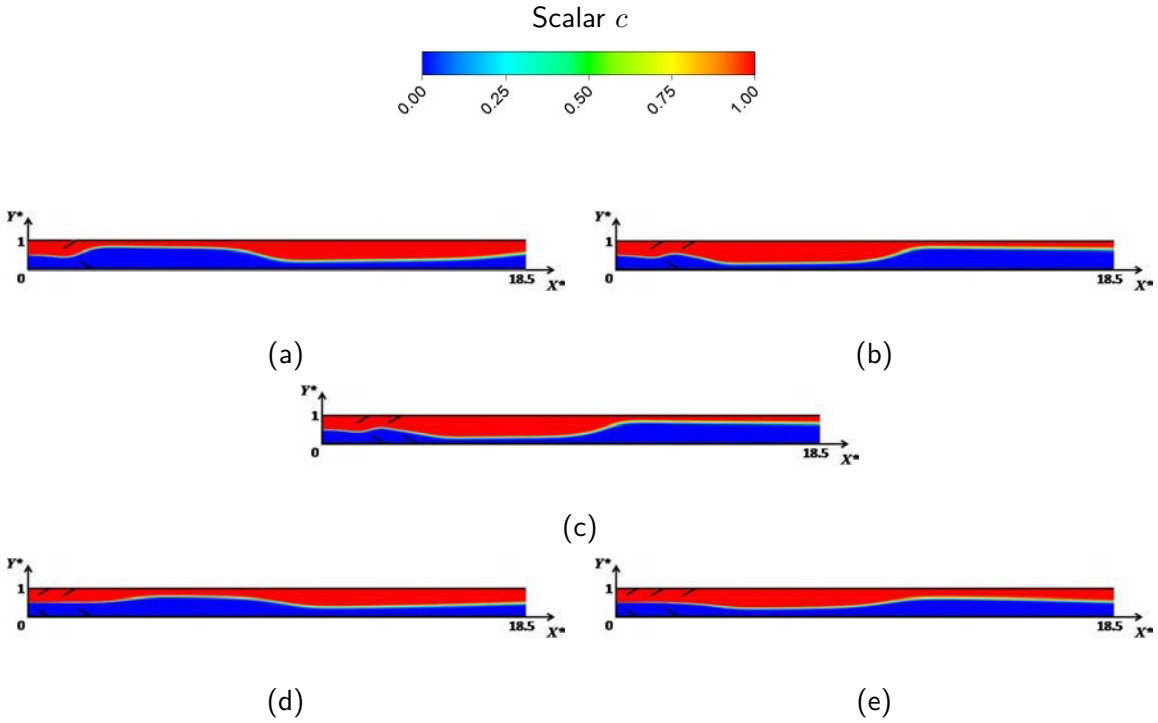

Figure 5.6: Snapshots of scalar c for rigid cases (a) 0CP-2RVG, (b) 0CP-3RVG, (c) 0CP-4RVG, (d) 2CP-2RVG and (e) 2CP-3RVG

In order to quantify the mixing efficiency based on the passive scalar values in the channel, we use a global mixing index ($\mathrm{MI}_{c,outlet}$) as in Lambert and Rangel [Lambert and Rangel, 2010], computed at the channel outlet and defined by:

$$\mathrm{MI}_{c,outlet} = 1 - \frac{1}{c_{ave}(t)} \left[\frac{\sum_{j=1}^{n} \left(c_j(y,t) - c_{ave}(t) \right)^2}{n} \right]^{1/2} dt \tag{5.14}$$

where $c_j(y,t)$ is the outlet scalar value at a given y position and at a given time t, $c_{ave}(t)$ is the averaged value of c at the outlet and at time t. n is the number of cells in y direction at the outlet position, i.e. the number of samples where the concentration value is extracted. For no mixture case $\mathrm{MI}_{c,outlet}$ is null whereas it gets to 1 for a fully mixed case.

Figure 5.8 depicts the temporal evolution of the global mixing index for all the flexible cases studied. After 4 seconds, the flows have reached their quasi-periodic regime.

First, it can be seen that the 0CP-2FVG case displays the lowest mixing index as the FVGs undergo nearly negligible displacement amplitudes. When adding more FVGs as in the 0CP-3FVG case, an increase in the maximum mixing index values can then be observed. We can yet notice some sudden temporal drops in the signal due to KAM islands reaching the outlet of the channel. These decreases in the signal tend to be reduced when adding FVGs and are totally absent in the 2CP-3FVG case indicating the destructuration of the KAM islands. This observation eventually correlates well with the previous trends qualitatively highlighted through the scalar field descriptions.

As far as mixing quality is concerned, not only the behavior as a function of time must be regarded but special care must also be brought in terms of mixing length property. We thus computed the time-averaged mixing index at different normalized streamwise positions in the channel by:

$$\overline{\mathrm{MI}}_c(x) = \frac{1}{t_2 - t_1} \int_{t_1}^{t_2} \left[1 - \frac{1}{c_{ave}(x,t)} \left[\frac{\sum_{j=1}^{n} \left(c_j(x,y,t) - c_{ave}(x,t) \right)^2}{n} \right]^{1/2} \right] dt \tag{5.15}$$

Figure 5.9 illustrates this time-averaged mixing index $\overline{\mathrm{MI}}_c(x)$ for both the rigid and flexible cases studied. One can first observe that the FVG configurations display a much higher mixing efficiency.

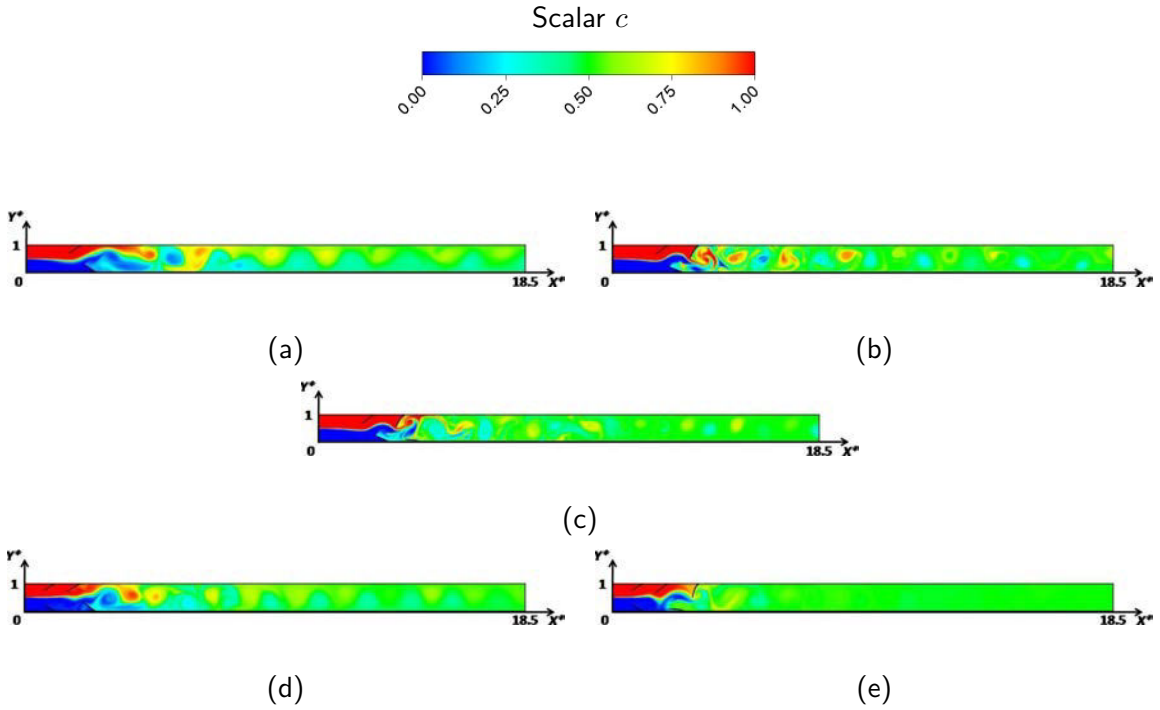

Figure 5.7: Snapshots of scalar c for flexible cases (a) 0CP-2FVG, (b) 0CP-3FVG, (c) 0CP-4FVG, (d) 2CP-2FVG and (e) 2CP-3FVG

Since flexible flaps cases exhibit mixing index values higher than 0.92 at the outlet, while these values do not exceed 0.17 for the corresponding rigid cases. Actually, the RVG cases only deviated the flow and do not make the scalar distributions mix, as already mentioned, whereas a full stirring of the flow is clearly shown by increasing FVG number in the channel. At the outlet, the mixing index is found to be 0.995 for the 2CP-3FVG case while it is 0.111 for its relative 2CP-3RVG case, corresponding to an 89% enhancement in the mixing efficiency.

When comparing the FVG configurations one another, addition of FVGs makes the mixing index increase. This is mostly explained by the mutual and increasing influence of the flap on their amplitude oscillation. The mixing phenomenon is then directly affected by the flaps ability to act as a mechanical agitator. Comparing the 0CP-2FVG case to the 0CP-3FVG case for instance, we notice that the latter exhibits better mixing in most of the channel positions as expected. However, when considering the local mixing index at $X^* > 14$, all profiles stand very close. The spatially integrated mixing index between 4 and 18.5, $\left(\frac{1}{18.5-4}\int_4^{18.5}\overline{\mathrm{MI}}_c(x)dX^*\right)$ is 0.847 for the 0CP-2FVG case while it is 0.878 for the 0CP-3FVG case, 0.919 for the 0CP-4FVG case, 0.899 for the 2CP-2FVG case and 0.995 for the 2CP-3FVG case. The 0CP-3FVG case shows an increase of 4% in mixture quality with respect to the 0CP-2FVG case, while the 0CP-4FVG case results in 8.5% increase in mixture quality. This specificity is once again due to the presence of poorer mixing when KAM islands are convected through the outlet, which also tends to reduce the time-averaged mixing index value. Comparing the co-planar cases with their relative non co-planar ones, we deduce an increase of 6% when comparing the 2CP-2FVG case to the 0CP-2FVG case, and similarly an increase of 13% in mixture quality when comparing the 2CP-3FVG to its relative 0CP-3FVG case.

Even if the same mixing quality is almost achieved whatever FVG configurations studied here, it can be recalled that mixing index values reached are far higher than the ones obtained in all the RVG cases. Moreover, a value of mixing index greater than 0.9 is always attained at the outlet of all the FVG configurations studied. One can eventually notice that when using co-planar flaps followed by alternating ones such as the 2CP-3FVG case, the mixing index reach very high value greater than 0.9 in a very short channel length (at $X^* = 4$). It could consequently be thought as having great potential to design more compact mixers, using self-sustained oscillations of flexible vortex generators since it leads to a shorter mixing length.

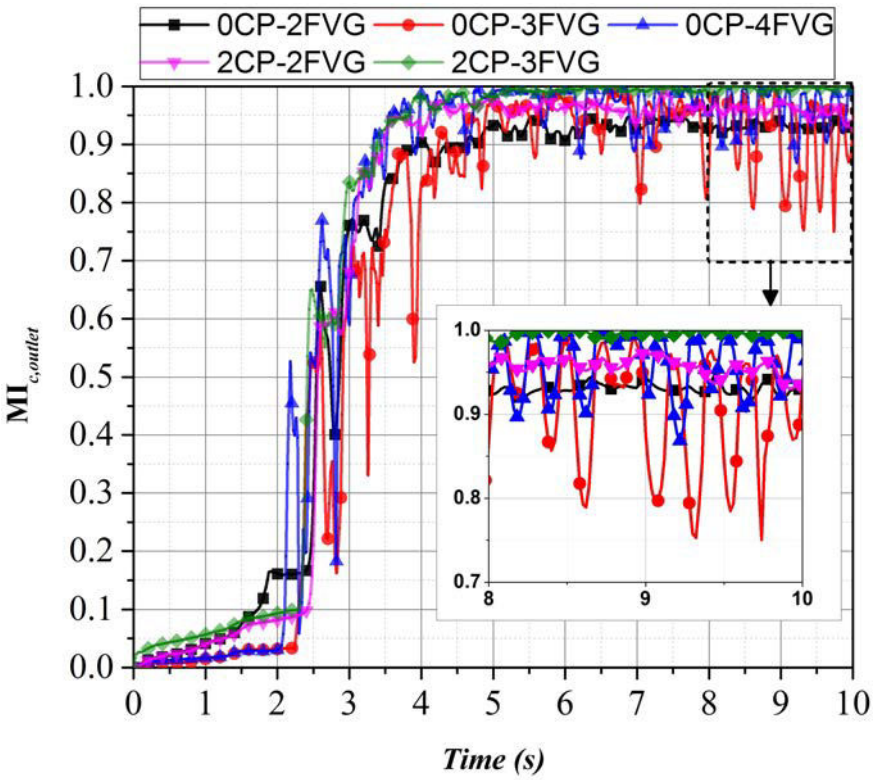

Figure 5.8: Global mixing index temporal variation for all the flexible cases studied

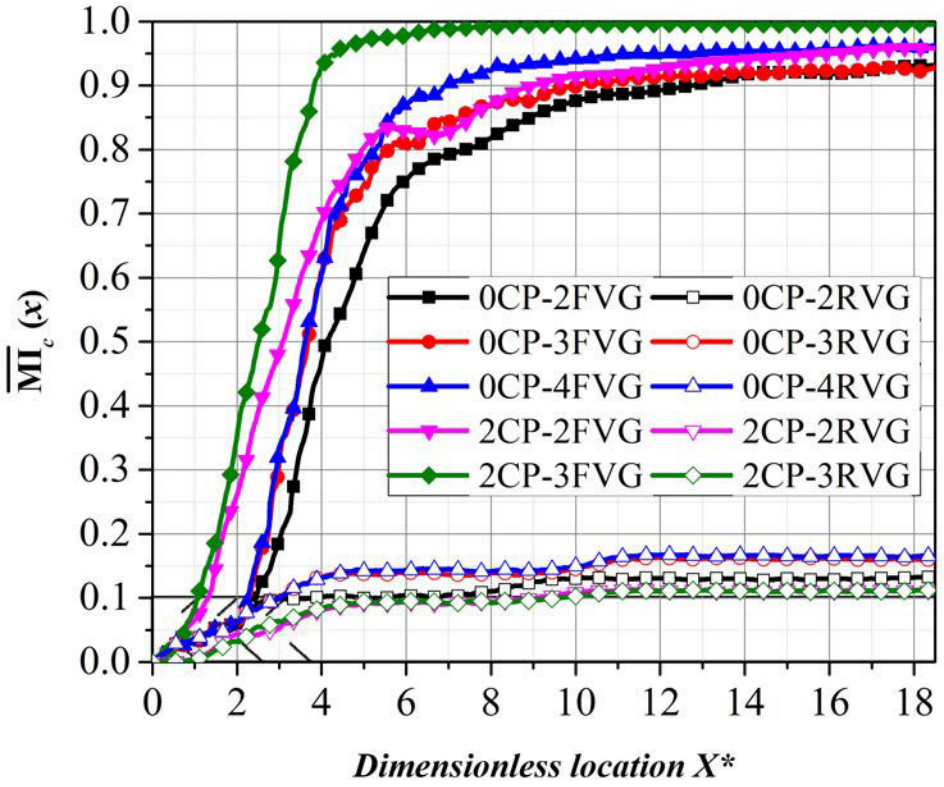

Figure 5.9: Comparison of the time-averaged mixing index of scalar c between the flexible cases (closed symbols) and the rigid cases (open symbols)

5.4.3 Thermal performance

In this section, numerical results are examined in terms of local Nusselt number Nu_x, global Nusselt number between the inlet and the outlet of the channel Nu_{0-L} and thermal performance factor η. The effect of increasing the system degree of freedom by adding downstream flaps, and the presence or absence of upstream co-planar flaps on heat transfer performance is numerically investigated. Finally the elastic cases are compared with their relative rigid cases.

Figure 5.10 shows steady-state distribution of the temperature field for the rigid cases studied. The cold region is clearly not well mixed with the hot near wall regions whatever the rigid configuration considered here, the cold main core fluid exits the channel outlet while maintaining almost the same cold temperature distribution. Thermal transfer taking place is mostly made by diffusion along the channel walls in the same way as a developing thermal boundary layer and some shear layer instabilities observable in some instantaneous temperature fields that could eventually lead to locally increase the thermal flux.

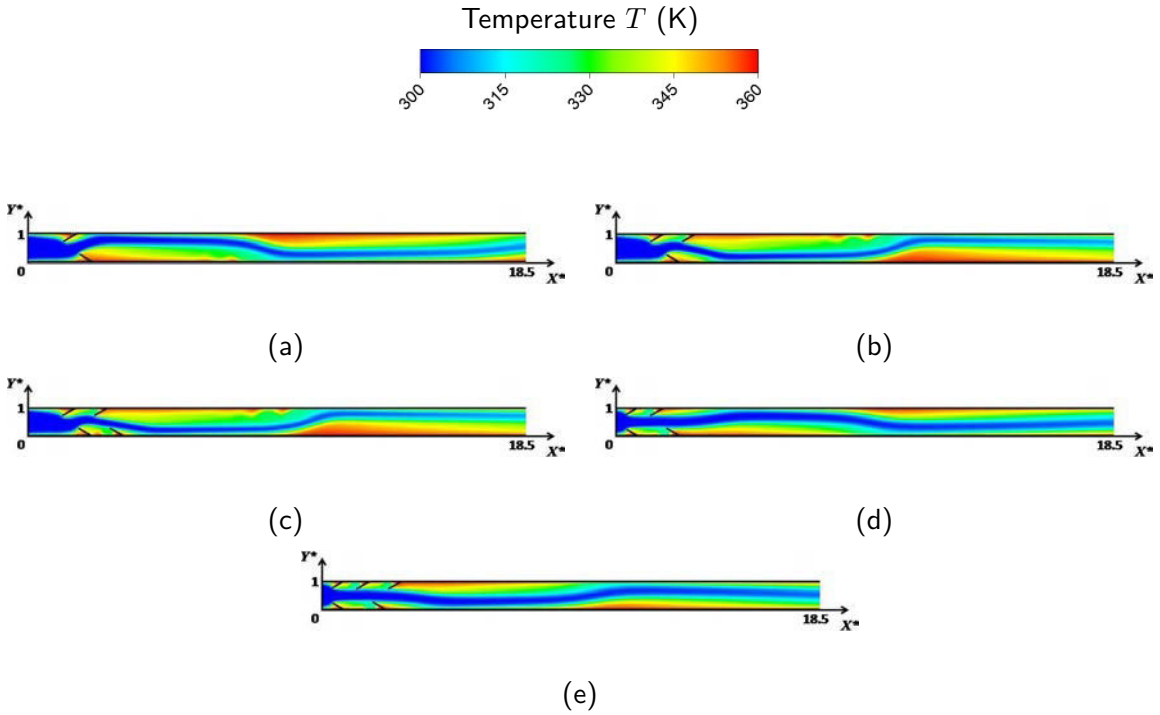

Figure 5.10: Steady temperature field T observed for rigid cases (a) 0CP-2RVG, (b) 0CP-3RVG, (c) 0CP-4RVG, (d) 2CP-2RVG and (e) 2CP-3RVG

Figure 5.11 then shows instantaneous fields of the temperature for the flexible cases. Due to the periodic oscillations of the flow and FVGs through fluid-structure interaction, temperature field is stirred and thermal transfer from the walls to the core of the fluid flow takes place. The complex vortex shedding pattern due to the shear layer instability offers in fact an important feature related to the existence of a constructive mode [Gopalkrishnan et al., 1994], where the vortices of the same rotating sense merge together to form larger eddies as shown in a previous study [Ali et al., 2016]. Vortex pairing produces vortices of higher strength, an essential criterion to disrupt the growth of the boundary layer and carry the hot fluid near the channel wall to mix with the core cold fluid. Further downstream, the vortices progressively dissipate and decrease in strength.

In order to highlight the main flow behaviors in the flexible cases, we observed several time instants during one oscillation period for the 2CP-3FVG case. Indeed, as it is to be noted that the flaps undergo the highest displacement amplitudes in this case, FSI and effects on heat transfer are more clearly observable. Figure 5.12 illustrates the structural oscillation of flaps C, D and E and captures one oscillation period for the three flaps. Four time instants are of particular interest and are specifically chosen. They are denoted τ_1, τ_2, τ_3 and τ_4 on the graph and can be characterized

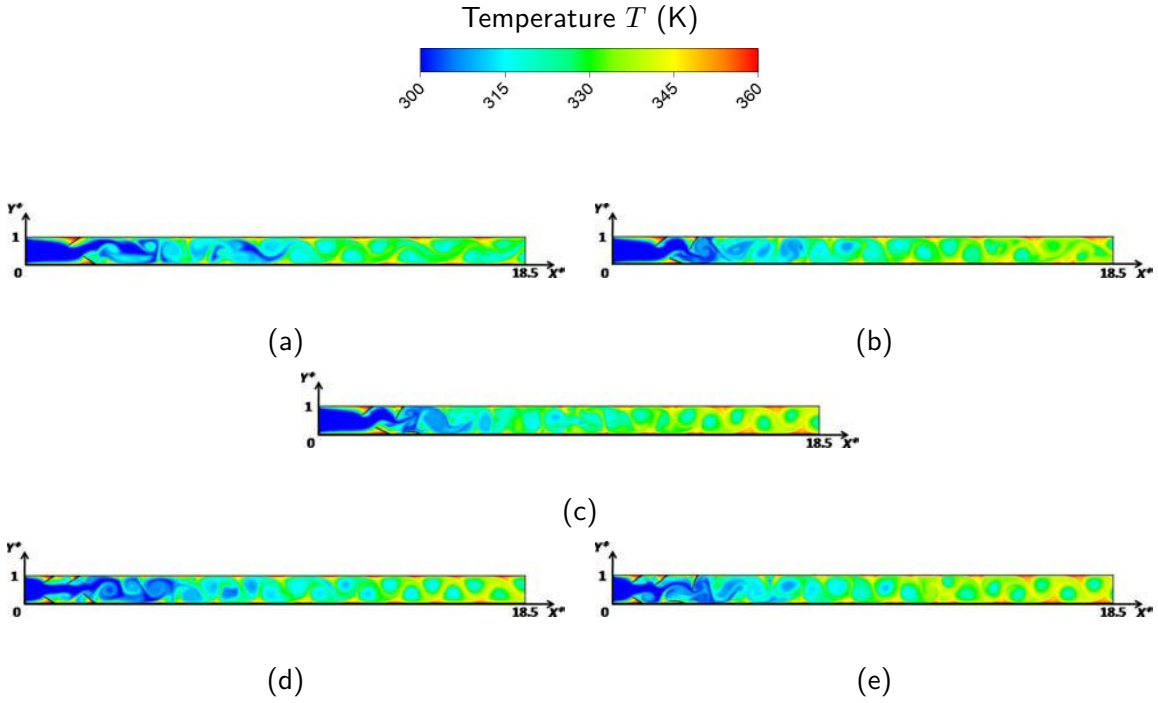

Figure 5.11: Snapshots of temperature in flexible cases (a) 0CP-2FVG, (b) 0CP-3FVG, (c) 0CP-4FVG, (d) 2CP-2FVG and (e) 2CP-3FVG

by a time τ normalized by $\overline{U}_{f,inlet}/H$.

Actually, time ($\tau_1 = 38.2$) represents the instant when flap E reaches its highest amplitude. Time ($\tau_2 = 38.5$) relates to the highest amplitude of flap C. Time ($\tau_3 = 38.9$) corresponds to a low amplitude of flap C and E but high amplitude of flap D. Finally, time ($\tau_4 = 39.2$) represents a relatively low amplitude for all the flaps. In Figure 5.12, we can notice that as flap C starts to reach its highest displacement amplitude, a drop in the amplitude of flap E is observed. Since the two aligned flaps C and E are located at the same wall, flap E benefits from the drafting phenomena provided by flap C upstream. Consequently, at this instant, flap E experiences a drop in drag, in addition to the energy stored in this flap that will force it to oscillate on the opposite streamwise direction to reach its minimum amplitude at time τ_3. Flap C and E which are located at the same upper wall approximately oscillate in phase, with a small time delay of 0.04 second, while flap C (resp. flap E) oscillates out of phase with flap D (resp. flap D) located at the opposite bottom wall with a delay of 0.08 second (resp. 0.12 second).

At the specific times τ_1 and τ_2, flaps C and E block partially the upper half of the channel, resulting in an acceleration of the fluid in the lower half and an interaction of the vortices with the bottom channel wall. Similarly at time τ_3, flap D reaches its highest amplitude, blocking the lower part of the channel and causing the fluid to accelerate in the upper part where the vortices therefore interact with the top channel wall. Figure 5.13 illustrates then the corresponding temperature fields at the four time instants a, b, c and d. It qualitatitvely displays the thermal boundary layer reduction along the wall (compared to rigid case), especially at the location of the flaps and even far in the wake of last flap E, clearly showing the ability of the vortices to penetrate the viscous sublayer. Because of the vortex intensity decrease when progressively dissipating downstream, temperature gradients at the wall and thus Nusselt number are also reduced. This is clearly observable in Figure 5.14 where the instantaneous Nusselt number profiles are depicted at both the bottom and top walls for the four time instants τ_1, τ_2, τ_3 and τ_4. Moreover, one can also notice that the peaks of the instantaneous Nusselt numbers at the top and bottom walls indicate the ability of the flap to reduce the thermal boundary layer. At time instants τ_1 and τ_2, as the fluid accelerates to the bottom wall due to the blockage of the upper part of the channel, we can notice the peaks in the bottom wall Nusselt number (Nu_{bw}) in Figure 5.14 (a, b). The same holds true in Figure 5.14 (c), as the fluid accelerates to the

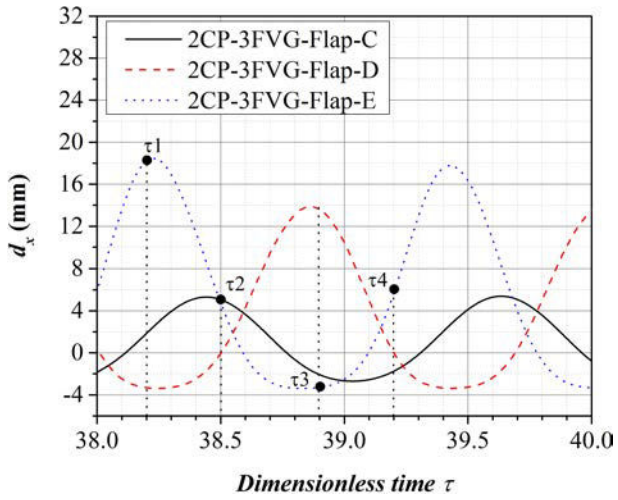

Figure 5.12: Flaps C, D and E structural oscillations in the x direction during one period for flexible case 2CP-3FVG. The time instants τ_1, τ_2, τ_3 and τ_4 are used in Figures 5.13 and 5.14

top wall, improving the heat transfer at this region (see the peaks of $\mathrm{Nu_{tw}}$). The Figure 5.14 (d) displays smaller peaks, as the flaps at this instant show smaller oscillation amplitudes with respect to the other instants. These observations made on the Nusselt number values correlates well the analysis of the fluid-structure interaction made from Figures 5.12 and 5.13.

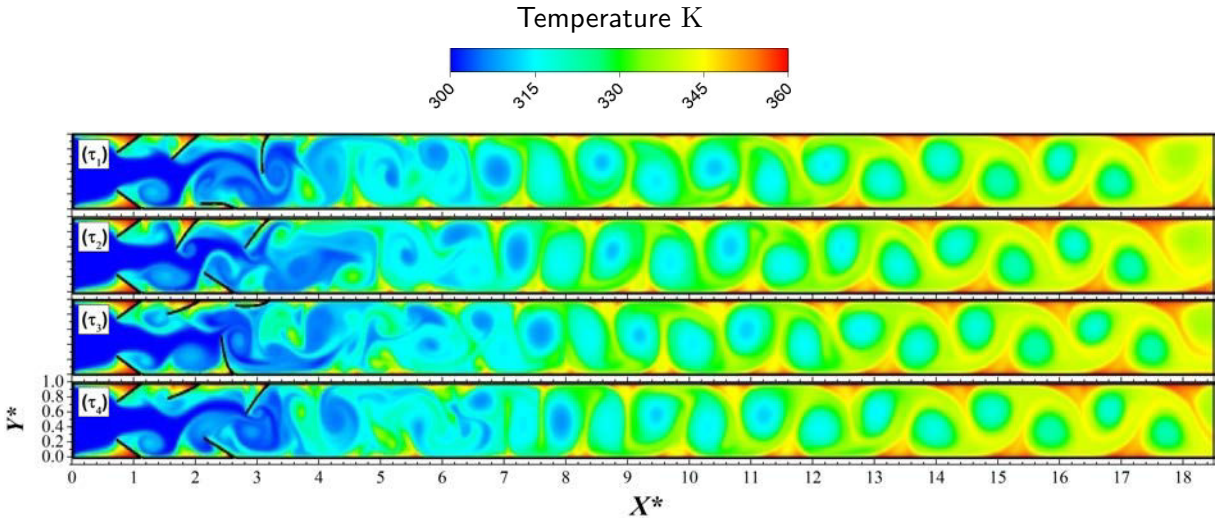

Figure 5.13: Temperature field snapshots for case 2CP-3FVG at the four time instants $\tau_1 = 38.2$, $\tau_2 = 38.5$, $\tau_3 = 38.9$ and $\tau_4 = 39.2$ shown in Figure 5.12

In order to quantify the heat transfer enhancement with respect to the increase in the number of alternating flaps and the effect of adding co-planar flaps upstream, we plot in Figure 5.15 the time-averaged local Nusselt number $\overline{\mathrm{Nu}}_x$ and compare the flexible cases to their relative rigid cases and also with respect to the empty channel simulation. Since in the rigid cases no vortices are present, we show that the flexible cases exhibit much higher $\overline{\mathrm{Nu}}_x$ than rigid cases at almost all the channel length. Moreover, small local increases of $\overline{\mathrm{Nu}}_x$ can be observed in the rigid cases that can be explained by the formation of spatially-limited shear layer instabilities. As previously reported, the strength of the vortices decreases with the streamwise position: it is also reflected here in the plots of the local Nusselt number which also decreases monotonically in all the flexible cases. The local Nusselt number peaks are due to the partial blockage of the flow by the flaps as explained previously. The increase in the number of flaps induces an increase in the displacement amplitude of each flap due to a stronger blocage effect in the frontal areas upstream the flaps. In addition, introducing two

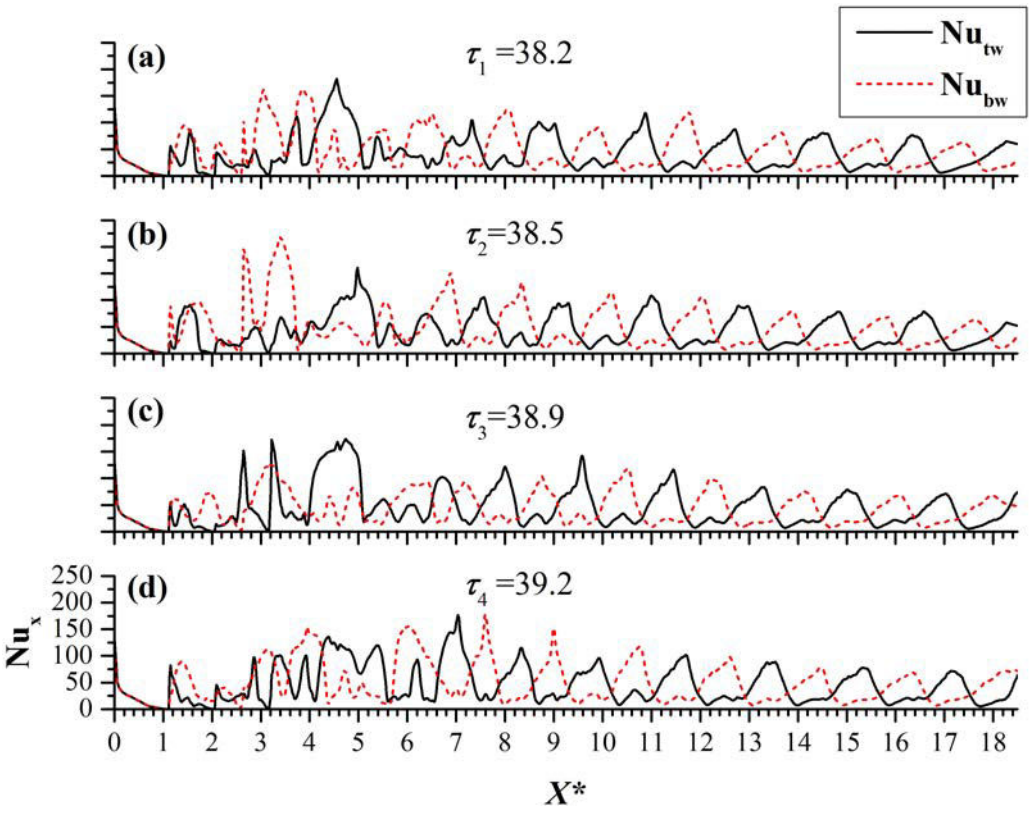

Figure 5.14: Instantaneous Nusselt numbers at the top ($\mathrm{Nu}_{tw}(x,t)$) and bottom ($\mathrm{Nu}_{bw}(x,t)$) walls of the channel for flexible case 2CP-3FVG at the four time instants τ_1, τ_2, τ_3 and τ_4 shown in Figure 5.12

co-planar flaps upstream also greatly influences the downstream FSI [Ali et al., 2016] and induces better thermal transfer.

This increase in amplitude of the FVG motion is thus directly correlated with the thermal exchange improvement as observed in Figure 5.15, where higher peaks are locally attained in $\overline{\mathrm{Nu}}_x$. Comparing each flexible flaps with respect to the empty channel, based on the integrated time-averaged local Nusselt number along all the channel length ($1/18.5\int_0^{18.5}\overline{\mathrm{Nu}}_x dX^*$), a great thermal enhancement is observed. For the non co-planar cases, the enhancement in local heat transfer is found to be about 178% for the 0CP-2FVG case, 278% for the 0CP-3FVG case and 317% for the 0CP-4FVG case. For the co-planar cases, the enhancement in local heat transfer is about 206% for the 2CP-2FVG case and about 317% for the 2CP-3FVG case. These results imply that large scale deformation plays a significant role in the augmentation of heat transfer.

When analyzing heat transfer performances, one must not only take into consideration the heat fluxes exchanged but also the potential pressure losses due to the introduction of the vortex generators. Hence, we computed the global Nusselt number Nu_{0-L} and friction factor f between the inlet and the outlet of the channel and time-averaged for $t > 4$ seconds for both the rigid and the flexible cases, where the flaps in these cases achieve quasi-periodic oscillations. They are obtained through the relations:

$$\mathrm{Nu}_{0-L} = \frac{\dot{m} c_p D_h}{2Lk} \frac{T_{b,outlet} - T_{b,inlet}}{T_w - T_{mean}} \tag{5.16}$$

where $\dot{m}$ is the mass flow rate, c_p is the specific heat, $T_{mean} = (T_{b,outlet} + T_{b,inlet})/2$ is the mean temperature and $T_{b,inlet}$ and $T_{b,outlet}$ are the bulk temperatures respectively at the channel inlet and outlet.

The friction factor f is moreover computed using:

$$f = \frac{2D_h}{4L} \frac{\Delta P}{\rho_f \overline{U}^2_{f,inlet}} \tag{5.17}$$

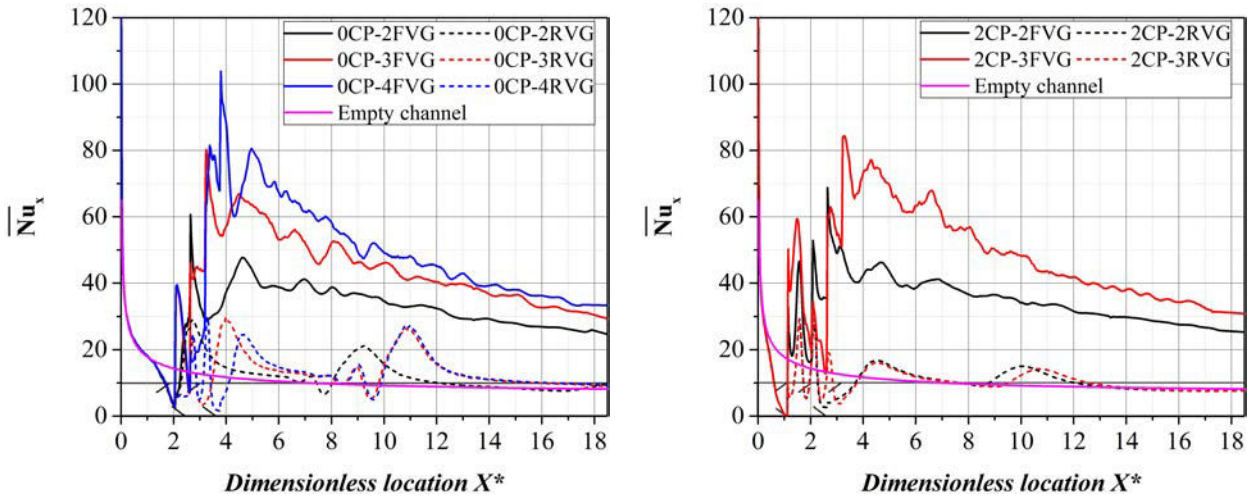

(a) (b)

Figure 5.15: Time-averaged local Nusselt number $\overline{\mathrm{Nu}}_x$ for all the cases studied, (a) with no co-planar flaps upstream, (b) with two co-planar flaps upstream

where $\overline{U}_{f,inlet}$ is the average flow velocity at the channel inlet and ΔP is the pressure drop between the channel inlet and outlet. This fluid friction is compared to the Fanning friction factor in a laminar flow regime given by:

$$f = 24/\mathrm{Re}_{D_h} \tag{5.18}$$

Results are presented in Figure 5.16 (a) and (b). The global Nusselt number is higher in the flexible cases than in the rigid cases and it is higher in the co-planar cases than in their relative non co-planar cases. The overall heat transfer enhancement is about 6% when comparing 0CP-2FVG/2CP-2FVG and also 6% for 0CP-3FVG/2CP-3FVG comparison. Moreover, compared to the empty channel, the overall heat transfer enhancement is about 174%, 250% and 275% for the 0CP-2FVG, 0CP-3FVG and 0CP-4FVG cases. For the co-planar cases, the overall heat transfer enhancement is about 192% and 273% for the 2CP-2FVG and 2CP-3FVG compared to the empty channel. The improvement in heat transfer and the disruption of the boundary layer always leads to a greater pressure drop in the channel. Figure 5.16 (b) shows the friction factor for all the cases studied. It is evident that the flexible flaps oscillation causes higher pressure loss, and it is higher in the cases where the flaps undergo larger deformations, which eventually increase the blockage in the channel.

Finally, a dimensionless factor, named the thermal performance factor η aiming at comparing the heat transfer efficiency at constant pumping power is computed. It is defined as the ratio of the convective heat transfer in the flexible or rigid cases to that in the empty channel according to the following relation [Promvonge and Thianpong, 2008]:

$$\eta = \left(\frac{\mathrm{Nu}_{(0-L)}}{\mathrm{Nu}_{(0-L),a}}\right)\left(\frac{f}{f_a}\right)^{-\frac{1}{3}} \tag{5.19}$$

where the a subscript corresponds to the empty channel results.

The thermal performance factor depicted in Figure 5.17 shows averaged values of 1.33 for the 0CP-2FVG case, 1.11 for the 0CP-3FVG case and 1.01 for the 0CP-4FVG case, meaning the elastic cases allows enhancing the heat transfer performance of 33%, 11% and 1% relatively to an empty channel configuration. Similarly, for the co-planar cases, we observe an increase of 34% of the thermal performance for the 2CP-2FVG case. The 2CP-3FVG case displays however a value of 0.97, indicating that global thermal performance is decreased compared to a smooth channel configuration. This can be explained by the counter-balancing effect of high pressure loss in comparison to the global Nusselt number increase, due to large FVG oscillations that create important blockage ratio within

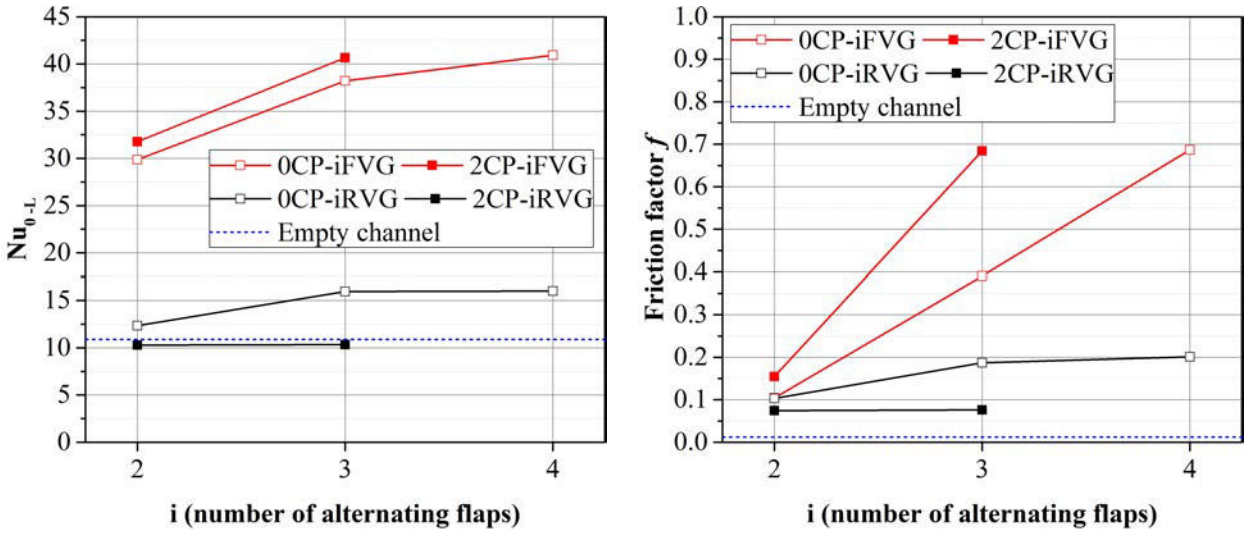

(a) (b)

Figure 5.16: (a) Global Nusselt number Nu_{0-L} and (b) friction factor f for all the flexible and rigid cases studied

the channel. The thermal performance for all the rigid cases remains lower than one since very little heat exchange is observed through the developing boundary layer and local shear layer instabilities only. Globally, the flexible cases provide enhancements of heat transfer performances almost twice compared to rigid cases.

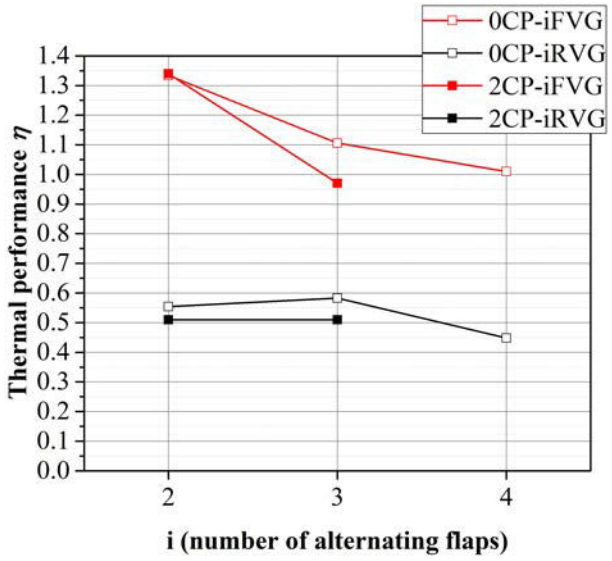

Figure 5.17: Thermal performance factor η for all the cases studied

5.5 Conclusion

This study presents an innovative way of enhancing heat transfer and mixing by using freely oscillation flexible vortex generators. Two-way strongly-coupled fluid structure interactions simulations are performed by coupling ANSYS Fluent (CFD solver) with ANSYS Mechanical (CSD solver). The effect of increasing the system degree of freedom by increasing the number of alternating flexible flaps and by the presence or absence of upstream co-planar ones, on heat transfer and mixing in a two dimensional channel is numerically investigated. The Reynolds number is held constant in all the

simulations with a value of 2000 based on the hydraulic diameter of the channel. Five flexible cases are studied which differ by the number of alternating flaps presented and the presence or absence of co-planar ones namely: 0CP-2FVG, 0CP-3FVG, 0CP-4FVG for the non co-planar cases and 2CP-2FVG, 2CP-3FVG for the co-planar cases. Moreover, all the flexible cases are compared with their relative rigid cases for which only the CFD solver is activated.

A series of gap to flaps and vortex to flaps interaction is observed, where the vortices shed by a flexible structure merge with the vortices of the same rotational sense produced by another structure or even by the same structure but from a previous cycle of oscillation. This act of merging produces vortices of high strength. Furthermore, an increase in the number of flaps, results in a lock-in state to undergo higher displacement amplitudes while they are previously out of lock-in with a lesser number of flaps such as in the 0CP-2FVG case. The addition of two co-planar flaps upstream restricts the flow passage and produces vortices that act as periodic forces on the downstream flaps, thus drastically augmenting their amplitudes compared to the non co-planar cases. The results show that as the oscillation amplitude increases, the vortex shed displays a greater ability to disrupt the growth of the thermal boundary layer which has a positive impact on the improvement of heat transfer enhancement but at the expense of a pressure drop increase. Moreover, the vortices generated due to the self-sustained oscillations of the flaps carry the hot fluid near the channel walls and move it towards the bulk region which gets replenished by the cold fluid and eventually enhance the mixing between the two. Compared to an empty channel the non co-planar cases show up to 275% increase in the global Nusselt number and up to 317% increase in the local Nusselt number with four FVG. Besides, the co-planar cases show up to 273% increase in the global Nusselt number and 317% increase in the local Nusselt number with three FVG. On the other hand, the increase in the number of flaps resulting in an increase of oscillation amplitudes has a great impact on augmenting the blockage ratio in the channel, thus resulting in higher pressure drops. The thermal performance factor has been investigated and shows values greater than one for all the flexible cases, except the 2CP-3FVG case where the flaps undergo the highest displacement amplitudes among all cases, hence the highest pressure drop. The non co-planar flexible cases show up to 33% increase in thermal performance while the co-planar ones show up to 34% enhancement. Eventhough good thermal performance can be achieved when using elastic structures, geometries, sizes, shapes and positions of FVG still need to be optimized for further improvement, however.

The mixing process is also investigated by studying the transport of a passive scalar through the channel flow. The mixing index is computed to quantify the mixing efficiency. The flexible flaps show a better ability to mix the two passive scalars achieving values higher than 0.92 in all the cases. While it does not exceed 0.17 for the corresponding rigid vortex generators cases. The enhancement in mixing efficiency is primarily caused by the high oscillation amplitudes where the flaps act as mechanical agitators mixing the two passive scalars sequentially. The large sized vortices eventually mix the two scalars located at the lower and upper half of the channel and thus are deemed to increase the mixing efficiency. Specifically, in the 2CP-3FVG case, a great mixing homogeneity is attained in a short portion of the channel which leads eventually to shorten mixing length and then more compact mixers. Although better performances could be assessed by optimizing some key parameters such as distance between the flaps or their length or by thinking about designing different flap shapes for instance, the work achieved here presents a new way to enhance mixing and heat transfer in laminar flows using passive structural oscillations of multiple flexible vortex generators, by relying on the fluid pumping power alone without the need of external power in order to control the flow. Further works are still to be undertaken in order to experimentally investigate the fluid-structure interactions and to perform case study on three-dimensional configurations to define improved designs.

Chapter 6

Three-dimensional numerical study of heat transfer and mixing enhancement in a circular pipe using self-sustained oscillating flexible vorticity generators

6.1 Introduction

Instabilities such as vortex-induced vibrations (VIV), galloping and fluttering occur when a fluid surrounding a structure supplies energy to the structure instead of absorbing it [Huang, 1995, Williamson and Govardhan, 2004]. Usually, most of the studies in engineering disciplines intend to suppress such instabilities either by adding weights or by operating below a critical speed. When operating at this particular velocity, the instability indeed leads to self-sustained flapping motions of the structure in the flow and potentially causes damage to it. Recently some authors think about using this phenomenon and benefit from this flapping motion instead by harvesting electricity using patches of piezoelectric materials attached to the structure surface [Michelin and Doaré, 2013, Akcabay and Young, 2012].

In the particular context of multifunctional heat exchangers/reactors, specific non deformable rigid vortex generators (RVG) are usually inserted in order to create secondary flows and disrupt the growth of the thermal boundary layer [Ahmed et al., 2012, Allison and Dally, 2007, Anxionnaz et al., 2008]. These RVGs are usually fixed and stay passive without any external control. Moreover, to add more flexibility to this technique, one can also think about making the vortex generators (VG) move by actively controlling the frequency and amplitude of oscillation of these VGs by relying on an external source of energy. This kind of study has been achieved for example by Lambert and Rangel [Lambert and Rangel, 2010] who studied the effect of actively oscillating thin elastic flaps on fluid mixing in a microchannel. They found that the mixing is the greatest when one flap oscillates with the largest amplitude displacements. The addition of another flap also lead to the highest mixing performance when the flaps oscillate out of phase with an angle of $\pi/2$. Furthermore, Yang and Chen [Yang and Chen, 2008] numerically studied the effect of a transversely oscillating cylinder on heat transfer of heated blocks in a two-dimensional channel flow. They concluded that heat transfer is remarkably enhanced when the lock-in regime is reached, i.e. when the vortex shedding frequency synchronizes with the structural oscillation frequency. However, in these above-mentioned studies, the flaps oscillate using an external source of energy. Previous studies have furthermore put in evidence that self-sustained oscillations can be obtained by relying on the flow energy itself. Indeed,

Note to reader: chapters 4, 5 and 6 were written in a format corresponding to the preparation of articles to be submitted in scientific journals. References are grouped at the end of thesis manuscript, however some repetitions may appear in these three chapters.

Ali *et al.* [Ali et al., 2015] proposed an innovative concept using passive-dynamic control of flexible vortex generators (FVGs) by creating an instability able to sustain the oscillatory motion in a two-dimensional channel. Their results show that the free elastic oscillations could improve the mixture quality up to 98% when comparing the corresponding configuration but using RVG instead. Moreover, the heat transfer displayed for the FVG case an increase up to 56% in the thermal performance and up to 134% in the overall heat transfer when compared to its relative RVG case. Furthermore, this fluid-structure interaction (FSI) problem caught the attention of several other authors. In fact, Shi *et al.* [Shi et al., 2014] performed numerical simulations on a benchmark for FSI problems already available in the literature and proposed by Turek and Hron [Turek and Hron, 2006], which consists of a two dimensional laminar flow around a flexible structure attached to a rigid cylinder. They included the effect of heat transfer to assess the thermal performance of the FSI benchmark and simulations were carried out at different Reynolds numbers calculated based on the rigid cylinder diameter ($\mathrm{Re}_D = 200 - 330$). They observed that the FSI problem strengthens the disruption of the thermal boundary layer by vortex interaction with the wall and improves the mixing process between the hot and cold fluid regions. Their results indicate that VIV could increase the Nusselt number of a maximum enhancement of about 90.1% with respect to an empty channel. Nevertheless, the heat transfer effect on the same Turek and Hron benchmark has also been investigated by Soti *et al.* [Soti et al., 2015] by varying the Prandtl number, the Reynolds number and the Young's modulus of the flap. The analyses suggest that larger Prandtl and Reynolds number tend to promote the thermal enhancement but with less efficiency. On the other hand, larger values of Young's modulus reduce the thermal enhancement and require much more pumping power.

In light of the increased attention on the potential of applying FSI problems and self-sustained oscillations to heat transfer and mixing in real applications, we propose in this paper a three-dimensional FSI study applied to a multifunctional heat exchanger/reactor configuration, namely the High-Efficiency-Vortex (HEV) geometry [Habchi et al., 2010b, Habchi et al., 2010a, Habchi et al., 2012]. It consists of five rows of trapezoidal vortex generators inserted as a 45° rotated arrays in a pipe and inclined opposite to the flow direction with an angle of 45° with respect to the pipe wall. The Reynolds number is held constant in the laminar regime with a value of 1500 based on the pipe diameter. The effect of using flexible vortex generators on heat transfer and mixing performances is numerically investigated by strongly coupling both fluid and structural solvers allowing FSI modeling. FVG and RVG cases are then compared by quantifying the Nusselt number, the thermal performance factor η, the synergy field principle and finally the mixing index to evaluate the mixture quality. Heavy and computationally expensive simulation is performed on the FSI problem in order to complete 30 seconds of physical time. The flow structures of the FVG case are analyzed by applying the method of proper orthogonal decomposition proposed by [Sirovich and Kirby, 1987] and the behavior of vortex formation and patterns are compared to the RVG case. To this aim, the mathematical formulation and numerical procedure is first presented in section 6.2. Section 6.3 presents the analyzed geometry and configurations through the description of the mesh and also initial and boundary conditions. The structural oscillations, flow patterns, heat transfer and mixing performances are next investigated in section 6.4 and section 6.7 is eventually dedicated to concluding remarks.

6.2 Mathematical formulation and numerical procedure

In this study, a partitioned approach for solving the numerical fluid structure interaction problem is adopted. This method involves three solvers, one for fluid motion, another one for structural displacements and a third one for remeshing procedure. In addition, a strongly coupled solution is considered especially efficient when large structural displacements are present. This is achieved by introducing an additional FSI outer loop, where the solutions of the fluid and the structure are recalculated until reaching the convergence criteria set on forces and displacements [Le Tallec and Mouro, 2001]. In this paper, this method is established by successively calling the ANSYS Fluent CFD-solver, and the ANSYS Mechanical CSD-solver [ANSYS, 2015].

Thus, the flow field is governed by the unsteady Navier-Stokes equations for an incompressible viscous laminar flow. These equations are solved in a computational domain which deforms in

time due to the flexible structure deformations. Therefore, an Arbitrary Lagrangian-Eulerian (ALE) formulation is used to solve the flow equations on a deforming mesh [Donea et al., 2004]. The ALE formulation of the Navier-Stokes equations is written as:

$$\nabla \cdot \mathbf{u_f} = 0 \tag{6.1}$$

$$\frac{\partial \mathbf{u_f}}{\partial t} + (\mathbf{u_f} - \mathbf{u_{m,f}}) \cdot \nabla \mathbf{u_f} = -\frac{\nabla p}{\rho_f} + \nu_f \nabla^2 \mathbf{u_f} \tag{6.2}$$

where $(\mathbf{u_f} - \mathbf{u_{m,f}})$ is the convective term with $\mathbf{u_f}$ the fluid velocity and $\mathbf{u_{m,f}}$ the mesh motion velocity in the fluid domain. The pressure is denoted by p, the density of the fluid by ρ_f and the kinematic viscosity by ν_f. The Eulerian and Lagrangian descriptions are obtained by setting $\mathbf{u_{m,f}} = 0$ or $\mathbf{u_{m,f}} = \mathbf{u_f}$, respectively.

The mass transport equation of a scalar *c* is considered to study the effect of the elastic flap deformations on fluid mixing:

$$\frac{\partial c}{\partial t} + (\mathbf{u_f} - \mathbf{u_{m.f}}) \cdot \nabla c = D_m \nabla^2 c \tag{6.3}$$

where D_m is the mass diffusivity of the scalar *c*. Here, the convective scalar mixing is only considered so mass diffusion term is set 0.

The heat equation is also solved in the fluid domain and is given by:

$$\frac{\partial T_f}{\partial t} + (\mathbf{u_f} - \mathbf{u_{m.f}}) \cdot \nabla T_f = \frac{k_{th}}{\rho_f C_p} \nabla^2 T_f \tag{6.4}$$

where T_f is the fluid temperature, k_{th} is the thermal conductivity and C_p is the specific heat.

The equation of motion for an elastic isothermal solid structure can be described from a Lagrangian point of view, i.e. in terms of the initial configuration at $t = 0$, and it reads:

$$\rho_s \frac{\partial^2 \mathbf{d_s}}{\partial t^2} = \nabla \cdot \left(\Sigma \cdot \mathbf{F^T} \right) + \rho_s f_b \tag{6.5}$$

where $\mathbf{d_s}$ is the displacement of the structure, f_b is the resulting body force, ρ_s is the density of the structure and **F** is the deformation gradient tensor given by:

$$\mathbf{F} = \mathbf{I} + \nabla \mathbf{d_s^T} \tag{6.6}$$

where **I** is the identity.

The second Piola-Kirchhoff stress tensor Σ is related to the Green Lagrangian strain tensor **G** following [Tukovic and Jasak, 2007, Bos, 2010b]:

$$\Sigma = 2\mu_s \mathbf{G} + \lambda_s tr\left(\mathbf{G}\right) \mathbf{I} \tag{6.7}$$

with **G** given by:

$$\mathbf{G} = \frac{1}{2} \left(\mathbf{F^T} \cdot \mathbf{F} - \mathbf{I} \right) \tag{6.8}$$

Here *tr* is the tensor trace, λ_s and μ_s are Lamé constants which are characteristics of the elastic material. They are linked to the Young modulus *E* and Poisson's coefficient ν_s by:

$$\lambda_s = \frac{\nu_s E}{(1 + \nu_s)(1 - 2\nu_s)} \tag{6.9}$$

$$\mu_s = \frac{E}{2(1 + \nu_s)} \tag{6.10}$$

Fluid-structure interaction problems with moving boundaries require a third coupled solver for an automatic internal mesh motion. The mesh motion solver in Fluent consequently deforms the internal fluid domain while maintaining the quality and validity of the deforming mesh. In this case,

the displacement of the fluid-structure interface, which is the result of the structural solver, is then used as a boundary condition for the mesh motion solver. The present study employs the Laplace smoothing equation given by the following expression:

$$\nabla \cdot (\gamma \nabla \mathbf{u_m}) = 0 \tag{6.11}$$

where γ is the mesh diffusion coefficient and $\mathbf{u_m}$ the mesh displacement velocity. The mesh diffusion coefficient used in this study is a function of the boundary distance:

$$\gamma = \frac{1}{l^\alpha} \tag{6.12}$$

where *l* is a normalized boundary distance and α is the diffusion parameter. A diffusion parameter α of 1.5 has been used in the present study, which preserves larger regions of the mesh near the moving boundary, and cause the regions away from the moving boundary to absorb more of the motion.

To avoid divergence problems especially caused by negative cell volumes, the mesh solver supports several remeshing methods. The one used in this study is the local cell remeshing that applies to tetrahedral cells in the domain. This method agglomerates cells that violate the skewness or size criteria and locally remeshes the agglomerated cells. If the new cells or faces satisfy the skewness criterion, the mesh is locally updated with the new cells (with the solution interpolated from the old cells) [ANSYS, 2015]. Otherwise, the new cells are discarded and the old cells are retained. In the present study a maximum cell skewness of 0.7 has been used for remeshing with cell size criterion depending on the minimum and maximum length scale of the mesh.

In order to perform the load and motion transfer between the different meshes for fluid and structure, the General Grid Interface (GGI) mapping algorithm is used [Galpin et al., 1995]. At each time step, the FSI iteration loop sequentially calls the structural solver, the mesh motion algorithm and then the fluid solver until the convergence limits for displacements and forces are reached. An under-relaxation factor for both displacement and force is set to unity for all the simulations performed and convergence criteria set to 10^{-4} on force and displacement.

The pressure-velocity coupling is established using the Coupled algorithm [ANSYS, 2015], which solves the momentum and pressure-based continuity equations together. The convergence criteria for pressure, velocity, energy and scalar is set to 10^{-6}. The Laplace mesh smoothing convergence criteria is set to 10^{-4}. Temporal discretization is performed using a first order implicit scheme and the time step used for all the present simulations is set to 5×10^{-4} sec (≈ 400 time steps per period of oscillation)..

Eventually, only the ANSYS Fluent CFD-solver is activated for the numerical simulations carried out with rigid vortex generators, with the above mentioned parameters kept identical.

The overall procedure described above has already been validated in previous studies in two-dimensional flow configurations and more details can be found in Ali *et al.* [Ali et al., 2015]. Moreover, taking into account the third component in the spanwise direction of the flow must not modify conclusion regarding the validation of the numerical solvers and coupling.

6.3 Problem description

The computational domain consists of a three-dimensional flow in a circular pipe where vortex generators are placed along the walls. In this section, we present the studied configurations and associated boundary and initial conditions, followed by a mesh validation study.

6.3.1 Problem description: geometries, initial and boundary conditions

In the present study, an HEV-like geometry is investigated as shown in Figure 6.1. It consists of a round pipe with a diameter $d = 54$ mm in which five arrays (A, B, C, D, E) of FVGs are inserted. Each array is composed of four diametrically opposed trapezoidal VGs inclined to the wall at an angle $\beta = 45°$ and directed inversely to the main flow direction. Each trapezoidal VG has a height of $h = 16$ mm, a base length of $b = 15$ mm, an opposite parallel side to the base with a length

$a = 10\ \mathrm{mm}$ and a thickness $e = 0.2\ \mathrm{mm}$. The distance between two successive FVG arrays is $30\ \mathrm{mm}$. It should be noted that arrays B and D undergo a $\theta = 45°$ tangential rotation with respect to array A. The FVGs orientations of the arrays A, C and E follow a cardinal direction notation commonly denoted by their initials n for north, e for east, s for south and w for west. On the other hand, FVGs orientations of the arrays B and D follow similarly the notation ne for northeast, se for southeast, sw for southwest and nw for northwest. Thus, every FVG can be located by its row letter followed by its cardinal directon. For example, FVG An points to the tab in the first row A and at the top position (north n). The FVG configuration is further compared to its relative RVG case in terms of flow structures, heat transfer and mixing quality.

No slip boundary conditions are set at the pipe wall. The outlet is set at zero pressure and Neumann zero for velocity. A parabolic laminar velocity profile corresponding to a fully developed laminar flow is set at the flow inlet:

$$U_{f,inlet} = 2\overline{U}_{f,inlet}\left[1 - \left(\frac{4(x^2 + y^2)}{d^2}\right)\right] \tag{6.13}$$

where $\overline{U}_{f,inlet}$ is the mean flow velocity at the inlet.

To characterize the mixing process, the fluid domain is initially divided into two equal parts: at $x > 0$, c is set to 1 and at $x < 0$, c is set to 0 as shown in Figure 6.1 (b). Zero flux boundary conditions are prescribed for the mass transport equation along the walls and the rigid/flexible flaps.

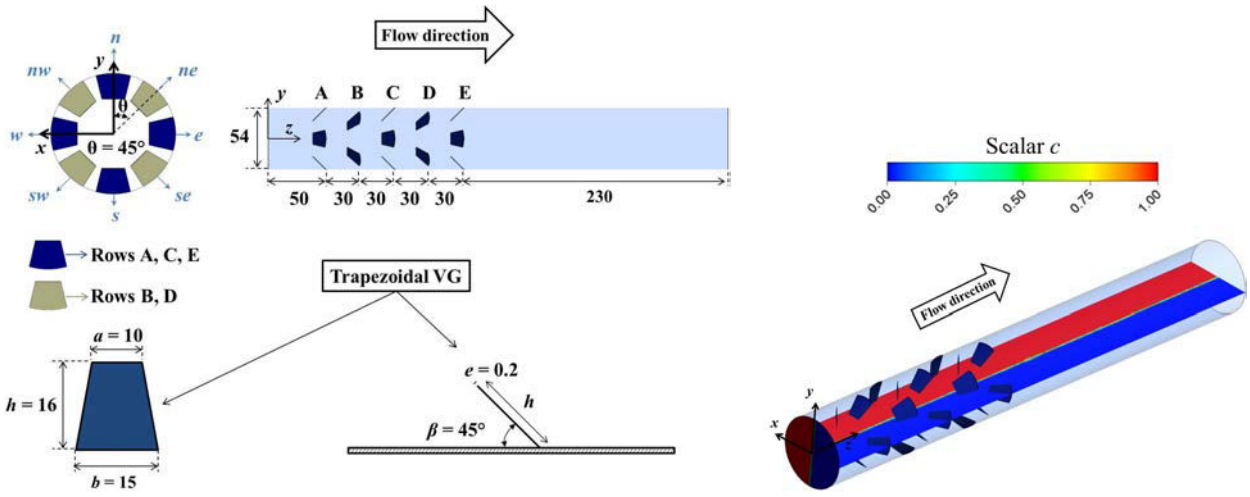

(a) (b)

Figure 6.1: HEV geometry: (a) tab dimensions (in mm) and (b) Initial scalar field distribution in the fluid domain

To characterize the heat transfer process, the same conditions are set for both FVG and RVG cases with a uniform wall temperature $T_w = 360\ \mathrm{K}$ imposed at the tube wall. The laminar parabolic velocity profile is prescribed at the inlet with a uniform inlet temperature $T_{in} = 300\ \mathrm{K}$. The rigid/flexible tabs are treated as insulating material with zero heat flux along them.

Finally, the physical properties of the FVGs/RVGs and the flow conditions are summarized in Table 6.1.

Table 6.1: Physical parameters and flow conditions for all cases

Cases	ρ_s (kg/m^3)	ν_s	E (Pa)	$Re_d = (\overline{U}_{f,inlet}d)/\nu_f$
FVG	1000	0.45	1×10^6	1500
RVG	1000	-	-	1500

6.3.2 Grid size independence study

The three dimensional FSI problem is very computationally expensive to run and considering to do a mesh validation study is not reasonable (for instance, the FSI simulation ran during seven months to bypass the transitional state from initial conditions to periodic state and finally reached 30 seconds physical time modeled). For this reason the mesh study is thus conducted on steady-state simulations of the RVG case and the final retained mesh is used for both unsteady FVG and RVG cases. The fluid domain is discretized with tetrahedral cells using three different mesh densities, refined at the pipe wall and at the fluid-structure interface, i.e. the elastic/rigid tabs. The three mesh densities and their main characteristics are summarized in Table 6.2.

Table 6.2: Global meshes characteristics used for grid size independance study

	Mesh 1	Mesh 2	Mesh 3
Initial number of cells (N)	619534	1074375	1845922
Grid size $h_g = \left[\frac{1}{N}\sum_{i=1}^{N}(\Delta V_i)\right]^{\frac{1}{2}}$	11.39×10^{-4}	9.48×10^{-4}	7.91×10^{-4}
Grid refinement factor $r = h_i/h_j$	-	$h_2/h_1 = 1.32$	$h_3/h_2 = 1.31$

where ΔV_i is the volume of the i^{th} cell.

To determine the appropriate mesh density for grid size independence, the simulations are performed on increasing mesh densities. The mesh validity verification is based on the method proposed by Celik *et al* [Celik et al., 2008] where the grid convergence index (GCI) and the apparent order of convergence (p_c) can be obtained. Since the heat transfer strongly depends on the near-wall refinement, the Nusselt number Nu_z is chosen for the mesh validity verification and is expressed as:

$$\mathrm{Nu}_z = \frac{q''_w(z)d}{k(T_w - T_b(z))} \tag{6.14}$$

where q''_w is the averaged heat flux along a circle that has a diameter equal to that of the pipe at a position z, T_w the temperature along the walls, k is the thermal conductivity of air and $T_b(z)$ is the local bulk temperature defined by:

$$T_b(z) = \frac{\int_A U(x,y,z)T(x,y,z)dA}{\int_A U(x,y,z)dA} \tag{6.15}$$

where A represents the local cross-section of the pipe.

The results obtained from applying the method of Celik *et al* [Celik et al., 2008] are summarized in Table 6.3, where $\phi_{refined}$ is the variable calculated from the solution of the refined mesh, ϕ_{ext} is the extrapolated variable and e_a^{23} is the relative error between Mesh 3 and Mesh 2. Extensive information about the calculation of these parameters can be found in Celik *et al* [Celik et al., 2008]. It can be concluded from Table 6.3 that the uncertainty in the fine-grid solution is about 2.01% for the integrated Nusselt number (along all the pipe length $L = 0.4$ m). The refined Mesh 3 is thus considered as a reliable reference mesh density for the FVG and RVG simulations.

Table 6.3: Estimated order of convergence p_c and GCI for refined Mesh 3

Parameter	$\phi_{refined}$	ϕ_{ext}	e_a^{23} (%)	p_c	GCI (%)
$\frac{1}{L}\int_0^L \mathrm{Nu}_z dz$	17.55	17.8	0.85	1.58	2.01

6.4 Results and discussion

In this section, the structural oscillation behavior in the FVG case is presented, then the flow analysis is based on the proper orthogonal decomposition technique to identify the different vortex modes. In addition, we compare the FVG case to its relative RVG case in order to identify the effect of structural oscillations on heat transfer and mixing performances.

6.4.1 Structural oscillations

The displacement of the tip position of every tab is first depicted in the z direction. The tab oscillation amplitudes actually increase with time until reaching a quasi-periodic regime at time $t > 19$ s displaying a sinusoidal pattern of oscillation. For clarity reasons, only the last second of simulation is presented in Figure 6.2. From this temporal signals, we can see that at rows B and D, the tabs almost show no significant oscillations whereas at rows A, C and E, the tabs undergo large displacement amplitudes. Since the rows B and D undergo a 45° tangential rotation, the deformations of tabs in rows A, C and E have small influence on their motions. Thus the interaction of tabs between two rows B and D is apparently weaker than the interaction of tabs in three rows A, C and E.

Figure 6.3 illustrates then the deformation cycle of tabs during one cycle of oscillations. The wireframes are used to indicate the initial fixed position of the tabs before any fluid forces applied. In fact, as the tabs An and As reach their minimum amplitudes and tabs Ae and Aw reach their maximum amplitudes as shown in Figure 6.3 (b), the flow is now oriented in the region from s to n and blocked in the region from e to w. Consequently, the drag forces will be concentrated on the wake region, especially at row C and at tabs Cn and Cs, since the trajectory of flow to Cw and Ce is blocked by the upstream tabs Aw and Ae. Nevertheless, when the tabs Aw and Ae reach their highest position as shown in Figure 6.3 (b), their stored kinetic energy will make them revert backward with a motion opposed to that of the flow to reach their minimum amplitude as shown in Figure 6.3 (e). Hence, this will allow the flow to exert forces at tabs Cw and Ce. The same holds true when analyzing rows C and E. Moreover, due to this drafting effect and this alternating behavior in subjecting every tab to high/low loads, a phase shift is produced between the rows. Indeed, tabs in row C oscillate out of phase with tabs in row A. Similarly, tabs of row E oscillate out of phase with tabs of row C and as a result are in phase with tabs of row A. The amplitude of oscillations are summarized in Table 6.4. Since the displacements of rows B and D are relatively small (order of 10^{-4} m), we only present results corresponding to tabs in rows A, C and E. Since the signal of the displacement is quasi-periodic, the mean amplitude MA of flap E can moreover be expressed by:

$$\mathrm{MA} = \frac{1}{N_{peak}} \sum_{i=1}^{N_{peak}} |z_{i_{peak}} - \overline{z}| \tag{6.16}$$

where N_{peak} is the number of maximum and minimum peaks in the signal, $z_{i_{peak}}$ are the individuals maximum and minimum values and $\overline{z}$ is the mean displacement. The amplitude calculation is performed from $t_1 = 19$ s till $t_2 = 30$ s in order to omit the non periodic region in the signal. It is important to note that tabs of the first row A experience the highest amplitude oscillations since the first row is subjected to the highest drag forces and the rows downstream experience a drafting effect and consequently a reduction in drag. However, the tabs of row E undergo larger amplitude oscillations than tabs of row C, this could be explained by the fact that the motions of tabs of row E are unrestricted nor influenced by further downstream tabs.

Table 6.4: Mean oscillation amplitudes MA (in mm) in the z direction for tabs rows A, C and E

Row	n	e	s	w
A	4.33	4.45	4.43	4.33
C	3.43	3.42	3.17	3.51
E	3.79	3.58	3.59	3.63

In order to calculate the phase shift angle of every tab calculated with respect to tab An, we compute the Fast Fourier Transformation (FFT) on the cross-correlation of the two signals of interest. Then the phase angle identified at the highest frequency peak can be considered as the phase shift. The results are summarized in Table 6.5: if the phase angle is negative, it means that tab An is lagging, otherwise An is considered leading. It can be shown that the tabs in row A oscillate out of phase with the tabs in rows C and approximately in phase with the tabs in rows E. Moreover, in a given row, the tabs located at the cardinal direction n and s oscillate out of phase with the tabs at the cardinal directions e and w. For example, in row A, the tabs An lags tabs Ae and Aw with a phase difference of 173.53° and 167.4° respectively. However, tab An approximately oscillate in phase with the south relative tab As with a small phase difference of 6.8°.

Table 6.5: Phase angle in degrees for tabs rows A, C and E

Row	n	e	s	w
A	0°	-173.53°	6.8°	-167.4°
C	-135.85°	32.32°	-138.96°	32.11°
E	50.75°	-131.83°	48.5°	-140.77°

Finally we compute the natural frequency of the trapezoidal tabs by using the Block Lanczos mode extraction method [ANSYS, 2015]. The natural frequency f_N is equal to 5.1 (Hz). An important feature is that the structural oscillation frequencies of all the tab appear to be really close to the natural frequency with a value f_e=4.86 (Hz), leading to a resonance effect. This resonance effect will synchronize with the frequency of appearance of the vortex modes f_v and will be demonstrated in the section 6.4.2 using the proper orthogonal decomposition technique to analyze the flow. The FFT on the displacement signal is presented in Figure 6.4 to clearly identify a peak oscillation frequency close to the fundamental frequency. The tabs in the three rows A, C and E display higher power spectrum density (PSD) peaks than those located in rows B and D at the fundamental frequency. This is due to the fact that the energy transfer between the fluid and the tabs at locations A, C and D are more significant and results eventually in larger displacement amplitudes than rows B and D. However, with a lower number of rows that are tangentially rotated as rows B and D (as opposed to three non rotated rows A, C and D), the interaction and energy transfer between the tabs and the fluid forces is smaller and results in lower PSD peaks as shown in Figure 6.4 (b) and (d), which eventually leads to smaller oscillation amplitudes.

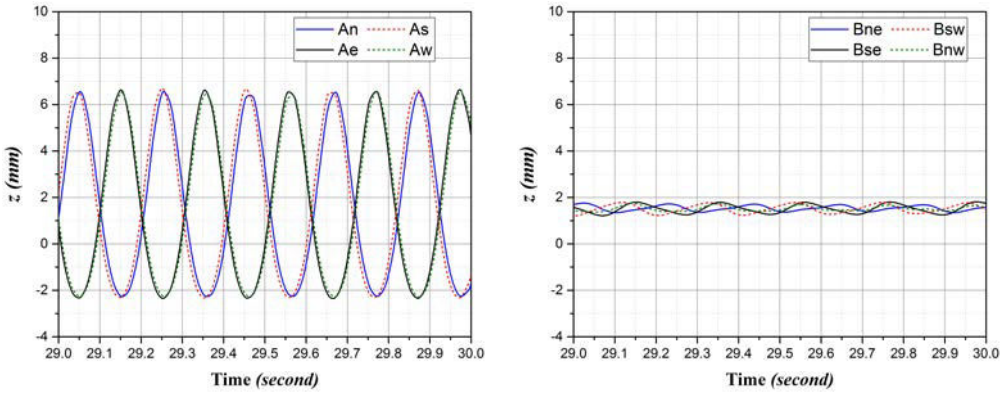

(a)

(b)

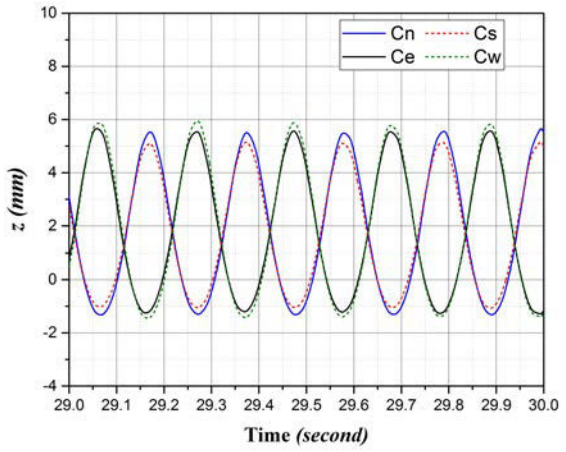

(c)

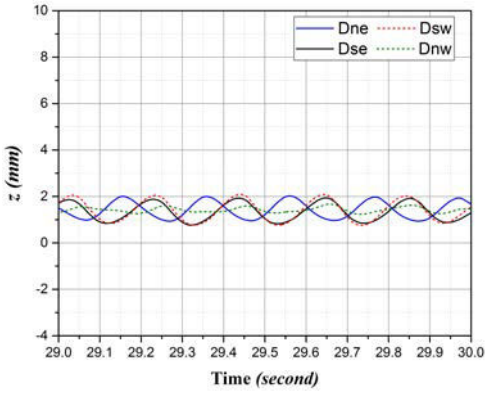

(d)

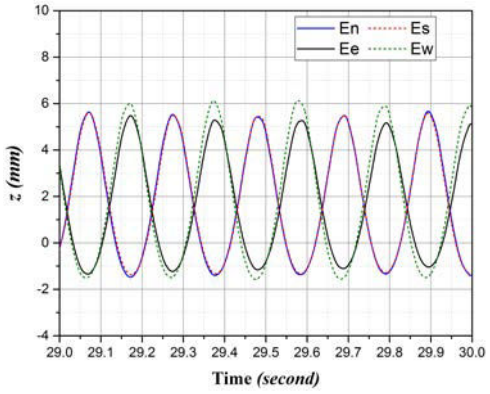

(e)

Figure 6.2: Structure oscillations in z direction during the last one second for the FVG case at different row positions (a) row A, (b) row B, (c) row C, (d) row D and (e) row E as a function of time

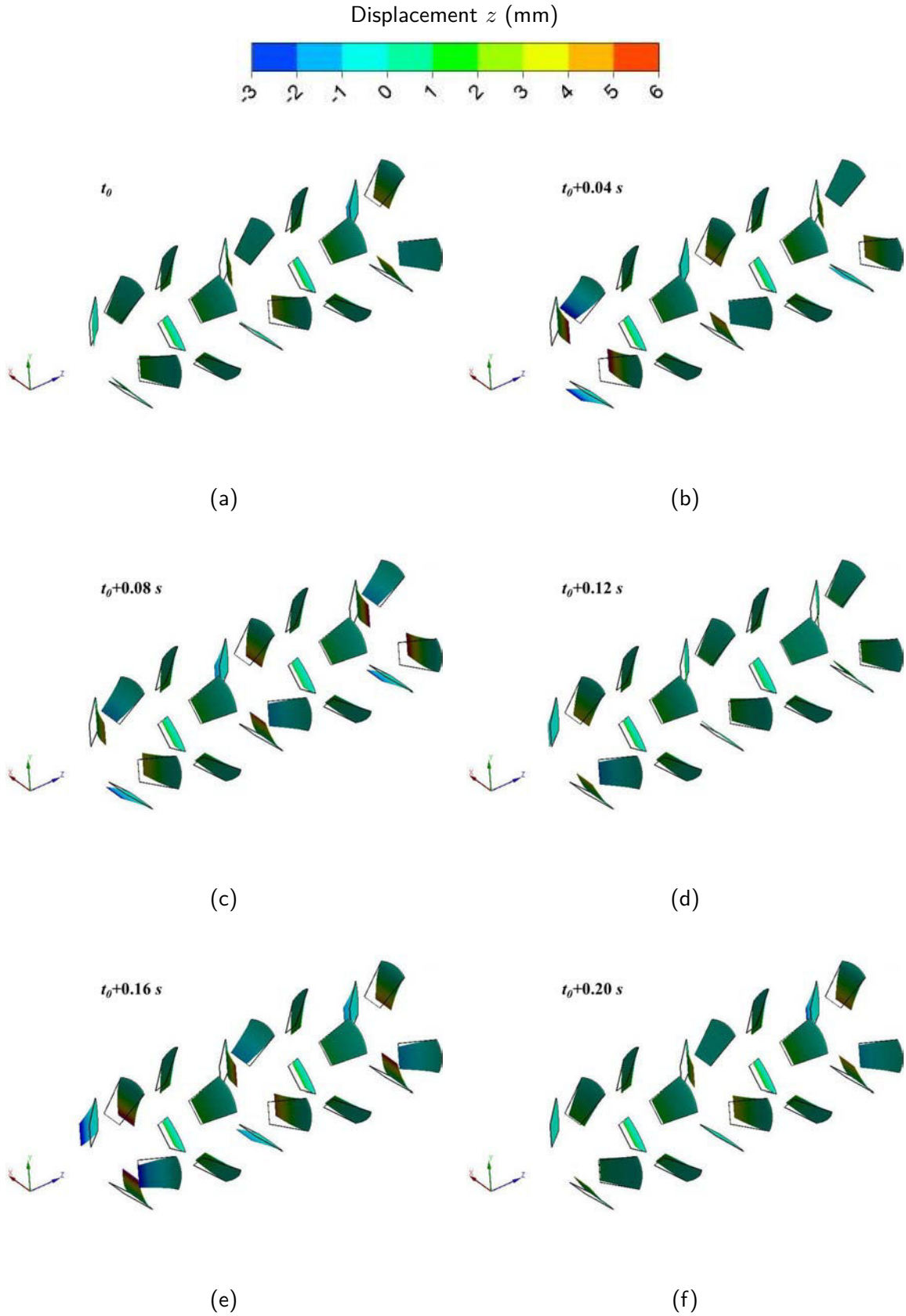

Figure 6.3: 3D perspective view of tabs deformations during one period of oscillation; the fixed wireframe represents the initial position of every tab

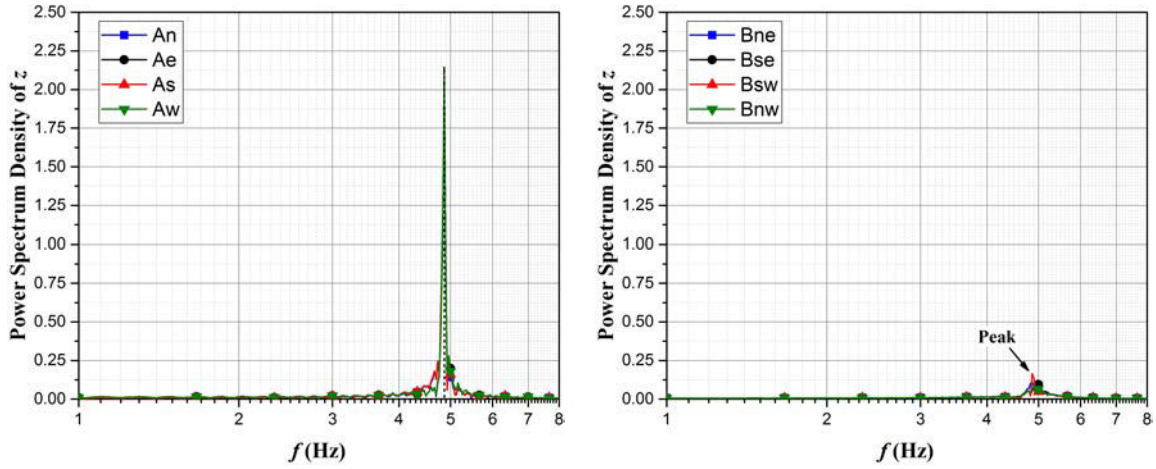

(a)

(b)

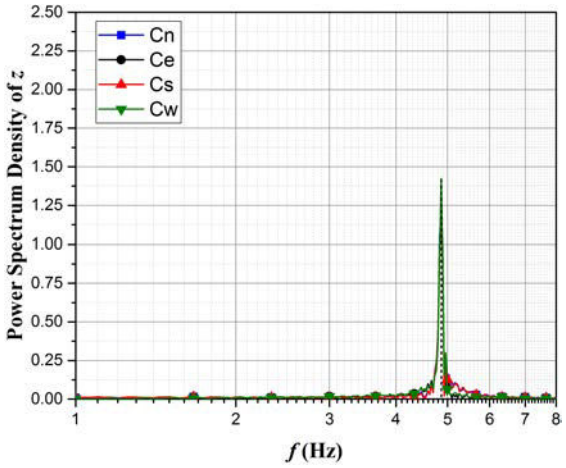

(c)

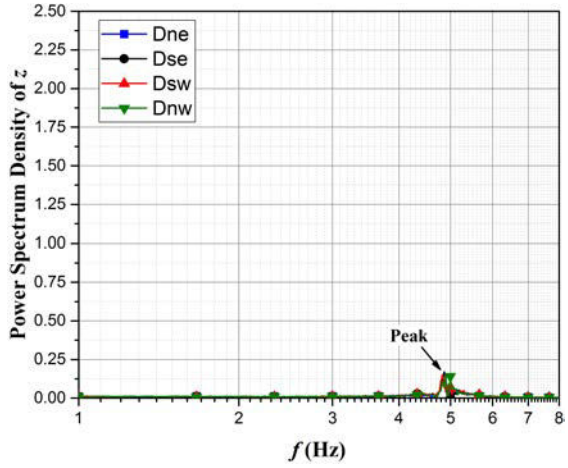

(d)

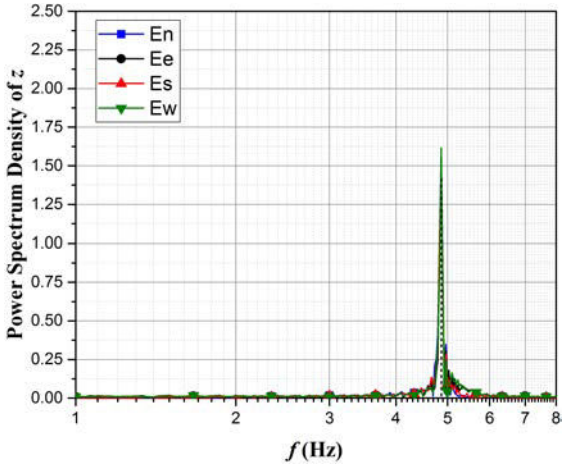

(e)

Figure 6.4: Power Spectrum Density of the displacement signal for FVG case at different row positions (a) row A, (b) row B, (c) row C, (d) row D and (e) row E

6.4.2 Flow patterns and proper orthogonal decomposition (POD)

Figure 6.5 shows the helicity distribution at different row positions for the RVG case, typically downstream of row A in Figure 6.5 (a), row C in Figure 6.5 (b) and row E in Figure 6.5 (c). The helicity ($H = \mathbf{u}.\mathbf{w}$) is defined as the dot product of the velocity vector $\mathbf{u}$ and the vorticity vector $\mathbf{w}$.

Trapezoidal vortex generators when set at a certain angle relative to the pipe wall can create a pressure difference between the high momentum area of the core fluid and the low momentum area downstream in the wake region. This effect initiates a swirling motion that gives birth to two large counter-rotating vortices (CVP) denoted at index positions 1 and 2 as in Figure 6.5 (a), (b) and (c). Secondary counter-rotating vortices are also observed at index positions 3, 4, 5 and 6, above and below every primary CVP. These vortices are caused by the interaction of the high radial velocity induced by the primary CVP with the stagnant fluid region near the wall (index positions 3 and 4) or with the low momentum region at the wake of the tab (index position 5 and 6). In addition to the longitudinal vortices, transverse vortices are also formed whose axis of rotation is perpendicular to the flow direction. Owing to the pressure difference across the tab, the flow wraps around and deflects inwards from the tab sides creating these transverse vortices.

Figure 6.5 (b) shows the helicity distribution downstream row C. The secondary vortices 5 and 6 have reached this row C after being convected from the previous row B. Hence, after each passage of arrays, the vortices increase in size and in strength. Moreover, we can observe the merging process of these secondary vortices with the primary CVP downstream the last row E (Figure 6.5 (c)) to form two large CVP that scale up to the trapezoidal tabs height. Figure 6.5 (d) illustrates then the streamlines and vectors of the velocity field in the wake of tab An. The flow is deflected upwards and over the tip of the tab, since the stagnation pressure in front of the tab is higher than the pressure above the free end. In particular, due to the lower pressure behind the tab, the flow over the top experiences downwash in the wake and results in a reversed vortex motion. These recirculation vortices are considered bad for mixing and heat transfer since the fluid will stay trapped in the wake region and the only transport phenomenon that will be acting is diffusion.

In order to analyze the complex flow structures of the FVG case, we use the proper orthogonal decomposition technique. The present analysis uses the so called "Snapshot POD" which is introduced by Sirovich [Sirovich and Kirby, 1987]. Each time instance is considered to be a snapshot of the flow. The analysis is performed on 1500 snapshots on each of the three planes previously introduced in the RVG case (i.e. plane 1 at $z/d = 1.11$, plane 2 at $z/d = 2.22$ and plane 3 at $z/d = 3.33$). The analysis is based on the helicity scalar field (H_j^k), where index k runs through the N snapshots and j runs through the M positions of the helicity field in a given snapshot (i.e. $H_j = H(x_j, y_j, z_j)$). All the helicity components from the N snapshots are further arranged in a matrix $\mathbf{H}$ as follows:

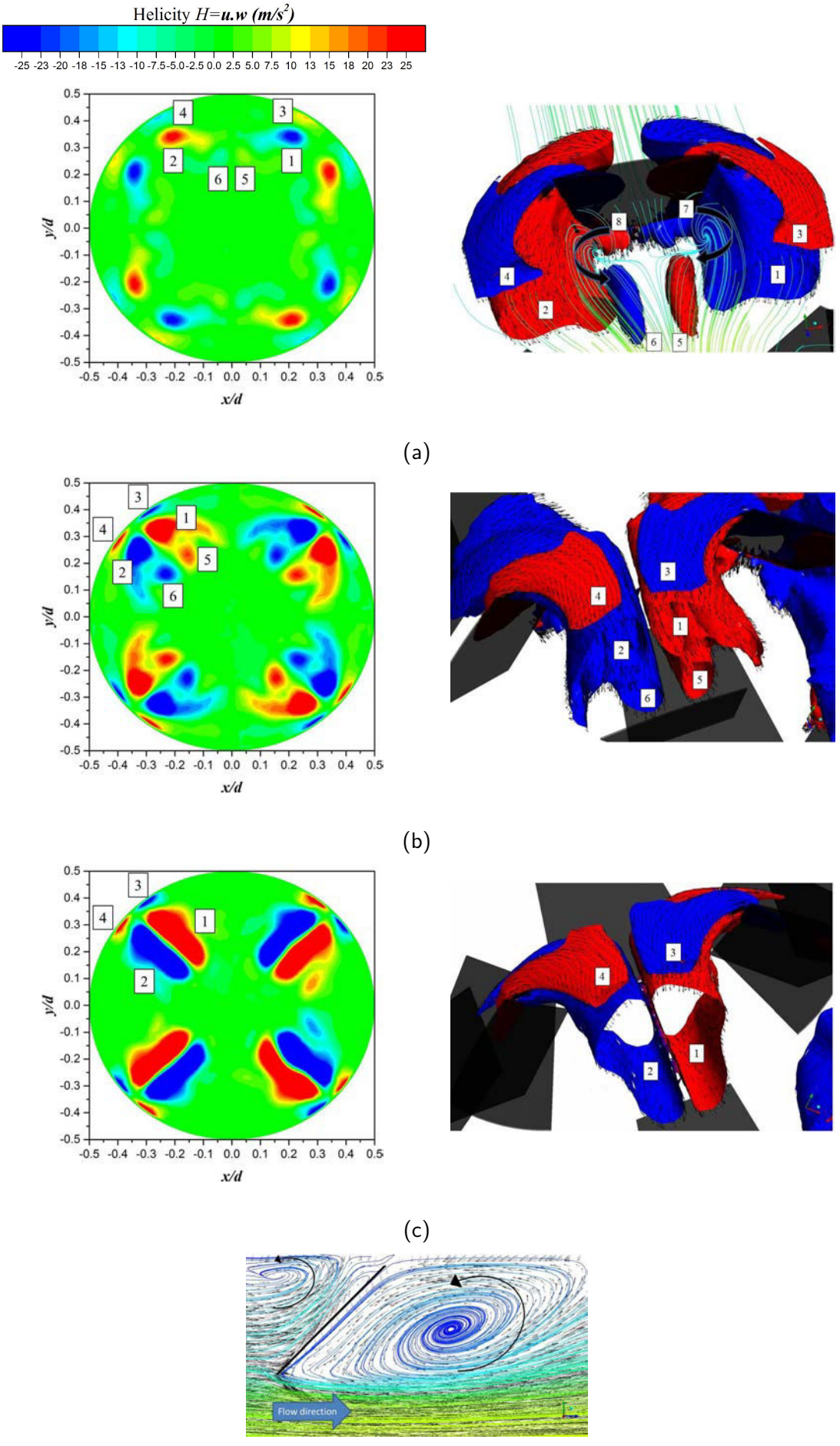

Figure 6.5: Helicity distribution (left side) and 3D view of helicity isoplanes (right side) for the RVG case at row positions, (a) $z/d = 1.11$ (downstream row A), (b) $z/d = 2.22$ (downstream row C) and (c) $z/d = 3.33$ (downstream row E); (d) is a side view of tab An

$$\mathbf{H} = [H^1 \;\; H^2 \;\; ... \;\; H^N] = \begin{bmatrix} H_1^1 & H_1^2 & \cdots & H_1^N \\ H_2^1 & H_2^2 & \cdots & H_2^N \\ \vdots & \vdots & \vdots & \vdots \\ H_M^1 & H_M^2 & \cdots & H_M^N \end{bmatrix} \tag{6.17}$$

Thus, the autocovariance matrix can be created as:

$$\widetilde{\mathbf{C}} = \mathbf{H}^T\mathbf{H} \tag{6.18}$$

The goal of the POD technique is to find a sequence of orthonormal basis functions ϕ^i (POD modes) by solving the eigenvalue problem of the autocovariance matrix $\widetilde{\mathbf{C}}$ as:

$$\widetilde{\mathbf{C}}\mathbf{v}^i = \lambda^i\mathbf{v}^i \tag{6.19}$$

Then according to the size of the eigenvalues, the solutions are arranged in decreasing order as:

$$\lambda^1 > \lambda^2 > ... > \lambda^N \geq 0 \tag{6.20}$$

The basis functions ϕ^i are obtained by projecting $\mathbf{H}$ onto the eigenvectors $\mathbf{v}$ of Eq.(6.19) with subsequent normalization, defined by:

$$\phi^i = \frac{\sum_{k=1}^{N} v_k^i H^k}{\left\| \sum_{k=1}^{N} v_k^i H^k \right\|} \;, \qquad i = 1, ..., N \tag{6.21}$$

where v_k^i is the k^{th} component of the eigenvector corresponding to λ^i from Eq.(6.19). The basis functions represent extracted flow patterns which are considered as coherent structures in the literature.

Each snapshot can be reconstructed from a series of POD modes with expansion coefficients a_i associated with each POD mode. The coefficients of each mode are computed by projecting the original helicity field onto the computed basis functions:

$$\mathbf{a}^k = \boldsymbol{\psi}^T H^k \tag{6.22}$$

where $\boldsymbol{\psi} = [\phi^1 \;\; \phi^2 \;\; ... \;\; \phi^N]$ is introduced. Thus, any snapshot can be represented as a linear combination of the basis functions as follows:

$$H^k = \sum_{k=1}^{S} a_i^k \phi^i \tag{6.23}$$

where S is the number of modes necessary for modeling the characteristics of the large scale data as a low dimensional model.

The POD coefficients $\mathbf{a}^k$ indicate how much a POD mode contributes in each time snapshot. The eigenvalues λ^i are proportional to the kinetic energy present in the flow and by sorting them in a decreasing order as in Eq.(6.20), the most energetic modes can be identified. The percentage of relative kinetic energy associated to each mode can be calculated by:

$$\%\epsilon_i = \frac{\lambda^i}{\sum_{i=1}^{N} \lambda^i} \times 100 \tag{6.24}$$

In the POD study, each plane contains 1500 snapshots, equally spaced at 0.02 seconds apart from each other and each snapshot contains 10000 data points, arranged as 100×100 points in the radial and tangential directions. The POD strategy is performed and implemented using

MATLAB [MATLAB, 2010]. It is convenient to realize that the basis functions do not necessarily reflect a real flow structure in the flow field. Instead, they represent a component of the flow field which can be reconstructed by summing over all the weighted modes.

Table 6.6 shows the values of the energy content distribution of the first 10 modes. The cumulative energy percentage is defined as $\%\xi_i = \sum_{i=1}^{N} \%\epsilon_i$. It can be seen that only the first four modes have significant contributions to the total energy in the unsteady flow with a total cumulative energy of 88.48% for plane 1, 76.14% for plane 2 and 64.94% for plane 3. Higher eigenvalues have contributions less than 5% and thus can be neglected. Figure 6.6 reveals that the convergence for the 100% quantity is smaller when indexing from plane downstream of row A (plane 1) to plane downstream of row C (plane 2) and finally to plane downstream of the last row E (plane 3). This is due to the fact that more complicated and small scales flow structures are being produced or convected from past arrays of tabs into the studied one, where the higher eigenmodes contribute more to the total flow energy. Thus, at plane 3, it is expected to find more small scales and complex flow structures, where higher modes are needed to recover more of the flow kinetic energy.

Figure 6.7 displays the time history variation during one second of the POD coefficients for the first four modes at the three different planes (i.e. plane 1, plane 2 and plane 3). The temporal modes have strong regular shapes and follow periodic cosine and sine functions. From the FFT figures, a peak at 4.86 Hz is observed which is equal to the frequency of oscillation previously calculated in section 6.4.1. This means that the frequency of how the vortices are being created and shed downstream of the tabs is synchronous with the frequency of oscillation and also with the fundamental frequency of the tabs. This phenomenon is identified as lock-in in the literature [Williamson and Govardhan, 2004]. Moreover, it can be seen that the POD coefficient variation of the first mode displays small amplitude oscillations, whether the other three modes oscillate with higher amplitudes around zero. This result suggests that if there is a steady component to the flow, then it will be automatically identified as the first mode. In addition, we observe that as the POD index number increases, the temporal behavior of the POD coefficients is degraded, which suggests that the higher POD modes contribute less to the flow energy.

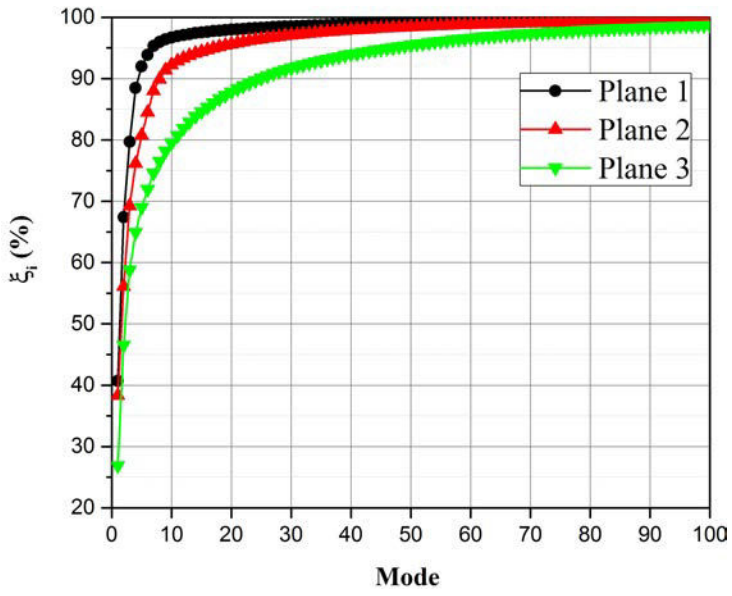

Figure 6.6: Cumulative energy content percentage $\%\xi_i$ associated with POD modes 1-100 using all the 1500 available snapshots for each plane

In the subsequent analysis, we present the four modes and the flow structures at plane 3, since more complex and coherent structures are present at this plane and the mechanism of vortex formation coupled with tabs oscillations is nearly the same for all the planes. Figure 6.8 illustrates the most energetic four modes which contain information about the vortex formation downstream of the last row E in the HEV configuration. It can be observed that mode 1 is the most energetic mode with

Table 6.6: Relative and cumulative modal energy percentage ($\%\epsilon_i$ and $\%\xi_i$) of the first 10 modes at different cross sectional planes for the FVG case

	Plane 1		Plane 2		Plane 3	
Modes	$\%\epsilon_i$	$\%\xi_i$	$\%\epsilon_i$	$\%\xi_i$	$\%\epsilon_i$	$\%\xi_i$
1	40.68	40.68	38.35	38.35	26.88	26.88
2	26.70	67.38	17.75	56.10	19.68	46.56
3	12.30	79.67	13.17	69.27	12.25	58.80
4	8.80	88.48	6.88	76.14	6.14	64.94
5	3.53	92.00	4.59	80.73	4.10	69.04
6	1.87	93.87	3.76	84.49	2.95	71.99
7	1.43	95.30	3.51	88.00	2.60	74.59
8	0.67	95.97	1.92	89.92	1.93	76.51
9	0.44	96.40	1.47	91.39	1.71	78.22
10	0.29	96.69	0.83	92.22	1.30	79.51

vortices arrangement very similar to the previous RVG case shown in Figure 6.5. It is important to note that the counter-rotating vortex pairs in mode 1 are localized near the pipe wall. As we investigate other modes, we can obviously conclude that the vortices are dislocated from their near wall position, and much more assembled at the pipe centerline. In addition, POD modes 3 and 4 represent weaker and higher number of small scale vortices, which represents 12.25% and 6.14% of the total flow energy whereas modes 1 and 2 represents 26.88% and 19.68% of the total flow energy. Mode 4 in particular can be associated with the velocity shear layers created at the sides of the tabs as they reach their maximum amplitude positions.

In order to represent a real flow snapshot, POD modes must be multiplied by their POD coefficients. Figure 6.9 shows the original helicity field along the reconstructed field for six time instants and during one period of oscillation. Helicity snapshots are first reconstructed using modes 1 and 2 which contribute to 46.56% of the total flow energy and secondly using all the four dominant modes which contributes to 64.94% of the total flow energy. Slight differences are present between the original and reconstructed data, which validate the implementation of the "Snapshot POD" algorithm notably, an infinite number of POD modes taken into consideration would be leading to the exact original data. The reconstructed data using the four dominant modes highlight well the signature of the flow structures that contributes the most to the flow energy and neglect the smallest energy structures. The first two eigenmodes represent the near wall vortices plus two pairs of counter rotating vortices located at the center which are either formed by the tabs Ee and Ew or the tabs En and Es as they reach their maximum positions. It is clear that the reconstruction using the eigenmodes 1 and 2 predicts all the near wall vortices, however they fail alone to predict the flow structures and the arrangement of the vortices at Figure 6.9 (c) and (e). The vortices at these time instants have a similar distribution and structure to mode 3 and mode 4. By further investigating the reconstructed snapshots using the four modes, we can clearly observe the development of the velocity shear layers along the two sides to the tabs (at index positions 3 and 4) as they reach their maximum positions.

These two velocity shear layers are actually reduced in size when the tabs deform in the opposite streamwise direction. At this plane, the shear layers disappear as the tabs reach their minimum near wall position as depicted in Figure 6.9 (c). New formation of the shear layers restarts at Figure 6.9 (f) where a new cycle of oscillation begins. Moreover, we can notice that the distance between the counter-rotating vortex pairs at index positions 1 and 2 gets smaller as the tabs reach their maximum positions and gets larger at the lower positions, where the tab has a lower impact angle with the flow. This is validated in the evolution of these vortices in Figures 6.9 (b), (d) and (f) for tabs Ee and Ew. Similarly, this phenomenon is observed for vortices at index positions 5 and 6.

In fact, looking at the flow structures in the time instants, an important feature is that the vortices are either arranged as packets in the upper and lower part of the domain or in the left and right part of the domain, since there is a phase shifting in the oscillations between tabs Ee and Ew with tabs En and Es. Hence, the tabs oscillations are associated with the phenomenon of creation, destruction and dislocation of the flow structures. This is found to be in contrast with the RVG case, where all flow structures are present near the wall and are not dislocated from their positions. Figure 6.10 shows the isoplanes of helicity at tab En during one period of oscillation. At Figure 6.10 (a), the tab is at its highest amplitude position. We can observe the velocity shear layer wrapping around the tab sides and being deflected towards the low pressure area in the wake region. As the tabs oscillate in the negative z-direction, these two shear layers change in shape and are more stretched horizontally than vertically since the deformation of the tabs reduces the contact of the flow with the two tabs sides. The velocity shear layers disappear at Figure 6.10 (d). At the minimum tabs position and since the incoming flow experiences a strong adverse streamwise pressure gradient coupled with the cross-stream gradient generated by the curvature of the flow around the tab, two large scale counter-rotating vortices are formed. These vortices resemble to the horseshoe vortex-like structure [Dong and Meng, 2004] which wraps around the tab in the region of the bottom boundary layer and extends with their two arms to the sides of the wake.

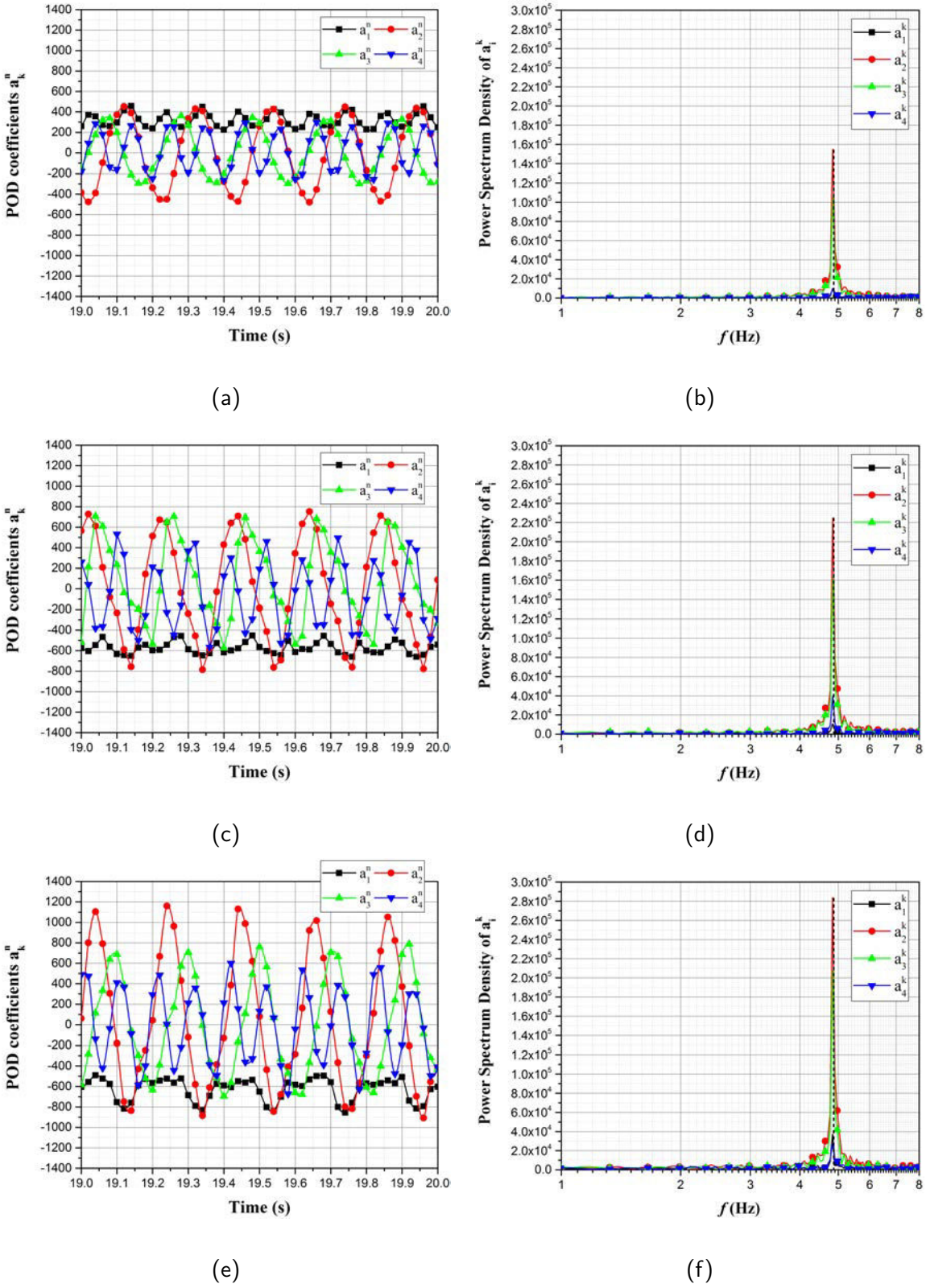

Figure 6.7: POD coefficients time variation of the first four POD modes during one second (left side) and their relative FFT at different plane positions (right side): (a), (b) plane 1 ($z/d = 1.11$); (c), (d) plane 2 ($z/d = 2.22$) and (e), (f) plane 3 ($z/d = 3.33$)

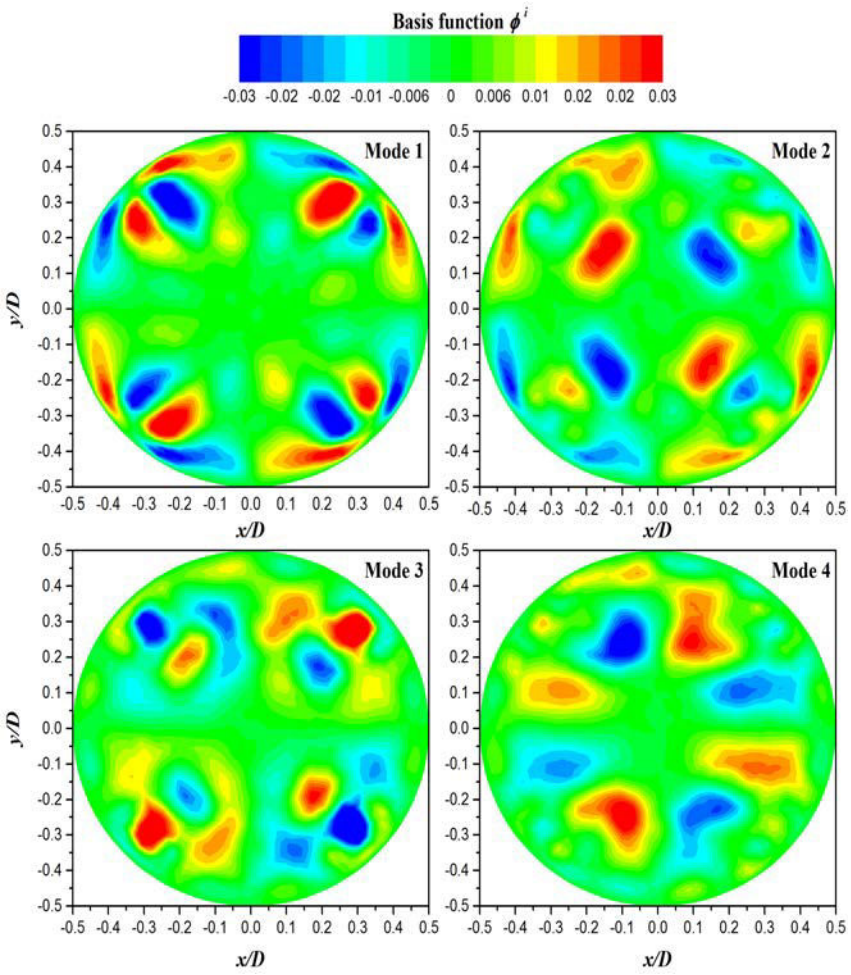

Figure 6.8: The first four spatial modes located at plane 3 ($z/d = 3.33$)

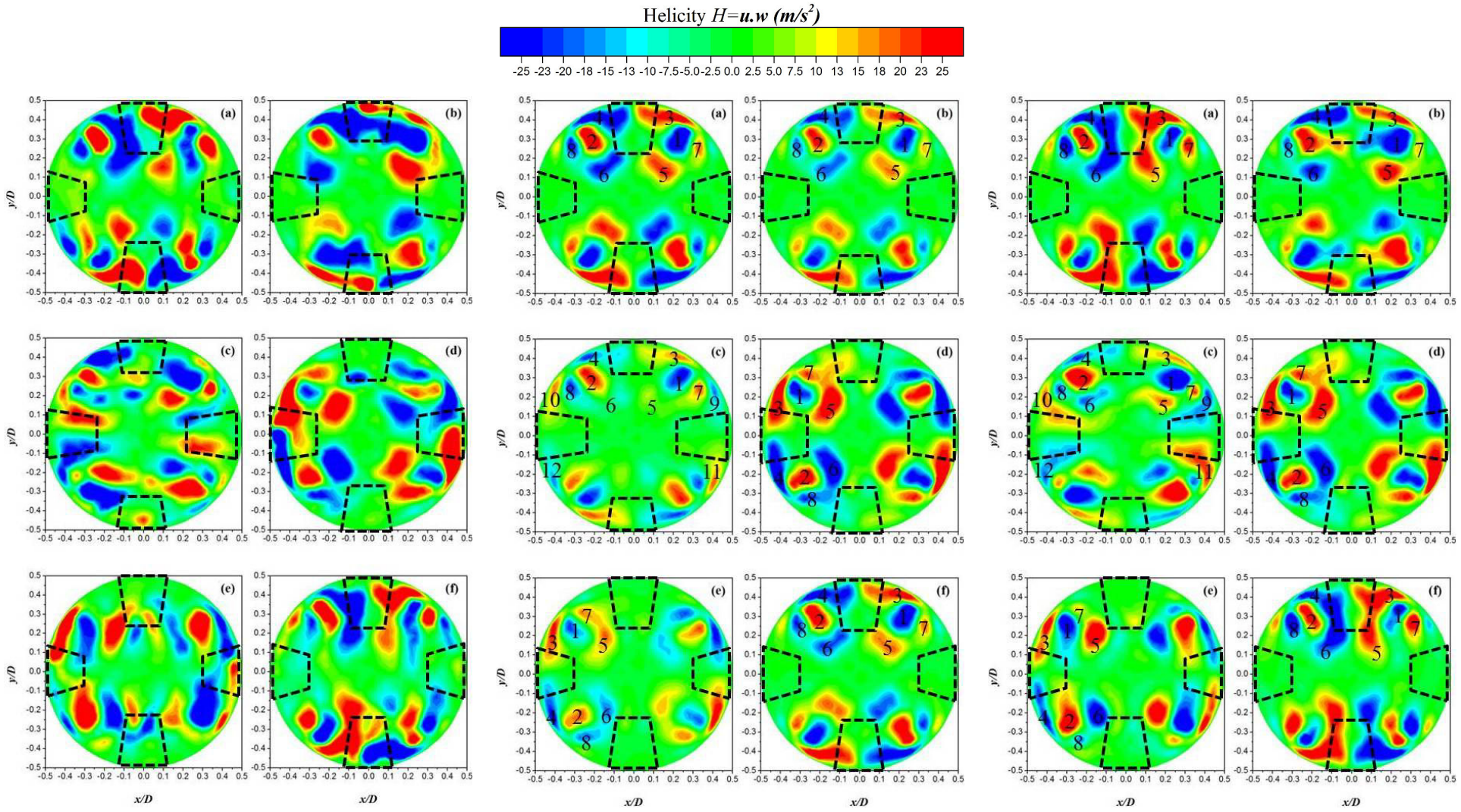

Figure 6.9: Original snapshots (columns 1 and 2), reconstructed snapshots using mode 1 and 2 (columns 2 and 3), and using the four dominant modes (columns 5 and 6) during one period of oscillation at plane 3 ($z/d = 3.33$): (a) t_0, (b) $t_0 + 0.04$ s, (c) $t_0 + 0.08$ s, (d) $t_0 + 0.12$ s, (e) $t_0 + 0.16$ s and (f) $t_0 + 0.20$ s. The dashed lines represent the tabs deformation positions

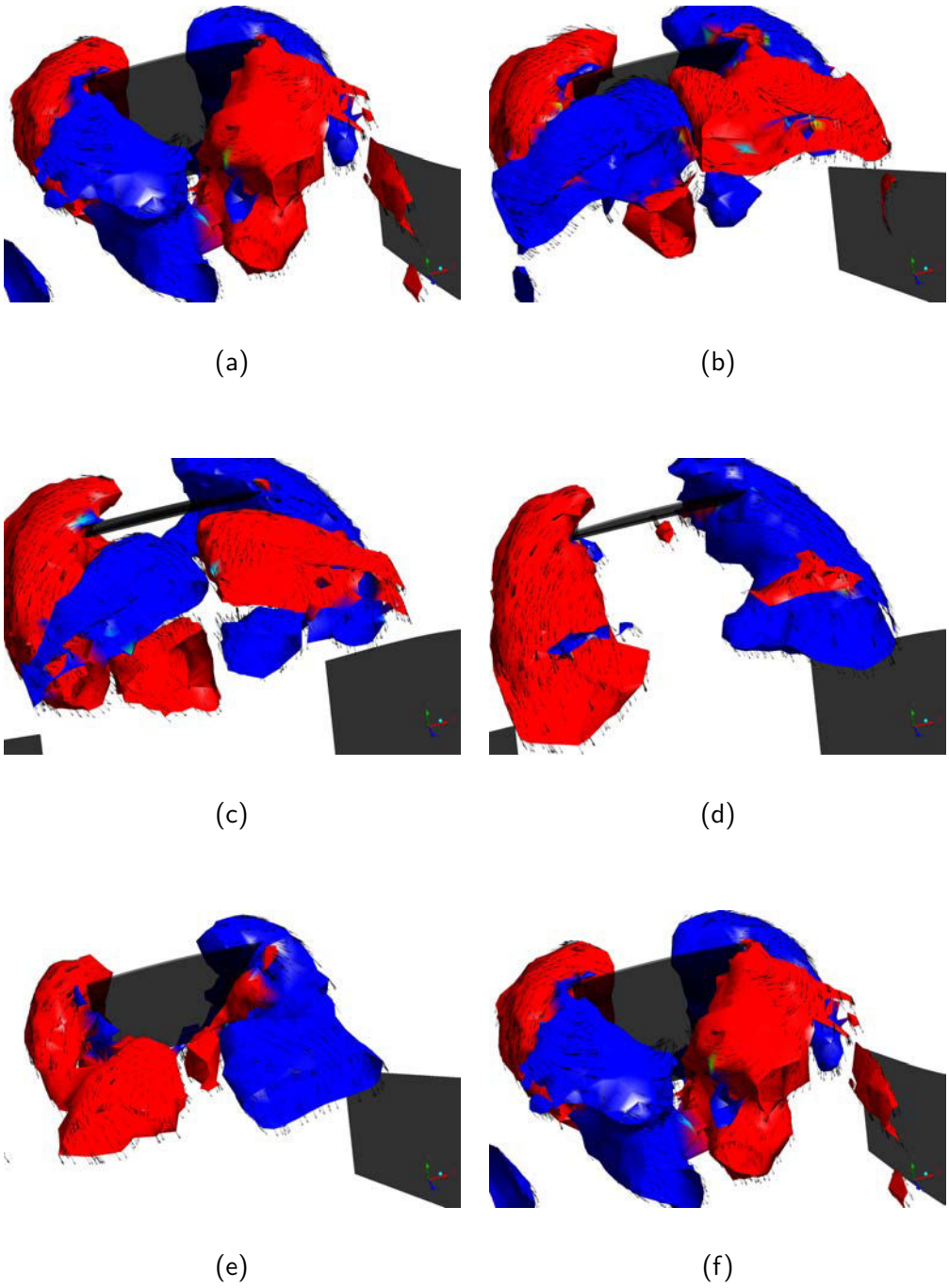

Figure 6.10: Three dimensional view of helicity isoplanes during one period of oscillation: (a) t_0, (b) $t_0 + 0.04$ s, (c) $t_0 + 0.08$ s, (d) $t_0 + 0.12$ s, (e) $t_0 + 0.16$ s and (f) $t_0 + 0.20$ s

6.5 Heat transfer performances

In this section, the temperature distribution comparison between the FVG and RVG cases are discussed, followed by quantification of the heat transfer performance using the parameters of Nusselt number Nu_z, thermal performance factor η and field synergy.

Figure 6.11 shows a side cross sectional view of the temperature distribution contours for the RVG case. It can be observed that the thermal boundary layer is renewed after each passage of tabs rows. However, overheated regions are present directly in the wake region behind the tabs. This can be explained by the streamwise velocity streamlines shown in Figure 6.12 where recirculation regions are found behind the tabs. In these regions, the heat stays trapped in the stagnant transverse vortices and can only be transported to the core region by diffusion. These recirculation regions are known

to have a negative impact on heat transfer performance.

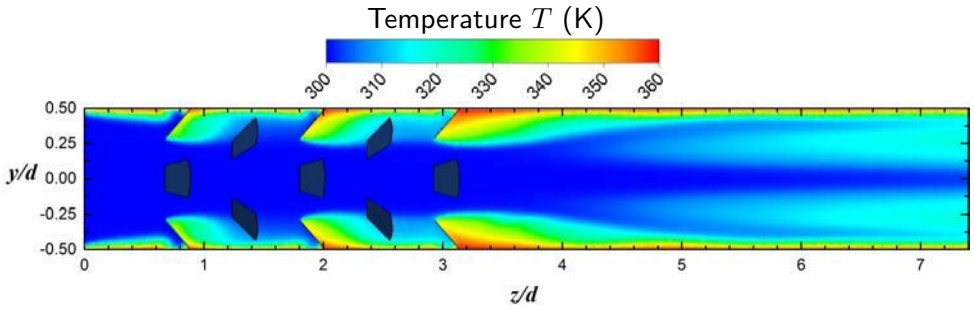

Figure 6.11: Temperature distribution for the RVG case in the tab symmetry plane yz

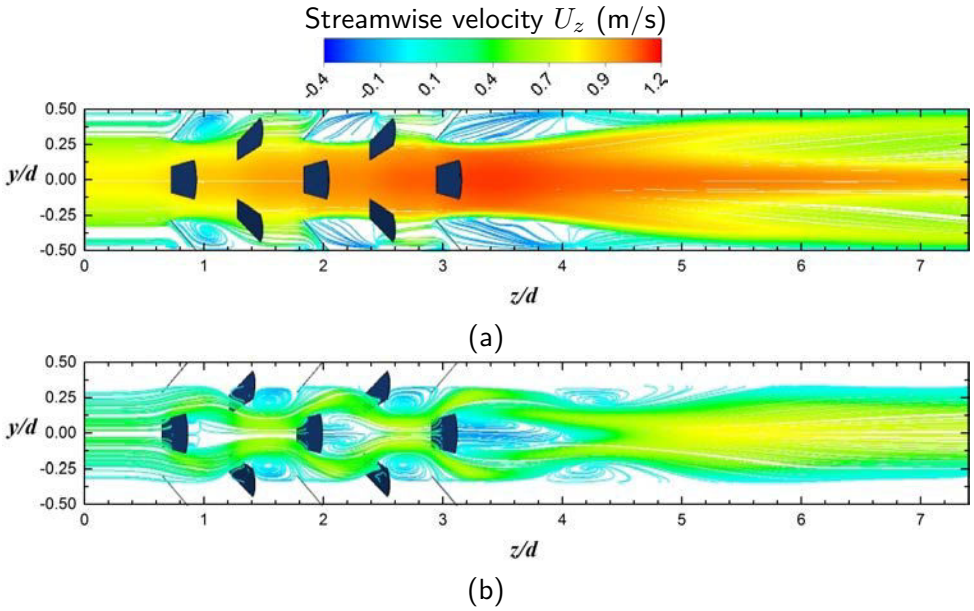

Figure 6.12: Streamwise velocity streamlines for the RVG case: (a) in the symmetry plane yz and (b) in the plane xz at position y/d=0.37

Figure 6.13 plots a side cross sectional view of the temperature distribution contours for the FVG case during one period of oscillation. By comparing Figure 6.11 and Figure 6.13, the presence of FVG displays clearly the impact of tabs oscillation on the wake region and the reduction of the thermal boundary layer and hence the elimination of the overheated regions behind the flexible tabs. Figure 6.14 shows the streamline velocity U_z distribution for the FVG case during one period of oscillation. By looking at Figure 6.14 and the zoomed-in region in Figure 6.15, we can see the unsteadiness of the flow behind the flexible tabs. In fact as a tab oscillates in the streamwise direction, a transverse vortex is formed which scales up to the tab length as seen in Figure 6.15. The transverse vortices are periodically shed due to the shear layer instability generated at the tip of each tab as stored kinetic energy is released and it then oscillates in the opposite streamwise direction. These vortices are convected downstream instead of being stationary like in the RVG case. This unsteadiness plays a crucial role in transporting the thermal energy from the wall to the core of the fluid or inversely from the core of the fluid to the wall.

In addition, by comparing Figure 6.11 and Figure 6.13, we can notice several important differences. In Figure 6.11 and at the wake region downstream of the last row E, the recirculation region extends from $z/d = 3$ to approximately $z/d = 4$ until the flow gets further deviated to a cone expanding shape reaching the wall boundaries after $z/d = 5$ and thus increasing the temperature gradients after this position. In contrast to the preceding observation, Figure 6.13 illustrates the reduction of the thermal boundary layer behind the tabs from $z/d = 3$ to $z/d = 4$ for the FVG case. However, after $z/d = 4$, the RVG case displays higher temperature gradients near the pipe wall and an important

reduction in the thermal boundary layer. In fact, because of the high streamwise deformation of the tabs of row E, the fluid experiences a jet-like flow which is mostly located at the pipe centerline and in partial contact with the wall. This effect deteriorates the heat transfer performance after this position for the FVG case.

In order to quantify the heat transfer process, we calculate the time-averaged local Nusselt number $\overline{\mathrm{Nu}}(z)$ along the pipe length by:

$$\overline{\mathrm{Nu}}(z) = \frac{1}{t_2 - t_1} \int_{t_1}^{t_2} \frac{q''_w(z,t)d}{k_{th}\left(T_w - T_b(z,t)\right)} dt \tag{6.25}$$

where t_1 is the time step at which periodic high amplitude oscillations are reached ($t_1 = 19$ seconds) and t_2 is the final instant in seconds.

Figure 6.16 shows the local Nusselt number for the FVG, RVG and empty pipe simulations. It can be seen that the evolution of the local Nusselt number is spatially periodic due to the presence of equally spaced arrays of tabs for both the FVG and RVG case. At each VG location, the Nusselt number starts to increase from the leading edge of the tab due to the generation of vortices and then progressively decreases downstream. The effect of transverse vortex shedding in the FVG case and the trapped flow remaining in the recirculation region in the RVG case previously mentioned is reflected in the local Nusselt number values. In fact, the FVG case displays higher values of Nusselt number than the RVG case at the wake region of every row i.e. after every peak of Nusselt number. Specifically, in the wake region of the last row ($z/d = 3$ to z/d=4), the Nusselt number is significantly higher in the FVG than in the RVG case, where it keeps decreasing at distances larger than $z/d = 4$. However, the Nusselt number in the RVG starts to increase at position $z/d = 4$, which is directly correlated to the deviation of the flow to the wall boundaries and elimination of the thermal boundary layer as seen in Figure 6.11. The intensification of the spatially averaged local Nusselt number ($\frac{1}{L}\int_0^L \mathrm{Nu}_z dz$) with respect to the empty pipe flow is about 112% for the FVG case and 105% for the RVG case.

Nevertheless, another difference found between the RVG and FVG cases from the plots of local Nusselt number in Figure 6.16 is that the peaks of Nu_z for the RVG case are surprisingly higher than the FVG case at positions where the tabs undergo high amplitude oscillations (row A ($z/d = 0.83$), row C ($z/d = 1.96$) and row E ($z/d = 3.07$)). Moreover, at the positions where the flaps have negligible oscillation amplitudes, the peaks for the FVG case are higher than that of the RVG case (row B ($z/d = 1.40$), row D ($z/d = 2.52$). To better explain the discrepancies of the peak local Nusselt between both cases and the reasons why the FVG case displays higher Nu_z peaks at low oscillation amplitudes and lower Nu_z peaks at higher oscillation amplitudes, we investigate the behavior of flow and heat transfer performances at rows C and D (Nu_z peaks at $z/d = 1.96$ and $z/d = 2.52$).

Figure 6.17 (a) and (b) shows the streamwise velocity at the center of the pipe along the x and y directions at position $z/d = 1.96$ where the tabs undergo high amplitude oscillation, whereas Figure 6.17 (c) and (d) are considered at positions $z/d = 2.52$ and associated with small amplitude oscillation. We can observe from Figure 6.17 (a) and (b) that the streamwise velocity for the FVG case is higher than the RVG case at the center due to the increase in the blockage area as the tabs deform to their streamwise positions. However, the velocity profile for the FVG case is narrower than the RVG case as the distance increases further from the center of the pipe. This is validated by the velocity contours of Figure 6.14 (c) as we can observe at position $z/d = 1.96$ the flow experiencing a high speed at the narrower neck area and a low speed at the wake of the tabs. The high speed flow impinges the next row D at position $z/d = 2.52$. We can clearly see the difference in the RVG case from Figure 6.12 where the flow have a wider neck region at $z/d = 1.96$ (row C) with lower maximum velocity at the center than the FVG case. Consequently, the flow impinges the next row D at position $z/d = 2.52$ at lower speed specifically at the wall since row D is tangentially rotated by an angle of $45°$. This is supported by the velocity profile of Figure 6.17 (c) and (d) where we can see the higher velocity distribution for the FVG case at positions $y/d < -0.3$ and $y/d > 0.3$ or $x/d < -0.3$ and $x/d > 0.3$. The increase in the velocity gradients near the wall further increases the convective heat transfer and induces an improved thermal effect.

Furthermore, we use the field synergy principle [Guo et al., 1998, Guo et al., 2005, Tao et al., 2002] to explain the difference between the FVG and RVG cases. The field synergy is briefly demonstrated hereafter, by considering every snapshot of the simulation as a one steady state solution and integrating the steady state form of the energy equation over the area of a given cross-section:

$$\rho_f C_p \iint_A (\boldsymbol{U} \cdot \boldsymbol{\nabla} T_f) dxdydz = q''_w \propto \mathrm{Nu} \tag{6.26}$$

where the total heat flux q''_w is proportional to the Nusselt number Nu. In fact, the Nusselt number depends on the dot product $\boldsymbol{U} \cdot \boldsymbol{\nabla} T_f = \| \boldsymbol{U} \| \times \| \boldsymbol{\nabla} T_f \| \times \cos(\alpha)$, where α is the intersection angle between the velocity vector and the temperature gradient. Usually, a smaller intersection angle means higher convective heat transfer. However, this is not consistently valid since we could have high intersection angles but also an increase in the magnitudes of velocity and the temperature gradients $\| \boldsymbol{U} \|$ and $\| \boldsymbol{\nabla} T_f \|$. Consequently, to have a feel of the heat transfer, we instead use the absolute values of the dot product $|\boldsymbol{U_{xy}} \cdot \boldsymbol{\nabla_{xy}} T_f|$ since it combines the effect of velocity and temperature gradients magnitudes and the intersection angles. The index xy denotes the velocity and temperature gradient in the (x,y) reference frame, in order to see the effect of secondary flows generated by the streamwise vortices on the heat transfer in a given cross sectional plane XY [Habchi et al., 2011]. In order to validate the use of the dot product $|\boldsymbol{U_{xy}} \cdot \boldsymbol{\nabla_{xy}} T_f|$, we plot the time variation of the integral $\iint_A |\boldsymbol{U_{xy}} . \boldsymbol{\nabla_{xy}} T_f| dxdy$ and the Nusselt number Nu as in Figure 6.18 (a) and (b) at cross sectional positions $z/d = 1.96$ and $z/d = 2.52$ for the FVG case. The results validate the use of $|\boldsymbol{U_{xy}} \cdot \boldsymbol{\nabla_{xy}} T_f|$ to assess the heat transfer behavior since the maximum and minimum peaks of local Nusselt are synchronized with the peaks of $\iint_A |\boldsymbol{U_{xy}} . \boldsymbol{\nabla_{xy}} T_f| dxdy$. The relative open symbols in Figure 6.18 (a) and (b) represent the RVG case. In fact, the values $|\boldsymbol{U_{xy}} \cdot \boldsymbol{\nabla_{xy}} T_f|$ are lower than those of the RVG case at $z/d = 1.96$ (row C) and are higher at $z/d = 2.52$ (row D), which correlates well with the local variation of Nusselt number displayed in Figure 6.16.

In order to relate the tabs displacement positions with the heat transfer performances, six time instants are shown in both Figure 6.18 and Figure 6.19 which cover an oscillation period and are equally spaced by 0.04 seconds. Furthermore, to compare the FVG and RVG cases at positions $z/d = 1.96$ and $z/d = 2.52$, the contours of $|\boldsymbol{U_{xy}} \cdot \boldsymbol{\nabla_{xy}} T_f|$ are shown in Figure 6.20 for the RVG case and in both Figure 6.21 and Figure 6.22 for the FVG case during these time instants. High values of $|\boldsymbol{U_{xy}} \cdot \boldsymbol{\nabla_{xy}} T_f|$ are observed at the two sides of each tabs in Figure 6.20, which highlights the formation of the counter rotating vortex pair (CVP), and at the free end where a shear layer is formed. The CVP radially mixes the hot near wall fluid with the cold core fluid. To compare the heat transfer performance with the FVG case, Figure 6.21 illustrates an important difference with the RVG case. In fact, at the six instants, the high values of $|\boldsymbol{U_{xy}} \cdot \boldsymbol{\nabla_{xy}} T_f|$ are not present in the four tab positions (n, e, s, w) at once. In contrast to the RVG case, they are either found at n and s or e and w since the tabs Cn and Cs oscillate out of phase with Ce and Cw. Another reason for this behavior is that if we take for example the tabs Cn and Cs, the high values of $|\boldsymbol{U_{xy}} \cdot \boldsymbol{\nabla_{xy}} T_f|$ are associated with streamwise high amplitude positions as at time instants t_2 and t_3. As the tabs tend to deform in their opposite streamwise minimal position, some vortex structures disappear especially the two shear layers that wrap the sides of the tabs. Consequently this has a negative effect on heat transfer and explain why the RVG case has better thermal performance at the position where the FVG undergo phase shifted oscillation, with maximum values of $|\boldsymbol{U_{xy}} \cdot \boldsymbol{\nabla_{xy}} T_f|$ found at two positions only at a given time whereas the RVG case display high values at the four positions simultaneously.

Furthermore at position $z/d = 2.52$ (row D), the FVG displays a higher peak of local Nusselt number than the RVG case as stated before in Figure 6.16. The distribution of $|\boldsymbol{U_{xy}} \cdot \boldsymbol{\nabla_{xy}} T_f|$ between Figure 6.20 (b) and the six time instants in Figure 6.22 is compared. The effect of the high amplitude oscillation at row C is in fact reflected in row D. Thus, as the tabs of row C (Cn and Cs) reach their maximum streamwise position at t_3 as shown in Figure 6.21, the flow accelerates and impinges row D at the north and south positions at t_4. It can be seen from Figure 6.15 (c) that the transverse vortex formed at the highest amplitude position of row C is reached after 0.04 seconds to row D as shown in Figure 6.15 (d). As expected, the effect of the high amplitude oscillation is seen at row D at time t_4 as Figure 6.22 displays higher values of $|\boldsymbol{U_{xy}} \cdot \boldsymbol{\nabla_{xy}} T_f|$ than the RVG case at the north and south position at t_4 , hence better heat transfer. The same holds true for the east and west

positions as we can observe in Figure 6.22 and specifically at t_6 where two regions of higher values of $|\boldsymbol{U_{xy}} \cdot \boldsymbol{\nabla_{xy}} T_f|$ are being formed due to the fluid acceleration caused by the maximum displacement of tabs Ce and Cw at time t_5.

The global Nusselt numbers Nu_{0-L} calculated for the empty pipe, RVG and FVG cases are next summarized in Table 6.7. The temporal mean of the FVG case is performed from an initial time $t_i = 19$ seconds till the final time $t_f = 30$ seconds. The overall heat transfer enhancement with respect to the empty pipe is about 118% for the FVG case and about 97% for the RVG case, which is a good indicator about the ability of the free flexible oscillation in enhancing heat transfer without relying on external additional source of energy. However, in order to compare the thermal efficiency of the RVG and the FVG cases, the thermal performance factor η [Promvonge and Thianpong, 2008] which is defined as the ratio of convective heat transfer in the studied geometry to that in a straight pipe flow can be written as:

$$\eta = \left(\frac{\mathrm{Nu}_{(0-L)}}{\mathrm{Nu}_{(0-L),0}} \right) \left(\frac{f}{f_0} \right)^{-\frac{1}{3}} \tag{6.27}$$

where the 0 subscript stands for the empty pipe results. The RVG case result is $\eta = 0.995$ while the FVG case result is approximately similar $\eta = 0.987$. Although the FVG case increases the overall heat transfer, it also induces a much higher penalty of pressure drop than the RVG case. The tabs motion absorbs the flow kinetic energy and at some time instants increases the pipe blockage ratio when reaching their maximum streamwise position. A further optimization should be thus done on the tabs mechanical properties, angle of attack or arrangement in order to intensify their thermal performance and reduce the pressure drop.

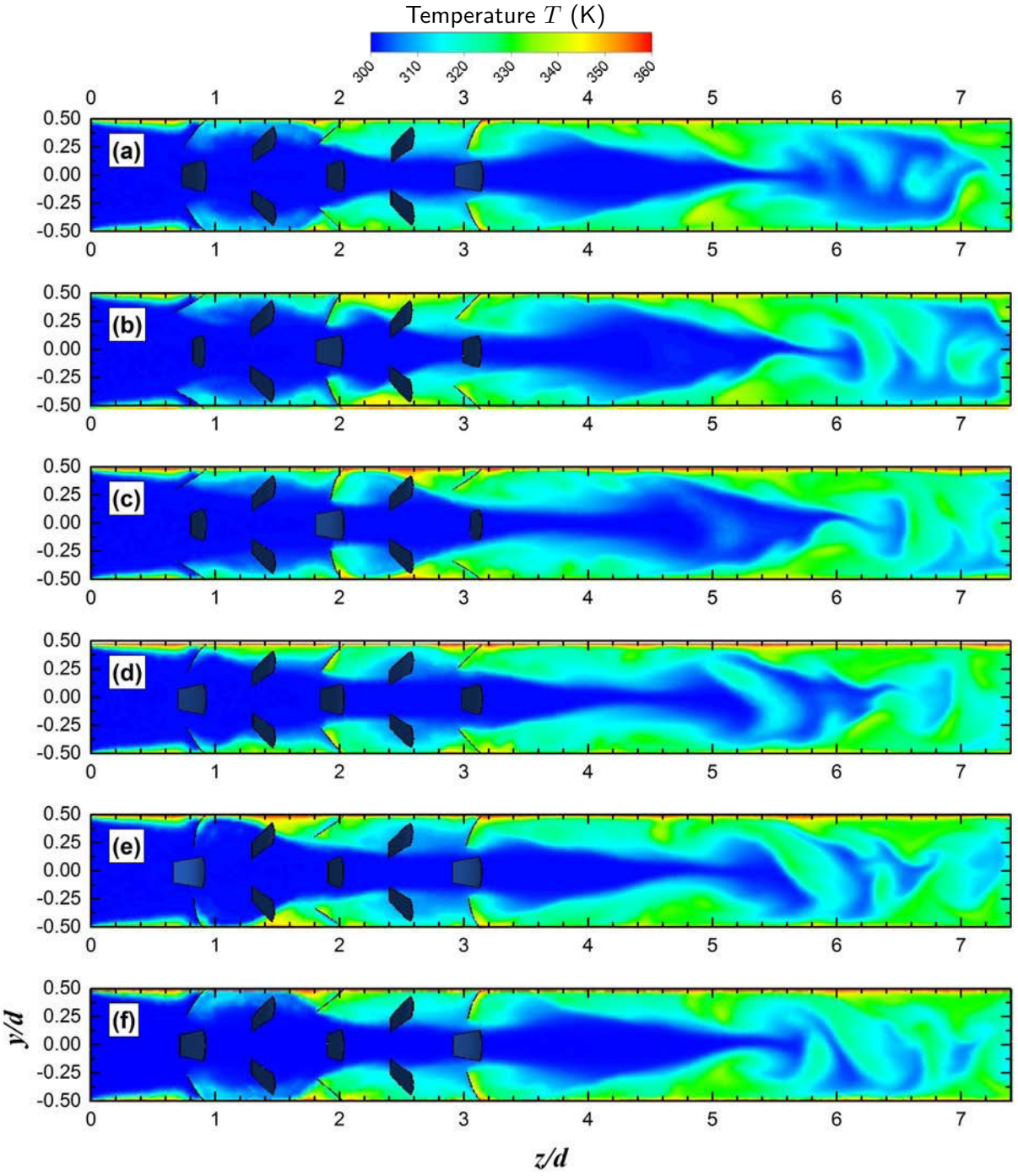

Figure 6.13: Temperature distribution for the FVG case in the tab symmetry plane yz during one period of oscillation: (a) t_0, (b) $t_0 + 0.04$ s, (c) $t_0 + 0.08$ s, (d) $t_0 + 0.12$ s, (e) $t_0 + 0.16$ s and (f) $t_0 + 0.20$ s

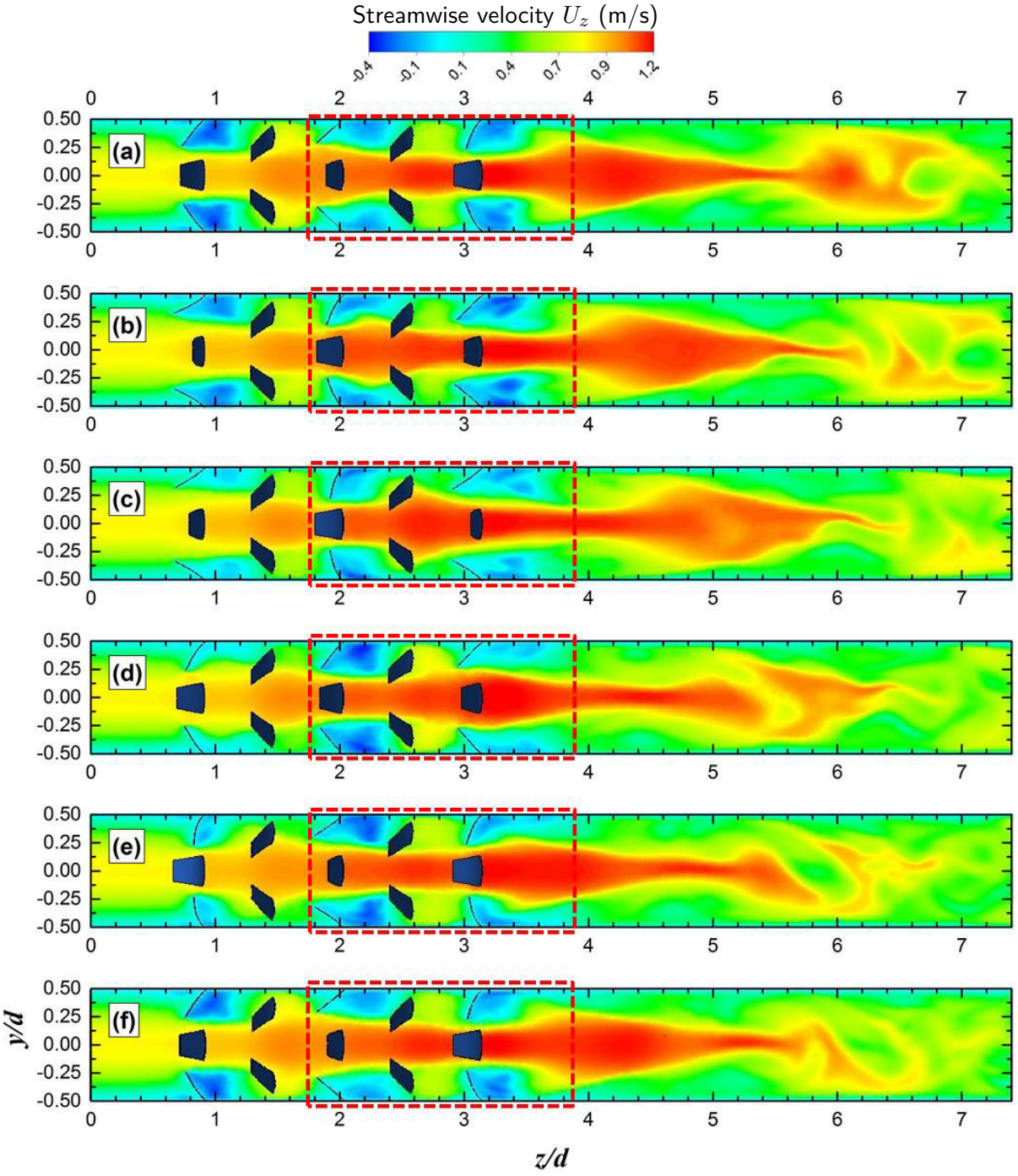

Figure 6.14: Streamwise velocity U_z distribution for the FVG case in the tab symmetry plane yz during one period of oscillation: (a) t_0, (b) $t_0 + 0.04$ s, (c) $t_0 + 0.08$ s, (d) $t_0 + 0.12$ s, (e) $t_0 + 0.16$ s and (f) $t_0 + 0.20$ s. The dotted region is zoomed in and shown in Figure 6.15

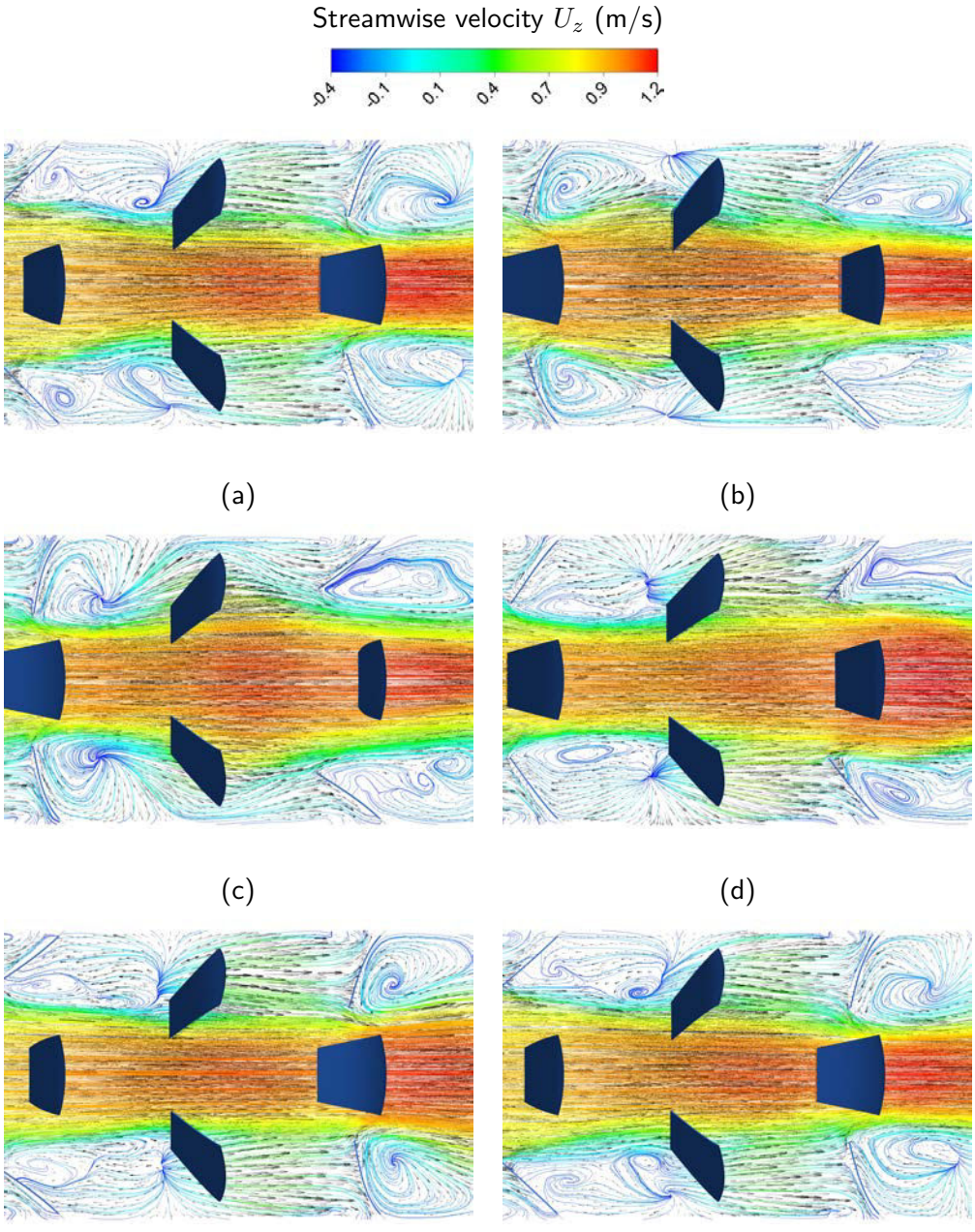

Figure 6.15: The zoomed in streamwise velocity distribution of the dotted region in Figure 6.14

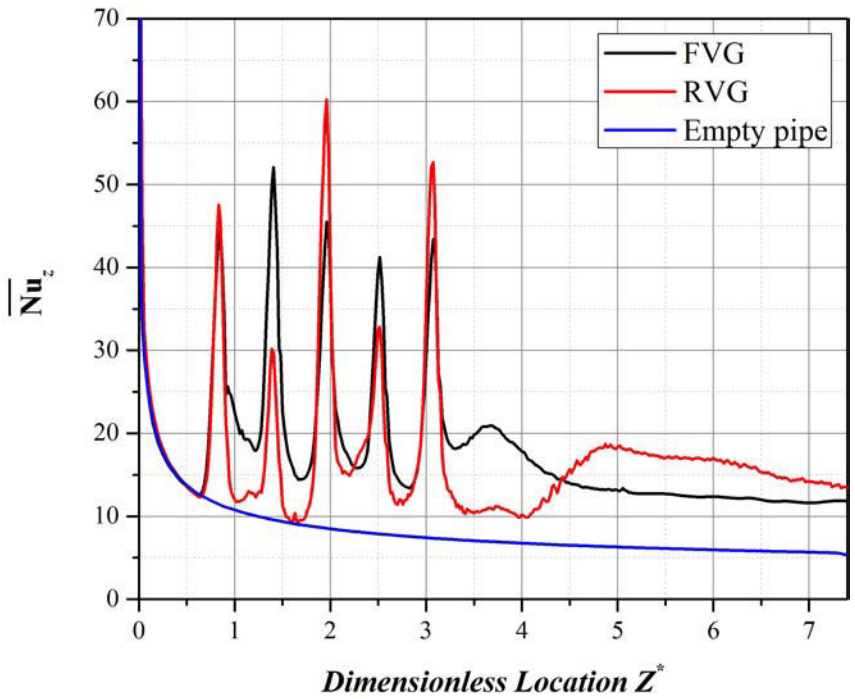

Figure 6.16: Time averaged local Nusselt number $\overline{\mathrm{Nu}}_z$ of the FVG and RVG cases with respect to the dimensionless location Z^*

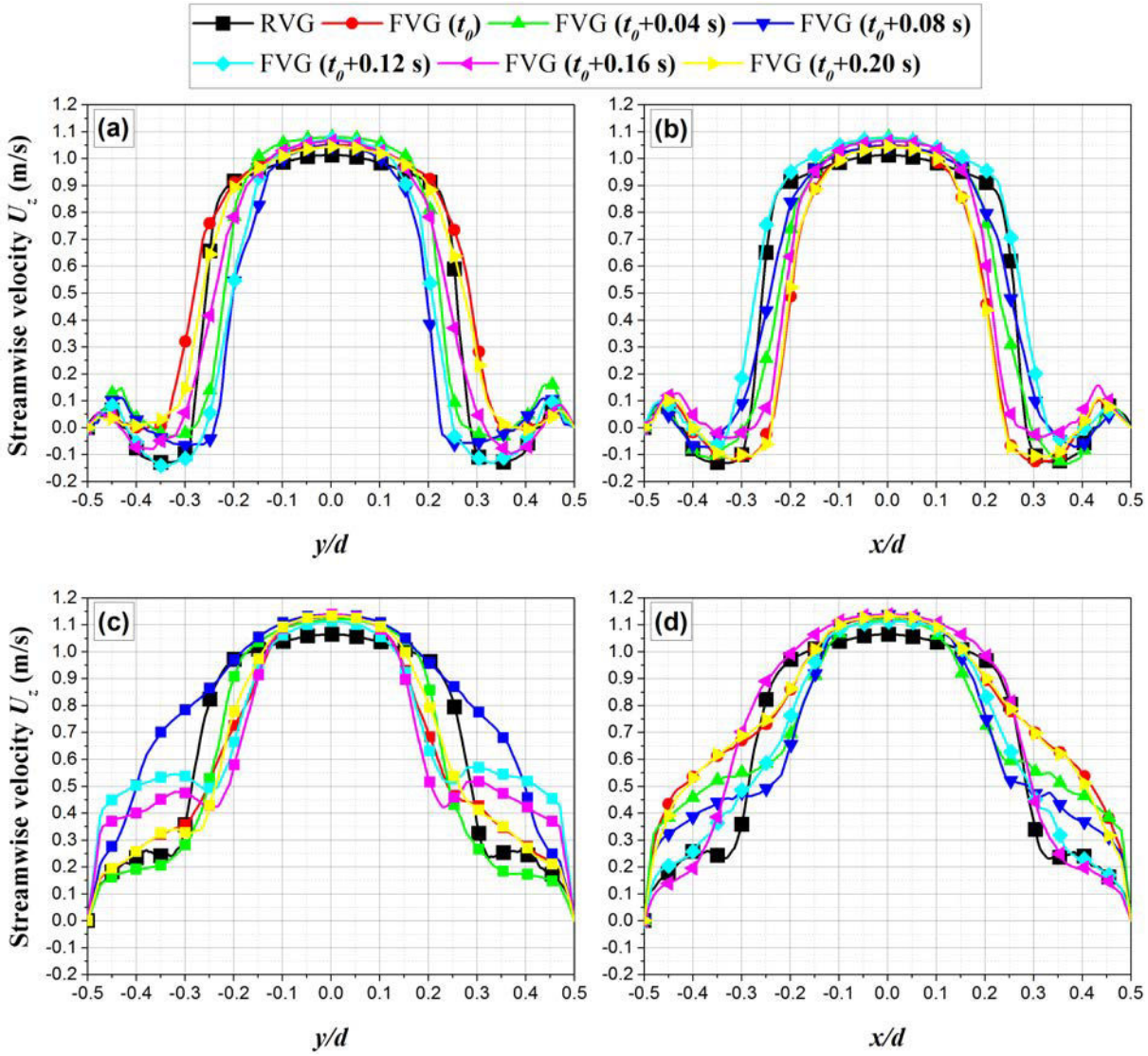

Figure 6.17: Streamwise velocity distribution along x and y directions at two different positions: (a), (b) at $z/d = 1.96$ and (c), (d) at $z/d = 2.52$

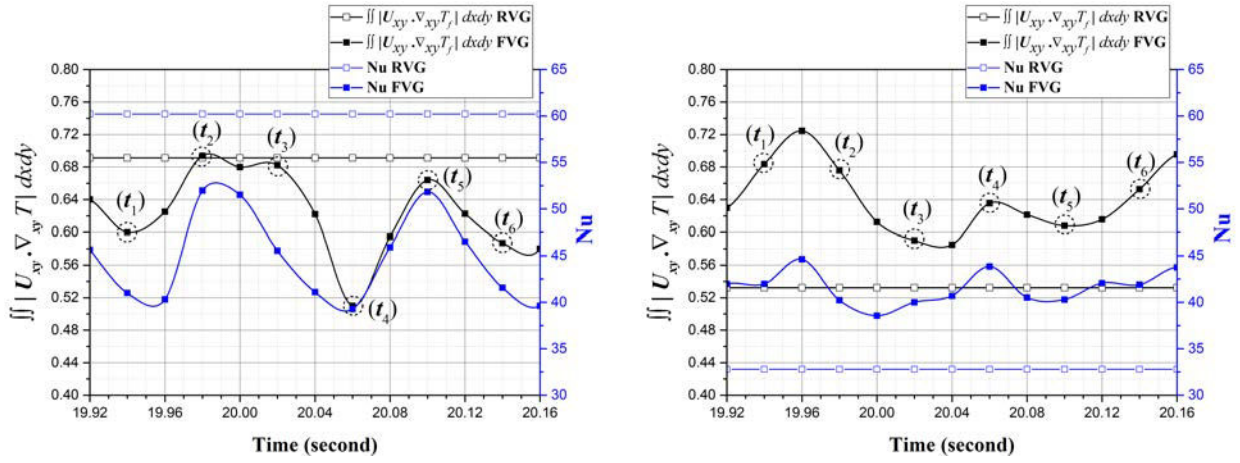

(a) (b)

Figure 6.18: Time variation of local Nusselt number Nu_z and $\iint |\boldsymbol{U_{xy}.\nabla_{xy}}T|dxdy$ during one period of oscillation for the FVG case at two different positions: (a) $z/d = 1.96$ (row C) and (b) $z/d = 2.52$ (row D). The RVG case is represented using constant lines with open symbols

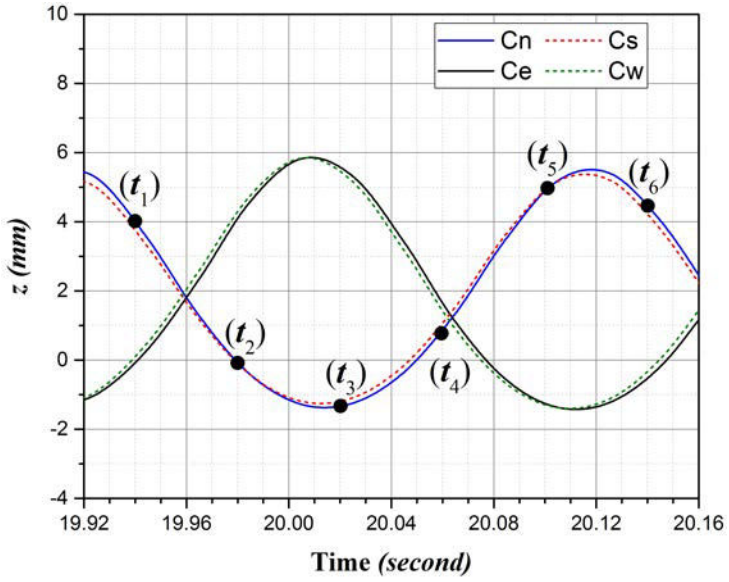

Figure 6.19: Displacement of tabs at row C in the z direction during one period of oscillation

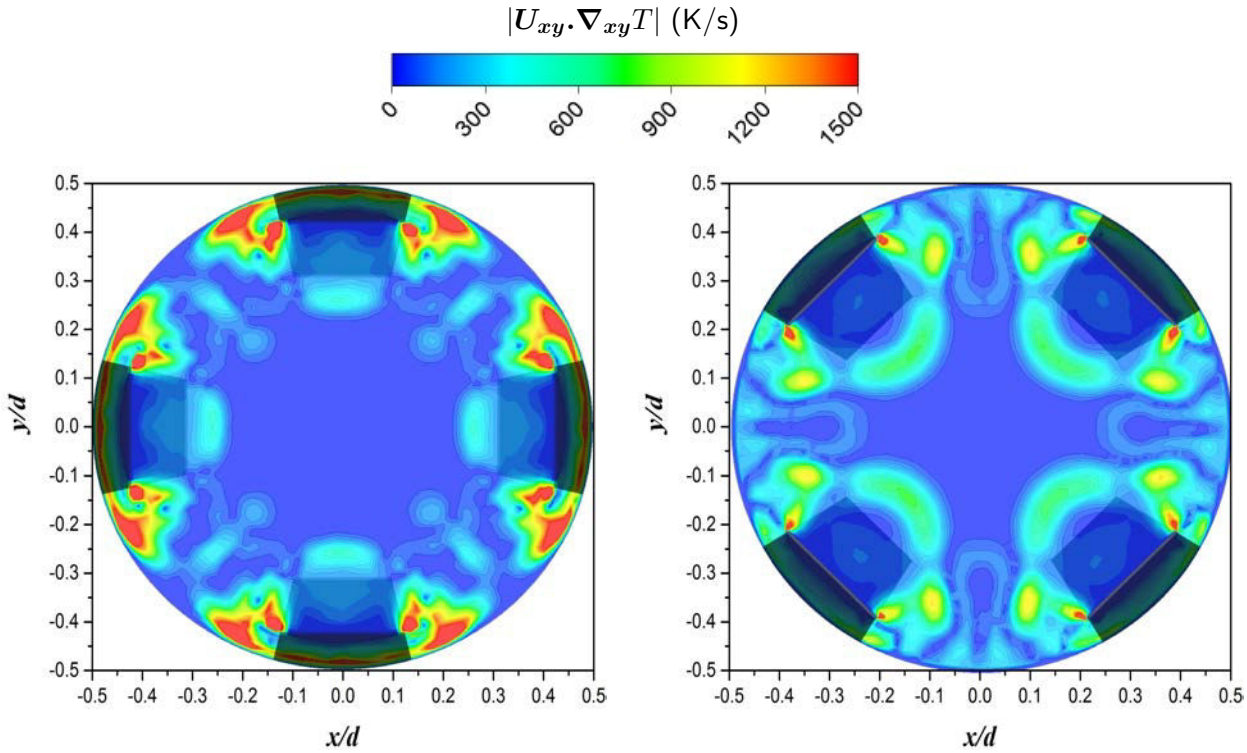

(a) (b)

Figure 6.20: Contours of $|U_{xy}.\nabla_{xy}T|$ for the RVG case at two different positions: (a) $z/d = 1.96$ (row C) and (b) $z/d = 2.52$ (row D)

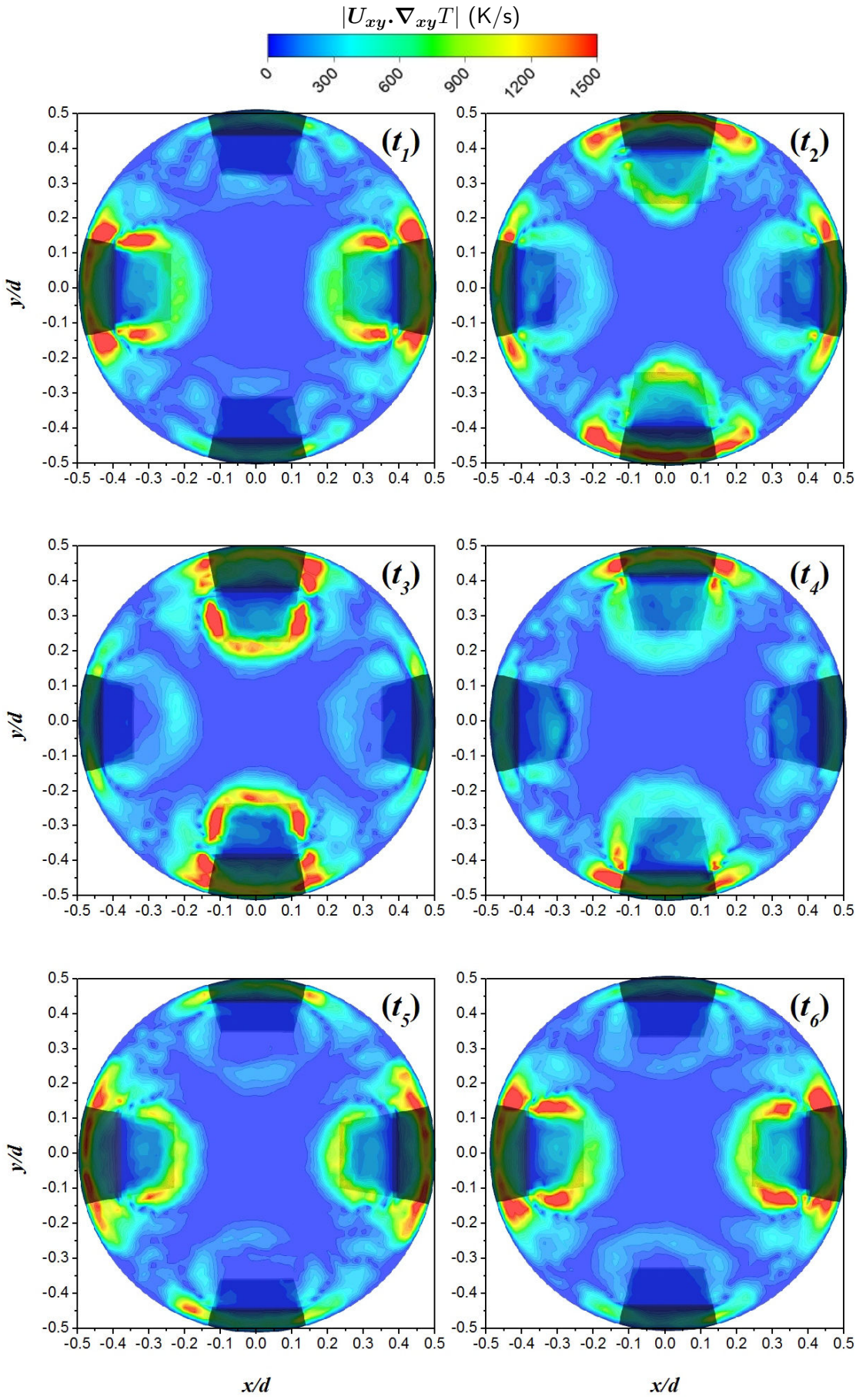

Figure 6.21: Contours of $|U_{xy}.\nabla_{xy}T|$ for the FVG case at position $z/d = 1.96$ (row C) during one period of oscillation

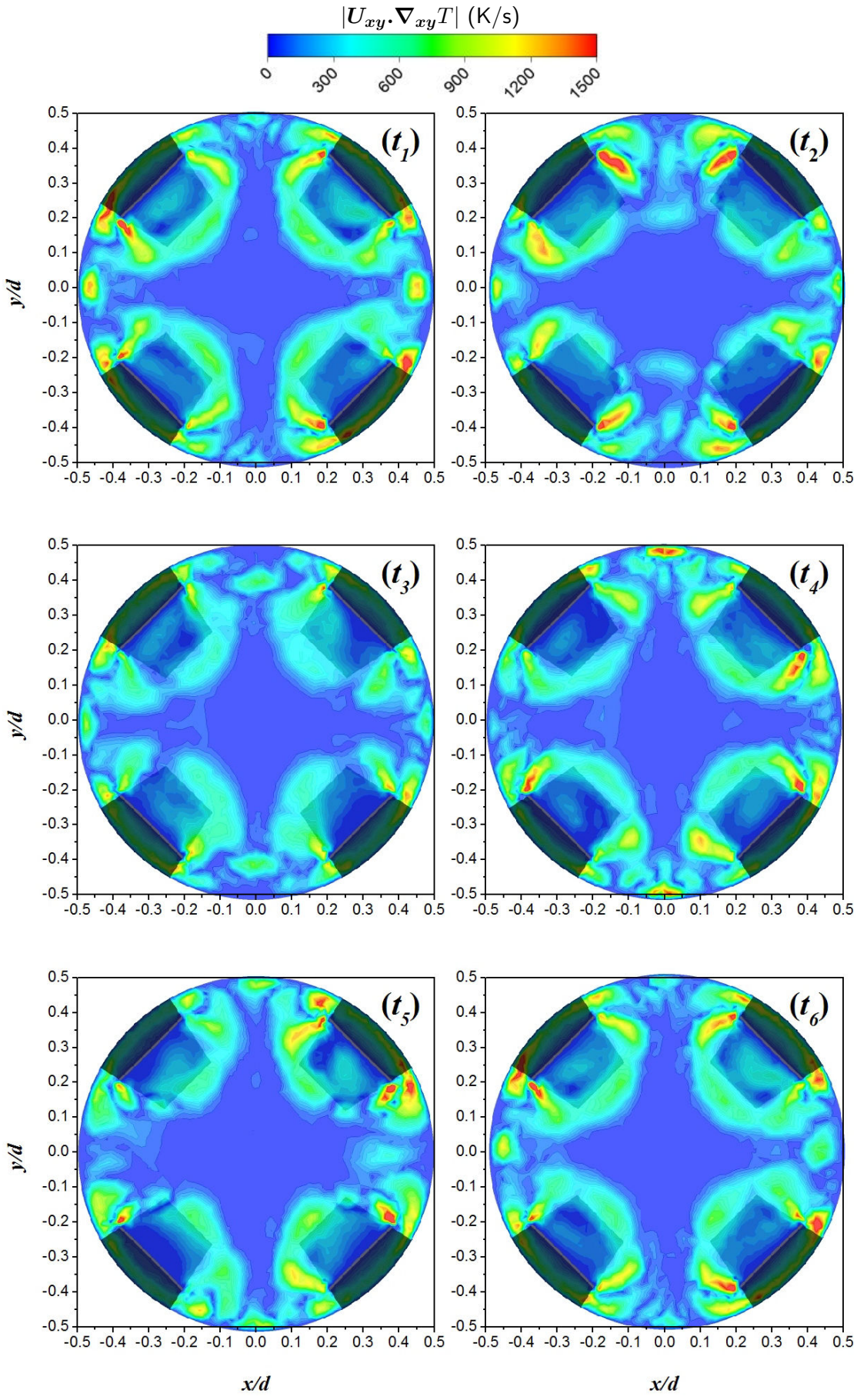

Figure 6.22: Contours of $|U_{xy}.\nabla_{xy}T|$ for the FVG case at position $z/d = 2.52$ (row D) during one period of oscillation

Table 6.7: Statistical information about the global Nusselt number Nu_{0-L} computed at the outlet of the pipe for the different cases

Nu_{0-L}	FVG	RVG	Empty pipe
Mean	18.061	16.394	8.301

6.6 Mixing analysis

In this section, the mixing performance is compared between the two FVG and RVG cases. As shown previously in Figure 6.1, the scalar field is initially divided into a left half $c = 0$ and a right half $c = 1$ and then mixes with the flow instability. The mixing performance is evaluated for both cases by computing the mixing index (MI) of the passive scalar c.

Figure 6.23 shows the scalar distribution downstream of the last row E at a position $z/d = 3.33$ for the RVG case. It is observed that the tabs Ee and Ew have small or even negligible effect on mixing since the vortices formed by these tabs are localized in the right and left planes and no scalar exchange is occurring between the two halves. However the mixing is more clearly observed at the north and south positions where the vortices are formed at the wake downstream these tabs and near the separation zone of the two different scalar halves. The role of these vortices is thus to engulf one scalar into another.

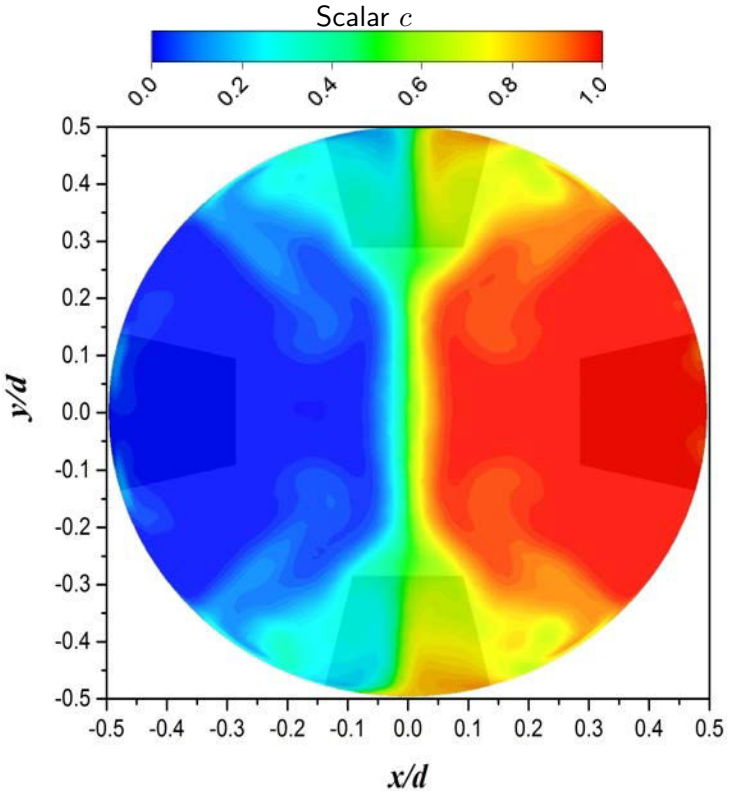

Figure 6.23: Scalar field distribution at a cross sectional view $(z/d = 3.33)$ for the RVG case

Figure 6.24 displays the scalar distribution for the FVG case at a position $z/d = 3.33$ during four time instants. Here the mixed zone is much larger at the center since the tab oscillation dislocates the vortices to the center of the tube allowing a greater exchange of different scalar concentration, as stated before in section 6.4.2. The mixing layer is propagated from the north side to the south side and varies in thickness as the tab change in position. This thickness is much likely influenced by the position of tabs Ee and Ew. In fact, as the tabs Ee and Ew reach a high streamwise amplitude

position, an area of negative pressure in the wake of these tabs is created. As a result, the flow rushes from the center to the negative area region, stretching along the mixing layer presented at the center of the pipe as in Figure 6.24 (t_3 and t_4). Moreover, at the north and south positions and at the tab left and right sides, we can observe that as the tabs oscillate in the opposite streamwise direction, the region of well mixed scalar expands as shown by the vectors drawn on Figure 6.24. This is explained by the fact that as the tabs oscillate in the opposite streamwise direction, the horseshoe-like vortex wraps around the tab by a much wider turn since the adverse and cross pressure gradient are higher in the opposite streamwise motion. This phenomenon is furthermore illustrated in Figure 6.25, which shows the streamlines around tab En at two positions: (a) maximum positions where the flow wraps the side of the tabs and enters the negative pressure region directly and (b) where the flow takes a much wider wrap, turns around the two sides of the tabs and gets responsible for the effect seen in the expanding vector drawn on Figure 6.24.

To quantitatively analyze the mixing performance, we calculate the mixing index as in Lambert and Rangel [Lambert and Rangel, 2010] to assess the quality of the mixture observed in the RVG and FVG cases. Here, the mixing efficiency along all the pipe length is computed using the time-averaged mixing index at different positions in the pipe:

$$\overline{\mathrm{MI}}_c(z) = \frac{1}{t_2 - t_1} \int_{t_1}^{t_2} \left[1 - \frac{1}{c_{ave}(z,t)} \left[\frac{\sum_{j=1}^{n} \left(c_j(x,y,z,t) - c_{ave}(z,t) \right)^2}{n} \right]^{1/2} \right] dt \tag{6.28}$$

where $c_{ave}(z,t)$ is the averaged value of c at a given position z and at time t. n is the number of cells at a cross sectional position, i.e. the number of samples where the concentration value is extracted. Calculation is made from $t_1 = 19$ seconds to $t_2 = 30$ seconds to only include the quasi periodic oscillation regime. Consequently, for no mixture case, $\mathrm{MI} = 0$ and for fully mixed case, $\mathrm{MI} = 1$.

Figure 6.26 shows the local mixing index spatially varying for the FVG and RVG cases. It is clearly seen that the tabs oscillation enhances the mixture quality better than the RVG case since as analyzed before in the RVG case the vortices are always located near the wall position and not dislocated to the center near the mixing separation layer as in the FVG case. The vortices dislocated to the center act as internal agitators that mix the left with the right scalar zone. All along pipe length, the FVG configuration displays better mixing performance than the RVG case. In practical mixers, this will consequently lead to shorter mixing length and more compact equipments. The mixture quality at the outlet of the pipe reached finally 0.718 for the FVG case while it is only 0.243 for the RVG case, corresponding to a 195% increase in the mixing performance.

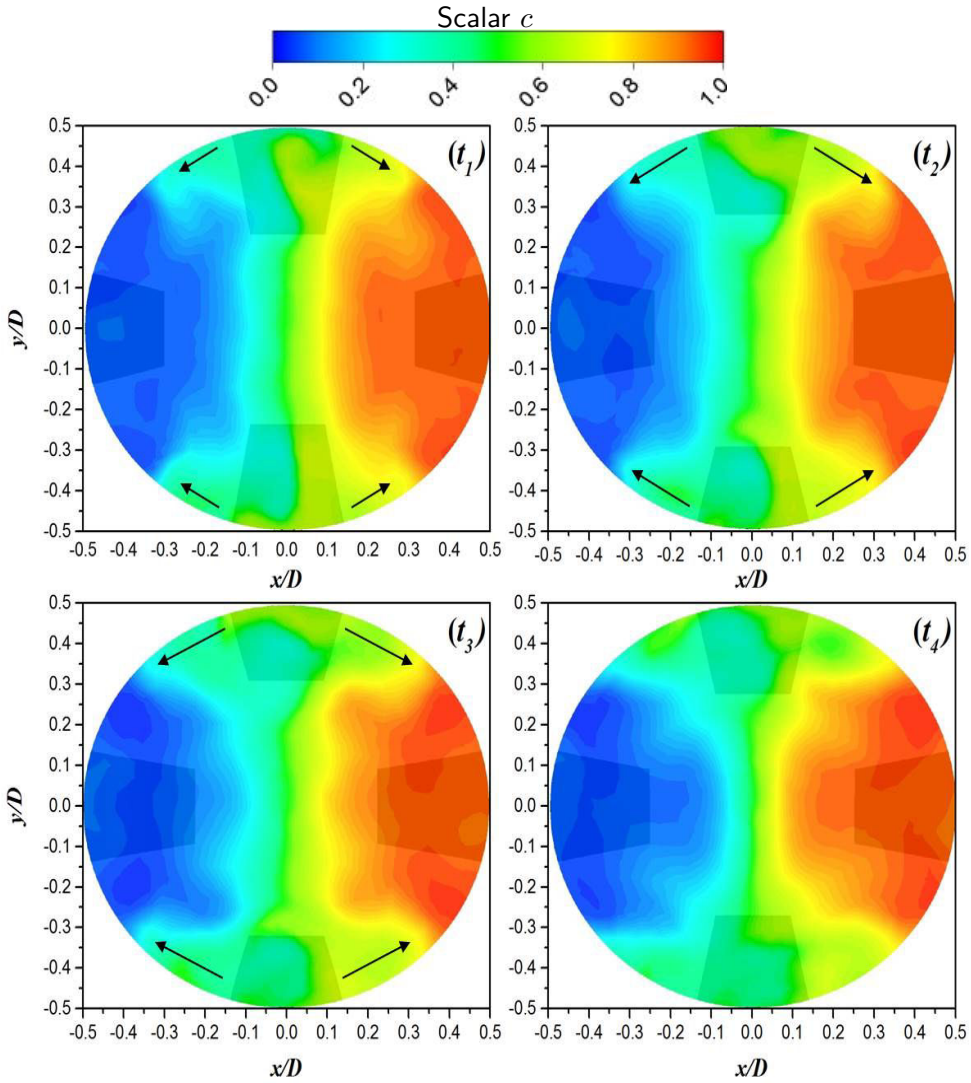

Figure 6.24: Scalar field distribution at a cross sectional view ($z/d = 3.33$) for the FVG case at four time instants equally spaced by 0.04 seconds

(a) (b)

Figure 6.25: Streamlines around a tab En during two time instants: (a) t_1 and (b) t_3

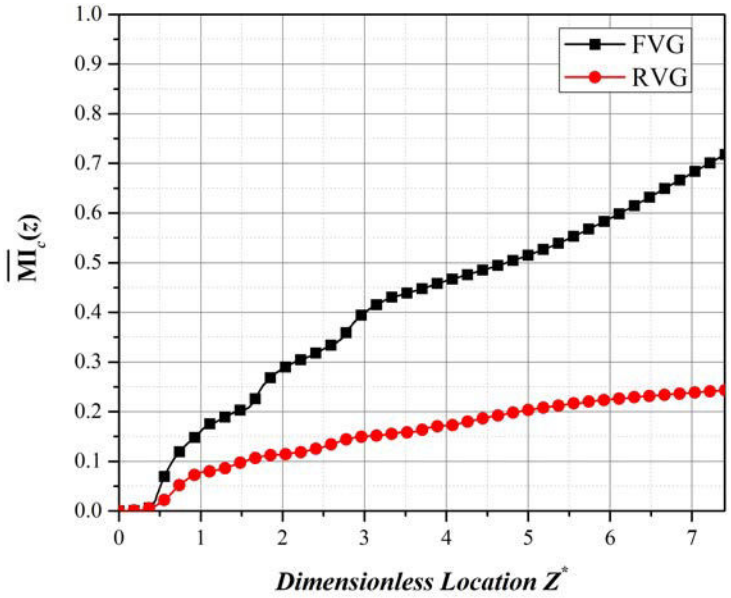

Figure 6.26: Local mixing index (MI_z) along all the pipe length for the FVG and RVG cases

6.7 Conclusion

In the present work, numerical simulation of fluid structure interaction is performed in order to assess the performance of flexible trapezoidal vortex generators (FVG) compared to rigid vortex generators (RVG) in terms of heat and mixing performances. The simulation for the FVG case is done by coupling ANSYS Fluent CFD solver, ANSYS Mechanical CSD solver and a third solver for mesh motion and remeshing operations to avoid negative cell volumes caused by the large displacement of the FVG.

Five rows of trapezoidal VGs are placed in an HEV configuration and tangentially rotated by an angle of 45° with respect to each others. After a transient period, the FVGs in the rows A, C and E undergo self sustained large displacement oscillation with a frequency approximately equal to their natural frequency. However, the FVGs in rows B and D show small oscillation amplitudes. Consequently, much more FVGs interaction is obtained in rows A, C and E and is also relevant with observation previously made in two-dimensional FVG configurations [Ali et al., 2016] where three successive flaps were needed to reach a self-sustained oscillating system. Thus for future simulation, it is to be waited that adding a sixth tangentially rotated row F may have drastic effect on the oscillation of FVG located in rows B and D. Moreover, it is observed that for a given row, tabs located at the north and south positions always oscillate out of phase with tabs located at the east and west positions.

The flow patterns for the RVG and FVG cases have then been analyzed. The RVG case shows steady streamwise counter-rotating vortex pair (CVP) generated downstream the RVGs due to the pressure difference between the high momentum core fluid and the low momentum fluid present in the wake region. These CVPs play a crucial role as internal agitators between the hot fluid near the wall and the cold fluid in the core. Additional transverse vortices are present in the wake of the tabs and can be considered to have a negative impact on heat transfer since the stagnant fluid stays trapped in this region and overheated regions remain there. Moreover, for the FVG case, the proper orthogonal decomposition (POD) technique has been applied to analyze the flow structures. The first four most energetic modes are used for the analysis as they contain most of the flow kinetic energy. An FFT is performed on the temporal evolution of the POD coefficients and reveals a frequency peak equal to the frequency of tabs oscillation and corresponding to the fundamental frequency of the tabs. In this lock-in regime, the vortex shedding supplies energy to the structure instead of damping it resulting in a large amplitude oscillation. Nevertheless, from snapshot reconstruction based on the four most energetic modes, in order to eliminate the modes that contribute to less than 5% of the flow kinetic energy, the tabs oscillations are found to not only be responsible for vortices creation, but are also responsible for operations of creation, destruction and dislocation of vortices. At the highest amplitudes positions, two high velocity shear layers wrap the two sides of the tabs and displace to the negative region behind the tabs. As the tabs oscillate in the opposite streamwise direction, these velocity shear layers are compressed in size as they disappear at the minimum amplitude. Then at this position, a horseshoe vortex forms and extends its two arms to each side of the tabs and into the wake region and may reach the center of the pipe. The major difference between the RVG and FVG case lies in the fact that the vortices are always located near the wall and at the tabs positions in the RVG case, while they are much more displaced towards the center and are either presented as packs in the north and south position or either in the east and west positions when the FVG configuration is considered.

In order to analyze the local performance of heat transfer between the two cases, the local Nusselt number is then determined. The FVG case is found to perform better in removing the heated regions at the wake of tabs and to exhibit also higher performance at the tabs positions where they undergo lower amplitude oscillations. At the positions where the tabs undergo high amplitude oscillations, the RVG case seems to perform better heat transfer. A local analysis is performed using the field synergy principle, where high values of the dot product of $|\boldsymbol{U_{xy}} \cdot \boldsymbol{\nabla_{xy}} T_f|$ can be correlated with good heat transfer ability. Conclusions drawn from this study are: as the tabs oscillate in the opposite streamwise direction, much of the flow structure and vortex intensity are degraded, as opposed to the RVG case where the tabs are always fixed to a specific high angle to the flow. Since the tabs oscillate out of phase at a given row, the vortices are either present at the north and south positions

or east and west positions, which have a negative impact on heat transfer. However as the tabs oscillate in large amplitudes in rows A, C and D, they create high velocity flow, due to the increase in the blockage area which in return force the fluid to impact the next negligibly oscillating rows at high velocity (rows B and D), hence displaying at the latter row location (B and D) a better convective heat transfer than the RVG case. In terms of global heat transfer analysis, the overall heat transfer enhancement with respect to empty pipe is about 118% for the FVG case and about 97% for the RVG case. Moreover, the thermal performance factor η is evaluated and compared in both RVG and FVG cases to a straight pipe flow configuration. It is notably found to be below one for both cases: 0.995 for the RVG case and 0.987 for the FVG case. This clearly displays the increase in pressure drop penalty in both cases. This observation can be somewhat different from other studies where authors found that RVGs can actually improve heat transfer in HEV geometries in turbulent flow regimes, but one has to keep in mind that studied configurations deal with laminar flow here. Moreover, the authors believe that good thermal performance can be achieved using optimized designs of FVGs. No optimization study have been performed in the time being but could be achieved using experimental approach for example in order to overcome the computationally expensive simulations due to fluid-structure interaction problem.

Finally, the mixing performance is compared between the RVG and FVG cases by analyzing the mixture quality of a passive scalar equally divided into the right and left side of the pipe at its initial stage ($c = 1$ for $x > 0$ and $c = 0$ for $x < 0$). It is observed that the FVGs greatly help in enhancing the mixing performance by stretching and engulfing the scalars into each initially separated halves since the vortices of the FVG case are much more dislocated to the center of the pipe and at the position of the separation zone between the two scalars.This is shown by the wider high quality mixture zone appearing at the center. The oscillations of the tabs, especially at the opposite streamwise direction, stretch out the two scalars to both lateral sides of the tabs and increase the mixture quality. The local mixing index $\mathrm{MI}_c(z)$ is then determined and the FVG case displays higher values in nearly all along the pipe length than the RVG case and can thus lead to more compact and shorter mixers/reactors. The mixture quality enhancement is eventually increased by about 195% in the FVG case compared to the RVG case.

Conclusions and perspectives

Concluding remarks

The objective of this study was to investigate the use of fluid-structure interaction (FSI) for analyzing and enhancing heat transfer and mixing performances in multi-functional heat exchangers/reactors. A first target was to qualify and evaluate configuration designs that maintain self-sustained oscillations of flexible vortex generators (FVG). Detailed overview about heat transfer and mixing enhancement methods was first presented in a literature review, mainly divided into passive and active methods with emphasis on vortex generators and forced structural oscillations. Vortex generators are one of the passive methods that create secondary flows, disrupt the growth of the boundary layer and create swirling flows that enhance exchange between the walls and the core fluid, thus improving heat transfer. However since the number of vortices generated by these passive methods is limited, active methods provide an additional flexibility by controlling frequency, velocity and oscillations amplitude of the vortex generators, hence influencing the number and strength of the vortices created. Nevertheless, active methods require the implementation of an additional external source of energy to control the vortex generators causing an increased complexity of installing the system and more energy consumption.

Based on the systems presented above, an innovative way of enhancing heat transfer and mixing by using freely oscillating flexible vortex generators is suggested. This method requires to search and understand other disciplines in engineering such as vortex-induced vibrations of structures. In VIV, a phenomenon called lock-in occurs when the frequency of vortex shedding matches the frequency of structural oscillations and as a result, creates large amplitude oscillations. Consequently, in order to numerically simulate this phenomena and explore its heat transfer and mixing enhancement potential, one must choose the right FSI model for better accuracy and stability. Thus an overview of the available FSI numerical methods in the literature is highlighted that ranges from one way weakly coupled algorithms to two way strongly coupled algorithms. The latter partitioned approach is used in all the simulations performed in this study especially when dealing with large deformation problems. The coupled fluid-structure interaction numerical simulations are carried out by a strong coupling between ANSYS Fluent CFD-solver and ANSYS Mechanical CSD-solver. The fluid flow is solved via an Arbitrary Lagrangian-Eulerian (ALE) formulation that deforms in time, and solid deformations are computed by taking into account large structural deformation and strong coupling between the fluid and solid solvers. In addition to the CFD and CSD solver, a third mesh motion solver is required to deform the fluid mesh and track the high structural deformations at the fluid-solid interface while maintaining a good quality of the mesh and minimizing deterioration. In order to avoid divergence problems, especially those caused by negative cell volumes when large deformation occurs, remeshing methods are used that agglomerate cells which violate a skewness or a size criteria and preserve a good mesh quality across the computational domain.

In order to validate the used partitioned approach, a numerical benchmark proposed by Tureck and Hron [Turek and Hron, 2006] has been chosen for the validation. This numerical benchmark is considered among the most challenging FSI benchmarks presented in the literature where the resulting oscillation offers two main instabilities: one that is connected to large amplitude oscillations and requires a careful attention to the mesh motion solver settings and the other is connected to the added mass effect when the density of the structure is very close to the density of the fluid medium. Thus strongly coupled algorithm with a fixed-point outer iteration loop is performed on the fluid

and solid inner iterations with a stopping criteria depending on the convergence of the exchanged fluid forces and displacements between the two solvers. After validation of the FSI numerical solver, several configurations that rely on self-sustained oscillations of FVG are proposed and analyzed based on their capabilities of heat transfer and mixing. A summary about the goal of each configuration and the essential conclusions is given below:

- In the first study, two dimensional laminar flow is numerically investigated where the computational domain consists of four distant FVG mounted on opposite channel walls with an arrangement of two co-planar FVG followed by two alternating ones downstream. Two cases are studied depending on the Reynolds number (based on the bulk velocity and the channel height) set to 1000 and 1850. FVG efficiency is compared to their corresponding rigid vortex generators cases (RVG). It is found that the flaps oscillations increase the velocity gradients and generates unsteady vortices that detach from the tip of each flap due to shear layer instability. The mixing process is quantified by the transport of a passive scalar through the domain. The FVG high oscillation amplitudes act as a mechanical pump that sequentially pump scalar of different values and improve the mixture quality with up to 98% increase when compared to the relative RVG. Moreover, heat transfer performances are evaluated in terms of local and global Nusselt numbers. Higher peaks of local Nusselt number are observed at the position where the flaps undergo large deformations when compared to the fixed RVG. An increase of up to 97% in the local heat transfer and 134% increase in the global heat transfer is obtained when using elastic flaps instead of rigid ones.

- In the second study, the main objective was to investigate the effect of increasing number of degree of freedom of the system by increasing the number of alternating flaps and the effect of adding or removing the two co-planar flaps upstream on the production of large amplitude oscillations while maintaining a fixed Reynolds number of 2000. The results show that a minimum of three alternating flaps is needed to produce an instability that leads to large displacement oscillations when the co-planar flaps are not present upstream. However, the introduction of two co-planar flaps upstream destabilize the flow by creating periodic forces that act on the downstream flaps and by artificially increasing the reduced velocity that induce the alternating flaps to be in a lock-in state. It is also observed that the additional alternating flaps display an increase in drag forces since they oscillate in resonance and at the same frequency as the incoming flow produced by the flaps upstream and thus resulting in higher displacement amplitudes. This study shows also an important feature: when designing for large amplitude oscillations, instead of increasing the reduced velocity by increasing the flow velocity for example to achieve a state of lock-in, one can influence the oscillation amplitude by increasing the number of flaps and creating more interaction between them. As the literature in VIV suggest, the addition of a second cylinder downstream, a widening of the lock-in region is observed in which the high amplitude response is significant.

- The third study is based on the configurations of the second study but with the main objective to explore and analyze the heat transfer and mixing performances. In fact, vortices that shed from the oscillations of the flexible structures merge with vortices of the same rotational sense that are shed from another structure or from the same structure but from a previous cycle of oscillations. The act of merging produces vortices of higher strength and eventually has positive impact on heat transfer and mixing performances. In fact, when compared to an empty channel, the non co-planar cases show up to 275% increase in the global Nusselt number and up to 317% increase in the local Nusselt number with four alternating FVG. On the other hand, the co-planar cases display an increase of up to 273% increase in the global Nusselt number and 317% increase in the local Nusselt number with three FVG. However, when increasing the number of flaps, the interaction between the flaps, especially those located at the same upper or lower channel walls, results in a drastic increase in oscillation amplitudes, thus increasing the blockage ratio in the channel, hence implying higher pressure drops. The thermal performance factor is computed which shows a value greater than one for all the flexible cases except the case 2CP-3FVG where the flaps undergo the highest displacement amplitudes among all the

cases thus the highest pressure drops. Furthermore, the mixing quality is evaluated through the transport of a passive scalar where the flexible cases show better ability for mixing with a mixture quality higher than 0.9 for all the flexible cases. The highest mixing homogeneity is correlated with the highest oscillation amplitudes as in the 2CP-3FVG case.

- The fourth article investigates a three dimensional HEV configuration with flexible trapezoidal vortex generators inclined with an angle of 45° with respect to the wall and reversed opposite to the flow direction. The flow regime is laminar with a Reynolds number set to 1500 based on the diameter of the pipe. The FVG case is compared with respect to its relative RVG case in terms of flow patterns and heat transfer and mixing performances. A POD technique is implemented in Matlab and used to explore the flow structures of the FVG case where it reveals small scale and complex flow structures in which higher POD modes are required to recover more of the flow kinetic energy. Moreover, Fast Fourier Transformation is applied on the temporal variation of the POD coefficients which displays a dominant peak in the flow and corresponds to the vortices periodic formation and detachment. This dominant frequency synchronizes well with the structural oscillation frequency and the fundamental frequency, reaching a lock-in state. Moreover, a synergy analysis is applied to display areas of high and low heat transfer in conjunction with the FVG position during one cycle of oscillation. The field synergy reveals regions of high heat transfer where the FVG is at its maximum position where high velocity shear layers are formed and wrapped on the tabs side. The low heat transfer regions are located where the FVG is at its minimum amplitude position in which the velocity shear region is no more present and the number of formed vortices decreases. Since the oscillation of the FVG in the same array plane is out of phase, we are left with only two high heat transfer regions since just two of the diametrically opposed FVG are located at their highest amplitude positions at a given time instant and the other two are out of phase and located at their minimum amplitude positions with low heat transfer regions surrounding them. This is found to be opposite in the RVG case where the RVG are fixed and always located in their initial high angle position with high heat transfer regions. However, in the FVG case and in the arrays where the tabs display non significant oscillations, the synergy analysis and local Nusselt number reveals that the FVG performs better heat transfer although this is counter-intuitive at a first glance. In fact, the high amplitude oscillations in the array upstream induces the flow to impinge the low amplitude oscillating row at higher velocities. Since at this row, the FVG keeps their velocity shear layers formed and not suppressed, they display better heat transfer capabilities than the RVG case.

Finally, this study identified several configuration designs for self-sustained oscillations of flexible vortex generators. It relies only on the fluid forces themselves without any external source of energy leading to more energy efficient and compact MHER. However, there will always be suggestions and ideas to improve the designs provided in this manuscript, since the method proposed and the fluid structure interaction field applied to heat transfer and mixing enhancement still didn't reached its maturity level and can still be considered very new. As the first results look promising, the proposed configurations serve as a base for more future studies and investigations and some of them are highlighted in the next section.

Perspectives

The studies done in this manuscript by numerical FSI simulations are considered very computationally expensive and challenging. The time to perform unsteady two-dimensional simulation as in Chapter 2, 3, 4 and 5 could range from one month to two months period per one FSI simulation. Moreover, the last three-dimensional HEV configuration presented in Chapter 6 required a period of seven months simulation time to finalize. Of course, this does not include all the trials and designs done that didn't achieve a certain objective. Consequently, the solver settings, initial and boundary conditions should be chosen very carefully as excessive amount of stop/restart for the numerical FSI simulation is not recommended, especially at a time instant where the flap is in its large deformation position,

since it will eventually result in high interpolation and mapping errors at the fluid-solid interface. Based on the above, the need for implementation of an open-source (such as OpenFOAM [Weller et al., 1998]) highly-scalable parallel FSI solver is still a requirement since it will eventually reduce the computational time and would allow to investigate more geometries and optimization configurations in a short period of time.

Moreover, when large structural deformation occurs, the remeshing algorithm agglomerates the cells that violate a skewness or a size criteria and replaces them with better quality cells, thus preventing the mesh from excessive deterioration. However, this does not always guarantee a mesh motion without negative cell volume divergence problems, since the automatic remeshing is always called after structural deformation. Thus, if the time step chosen is large enough compared to the smallest cell near the fluid-solid interface, this cell will be compressed or stretched to a negative volume before the remeshing solver is invoked. This was the main reason that in the two-dimensional studies performed in this manuscript, the time step was restricted to as low as 10^{-4} s. Nevertheless, the remeshing algorithms available only perform well with tetrahedral, wedges and prism cells but don't support hexahedral cells. The layering algorithm supports hexahedral cells remeshing but it's only efficient when the motion is purely translational, thus it was necessary to perform the meshing with only tetrahedral cells which eventually increases the number of cells in the domain and requires much more CPU memory. As a matter of fact, the dynamic mesh motion should be treated very carefully in FSI simulations which add to the complexity of performing such simulations. The solution could lie in the implementation or use of meshless methods such as smoothed particle hydrodynamics (SPH) [Rabczuk et al., 2010] or algorithms that models the fluid-structure interaction problem by considering non-matching overlapping meshes such as the immersed boundary method [Sotiropoulos and Yang, 2014] or the fictious domain method [Baaijens, 2001].

Nevertheless, in terms of heat transfer and mixing performances, the two-dimensional FVG cases presented in this manuscript can be subjected to further studies. Although these configurations show a dramatic ability to enhance heat transfer and mixing, a high pressure drop increase is observed in these studies and the thermal performance is less than one in some cases. An optimization could be performed and several parameters can be adjusted such as the Young's modulus of the material, the distance between the flaps, flaps height or thickness and angle of inclination with respect to the wall (inclined opposite to the flow direction or inclined in the flow direction). The effect of each parameter on thermal performance and mixing can be investigated and more conclusions can be drawn. Moreover, to better quantify the chaotic mixing of the flow, Lagrangian particles can be injected at the inlet of the computational domain in order to compute the Lyapunov exponent, the residence time distribution and obtain the Poincaré section at different positions. Using these methods, regions of good and bad mixing, or chaotic and elliptic regions can be distinguished. Hence, different flap arrangements or properties can be investigated to find a link between chaos and flexible flap motion. For example, it could be interesting to explore the effect of increasing the number of flaps on creating a non-symmetrical oscillatory motion that could result in chaotic mixing.

Furthermore, all the geometries presented above deal with laminar flow while the turbulent flow regime is almost neglected in these studies. More studies can be performed to explore higher Reynolds numbers and maybe different solid materials with higher stiffness. In fact, the present study main objective was to preserve a laminar regime, which implied the use of highly flexible materials in order to obtain flaps that are more compliant with the low fluid forces. An interesting study would be to perform different numerical simulations of one flap inside a confined area as in a MHER, at different increasing reduced velocities by increasing the flow velocity. The objective of this study would be to find a critical velocity or a range of reduced velocities for which the high amplitude self-sustained oscillations are present. A second goal could be to determine the transfer function of the flexible flap. Since in VIV, the studies are usually performed on elastic-mounted rigid cylinders and in context where no confined walls are present, so the behavior of elastic materials with increasing reduced velocities in conditions similar to heat exchangers could be interesting to study. On the other hand, the present numerical simulations deal with high mass ratios ($m^* = 1000$) since they are carried out in air medium. As we saw in VIV, low mass ratio studies result in widening of the synchronization regime and a higher upper response branch is observed which was absent in the experiments done

by Feng, carried out in air [Feng, 1968]. A comparison between air and water fluid mediums can be performed to exhibit the differences between structural responses since the added mass effect is important in low mass ratios cases. In fact, due to the added mass effect, the structural weight is increased with a mass approximately equal to the mass of the displaced fluid by the structural motion, hence this will reduce the structural natural frequency and the response. In the present studies, the natural frequency of the structure computed in vacuum is approximated the same of the natural frequency of the structure in air, since the mass of air displaced by the structure relative to the mass of the structure itself is negligible. There exists already an approximate analytic solution provided by Weigert *et al.* [Weigert et al., 1996] to calculate the natural frequency of an immersed body, however an algorithm can be implemented by coupling the solid constitutive equation with the surrounding fluid equation described by a pressure acoustic equation as in [Nowak and Zieliński, 2012], to allow better prediction of the natural frequency of immersed bodies. However, one must take into account that the added mass instability will require more FSI outer iterations to achieve convergence on forces and displacements which will add to the complexity of simulating the FSI problems at low mass ratios.

In addition, more unsteady three dimensional simulations can be performed or different parameters can be changed based on the HEV configurations presented in Chapter 6. For example, adding a sixth row of four diametrically opposed FVG tangentially rotated by a 45° could influence the rows B and D to oscillate at higher amplitudes due to increased interactions between the FVG similarly found in rows A, C and E. On the other hand, experimental benches would be a better substitute to lengthy numerical simulations in the meantime since no highly scalable parallel solver is available. Finally, this study is a start for a lot of more investigations and research since the parameters that govern the motion and its implications on heat transfer and mixing enhancement need more deep research to reach its full maturity level. As seen from this section, the studies already presented in this manuscript can open the door to different kind of other future works.

Bibliography

Abdelkefi, A., Hajj, M., and Nayfeh, A. (2012). Phenomena and modeling of piezoelectric energy harvesting from freely oscillating cylinders. *Nonlinear Dynamics*, 70(2):1377–1388.

Ahmed, H. E., Mohammed, H. A., and Yusoff, M. Z. (2012). An overview on heat transfer augmentation using vortex generators and nanofluids: Approaches and applications. *Renewable and Sustainable Energy Reviews*, 16(8):5951–5993.

Akaydın, H., Elvin, N., and Andreopoulos, Y. (2010). Wake of a cylinder: a paradigm for energy harvesting with piezoelectric materials. *Experiments in Fluids*, 49(1):291–304.

Akcabay, D. T. and Young, Y. L. (2012). Hydroelastic response and energy harvesting potential of flexible piezoelectric beams in viscous flow. *Physics of Fluids*, 24(5):054106.

Al-Mdallal, Q., Lawrence, K., and Kocabiyik, S. (2007). Forced streamwise oscillations of a circular cylinder: Locked-on modes and resulting fluid forces. *Journal of Fluids and Structures*, 23(5):681–701.

Ali, S., Habchi, C., Menanteau, S., Lemenand, T., and Harion, J.-L. (2015). Heat transfer and mixing enhancement by free elastic flaps oscillation. *International Journal of Heat and Mass Transfer*, 85:250–264.

Ali, S., Menanteau, S., Habchi, C., Lemenand, T., and Harion, J.-L. (2016). Towards self-sustained oscillations of multiple flexible vortex generators. *Submitted to Journal of Fluids and Structures*.

Ali, S., Menanteau, S., Habchi, C., Lemenand, T., Harion, J.-L., and ELMarakbi, A. (2013). Étude numérique de l'interaction entre un écoulement de type von-kármán et une structure élastique. 21$^{\text{ème}}$ Congrès Français de Mécanique, 26 au 30 août 2013 Bordeaux, France (FR).

Allen, J. and Smits, A. (2001). Energy harvesting eel. *Journal of Fluids and Structures*, 15(3):629–640.

Allison, C. and Dally, B. (2007). Effect of a delta-winglet vortex pair on the performance of a tube–fin heat exchanger. *International Journal of Heat and Mass Transfer*, 50(25):5065–5072.

ANSYS (2015). ANSYS Academic Research, Release 15.0, Help system, ANSYS, Inc.

Anxionnaz, Z., Cabassud, M., Gourdon, C., and Tochon, P. (2008). Heat exchanger/reactors (hex reactors): Concepts, technologies: State-of-the-art. *Chemical Engineering and Processing: Process Intensification*, 47(12):2029 – 2050.

Aref, H. (1984). Stirring by chaotic advection. *Journal of Fluid Mechanics*, 143:1–21.

Assi, G., Meneghini, J., Aranha, J., Bearman, P., and Casaprima, E. (2006). Experimental investigation of flow-induced vibration interference between two circular cylinders. *Journal of Fluids and Structures*, 22(6):819–827.

Baaijens, F. (2001). A fictitious domain/mortar element method for fluid-structure interaction. *International Journal for Numerical Methods in Fluids*, 35(7):743–761.

Bathe, K. (2006). *Finite element procedures*. Klaus-Jurgen Bathe.

Bejan, A. and Kraus, A. (2003). *Heat Transfer Handbook*. Number v. 1 in Heat Transfer Handbook. Wiley.

Berger, S., Talbot, L., and Yao, L. (1983). Flow in curved pipes. *Annual review of fluid mechanics*, 15(1):461–512.

Bernitsas, M., Raghavan, K., Ben-Simon, Y., and Garcia, E. (2008). VIVACE (Vortex Induced Vibration Aquatic Clean Energy): A new concept in generation of clean and renewable energy from fluid flow. *Journal of Offshore Mechanics and Arctic Engineering*, 130(4):041101.

Blom, F. (1998). A monolithical fluid-structure interaction algorithm applied to the piston problem. *Computer methods in applied mechanics and engineering*, 167(3):369–391.

Bokaian, A. and Geoola, F. (1984). Wake-induced galloping of two interfering circular cylinders. *Journal of Fluid Mechanics*, 146:383–415.

Bos, F. (2010a). *Numerical simulations of flapping foil and wing aerodynamics: Mesh deformation using radial basis functions*. TU Delft, Delft University of Technology.

Bos, F. M. (2010b). *Numerical simulations of flapping foil and wing aerodynamics*. Phd, Technical University of Delft.

Bothe, D., Stemich, C., and Warnecke, H.-J. (2006). Fluid mixing in a T-shaped micro-mixer. *Chemical Engineering Science*, 61(9):2950–2958.

Bourguet, R., Karniadakis, G. E., and Triantafyllou, M. S. (2011). Lock-in of the vortex-induced vibrations of a long tensioned beam in shear flow. *Journal of Fluids and Structures*, 27(5â€“6):838 – 847.

Celik, I. B., Ghia, U., Roache, P. J., Freitas, C. J., Coleman, H., and Raad, P. E. (2008). Procedure for estimation and reporting of uncertainty due to discretization in CFD applications. *Journal of Fluids Engineering*, 130:0780011–0780014.

Cetiner, O. and Rockwell, D. (2001). Streamwise oscillations of a cylinder in a steady current. part 1. locked-on states of vortex formation and loading. *Journal of Fluid Mechanics*, 427:1–28.

Chang, C. (2010). Hydrokinetic energy harnessing by enhancement of flow induced motion using passive turbulence control, naval architecture and marine engineering. *University of Michigan, Ann Arbor, MI, USA*.

Chaté, H., Villermaux, E., and Chomaz, J.-M. (2012). *Mixing: chaos and turbulence*, volume 373. Springer Science & Business Media.

Chemineer, I. (2015). "Kenics: Static mixing technology". Website, http://www.chemineer.com/products/kenics/km-mixers.html.

Chemtech, S. (2015). "SMX plus Static Mixer". Website, https://www.sulzer.com/en/Products-and-Services/Mixpac-Cartridges-Applications-Static-Mixers/Static-Mixers/General-Purpose-Mixers/SMX-plus.

Cheng, C., Hong, J., and Aung, W. (1997). Numerical prediction of lock-on effect on convective heat transfer from a transversely oscillating circular cylinder. *International Journal of Heat and Mass Transfer*, 40(8):1825–1834.

Dai, H., Abdelkefi, A., and Wang, L. (2014). Piezoelectric energy harvesting from concurrent vortex-induced vibrations and base excitations. *Nonlinear Dynamics*, 77(3):967–981.

Dautzenberg, F. and Mukherjee, M. (2001). Process intensification using multifunctional reactors. *Chemical Engineering Science*, 56(2):251–267.

Dean, W. and Hurst, J. (1959). Note on the motion of fluid in a curved pipe. *Mathematika*, 6(01):77–85.

Depaiwa, N., Chompookham, T., and Promvonge, P. (2010). Thermal enhancement in a solar air heater channel using rectangular winglet vortex generators. In *Energy and Sustainable Development: Issues and Strategies (ESD), 2010 Proceedings of the International Conference on*, pages 1–7. IEEE.

Donea, J., Giuliani, S., and Halleux, J. (1982). An arbitrary lagrangian-eulerian finite element method for transient dynamic fluid-structure interactions. *Computer Methods in Applied Mechanics and Engineering*, 33(1):689–723.

Donea, J., Huerta, A., Ponthot, J. P., and Rodriguez-Ferran, A. (2004). *Arbitrary Lagrangian Eulerian Methods*. John Wiley & Sons, Ltd.

Dong, S. and Meng, H. U. I. (2004). Flow past a trapezoidal tab. *Journal of Fluid Mechanics*, 510:219–242.

Ekici, K., Kielb, R. E., and Hall, K. C. (2013). The effect of aerodynamic asymmetries on turbomachinery flutter. *Journal of Fluids and Structures*, 36:1–17.

Erturk, A., Vieira, W., De Marqui Jr, C., and Inman, D. (2010). On the energy harvesting potential of piezoaeroelastic systems. *Applied Physics Letters*, 96(18):184103.

Farnell, D., David, T., and Barton, D. (2004). Coupled states of flapping flags. *Journal of Fluids and Structures*, 19(1):29–36.

Felippa, C. and Park, K. (1980). Staggered transient analysis procedures for coupled mechanical

systems: formulation. *Computer Methods in Applied Mechanics and Engineering*, 24(1):61–111.

Feng, C. (1968). The measurement of vortex induced effects in flow past stationary and oscillating circular and d-section cylinders. Master's thesis, University of British Columbia.

Ferrouillat, S., Tochon, P., and Peerhossaini, H. (2006). Micromixing enhancement by turbulence: application to multifunctional heat exchangers. *Chemical Engineering and Processing: Process Intensification*, 45(8):633–640.

Fiebig, M. (1998). Vortices, generators and heat transfer. *Chemical Engineering Research and Design*, 76(2):108–123.

Fiebig, M., Kallweit, P., Mitra, N., and Tiggelbeck, S. (1991). Heat transfer enhancement and drag by longitudinal vortex generators in channel flow. *Experimental Thermal and Fluid Science*, 4(1):103–114.

Fournier, M.-C., Falk, L., and Villermaux, J. (1996). A new parallel competing reaction system for assessing micromixing efficiency - experimental approach. *Chemical Engineering Science*, 51(22):5053–5064.

Fu, W. and Tong, B. (2002). Numerical investigation of heat transfer from a heated oscillating cylinder in a cross flow. *International Journal of Heat and Mass Transfer*, 45(14):3033–3043.

Galpin, P., Broberg, R., and Hutchinson, B. (1995). Three dimensional navier stokes predictions of steady-state rotor/stator interaction with pitch change. *Third Annual Conference of the CFD Society of Canada*.

Ghanem, A., Habchi, C., Lemenand, T., Della Valle, D., and Peerhossaini, H. (2013a). Energy efficiency in process industry - high-efficiency vortex (HEV) multifunctional heat exchanger. *Renewable Energy*, 56:96–104.

Ghanem, A., Lemenand, T., Della Valle, D., and Peerhossaini, H. (2013b). Transport phenomena in passively manipulated chaotic flows: split-and-recombine reactors. In *ASME 2013 Fluids Engineering Division Summer Meeting*. American Society of Mechanical Engineers.

Ghanem, A., Lemenand, T., Della Valle, D., and Peerhossaini, H. (2014). Static mixers: Mechanisms, applications and characterization methods - A review. *Chemical Engineering Research and Design*, 92(2):205–228.

Gopalkrishnan, R., Triantafyllou, M. S., Triantafyllou, G. S., and Barrett, D. (1994). Active vorticity control in a shear flow using a flapping foil. *Journal of Fluid Mechanics*, 274:1–21.

Greenshields, C. and Weller, H. (2005). A unified formulation for continuum mechanics applied to fluid-structure interaction in flexible tubes. *International Journal for Numerical Methods in Engineering*, 64(12):1575–1593.

Guo, Z., Li, D., and Wang, B. (1998). A novel concept for convective heat transfer enhancement. *International Journal of Heat and Mass Transfer*, 41(14):2221–2225.

Guo, Z.-Y., Tao, W.-Q., and Shah, R. (2005). The field synergy (coordination) principle and its applications in enhancing single phase convective heat transfer. *International Journal of Heat and Mass Transfer*, 48(9):1797–1807.

Habchi, C., Lemenand, T., Della Valle, D., Pacheco, L., Le Corre, O., and Peerhossaini, H. (2011). Entropy production and field synergy principle in turbulent vortical flows. *International Journal of Thermal Sciences*, 50(12):2365–2376.

Habchi, C., Lemenand, T., Della Valle, D., and Peerhossaini, H. (2009). Liquid/liquid dispersion in a chaotic advection flow. *International Journal of Multiphase Flow*, 35(6):485–497.

Habchi, C., Lemenand, T., Della Valle, D., and Peerhossaini, H. (2010a). Turbulence behavior of artificially generated vorticity. *Journal of Turbulence*, 11(36):1–18.

Habchi, C., Lemenand, T., Della Valle, D., and Peerhossaini, H. (2010b). Turbulent mixing and residence time distribution in novel multifunctional heat exchangers reactors. *Chemical Engineering and Processing: Process Intensification*, 49(10):1066–1075.

Habchi, C., Russeil, S., Bougeard, D., Harion, J.-L., Lemenand, T., Della Valle, D., and Peerhossaini, H. (2012). Enhancing heat transfer in vortex generator-type multifunctional heat exchangers. *Applied Thermal Engineering*, 38:14–25.

Habchi, C., Russeil, S., Bougeard, D., Harion, J.-L., Lemenand, T., Ghanem, A., Della Valle, D.,

and Peerhossaini, H. (2013). Partitioned solver for strongly coupled fluid–structure interaction. *Computers & Fluids*, 71:306–319.

He, Y. and Tao, W. (2014). Numerical studies on the inherent interrelationship between field synergy principle and entransy dissipation extreme principle for enhancing convective heat transfer. *International Journal of Heat and Mass Transfer*, 74:196–205.

Hover, F. and Triantafyllou, M. (2001). Galloping response of a cylinder with upstream wake interference. *Journal of Fluids and Structures*, 15(3):503–512.

Huang, L. (1995). Flutter of cantilevered plates in axial flow. *Journal of Fluids and Structures*, 9(2):127–147.

Hübner, B., Walhorn, E., and Dinkler, D. (2004). A monolithic approach to fluid–structure interaction using space–time finite elements. *Computer Methods in Applied Mechanics and Engineering*, 193(23):2087–2104.

Irons, B. and Tuck, R. (1969). A version of the aitken accelerator for computer iteration. *International Journal for Numerical Methods in Engineering*, 1(3):275–277.

Issa, R. (1986). Solution of the implicitly discretised fluid flow equations by operator-splitting. *Journal of computational physics*, 62(1):40–65.

Jacobi, A. and Shah, R. (1995). Heat transfer surface enhancement through the use of longitudinal vortices: a review of recent progress. *Experimental Thermal and Fluid Science*, 11(3):295–309.

Jasak, H. and Tukovic, Z. (2006). Automatic mesh motion for the unstructured finite volume method. *Transactions of FAMENA*, 30(2):1–20.

Jasak, H. and Tukovic, Z. (2010). Dynamic mesh handling in openfoam applied to fluid-structure interaction simulations. In *Proceedings of the V European Conference Computational Fluid Dynamics, Lisbon, Portugal, June*, pages 14–17.

Jasak, H. and Weller, H. (2000). Application of the finite volume method and unstructured meshes to linear elasticity. *International journal for numerical methods in engineering*, 48(2):267–287.

Jiang, F., Drese, K., Hardt, S., Küpper, M., and Schönfeld, F. (2004). Helical flows and chaotic mixing in curved micro channels. *AIChE journal*, 50(9):2297–2305.

Kassiotis, C., Ibrahimbegovic, A., and Matthies, H. (2010). Partitioned solution to fluid–structure interaction problem in application to free-surface flows. *European Journal of Mechanics-B/Fluids*, 29(6):510–521.

Kays, W. and London, A. (1984). Compact heat exchangers.

Khalak, A. and Williamson, C. (1997). Investigation of relative effects of mass and damping in vortex-induced vibration of a circular cylinder. *Journal of Wind Engineering and Industrial Aerodynamics*, 69:341–350.

Khalak, A. and Williamson, C. (1999). Motions, forces and mode transitions in vortex-induced vibrations at low mass-damping. *Journal of Fluids and Structures*, 13(7):813–851.

Khatavkar, V., Anderson, P., den Toonder, J., and Meijer, H. (2007). Active micromixer based on artificial cilia. *Physics of Fluids*, 19(8):083605.

King, R. and Johns, D. (1976). Wake interaction experiments with two flexible circular cylinders in flowing water. *Journal of Sound and Vibration*, 45(2):259–283.

Kiwi-Minsker, L. and Renken, A. (403-430, 2010). Intensification of catalytic process by microstructured reactors. *Microchemical Engineering in Practice*.

Kohlert, C., Reher, E., and Bothmer, D. (1986). Intensification of the calendering process with the help of wedge-shaped parts. *Advances in Polymer Technology*, 6(3):259–265.

Küttler, U. and Wall, W. (2008). Fixed-point fluid–structure interaction solvers with dynamic relaxation. *Computational Mechanics*, 43(1):61–72.

Lambert, R., Das, S., Madou, M., Chakraborty, S., and Rangel, R. (2008). Rapid macromolecular synthesis in a microfluidic channel with an oscillating flap. *International Journal of Heat and Mass Transfer*, 51(17):4367–4378.

Lambert, R. and Rangel, R. (2010). The role of elastic flap deformation on fluid mixing in a microchannel. *Physics of Fluids*, 22(5):052003.

Le Tallec, P. and Mouro, J. (2001). Fluid structure interaction with large structural displacements. *Computer Methods in Applied Mechanics and Engineering*, 190(24â€“25):3039–3067.

Lemenand, T., Habchi, C., Della Valle, D., Bellettre, J., and Peerhossaini, H. (2014). Mass transfer and emulsification by chaotic advection. *International Journal of Heat and Mass Transfer*, 71:228–235.

Levinbuk, M. and Kustov, L. (2001). New catalytic systems utilized to intensification of secondary oil-refining process without considerable revamping of available commercial units. *Chemie Ingenieur Technik*, 73(6):667–667.

Li, M., Zhou, W., Zhang, J., Fan, J., He, Y., and Tao, W. (2014). Heat transfer and pressure performance of a plain fin with radiantly arranged winglets around each tube in fin-and-tube heat transfer surface. *International Journal of Heat and Mass Transfer*, 70:734–744.

Li, S., Yuan, J., and Lipson, H. (2011). Ambient wind energy harvesting using cross-flow fluttering. *Journal of Applied Physics*, 109(2):026104.

Liu, S., Hrymak, A., and Wood, P. (2006). Laminar mixing of shear thinning fluids in a SMX static mixer. *Chemical Engineering Science*, 61(6):1753–1759.

Ma, H., Chen, B., Lan, H., Lin, K., and Chao, C. (2009). Study of a led device with vibrating piezoelectric fins. In *Semiconductor Thermal Measurement and Management Symposium, 2009. SEMI-THERM 2009. 25th Annual IEEE*, pages 267–272. IEEE.

Ma, J., Huang, Y. P., Huang, J., Wang, Y. L., and Wang, Q. W. (2010). Experimental investigations on single-phase heat transfer enhancement with longitudinal vortices in narrow rectangular channel. *Nuclear Engineering and Design*, 240(1):92–102.

Mackley, M. and Stonestreet, P. (1995). Heat transfer and associated energy dissipation for oscillatory flow in baffled tubes. *Chemical Engineering Science*, 50(14):2211–2224.

Mahír, N. and Altaç, Z. (2008). Numerical investigation of convective heat transfer in unsteady flow past two cylinders in tandem arrangements. *International Journal of Heat and Fluid Flow*, 29(5):1309–1318.

MATLAB (2010). *version 7.10.0 (R2010a)*. The MathWorks Inc., Natick, Massachusetts.

Mehmood, A., Abdelkefi, A., Hajj, M., Nayfeh, A., Akhtar, I., and Nuhait, A. (2013). Piezoelectric energy harvesting from vortex-induced vibrations of circular cylinder. *Journal of Sound and Vibration*, 332(19):4656–4667.

Mengeaud, V., Josserand, J., and Girault, H. (2002). Mixing processes in a zigzag microchannel: finite element simulations and optical study. *Analytical chemistry*, 74(16):4279–4286.

Michelin, S. and Doaré, O. (2013). Energy harvesting efficiency of piezoelectric flags in axial flows. *Journal of Fluid Mechanics*, 714:489–504.

Min, C., Qi, C., Kong, X., and Dong, J. (2010). Experimental study of rectangular channel with modified rectangular longitudinal vortex generators. *International Journal of Heat and Mass Transfer*, 53(15):3023–3029.

Mirzaee, H., Dadvand, A., Mirzaee, I., and Shabani, R. (2012). Heat transfer enhancement in microchannels using an elastic vortex generator. *Journal of Enhanced Heat Transfer*, 19(3).

Mittal, S. and Kumar, V. (2001). Flow-induced oscillations of two cylinders in tandem and staggered arrangements. *Journal of Fluids and Structures*, 15(5):717–736.

Nguyen, N. (2011). *Micromixers: fundamentals, design and fabrication*. William Andrew.

Nowak, Ł. and Zieliński, T. (2012). Acoustic radiation of vibrating plate structures submerged in water. *Hydroacoustics*, 15:163–170.

OFM Research Group (2015). Oscillatory flow mixing. Website. http://www.ceb.cam.ac.uk/pages/oscillatory-flow-mixing.html, University of Cambridge, Departement of Chemical Engineeing and Biotechnology.

Ongoren, A. and Rockwell, D. (1988). Flow structure from an oscillating cylinder part 1. mechanisms of phase shift and recovery in the near wake. *Journal of Fluid Mechanics*, 191:197–223.

Panov, A., Usmanova, R., Zaikov, V., and Zaikov, G. (2006). Intensification of dust removal process. *Journal of applied polymer science*, 101(5):3357–3360.

Patankar, S. and Spalding, D. (1972). A calculation procedure for heat, mass and momentum transfer in three-dimensional parabolic flows. *International Journal of Heat and Mass Transfer*, 15(10):1787–1806.

Patnaik, B., Narayana, P., and Seetharamu, K. (1999). Numerical simulation of vortex shedding past

a circular cylinder under the influence of buoyancy. *International Journal of Heat and Mass Transfer*, 42(18):3495–3507.

Piperno, S. (1997). Explicit/implicit fluid/structure staggered procedures with a structural predictor and fluid subcycling for 2D inviscid aeroelastic simulations. *International Journal for Numerical Methods in Fluids*, 25(10):1207–1226.

Pottebaum, T. and Gharib, M. (2006). Using oscillations to enhance heat transfer for a circular cylinder. *International journal of heat and mass transfer*, 49(17):3190–3210.

Promvonge, P. and Thianpong, C. (2008). Thermal performance assessment of turbulent channel flows over different shaped ribs. *International Communications in Heat and Mass Transfer*, 35(10):1327–1334.

Rabczuk, T., Gracie, R., Song, J., and Belytschko, T. (2010). Immersed particle method for fluid–structure interaction. *International Journal for Numerical Methods in Engineering*, 81(1):48–71.

Rao, S. (2011). *Mechanical Vibrations*. Number v. 978, nos. 0-212813 in Mechanical Vibrations. Prentice Hall.

Rauline, D., Le Blévec, J., Bousquet, J., and Tanguy, P. (2000). A comparative assessment of the performance of the kenics and smx static mixers. *Chemical Engineering Research and Design*, 78(3):389–396.

Reymond, O., Murray, D., and Donovan, T. (2008). Natural convection heat transfer from two horizontal cylinders. *Experimental Thermal and Fluid Science*, 32(8):1702–1709.

Ristroph, L. and Zhang, J. (2008). Anomalous hydrodynamic drafting of interacting flapping flags. *Physical Review Letters*, 101(19):194502.

Sanders, P. and Thole, K. (2006). Effects of winglets to augment tube wall heat transfer in louvered fin heat exchangers. *International Journal of Heat and Mass Transfer*, 49(21):4058–4069.

Sarpkaya, T. (2004). A critical review of the intrinsic nature of vortex-induced vibrations. *Journal of Fluids and Structures*, 19(4):389–447.

Schäfer, M. and Teschauer, I. (2001). Numerical simulation of coupled fluid–solid problems. *Computer Methods in Applied Mechanics and Engineering*, 190(28):3645–3667.

Schouveiler, L. and Eloy, C. (2009). Coupled flutter of parallel plates. *Physics of Fluids*, 21(8):081703.

Shelat, M. and Sharratt, P. (2004). Use of compact heat exchanger as flexible reactor. In *AIChE Annual Meeting, Austin, TX, USA*.

Shi, J., Hu, J., Schafer, S., and Chen, C. (2014). Numerical study of heat transfer enhancement of channel via vortex-induced vibration. *Applied Thermal Engineering*, 70(1):838–845.

Sirovich, L. and Kirby, M. (1987). Low-dimensional procedure for the characterization of human faces. *JOSA A*, 4(3):519–524.

Slone, A., Pericleous, K., Bailey, C., Cross, M., and Bennett, C. (2004). A finite volume unstructured mesh approach to dynamic fluid–structure interaction: an assessment of the challenge of predicting the onset of flutter. *Applied Mathematical Modelling*, 28(2):211–239.

Song, J., Kim, T., and Jin Song, S. (2012). Experimental determination of unsteady aerodynamic coefficients and flutter behavior of a rigid wing. *Journal of Fluids and Structures*, 29:50–61.

Soti, A. K., Bhardwaj, R., and Sheridan, J. (2015). Flow-induced deformation of a flexible thin structure as manifestation of heat transfer enhancement. *International Journal of Heat and Mass Transfer*, 84:1070–1081.

Sotiropoulos, F. and Yang, X. (2014). Immersed boundary methods for simulating fluid–structure interaction. *Progress in Aerospace Sciences*, 65:1–21.

Stankiewicz, A. and Moulijn, J. (2000). Process intensification: transforming chemical engineering. *Chemical Engineering Progress*, 96(1):22–34.

STAR-CCM+ (2004). CD-adapco Group Releases.

Tang, L., Païdoussis, M., and Jiang, J. (2009). Cantilevered flexible plates in axial flow: energy transfer and the concept of flutter-mill. *Journal of Sound and Vibration*, 326(1):263–276.

Tao, W.-Q., Guo, Z.-Y., and Wang, B.-X. (2002). Field synergy principle for enhancing convective heat transfer—its extension and numerical verifications. *International Journal of Heat and Mass Transfer*, 45(18):3849–3856.

Tao, Y., He, Y., Huang, J., Wu, Z., and Tao, W. (2007). Three-dimensional numerical study of

wavy fin-and-tube heat exchangers and field synergy principle analysis. *International Journal of Heat and Mass Transfer*, 50(5):1163–1175.

Thomas, P. and Lombard, C. (1979). Geometric conservation law and its application to flow computations on moving grids. *AIAA journal*, 17(10):1030–1037.

Thompson, J., Soni, B., and Weatherill, N. (1998). *Handbook of grid generation*. CRC press.

Timité, B., Castelain, C., and Peerhossaini, H. (2011). Mass transfer and mixing by pulsatile three-dimensional chaotic flow in alternating curved pipes. *International Journal of Heat and Mass Transfer*, 54(17):3933–3950.

Tukovic, Z. and Jasak, H. (2007). Updated lagrangian finite volume solver for large deformation dynamic response of elastic body. *Transaction of FAMENA*, 31(1):1–16.

Tuković, Ž. and Jasak, H. (2007). Updated lagrangian finite volume solver for large deformation dynamic response of elastic body. *Transactions of FAMENA*, 31(1).

Turek, S. and Hron, J. (2006). *Proposal for Numerical Benchmarking of Fluid Structure Interaction Between an Elastic Object and Laminar Incompressible Flow*. Ergebnisberichte angewandte Mathematik. Univ.

Ugural, A. and Fenster, S. (2003). *Advanced strength and applied elasticity*. Prentice Hall PTR.

Wall, W., Genkinger, S., and Ramm, E. (2007). A strong coupling partitioned approach for fluid–structure interaction with free surfaces. *Computers & Fluids*, 36(1):169–183.

Webb, R. (1987). *Enhancement of single-phase heat transfer*. Wiley, New York.

Webb, R. (1994). *Principles of enhanced heat transfer*. Wiley-Interscience publication. John Wiley & Sons.

Weigert, S., Dreier, M., and Hegner, M. (1996). Frequency shifts of cantilevers vibrating in various media. *Applied Physics Letters*, 69(19):2834–2836.

Weller, H., Tabor, G., Jasak, H., and Fureby, C. (1998). A tensorial approach to computational continuum mechanics using object-oriented techniques. *Computers in physics*, 12(6):620–631.

Wiggins, S. and Ottino, J. (2004). Foundations of chaotic mixing. *Philosophical Transactions of the Royal Society of London A: Mathematical, Physical and Engineering Sciences*, 362(1818):937–970.

Williamson, C. and Govardhan, R. (2004). Vortex-induced vibrations. *Annu. Rev. Fluid Mech.*, 36:413–455.

Williamson, C. and Roshko, A. (1988). Vortex formation in the wake of an oscillating cylinder. *Journal of Fluids and Structures*, 2(4):355–381.

Wu, J. and Tao, W. (2007). Investigation on laminar convection heat transfer in fin-and-tube heat exchanger in aligned arrangement with longitudinal vortex generator from the viewpoint of field synergy principle. *Applied Thermal Engineering*, 27(14):2609–2617.

Wu, J. and Tao, W. (2008a). Numerical study on laminar convection heat transfer in a channel with longitudinal vortex generator. Part B: Parametric study of major influence factors. *International Journal of Heat and Mass Transfer*, 51(13):3683–3692.

Wu, J. and Tao, W. (2008b). Numerical study on laminar convection heat transfer in a rectangular channel with longitudinal vortex generator. Part A: Verification of field synergy principle. *International Journal of Heat and Mass Transfer*, 51(5):1179–1191.

Xu, J. and Zou, J. (1996). Non-overlapping domain decomposition methods. *Submitted to SIAM Review*.

Yakut, K., Sahin, B., Celik, C., Alemdaroglu, N., and Kurnuc, A. (2005a). Effects of tapes with double-sided delta-winglets on heat and vortex characteristics. *Applied Energy*, 80(1):77–95.

Yakut, K., Sahin, B., Celik, C., Alemdaroglu, N., and Kurnuc, A. (2005b). Effects of tapes with double-sided delta-winglets on heat and vortex characteristics. *Applied Energy*, 80(1):77 – 95.

Yang, S. (2003). Numerical study of heat transfer enhancement in a channel flow using an oscillating vortex generator. *Heat and Mass Transfer*, 39(3):257–265.

Yang, Y. and Chen, C. (2008). Numerical simulation of turbulent fluid flow and heat transfer characteristics of heated blocks in the channel with an oscillating cylinder. *International Journal of Heat and Mass Transfer*, 51(7):1603–1612.

Yang, Y. and Strganac, T. W. (2013). Experiments of vortex-induced torsional oscillation of a flat

plate in cross flow. *AIAA Journal*, 51(6):1522–1526.

Yu, Y., Simon, T., Zhang, M., Yeom, T., North, M., and Cui, T. (2014). Enhancing heat transfer in air-cooled heat sinks using piezoelectrically-driven agitators and synthetic jets. *International Journal of Heat and Mass Transfer*, 68:184–193.

Zdravkovich, M. (1985). Flow induced oscillations of two interfering circular cylinders. *Journal of Sound and Vibration*, 101(4):511–521.

Zeng, M., Tang, L., Lin, M., and Wang, Q. (2010). Optimization of heat exchangers with vortex-generator fin by taguchi method. *Applied Thermal Engineering*, 30(13):1775 – 1783.

Zhang, J., He, Y., and Tao, W. (2009). 3D numerical simulation on shell-and-tube heat exchangers with middle-overlapped helical baffles and continuous baffles–Part II: Simulation results of periodic model and comparison between continuous and noncontinuous helical baffles. *International Journal of Heat and Mass Transfer*, 52(23):5381–5389.

Zhu, L. (2009). Interaction of two tandem deformable bodies in a viscous incompressible flow. *Journal of Fluid Mechanics*, 635:455–475.

Appendix A

OpenFOAM results and development

A.1 Introduction

The OpenFOAM library [Weller et al., 1998] has been used to upgrade an original fluid-structure interaction solver to use the update ALE formulation and to implement the PIMPLE algorithm for the fluid solver and to further implement the heat coupling algorithm. Numerical formulations and procedures are described in details in the following sections.

A.2 Numerical procedure: Mass, moment and displacement conservation equations

A partitioned solver for strongly coupled fluid-structure interaction has been developed using the C++ library OpenFOAM 1.6-ext [Weller et al., 1998]. The nonlinear elastic deformation problem is discretized by the method proposed by Jasak and Weller [Jasak and Weller, 2000]. The internal mesh motion is solved by using the Laplace smoothing equation with variable mesh diffusivity [Jasak and Tukovic, 2006].

The flow field is governed by mass conservation and Navier-Stokes equations for a laminar viscous incompressible flow. The Arbitrary Lagrangian-Eulerian (ALE) formulation is used to solve the fluid flow [Donea et al., 1982]. Equations are thus given by:

$$\nabla \cdot \mathbf{u_f} = 0 \tag{A.1}$$

$$\frac{\partial \mathbf{u_f}}{\partial t} + (\mathbf{u_f} - \mathbf{u_{m,f}}) \cdot \nabla \mathbf{u_f} = -\frac{\nabla p}{\rho_f} + \upsilon_f \nabla^2 \mathbf{u_f} \tag{A.2}$$

where $(\mathbf{u_f} - \mathbf{u_{m,f}})$ is the convective term. The Eulerian and Lagrangian descriptions are obtained respectively by setting $\mathbf{u_{m,f}} = 0$ or $\mathbf{u_{m,f}} = \mathbf{u_f}$, with $\mathbf{u_{m,f}}$ being the mesh velocity in the fluid domain.

The equations of motion of the elastic structure can be thought from a Lagrangian point of view by:

$$\rho_s \frac{\partial^2 \mathbf{d_s}}{\partial t^2} = \nabla \cdot \left(\Sigma \cdot \mathbf{F^T} \right) + \rho_s f_b \tag{A.3}$$

where $\mathbf{d_s}$ is the displacement of the structure, f_b is the resulting body force and $\mathbf{F}$ is the deformation gradient tensor given by:

$$\mathbf{F} = \mathbf{I} + \nabla \mathbf{d_s^T} \tag{A.4}$$

where $\mathbf{I}$ is the identity matrix. The second Piola-Kirchhoff stress tensor is related to the Green Lagrangian strain tensor $\mathbf{G}$ using the following equation [Bos, 2010a, Tuković and Jasak, 2007]:

$$\sum = 2\mu_s \mathbf{G} + \lambda_s \, tr\,(\mathbf{G})\, \mathbf{I} \tag{A.5}$$

where

$$\mathbf{G} = \frac{1}{2}\left(\mathbf{F}^{\mathbf{T}} \cdot \mathbf{F} - \mathbf{I}\right) \tag{A.6}$$

tr is the tensor trace, λ_s and μ_s are Lamé constants which are characteristics of the elastic material. They are linked to the Young modulus E and Poisson's coefficient υ_s by:

$$\lambda_s = \frac{\upsilon_s E}{(1+\upsilon_s)(1-2\upsilon_s)} \tag{A.7}$$

$$\mu_s = \frac{E}{2(1+\upsilon_s)} \tag{A.8}$$

The spatial discretization of the linear momentum conservation law uses the updated Lagrangian formulation developed by Tucovic and Jasak [Tuković and Jasak, 2007].

A.3 Mesh deformation

A non-uniform structured quadrilateral mesh is generated using the software Gambit where the mesh is refined at the wall boundaries and at the fluid-structure interface taking into consideration the high pressure and velocity gradients at these locations. The internal mesh solver deforms the fluid domain while maintaining the quality and validity of the deforming mesh and the displacement result of the structural solver is used as a boundary condition for the mesh motion solver. In the present study the Laplace smoothing equation is used and is discretized using the finite element method:

$$\nabla \cdot (\gamma \nabla \mathbf{u_m}) = 0 \tag{A.9}$$

where γ is the mesh diffusion coefficient and $\mathbf{u_m}$ is the mesh velocity given by $\mathbf{u_m} = (\mathbf{x}_{t+\delta t} - \mathbf{x}_t)/\delta t$, with $\mathbf{x}$ the mesh position.

When the Laplace equation governs the mesh motion, the boundary deformation is not uniform throughout the domain. The nature of the equation is such that point movement is the largest adjacent to the moving boundary, potentially leading to local deterioration in mesh quality [Jasak and Tukovic, 2010]. It has been shown that less distortion can be achieved by applying a variable diffusivity in the Laplacian term using the distance-based method where the diffusion coefficient γ is a function of the cell distance to the nearest moving boundary ℓ through the following relation:

$$\gamma(\ell) = \frac{1}{\ell^2} \tag{A.10}$$

Temporal discretization is performed using a second order implicit scheme which is unconditionally stable. The time step is automatically adapted during the simulations by using a predefined maximal Courant number $Co_{\max} = 1$. The pressure–velocity coupling equation is established using the PIMPLE algorithm which combines both PISO [Issa, 1986] and SIMPLE [Patankar and Spalding, 1972] algorithms, enhancing thus the accuracy of the numerical simulations especially when using large time steps in a moving mesh.

A.4 Implicit fixed-point coupling with fixed point Aitken's relaxation

A linear volume-to point interpolation is used to transform the data stored in the cell center at the fluid structure interface, namely the pressure and the stresses, in order to use them as boundary conditions for the fluid solver or the solid solver. An implicit fixed-point algorithm with dynamic relaxation is used to couple in an accurate way the fluid solver, the solid solver and the mesh solver, and to enforce the equilibrium at the fluid structure interface [Küttler and Wall, 2008]. This iterative algorithm is executed at each time step where, in every outer iteration j , the fluid and structure fields are solved until fulfilling convergence criterion.

Let $\mathbf{d}^{\mathbf{\Gamma}}_{i,j}$ the interface displacement at time step i and for outer iteration j, for each time step and for $j = 1$, an interface displacement predictor $\tilde{\mathbf{d}}^{\mathbf{\Gamma}}$ is used to improve the convergence and performance of the solver.

$$\begin{aligned}
&\text{Order } 0: \quad \tilde{\mathbf{d}}^{\mathbf{\Gamma}}_{i+1,1} = \mathbf{d}^{\mathbf{\Gamma}}_{i,N} && for\ \ i = 1 \\
&\text{Order } 1: \quad \tilde{\mathbf{d}}^{\mathbf{\Gamma}}_{i+1,1} = \mathbf{d}^{\mathbf{\Gamma}}_{i,N} + \delta t\, \mathbf{u}^{\mathbf{\Gamma}}_{i,N} && for\ \ i = 2 \\
&\text{Order } 3: \quad \tilde{\mathbf{d}}^{\mathbf{\Gamma}}_{i+1,1} = \mathbf{d}^{\mathbf{\Gamma}}_{i,N} + \tfrac{\delta t}{2}\left(3\mathbf{u}^{\mathbf{\Gamma}}_{i,N} - \mathbf{u}^{\mathbf{\Gamma}}_{i-1,N}\right) && for\ \ i \geq 3
\end{aligned} \tag{A.11}$$

where N is the last number of iterations ($j = 1$ to N). Then the mesh is moved using the predicted interface displacement as boundary condition, and the new internal mesh motion velocity is obtained and then transferred to the fluid flow solver. Next, the fluid flow problem is solved in ALE formulation, using PIMPLE algorithm for pressure-velocity coupling. Then the pressure and viscous stresses are computed and transferred to the fluid-structure interface as boundary conditions for the solid solver. The solid solver is executed to find the predicted displacement $\tilde{\mathbf{d}}^{\mathbf{\Gamma}}_{i+1,j+1}$. When the stiffness of the solid structure is very small or the ratio of the fluid density to the solid density is large, the impact of the fluid flow on the structure will be very important and thus the predicted interface displacement will not match the result $\tilde{\mathbf{d}}^{\mathbf{\Gamma}}_{i+1,\,j+1} \neq \mathbf{d}^{\mathbf{\Gamma}}_{i+1,\,j}$. Therefore, an iterative correction of the interface displacement must be used. This iterative approach can be represented by:

$$\mathbf{d}^{\mathbf{\Gamma}}_{i+1,\,j+1} = \mathbf{d}^{\mathbf{\Gamma}}_{i+1,\,j} + \alpha_{i+1,\,j+1}\, \mathbf{r}^{\mathbf{\Gamma}}_{i+1,\,j+1} \tag{A.12}$$

where $\mathbf{r}^{\mathbf{\Gamma}}_{i+1,\,j+1} = \tilde{\mathbf{d}}^{\mathbf{\Gamma}}_{i+1,\,j+1} - \mathbf{d}^{\mathbf{\Gamma}}_{i+1,\,j}$ is the interface residual and $\alpha_{i+1,\,j+1}$ is the relaxation parameter. The iterative procedure requires stopping criteria; therefore, an outer-loop relative error is defined by the length scaled Euclidian norm of the interface displacement residual $\mathbf{r}^{\mathbf{\Gamma}}_{i+1,\,j+1}$ adapted from [Küttler and Wall, 2008, Kassiotis et al., 2010]:

$$\xi^{\mathbf{\Gamma}}_{i+1,\,j+1} = \frac{\left\|\mathbf{r}^{\mathbf{\Gamma}}_{i+1,\,j+1}\right\|_{\max}}{\sqrt{n_{eq}}} \tag{A.13}$$

where n_{eq} is the length of the vector $\mathbf{r}^{\mathbf{\Gamma}}_{i+1,\,j+1}$, which is in this case $n_{eq} = 3$. This equation is computed in the step just before the convergence test. The stopping value for the outer-loop iterations is fixed at $\xi^{\Gamma}_{i+1,j+1} = 10^{-7}$. Below this value, the outer iterations stop and a new time step begins. The dynamic relaxation parameter $\alpha_{i+1,\,j+1}$ is evaluated in every iteration j by using the Aitken Δ^2 method given by Irons and Tuck [Irons and Tuck, 1969]. This method uses two previous iterations to determine the current solution. Thus considering $\mathbf{r}^{\mathbf{\Gamma}}_{i+1,\,j+1} = \tilde{\mathbf{d}}^{\mathbf{\Gamma}}_{i+1,\,j+1} - \mathbf{d}^{\mathbf{\Gamma}}_{i+1,\,j}$ and $\mathbf{r}^{\mathbf{\Gamma}}_{i+1,\,j+2} = \tilde{\mathbf{d}}^{\mathbf{\Gamma}}_{i+1,\,j+2} - \mathbf{d}^{\mathbf{\Gamma}}_{i+1,\,j+1}$, the relaxation parameter reads:

$$\alpha_{i+1,\,j+1} = -\alpha_{i+1,\,j}\, \frac{\left(\mathbf{r}^{\mathbf{\Gamma}}_{i+1,\,j+1}\right)^{\mathbf{T}} \cdot \left(\mathbf{r}^{\mathbf{\Gamma}}_{i+1,\,j+2} - \mathbf{r}^{\mathbf{\Gamma}}_{i+1,\,j+1}\right)}{\left|\mathbf{r}^{\mathbf{\Gamma}}_{i+1,\,j+2} - \mathbf{r}^{\mathbf{\Gamma}}_{i+1,\,j+1}\right|^2} \tag{A.14}$$

As two previous iterations are required, the relaxation parameter for the first under-relaxation cycle $\alpha_{i+1,\,1}$ cannot be calculated. Moreover, the last relaxation parameter from the previous time step $\alpha_{i,N}$ may be too small to use as first value for the next time step. Therefore, it is suggested [Küttler and Wall, 2008, Kassiotis et al., 2010, Irons and Tuck, 1969] to use a constrained parameter $\alpha_{\max}$ and hence:

$$\alpha_{i+1,1} = \max\left(\alpha_{i,N},\, \alpha_{\max}\right) \tag{A.15}$$

A.5 Strategies for handling heat transfer coupling

Having chosen the method for the fluid structure interaction, two different strategies can be implemented for the calculation of the heat transfer. The first possibility is to calculate the temperature in the whole domain for every FSI iteration. As this is similar to the monolithical procedure for the force-displacement coupling, it suffers from some drawbacks since the cost to solve most of the algebraic systems obtained after discretization is non linear.

Having two solvers for each domain of interest and partitioned coupling approach for the force-deformation coupling, a more logical way seems to use the non-overlapping Schwarz domain decomposition method. In this case the temperature transport equation is solved in each domain and an iterative procedure is used on the boundary interface which consists of prescribing alternately boundary conditions of Dirichlet and Neumann types. Following Xu and Zou [Xu and Zou, 1996], we first split the whole computational domain of its natural fluid-solid interface. We denote by $\Gamma_{fsi} = \partial\Omega_f \cap \partial\Omega_s$ the interface between the two subdomains. For the sake of simplicity in every computational subdomain, the equation for the temperature is written as:

$$L_f \mathrm{T} = \mathrm{Q}_f \ \text{ with } \ \mathrm{T} = t_f^0 \ \text{ on } \ \Gamma_f^d \quad \text{and} \quad \mathrm{q} = q_f^0 \ \text{ on } \ \Gamma_f^n$$

$$L_s \mathrm{T} = \mathrm{Q}_s \ \text{ with } \ \mathrm{T} = t_s^0 \ \text{ on } \ \Gamma_s^d \quad \text{and} \quad \mathrm{q} = q_s^0 \ \text{ on } \ \Gamma_s^n \tag{A.16}$$

where L_f and L_s are some linear operators, Γ_f^d and Γ_s^d are the boundaries of both fluid and solid domains with prescribed temperature t_f^0 and t_s^0 (Dirichlet boundary conditions), respectively Γ_f^n and Γ_s^n are the Neumann boundaries, with prescribed flux q_f^0 and q_s^0 and Q is a source term. In order to close the whole formulation, the classical two steps iterative Schwarz alternating procedure is applied for prescribing interface conditions on the boundary Γ_{fsi}. For the iteration k the method can be written as:

STEP 1 :

$$\begin{aligned}
L_f \mathrm{T}^{2k+1} &= \mathrm{Q}_f & & \\
\mathrm{T}^{2k+1} &= t_f^0 & &\text{on } \Gamma_f^d \\
\mathrm{q}^{2k+1} &= q_f^0 & &\text{on } \Gamma_f^n \\
\lambda_1 \mathrm{T}^{2k+1} + (1-\lambda_1)\mathrm{q}^{2k+1} &= \lambda_1 \mathrm{T}^{2k} + (1-\lambda_1)\mathrm{q}^{2k} & &\text{on } \Gamma_{fsi}
\end{aligned} \tag{A.17}$$

and for the next step as follows:

STEP 2 :

$$\begin{aligned}
L_f \mathrm{T}^{2k+2} &= \mathrm{Q}_s & & \\
\mathrm{T}^{2k+2} &= t_s^0 & &\text{on } \Gamma_s^d \\
\mathrm{q}^{2k+2} &= q_s^0 & &\text{on } \Gamma_s^n \\
\lambda_2 \mathrm{T}^{2k+2} + (1-\lambda_2)\mathrm{q}^{2k+2} &= \lambda_2 \mathrm{T}^{2k+1} + (1-\lambda_2)\mathrm{q}^{2k+1} & &\text{on } \Gamma_{fsi}
\end{aligned} \tag{A.18}$$

Choosing the parameters λ_1 and λ_2 to be 1 and 0, respectively, we get a Dirichlet-Neumann alternative Schwarz decomposition method. The calculated temperature from the previous iteration

on the fluid-solid interface is used as a Dirichlet boundary condition for the temperature in the fluid solver. The resulting boundary thermal flux is then set as a boundary condition in the solid solver and the procedure continues until fulfilling the defined convergence criterion. A dual to the described procedure is applied when $\lambda_1 = 0$ and $\lambda_2 = 1$.

A.6 Numerical validation

A.6.1 Fluid-structure interaction

The same numerical benchmark presented in Chapter 2 for the case FSI2 as named in the original paper of Turek and Hron [Turek and Hron, 2006] is used for the validation of the OpenFOAM solver. Figure A.1 shows the displacement amplitudes of vorflex solver that relies on the ALE formulation (for more details about the vorflex solver, please refer to Habchi *et al.* [Habchi et al., 2013]), the PISO solver that relies on the updated ALE and the PIMPLE solver that relies also on the updated ALE but uses the PIMPLE algorithm to numerically solve the Navier-Stokes equations. It is to be noticed that the three solvers were using the same mesh with 20 000 structured quadrilateral cells refined at the walls and the fluid structure interface. The original vorflex solver showed a non physical solution with x-amplitudes of -0.005 m and y-amplitudes of 0.03 m which are far from the expected reference results of the benchmark [Turek and Hron, 2006] with a deviation of approximately 50%.

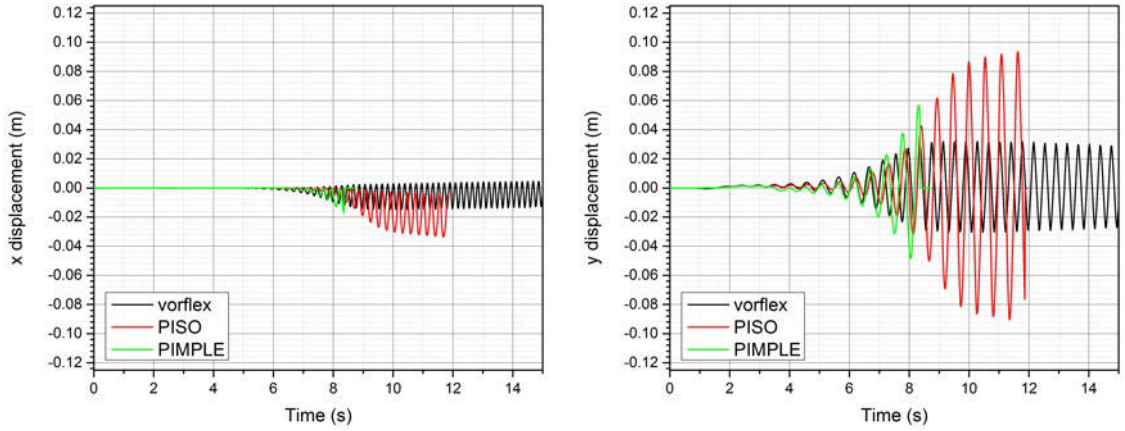

(a) (b)

Figure A.1: Oscillation amplitudes as function of time. (a) x-displacement; (b) y-displacement

As far as the PISO and PIMPLE solvers are concerned, the simulations couldn't get past the 12 seconds of physical time as the oscillation amplitudes were getting higher (though closer to the reference results of the benchmark).The results are summarized in Table A.1.

Table A.1: Displacements between solvers and related reference results

	PISO (U-ALE solver)	PIMPLE (U-ALE solver)	ALE solver	Reference results
x-displacement (cm)	-1.75± 1.25	N/A	0.3± 0.08	-1.458± 1.244
y-displacement (cm)	0.5± 7.5	N/A	0.25± 2.75	0.123

Actually, when the solution got closer to the maximum position of the flap during oscillation, divergence occured due to the presence of negative volume cells, non-overlapping fluid and solid

meshes, which created a lot of convergence problems as the mesh motion solver couldn't handle the large deformations at the fluid solid interface. Indeed, as depicted in Figure A.2, the mesh is very distorted at the tip of the flap for the ALE formulation. In the Updated ALE formulation, the mesh is conserved at the tip of the flap but the distortion propagates to the channel wall.

Problems met can finally be summarized as follows:

- Negative volume cells occur when facing large deformations problems,
- Absence of dynamic remeshing capabilities,
- Problems concerning stopping and restarting the solution that may lead to divergence, as the interpolation weights at the fluid-structure interface needed to be recalculated at start and error propagations could occur,
- Slow computational time due to the fact that the solution could take weeks to reach periodic oscillations after the transitory regime from initial condition, as the solvers were not yet parallelized.

As these difficulties of convergence were time consuming and diverted the work from the main objective, simulation strategy was modified by using Ansys workbench to couple fluid and structural solvers to model FSI. Nevertheless, the OpenFoam's solver was suitable for small structure deformations with no convergence or mesh motion problems: it was thus used to present our first results at the CFM (Congrès Français de Mécanique) conference [Ali et al., 2013] detailed in section A.7.

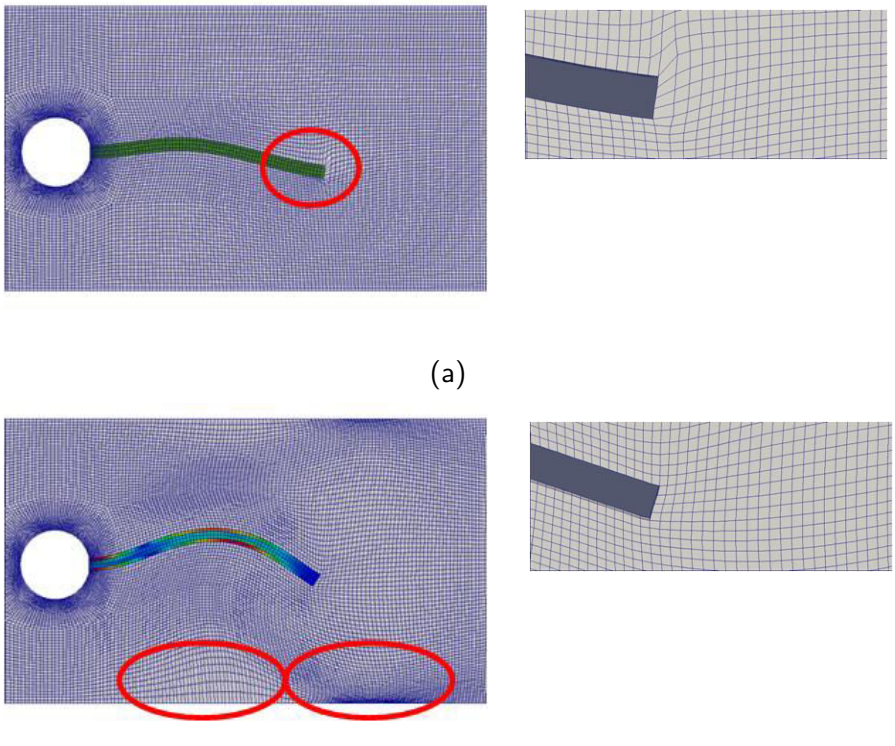

(a)

(b)

Figure A.2: Mesh distortion. (a) Solver of ALE formulation; (b) Solver of Update ALE formulation

A.6.2 Heat transfer coupling

The implementation of the heat coupling algorithm in the new solver was carried out in parallel of dynamic tests previously mentioned. It was tested on the geometry shown in Figure A.3 which consists of a void square cylinder inserted in a 2D channel, where a heat source of 400 K is generated

inside the cylinder and a laminar, incompressible fluid flow initially at 250 K interacts with the heated surface of the cylinder in contact with the fluid.

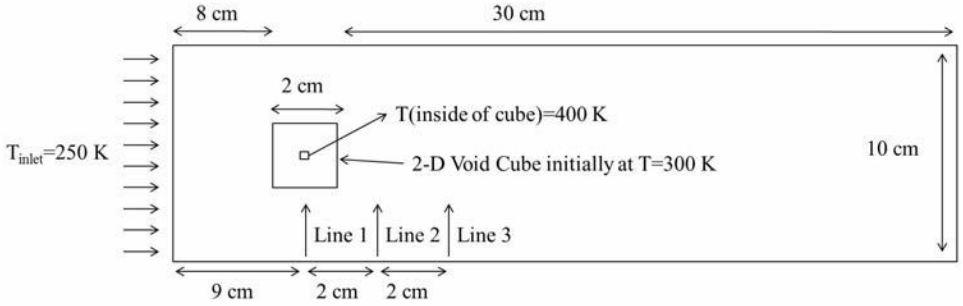

Figure A.3: Schematic view of computational domain used to validate the heat transfer coupling algorithm

The mean temperature profiles plotted at different locations i.e line 1, 2 and 3 are compared with STAR-CCM+ results [STAR-CCM+, 2004] as shown in Figure A.4. Whereas an exact match between the PIMPLE solver and the STAR-CCM+ software is observed at Line 1, a difference is visible as the location of the line probe studied gets further in the wake of the cylinder. These differences could have been put to further investigations regarding mesh, algorithms used to solve the fluid flow (as STAR-CCM+ uses the SIMPLE algorithm and that could result in differences in the velocity fields which will eventually have an influence on the temperature fields) for instance.

As the conclusions about the dynamic studies made the OpenFoam solver unsuitable for the large displacement oscillations of the flaps that would be the concern of the thesis work, this solution was abandoned during the end of the first PhD's year, however, and no further study was done on the heat transfer differences found.

A.6.3 Difficulties and problems

We encountered a lot of problems concerning the convergence of the solution and ultimately obtaining results after a lot of computational time. These problems can be summarized as follows:

- Negative volume cells when facing large deformations problems.
- Problems concerning stopping and restarting the solution, that may lead to divergence, as the interpolation weights at the fluid-structure interface may need to be recalculated and an error propagation occurs.
- Slow computational time, as the solution could take weeks and weeks to obtain results and finally achieve steady state oscillations.
- Absence of dynamic remeshing capabilities.
- The objective of this thesis is not to develop a solver, so the difficulties of convergence are time consuming and divert from the real objective which is to design a system of vortex generators that are flexible, dynamic and passive.

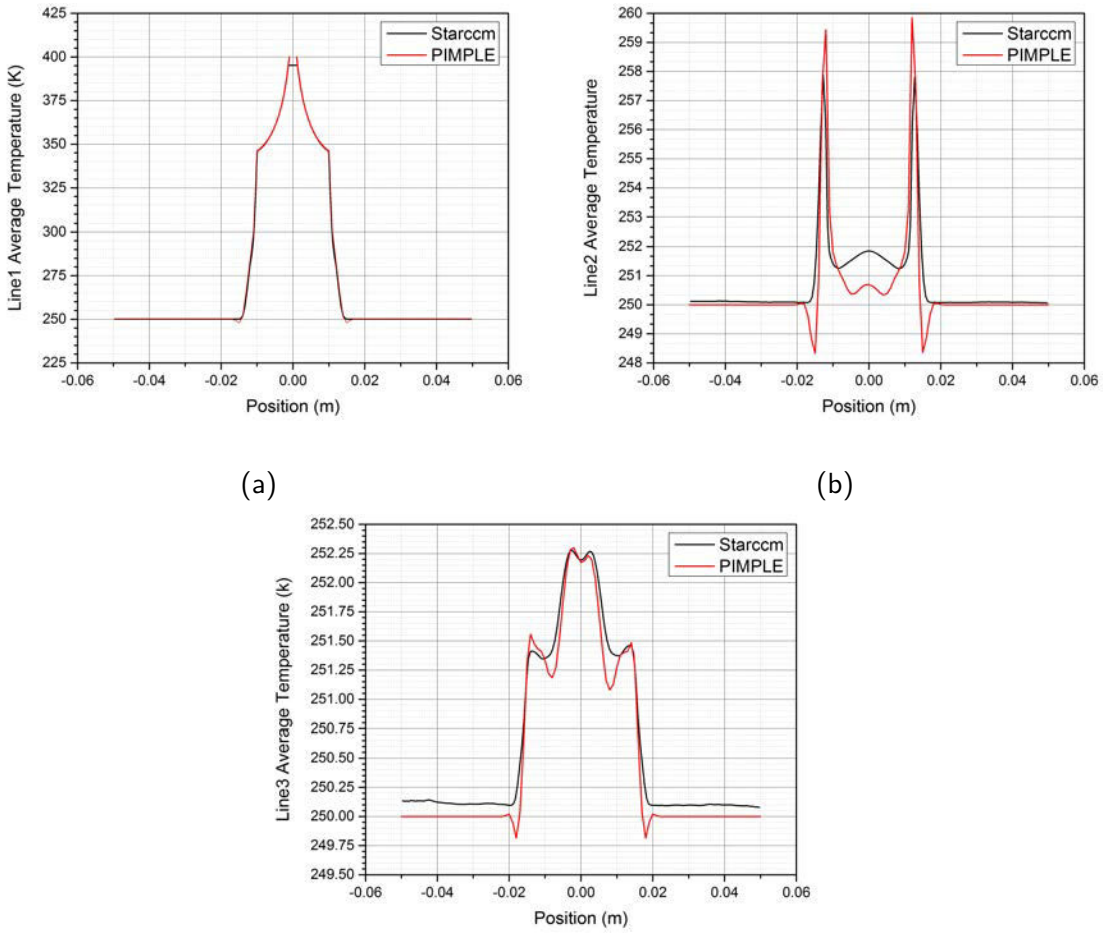

Figure A.4: Average temperatures in function of time at different locations: (a) Line 1; (b) Line 2; (c) Line 3

A.7 CFM 2013 conference

In this section, a study presented in the CFM 2013 conference (Congrès Français de Mécanique) [Ali et al., 2013] is added. In this work, oscillations of flaps are obtained in a passive dynamic way. More specifically, a square cylinder is inserted into a two-dimensional laminar flow. Downstream from the square two elastic flaps are inserted. Successive vortices in the wake of the square are produced and disrupted a flexible structure that oscillates and produce coherent vortex structures.

Numerical analysis and simulation of the interaction between a Von Kármán vortex street and elastic flaps

S. ALI[a,b,c], S. MENANTEAU[b,c], C. HABCHI[a], T. LEMENAND[d], J.-L. HARION[b,c], A. ELMARAKBI[e]

a. ETF, School of Engineering, Lebanese International University LIU, P.O. Box 146404 Mazraa, Beirut, Lebanon
b. Université Lille Nord de France, F-59000 Lille, France
c. Mines Douai, EI, F-59500 Douai, France
d. LUNAM Université, Thermofluid Complex Flows and Energy Research Group, LTN CNRS UMR 6607, 44306 Nantes, France
e. Department of Computing, Engineering and Technology, Faculty of Applied Sciences, University of Sunderland, Sunderland SR6 0DD, United Kingdom

Abstract:

The performance improvement of heat exchangers is a major challenge in many industries. Some of these heat exchangers use vortex generators to produce coherent structures that enhance the heat and mass transfer. The aim of this study is to numerically investigate the vortices generated by introducing flexible flaps into an oscillating and laminar flow. More specifically, a square cylinder is inserted into a two-dimensional domain such that a Von Kármán street vortex is generated. The successive wake vortices disrupt a flexible structure that oscillates and produce coherent structures.

The study is performed by numerical simulations. The fluid-solid coupling dynamics and the deformation of the flexible element are simulated using a tool developed with the open source library OpenFOAM. The finite volume method is used to discretize the geometry. The problem is then solved by using the PIMPLE algorithm and a partitioned approach for fluid-structure interaction. The dynamic solver is coupled with a mesh deformation procedure based on Laplace smoothing equation with variable mesh diffusion. The solvers and the coupling method used for modeling fluid-structure interaction are detailed first. The effects of the elastic properties of the flexible structure on the oscillations and the topology of the flow are then investigated.

Keywords: computational fluid dynamics, fluid-structure interaction, Aitken method, OpenFOAM, flexible flap.

1 Introduction

Over the years, many methods have been studied to enhance heat transfer in forced convection problems. A classification of single phase heat transfer enhancement as passive, active, or compound has been proposed by Webb [1]. Active methods require external power and involve electric, magnetic or acoustic fields. Passive methods involve surface modifications, fluid additives or introduction of protuberances in order to destabilize the flow. Compound methods involve the use of both active and passive techniques. Since active methods require external energy and thus an added cost, passive methods are more widely spread in several applications.

Valencia [2] performed a 2D numerical investigation of the unsteady laminar flow pattern and forced convective heat transfer in a channel with a built-in rectangular cylinder. His study shows that oscillatory separated flows result in a significant heat transfer enhancement about a maximum of 45% compared to two-dimensional channel flow. Yang [3] performed a numerical study of heat transfer enhancement in a channel flow using an oscillating vortex generator, the results showed a heat transfer efficiency index greater than 1.0 for almost all cases and in some cases an increment of heat transfer of about 115%.

In the present study, passive oscillating flaps can be obtained without the need of an additional force except the hydrodynamic forces of the flow itself on the flaps. More specifically, a square cylinder is inserted into a two-dimensional laminar flow. Downstream from the square two elastic flaps are inserted. Successive vortices in the wake of the square are produced and disrupt a flexible structure that oscillates and produce coherent vortex structures.

2 Numerical Procedure

A partitioned solver for strongly coupled fluid-structure interaction has been developed using the C++ library OpenFOAM 1.6-ext [4] and validated by Habchi *et al.* [5]. The nonlinear elastic deformation problem is discretized by the method proposed by Jasak and Weller [6]. The internal mesh motion is solved by using the Laplace smoothing equation with variable mesh diffusivity [7].

2.1 Mass, momentum and displacement conservation equations

The flow field is governed by mass conservation and Navier-Stokes equations for a laminar viscous incompressible flow. The Arbitrary Lagrangian-Eulerian (ALE) formulation is used to solve the fluid flow [8, 9]. Equations are thus given by:

$$\nabla \cdot \mathbf{u_f} = 0 \tag{1}$$

$$\frac{\partial \mathbf{u_f}}{\partial t} + \left(\mathbf{u_f} - \mathbf{u_{m,f}}\right) \cdot \nabla \mathbf{u_f} = -\frac{\nabla p}{\rho_f} + \upsilon_f \nabla^2 \mathbf{u_f} \tag{2}$$

where $\left(\mathbf{u_f} - \mathbf{u_{m,f}}\right)$ is the convective term. The Eulerian and Lagrangian descriptions are respectively obtained by setting $\mathbf{u_{m,f}} = 0$ or $\mathbf{u_{m,f}} = \mathbf{u_f}$, with $\mathbf{u_{m,f}}$ being the mesh velocity in the fluid domain.

The equations of motion of the elastic structure can be thought from a Lagrangian point of view by:

$$\rho_s \frac{\partial^2 \mathbf{d_s}}{\partial t^2} = \nabla \cdot \left(\mathbf{\Sigma} \cdot \mathbf{F^T}\right) + \rho_s f_b \tag{3}$$

where $\mathbf{d_s}$ is the displacement of the structure, f_b is the resulting body force and $\mathbf{F}$ is the deformation gradient tensor given by:

$$\mathbf{F} = \mathbf{I} + \nabla \mathbf{d_s^T} \tag{4}$$

where $\mathbf{I}$ is the identity matrix.

The spatial discretization of the linear momentum conservation law uses the updated Lagrangian formulation developed by Tucovic and Jasak [10].

2.2 Mesh deformation

In the present study the Laplace smoothing equation is used in order to automatically move the mesh at each time step:

$$\nabla \cdot \left(\gamma \nabla \mathbf{u_m}\right) = 0 \tag{5}$$

where γ is the mesh diffusion coefficient and $\mathbf{u_m}$ is the mesh velocity given by: $\mathbf{u_m} = \left(\mathbf{x}_{t+\delta t} - \mathbf{x}_t\right) / \delta t$, with $\mathbf{x}$ being the mesh position.

It has been shown that less mesh distortion can be achieved by introducing a variable diffusivity in the Laplacian operator. Using the distance-based method, this diffusion coefficient γ is defined as a function of the cell distance to the nearest moving boundary ℓ through the following [7]:

$$\gamma(\ell) = \frac{1}{\ell^2} \tag{6}$$

2.3 Implicit fixed-point coupling

An implicit fixed-point algorithm with dynamic relaxation is used to couple in an accurate way the three solvers (fluid, solid and mesh solvers) and to enforce the equilibrium at the fluid-structure interface [11]. This iterative algorithm is achieved at each time step i at which the fluid and structure fields are solved until fulfilling convergence criterion defined for an outer iteration j. Let $\mathbf{d}^{\Gamma}_{i,j}$ denotes the interface displacement at time step i and outer iteration j. At each time step i and for $j=1$, an interface displacement predictor $\tilde{\mathbf{d}}^{\Gamma}$ is used to improve the convergence and performance of the solver. Then the mesh is moved using the predicted interface displacement as boundary condition, and the new internal mesh motion velocity is obtained and transferred to the fluid flow solver. The fluid flow problem is then solved in ALE formulation using the PIMPLE algorithm for pressure-velocity coupling (a combination of PISO [12] and SIMPLE [13] algorithms). From this point, the pressure and viscous stresses are computed and transferred to the fluid-structure interface as boundary conditions for the solid solver. The solid solver is finally executed to find the predicted displacement $\tilde{\mathbf{d}}^{\Gamma}_{i+1,j+1}$.

3 Computational domain and test case configurations

The computational domain consists of a fixed square cylinder inserted in a two-dimensional channel followed by two elastic flaps, sharing a common rigid base as shown in FIG. 1. It is to be noted that the square cylinder is slightly translated to one side of the channel so that the wake vortices will impact the two flaps in a non-symmetrical way. Both flaps have a height h of 50 mm with a thickness of 3 mm, and the cylinder has a width D of 20 mm.

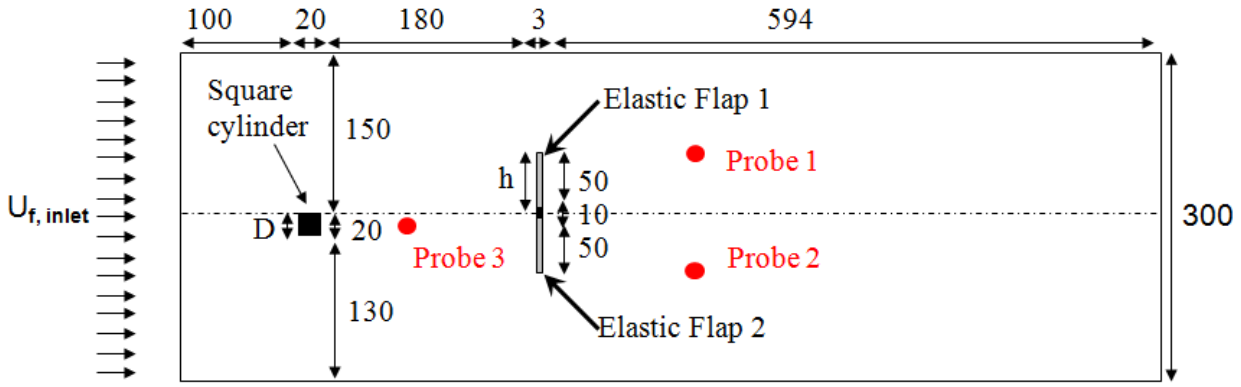

FIG. 1 - Schematic view of computational domain with mm as unit of length

The lateral walls are set as symmetry planes. The outlet condition is set as zero pressure gradient. The inlet velocity profile is considered to be uniform with a velocity of 0.6 m/s with a smooth increase of velocity during the first time steps to avoid a sudden impact on the elastic structures:

$$U_{f,inlet} = 0.6\left[1-\cos\left(\frac{\pi}{2}t\right)\right] \quad for\, t < 0.5\,\mathrm{sec} \tag{7}$$

$$U_{f,inlet} = 0.6\ m/s \quad for\, t \geq 0.5\,\mathrm{sec} \tag{8}$$

where $U_{f,inlet}$ is the fluid inlet velocity.

Three different cases are studied with the same flow configuration (kinematic viscosity, $\nu_f = 5.10^{-5}$ $m^2 s^{-1}$, density $\rho_f = 1$ kg m^{-3}). The Reynolds number based on the height of a flap, $\mathrm{Re}_h = U_{f,inlet}\, h / \upsilon_f$ is 600 while the Reynolds number Re_D, based on the width of the cylinder, is 240. As far as the flaps are concerned, one configuration has been set with rigid flaps while the two others have flexible flaps with different Young's modulus values, as reported in

.

In this paper the fluid domain consists of 22044 quadrilateral cells refined at the walls and at the fluid structure interface. The structural domain consists of 2000 quadrilateral cells.

Parameters	Rigid Flap Case: RF	Flexible Flap Case 1: FF1	Flexible Flap Case 2: FF2
ν_s	-	0.4	0.4
ρ_s (kg m^{-3})	-	400	400
E (10^5 Pa)	-	1	0.5

Table 1: Parameters of the flaps stiffness

4 Results: flow pattern and flap oscillations

4.1 Flow pattern

In order to highlight the coherent structures generated in both rigid and flexible flaps cases, snapshots of λ_2 criterion are depicted in FIG. 2 at two time steps taken after the flow stabilization in the RF and FF1 cases.

The λ_2 definition corresponds to the pressure minimum in a plane, when contributions of unsteady irrotational straining and viscous terms in the Navier-Stokes equations are discarded; it is the median of the three eigen values of $S^2+\Omega^2$, where S and Ω are respectively the symmetric and antisymmetric parts of the velocity gradient tensor $\nabla\mathbf{u}$. The vortices are thus characterized by positive values of the -λ_2 criterion and can easily be detected. It is to be noticed that a Von Kármán vortex street occurs behind the fixed square cylinder with a shedding frequency of $f \approx 4.5\ Hz$. The frequency is determined by performing a Fast Fourier Transformation on velocity oscillations computed at the probe 3 locations behind the square cylinder, as shown in FIG. 1. This frequency corresponds to a Strouhal number of $St=0.15$, calculated based on the square width $S_t = \frac{fD}{U_{f,inlet}}$. This wake region then disturbs the flaps located downstream in a non-symmetrical way. In FIG. 2, although the flaps are oscillating due to the upstream flow, it is unclear whether the mixing is enhanced with the flexible flaps from the λ_2 criterion visualization.

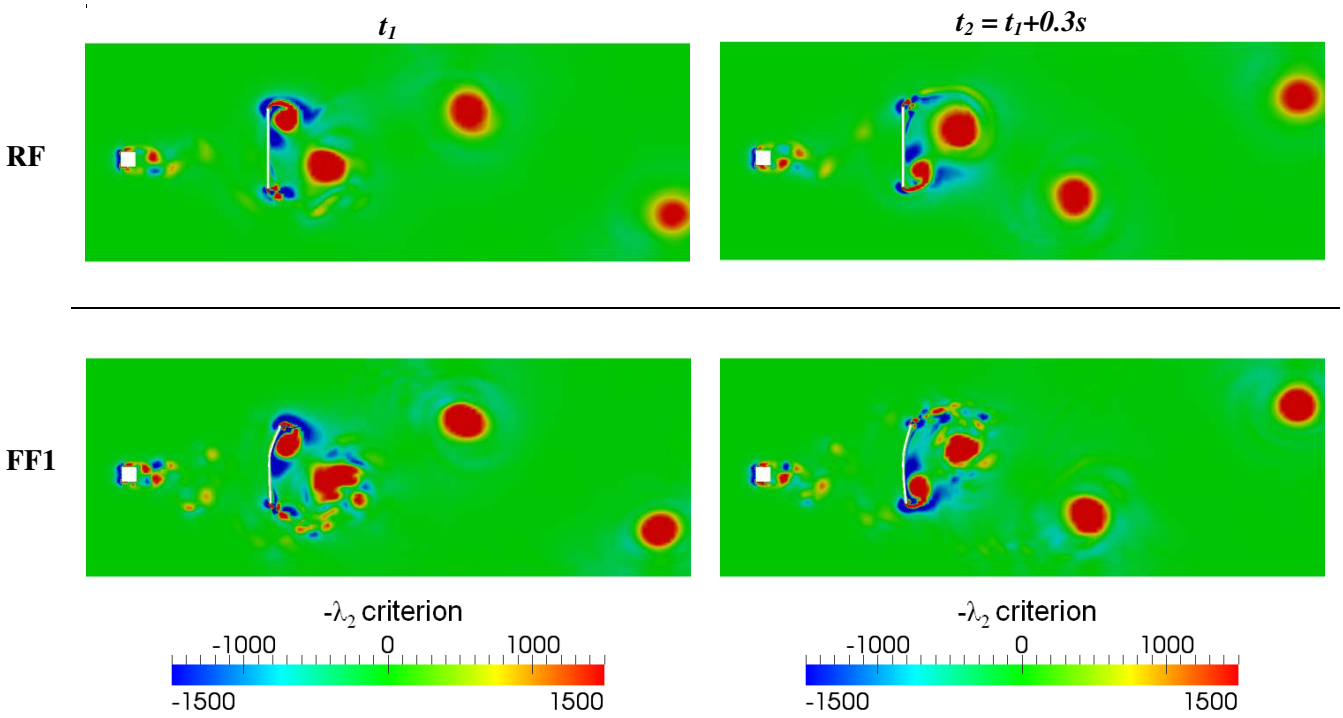

FIG. 2 - Snapshots of -λ_2 criterion for RF case (top figures) and FF1 (bottom figures) – Time step t_1 (left figures) has been arbitrary set and $t_2 = t_1+0.3s$ (right figures)

4.2 Effect of elasticity

In FIG. 3 relative displacement of each flap for the two cases corresponding to different Young's modulus is plotted (see Table 1). FIG. 4 shows a sample comparison where flow velocity magnitude is displayed behind flap 1 for FF2 and RF cases.

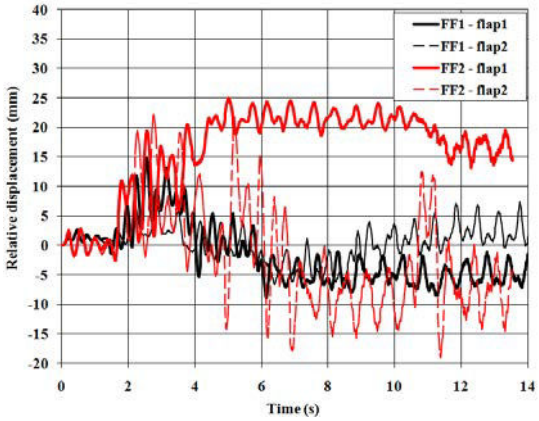

FIG. 3 - Relative displacements of flaps as a function of time for FF1 and FF2 cases

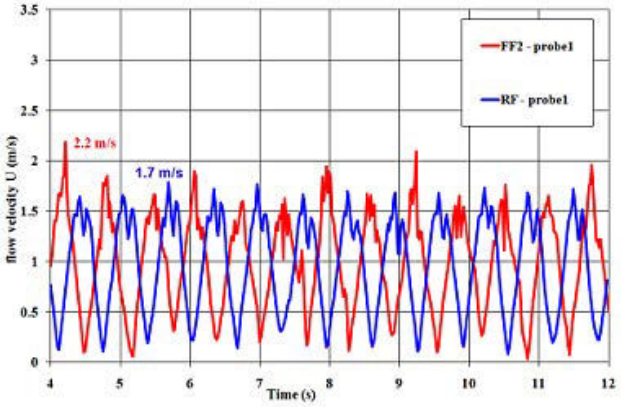

FIG. 4 - Flow velocity as a function of time at probe 1 location behind flap 1, for FF2 and RF cases

In FIG. 3, the mean relative displacement of flap1 increases from -1.63 mm in FF1 case to 16.1 mm in FF2 case, and the mean relative displacement of flap2 increases from 0.36 mm for FF1 to -1.66 mm for FF2, as the Young's modulus decreases from 1×10^5 Pa to 0.5×10^5 Pa. It seems that oscillations of both flaps in both cases have stabilized after 12 seconds, but more time steps are required in order to verify whether oscillations are self-sustained.

Cases		Flap maximum amplitude (mm)	Mean flow velocity (m/s)	Standard deviation	Minimum flow velocity (m/s)	Maximum flow velocity (m/s)
FF1	probe1	-8.55	0.48	0.413	0.005	1.656
	probe2	7.07	0.93	0.438	0.090	1.763
FF2	probe1	24.04	0.99	0.464	0.035	2.200
	probe2	-19.07	0.97	0.373	0.104	1.780
RF	probe1	-	0.96	0.462	0.083	1.727
	probe2	-	0.93	0.374	0.202	1.598

Table 2: Flap and flow parameters for the three cases computed at probe 1 and probe 2.

Table 2 shows that mean velocity increases from 0.48 m/s to 0.99 m/s and from 0.93 m/s to 0.97 m/s as the flap amplitude are higher in the flexible case FF2 than in FF1. Moreover FF2 displays higher mean velocity values than the rigid case (RF), as mean velocity increases from 0.96 m/s to 0.99 m/s and from 0.93 m/s to 0.97 m/s. It is worthy to notice that the maximum flow velocities for flexible cases are higher than for rigid cases with an increase up to 30%, from a maximum of 1.7 m/s in the rigid case to a maximum of 2.2 m/s in the elastic case as shown in FIG. 4.

After 12 seconds, when oscillations of flaps seem to stabilize, flap 2 for example reaches a lock-in frequency between flap oscillation frequency and shedding frequency at probe 1 with an approximate value of 1.5 Hz.

5 Conclusion

The coupled fluid-structure numerical simulations have been carried out using an in-house partitioned code developed using the open source C++ library OpenFOAM. The fluid flow is solved via an Arbitrary Lagrangian-Eulerian (ALE) formulation and the solid deformations are computed by taking into account large structural deformation and strong coupling between the flow and the elastic solid, performed by an adaptive iterative method using Aitken under-relaxation parameter.

The studied case consisted of two elastic flaps inserted at the median of a channel flow. The flaps oscillate in a passive way without additional external source as a vortex shedding behind a fixed square cylinder perturbed the upstream flow of the flaps. One configuration with rigid flaps is compared to two configurations with flexible flaps with varying Young modulus values. As main conclusions, flexible flaps cases resulted in higher amplitude of velocity oscillations in the wake region of the flaps, with an increase of velocity up to 30% for case FF2. Amplitudes of oscillations are thus found to be larger with reduced elasticity of the flaps. Eventually, vortices created by each flap are shown to induce disturbances of the motion on the adjacent flap, thus raising the chance of the oscillations to be self-sustained.

References

[1] Webb R.L., Enhancement of Single-Phase Heat Transfer, New York, Wiley Interscience, 1987.
[2] Valencia A., Heat transfer enhancement in a channel with a built-in rectangular cylinder, Heat and Mass Transfer, 30, 423-427, 1995.
[3] Yang S.-J., Numerical study of heat transfer enhancement in a channel flow using an oscillating vortex generator, Heat and Mass Transfer, 39, 257-265, 2002.
[4] *OpenFOAM, The Open CFD Toolbox - User Guide, 2013*
[5] Habchi C., Russeil S., Bougeard D.,. Harion J.-L, Lemenand T., Ghanem A., Partitioned solver for strongly coupled fluid–structure interaction, Computers & Fluids, 71, 306-319, 2013.
[6] Jasak H.and Weller H.G., Application of the finite volume method and unstructured meshes to linear elasticity, International Journal for Numerical Methods in Engineering, 48, 267-287, 2000.
[7] Jasak H. and Tukovic Z., Automatic mesh motion for the unstructured finite volume method, Trans FAMENA, 30, 1-18, 2007.
[8] Donea J., Huerta A., Ponthot J.-Ph., Rodriguez-Ferran A., Arbitrary Lagrangian–Eulerian Methods, Encyclopedia of Computational Mechanics, 1, JohnWiley & Sons, Ltd, 2004.
[9] Bos F.M., Numerical simulations of flapping foil and wing aerodynamics, PhD, Technical University of Delft, Netherlands, 2010.
[10] Tukovic Z., Jasak H., Updated lagrangian finite volume solver for large deformation dynamic response of elastic body, Transaction of FAMENA, 31, 1-16, 2007.
[11] Küttler U. and Wall W.A., Fixed-point fluid–structure interaction solvers with dynamic relaxation, Computational Mechanics, 43, 61-72, 2008.
[12] Issa R.I., Solution of the implicitly discretised fluid flow equations by operator-splitting, Journal of Computational Physics, 62, 40-65, 1985.
[13] Patankar S.V.and Spalding D.B., A calculation procedure for heat, mass and momentum transfer in three-dimensional parabolic flows, International Journal of Heat and Mass Transfer, 15, 1787-1806, 1972.

Appendix B

Etude de l'intensification des transferts de chaleur dans un écoulement laminaire par mise en place de générateurs de vorticité flexibles

"Study of heat transfer enhancement in a laminar flow regime by introduction of flexible vortex generators". The paper presented next has been published in the 12th CIFQ Proceedings, held in Quebec, CANADA, 8-10 June 2015.

XII[ème] Colloque Interuniversitaire Franco-Québécois
sur la Thermique des Systèmes
8-10 juin 2015, Sherbrooke
Québec (Canada)

CIFQ2015 / ART-03-24

ETUDE DE L'INTENSIFICATION DES TRANSFERTS DE CHALEUR DANS UN ECOULEMENT LAMINAIRE PAR MISE EN PLACE DE GENERATEURS DE VORTICITE FLEXIBLES

Samer **ALI**[a,b,*], Sébastien **MENANTEAU**[a], Charbel **HABCHI**[b], Jean-Luc **HARION**[a], Thierry **LEMENAND**[c]

[a] *Mines Douai, Energétique Industrielle, F-59508 Douai, France*
[b] *Lebanese International University LIU, Mechanical Engineering Dpt., Beirut, Liban*
[c] *LARIS - EA 7315, University of Angers - ISTIA, Angers, France*

RÉSUMÉ

La présente étude propose une solution originale d'intensification des transferts de chaleur d'un écoulement laminaire au moyen de générateurs de tourbillons souples. Plus spécifiquement, l'influence de la présence de deux, trois ou quatre perturbateurs flexibles positionnés alternativement le long des parois d'un canal aéraulique bidimensionnel sur le transfert de chaleur est étudiée. L'analyse des performances est réalisée à partir de résultats issus de simulations numériques tenant compte de l'interaction fluide-structure entre les éléments flexibles et le milieu fluide. Dans un premier temps, l'observation de la dynamique autoentretenue de l'écoulement et de la production de vorticité est analysée dans le but de mettre en évidence les phénomènes de formation des tourbillons puis leur déstructuration/appariement en fonction du mouvement des perturbateurs flexibles. Ensuite, l'efficacité énergétique de ce procédé est quantifiée au moyen d'une analyse locale et globale des transferts de chaleur, permettant ainsi de mettre en évidence le potentiel d'accroissement des performances par la mise en place de ces perturbateurs souples.

Mots Clés : *Interaction fluide-structure, perturbateurs flexibles, écoulement laminaire, amélioration de l'efficacité énergétique*

NOMENCLATURE

Symboles :

c_p	chaleur spécifique, J.kg^{-1}.K^{-1}
$\mathbf{d_s}$	vecteur déplacement du domaine solide, m
e	épaisseur du perturbateur, mm
E	module d'Young, Pa
f	coefficient de friction, -
f_e	fréquence d'oscillation, Hz
f_N	fréquence naturelle, Hz
f_v	fréquence de battement de sillage, Hz
$\mathbf{F}$	tenseur du gradient des déplacements, -
H	hauteur du canal bidimensionnel, mm
k	conductivité thermique, W.m^{-1}.K^{-1}
L	longueur du domaine d'étude, m
$\dot{m}$	débit massique, kg.s^{-1}
Nu	nombre de Nusselt, -
p	pression, Pa
$q"$	flux thermique moyen des parois haute et basse du canal, W.m^{-2}
Re	nombre de Reynolds, -
T	température, K
t	temps, s
$\mathbf{u}$	vecteur vitesse (composantes u,v), m/s
$\overline{U}_d$	vitesse débitante, m/s
(x,y)	coordonnées spatiales, m

Lettres grecques :

η	facteur d'efficacité, -
ν_f	viscosité cinématique du fluide, m^2.s^{-1}
ν_s	coefficient de Poisson, -
ρ	masse volumique, kg.m^{-3}
$\sum$	second tenseur des contraintes de Piola-Kirchhoff, -

Indices / Exposants :

d	grandeur débitante
f	grandeur du domaine fluide
g	grandeur globale
s	grandeur du domaine solide
p	grandeur pariétale

[*] auteur correspondant
Adresse électronique: samer.ali@liu.edu.lb

1. INTRODUCTION

Une méthode passive d'intensification des transferts de chaleur très largement répandue consiste à introduire des générateurs de vorticité rigides le long des parois d'une conduite de manière à brasser le fluide, déstructurer les couches limites et transférer ainsi la chaleur des parois vers le cœur de l'écoulement [1]. Dans les composants de type échangeur/réacteur multifonctionnel, des ailettes rectangulaires ou triangulaires sont notamment utilisées et génèrent d'excellentes performances de transfert thermique [2]. Les méthodes d'intensification dites actives présentent par ailleurs d'autres avantages qui permettent entre autre de brasser l'écoulement de manière plus efficiente en contrôlant par exemple l'oscillation d'un perturbateur placé dans un écoulement. Toutefois, cet accroissement de performance nécessite un apport externe d'énergie et complexifie le procédé par la mise en œuvre de systèmes annexes pour contrôler et maintenir le mouvement de la structure solide [3].

D'autres approches mettent en évidence le potentiel d'éléments flexibles introduits dans un écoulement dans le but de tirer profit de l'interaction fluide-structure et générer ainsi des phénomènes instationnaires susceptibles d'améliorer l'accroissement du transfert de chaleur. Une étude de Khanafer *et al.* [4] réalisée par modélisation en éléments finis de l'interaction fluide avec un élément souple en microcanal montre qu'un bruit blanc superposé à la vitesse débitante d'entrée peut induire une oscillation harmonique de la structure flexible. Une étude comparative a par ailleurs été menée par Mirzae *et al.* [5] par simulation numérique bidimensionnelle d'un microcanal en présence d'un fluide en écoulement forcé laminaire et présentant un perturbateur élastique ou rigide monté perpendiculairement à une paroi. L'analyse montre que le transfert de chaleur est plus important dans la configuration avec le générateur flexible et que, de surcroit, la perte de charge est moindre.

Nous proposons dans la présente étude d'utiliser l'interaction fluide-structure pour améliorer les transferts de chaleur dans un écoulement laminaire en introduisant des perturbateurs souples (FVG, Flexible Vortex Generator) le long des parois dans une configuration de canal bidimensionnel et d'analyser l'influence de la présence de plusieurs FVG dans le canal. L'oscillation libre des FVG et l'interaction avec l'écoulement est étudiée au moyen de simulations numériques 2D laminaires instationnaires. Dans un premier temps, nous détaillons la procédure numérique utilisée et les configurations qui font l'objet de cette étude. Ensuite, les résultats sont présentés et analysés en comparant les performances d'intensification des transferts de chaleur au sein de l'écoulement.

2. Formulation des équations et méthodes de résolution

L'écoulement est gouverné par les équations de conservation de la masse et de Navier-Stokes écrites avec une formulation Lagrange-Euler arbitraire (ALE, Arbitrary Lagrangian-Eulerian) afin de prendre en compte le mouvement à l'interface fluide-structure. En régime laminaire, ces équations prennent la forme suivante :

$$\nabla \cdot \mathbf{u_f} = 0 \tag{1}$$

$$\frac{\partial \mathbf{u_f}}{\partial t} + (\mathbf{u_f} - \mathbf{u_{m,f}}) \cdot \nabla \mathbf{u_f} = -\frac{\nabla p}{\rho_f} + \upsilon_f \nabla^2 \mathbf{u_f} \tag{2}$$

où $(\mathbf{u_f} - \mathbf{u_{m,f}})$ représente le terme convectif avec $\mathbf{u_f}$ le vecteur vitesse du fluide et $\mathbf{u_{m,f}}$ le vecteur vitesse du maillage du domaine fluide issu du déplacement de l'interface. La pression est notée p, la masse volumique du fluide ρ_f et la viscosité cinématique ν_f.

En intégrant ensuite la formulation ALE à l'équation de la chaleur dans le domaine fluide, la température est obtenue en résolvant :

$$\frac{dT_f}{dt} + (\mathbf{u_f} - \mathbf{u_{m,f}}) \cdot \nabla T_f = \frac{k}{\rho_f C_p} \nabla^2 T_f \tag{3}$$

où T_f est la température du fluide, k la conductivité thermique et C_p la chaleur spécifique du fluide.

Pour le domaine élastique, son déplacement peut être décrit d'un point de vue lagrangien uniquement, sous la forme :

$$\rho_s \frac{\partial^2 \mathbf{d_s}}{\partial t^2} = \nabla \cdot \left(\sum \cdot \mathbf{F}^{\mathbf{T}} \right) \tag{4}$$

où $\mathbf{d_s}$ représente le déplacement de la structure, ρ_s sa masse volumique et $\mathbf{F}$ le tenseur du gradient du déplacement s'exprimant comme :

$$\mathbf{F} = \mathbf{I} + \nabla \mathbf{d_s^T} \tag{5}$$

$\mathbf{I}$ représentant la matrice identité.

Dans la relation (4), $\sum$ désigne le second tenseur des contraintes de Piola-Kirchhoff et s'écrit :

$$\sum = \mu_s \left(\mathbf{F}^{\mathrm{T}} \cdot \mathbf{F} - \mathbf{I} \right) + \lambda_s \mathrm{tr} \left(\frac{1}{2} \left(\mathbf{F}^{\mathrm{T}} \cdot \mathbf{F} - \mathbf{I} \right) \right) \mathbf{I} \tag{6}$$

où μ_s et λ_s dénotent les constantes de Lamé et sont reliées aux propriétés élastiques du matériau via les relations :

$$\mu_s = \frac{E}{2(1+\nu_s)} \quad (7)$$

et

$$\lambda_s = \frac{\nu_s E}{(1+\nu_s)(1-2\nu_s)} \quad (8)$$

avec E le module d'Young et ν_s le coefficient de Poisson.

Cette étude est réalisée à travers l'environnement Ansys Workbench en couplant les solveurs Ansys Fluent pour l'écoulement et Ansys Structural Mechanical pour les contraintes mécaniques [6]. La résolution du système d'équations est réalisée dans le domaine fluide par l'algorithme couplé de pression-vitesse. La discrétisation spatiale utilise un schéma du second ordre et la discrétisation temporelle un schéma implicite du premier ordre avec un pas de temps fixé à 10^{-4} s assurant une valeur de la contrainte CFL inférieure à 1 en tout point de l'écoulement. Les critères de convergence pour les équations de poisson, quantité de mouvement et énergie sont fixés à 10^{-6}. Le critère de convergence de la boucle itérative de résolution du couplage fluide-structure permettant de transférer alternativement les contraintes visqueuses et forces de pression entre le fluide et le domaine solide élastique est fixé à 10^{-4}. Enfin, un algorithme de maillage adaptatif et remaillage partiel automatique a été employé proche des interfaces en mouvement. De plus amples détails sont disponibles dans l'article d'Ali *et al.* [7].

3. Description des domaines d'étude et des conditions initiales et limites

Le domaine d'étude considéré est un canal bidimensionnel dans lequel sont introduits plusieurs générateurs de vorticité flexibles inclinés d'un angle $\beta = 30^{\circ}$ par rapport aux parois du domaine (*Figure 1*). Trois configurations sont étudiées et diffèrent en fonction du nombre de FVG positionnés dans l'écoulement (2FVG, 3FVG et 4FVG). Les FVG A, B, C et D présentent une longueur de 30 mm et une épaisseur e de 0,75 mm et sont distants de 30 mm. Leurs propriétés élastiques sont définies dans le *Tableau 1*.

Une condition limite de paroi sans glissement est fixée aux parois du domaine et aux interfaces fluide-structure. La condition de pression est nulle en sortie de canal et est associée à une condition de gradient de vitesse nul. En entrée, un profil parabolique est introduit de manière à modéliser un écoulement en régime laminaire pleinement développé. Le nombre de Reynolds calculé à partir de la vitesse débitante et du diamètre hydraulique $D_h = 2H$ est égal à 2000 pour l'ensemble des configurations.

Le transfert de chaleur est généré à partir d'une condition de température uniforme aux parois du canal, T_w=360 K. Les FVG sont considérés adiabatiques dans cette étude. Le fluide entrant dans le canal est quant à lui à une température constante de 300 K. Le fluide considéré est de l'air et ses propriétés sont considérées invariantes en fonction de la température, avec une conductivité thermique k=0,0242 W/(m.K), une chaleur spécifique c_p=1006,43 J/(kg.K) et une viscosité cinématique $\nu_f = 1,46\times10^{-5}$ m^2 / s.

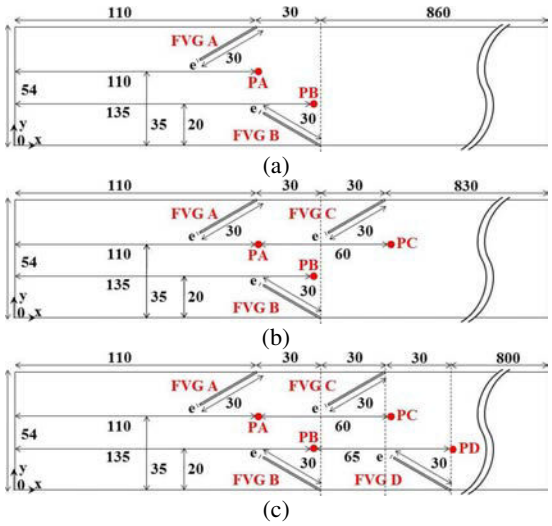

Figure 1 : Configurations d'étude (dimensions en mm), avec : (a) 2FVG, (b) 3FVG et (c) 4FVG

Tableau 1: Synthèse des propriétés mécaniques et conditions d'écoulement des configurations étudiées

Paramètres	*Valeurs*
ρ_s [kg/m^3]	1200
ν_s	0,4
E [10^6 Pa]	5
e [mm]	0,75
H [mm]	54
$\mathrm{Re}_{D_h} = \left(\overline{U}_{d,entree} D_h\right) / \nu_f$	2000

4. Résultats et analyse

Dans ce paragraphe, nous présentons dans un premier temps la topologie instationnaire de l'écoulement. Nous investiguons ensuite les transferts de chaleur associés et comparons au moyen d'analyses locale et globale les performances thermiques de chaque configuration.

4.1. Etude de l'instationnarité de l'écoulement

A partir de sondes numériques placées dans l'écoulement en aval de chaque FVG (PA, PB, PC, PD

sur la *Figure 1*) dans le but d'extraire les valeurs instationnaires de vitesse longitudinale, le spectre fréquentiel des régions de sillage a été tracé pour chaque configuration à partir d'une transformée de Fourier rapide (*Figure 2*). Dans la configuration 2FVG, la fréquence de battement observée vaut $f_v = 2,46Hz$ et correspond au rapport des fréquences $f_v / f_N \approx 0,52$ où $f_N = 4,8\ \mathrm{Hz}$ est la fréquence naturelle du FVG (dans le vide). Une étude comparable a été menée sur les fréquences d'oscillation des FVG et indique qu'ils oscillent dans tous les cas à leur fréquence naturelle, i.e. $f_e / f_N \approx 1$. La configuration 2FVG ne présente par conséquent pas de phénomène "Lock-In", c'est-à-dire que l'écoulement et les oscillations des FVG sont déphasés, tendant à réduire notablement l'amplitude des oscillations. En considérant la configuration 3FVG, l'énergie contenue dans le spectre de la vitesse longitudinale (i.e. intégrale de la densité spectrale de puissance, DSP) est sensiblement plus importante, impliquant de fait des amplitudes de fluctuation de vitesse plus importantes. Dans ce cas, le fluide induit une contrainte plus importante sous forme de pression sur les FVG. Pour cette configuration, un premier pic fréquentiel est observé à $f_v = 4,2\ \mathrm{Hz}$ et correspond à la fréquence naturelle des FVG dans l'air. Les FVG et l'écoulement interagissent alors à la fréquence naturelle d'oscillation des FVG via un effet "Lock-In" $(f_e \approx f_N \approx f_v)$, l'instationnarité de l'écoulement étant alors entretenue par cette interaction entre fluide et FVG. L'observation de ce phénomène d'effet "Lock-In" se retrouve également dans la DSP de la configuration 4FVG. D'autres pics de fréquence harmonique sont également visibles sur la *Figure 2* et indiquent l'apparition de nouvelles fréquences énergétiques supplémentaires, susceptibles d'initier une transition de l'écoulement d'un régime laminaire vers un régime chaotique, connu pour accroître les performances de transfert de chaleur.

La *Figure 3* illustre l'évolution temporelle du champ de vorticité. Un lâcher tourbillonnaire a lieu au niveau des extrémités des FVG A et B en raison du cisaillement produit entre la zone de vitesse amont et la région de sillage en aval des FVG présentant des vitesses plus faibles. Cette production de vorticité se produit pour les mêmes raisons au niveau de chaque perturbateur souple. Au fur et à mesure, les structures tourbillonnaires convectent dans l'écoulement et impactent les FVG placés en aval. Lorsque le FVG D atteint sa position d'équilibre instable (le long de la paroi à l'instant t_0), le comportement élastique du FVG associé aux forces de pression imposées par le fluide et à l'énergie cinétique emmagasinée, entraine le FVG dans le sens de l'écoulement en formant une structure vorticitaire visible à l'instant t_0+0,06 s. Cette structure est ensuite convectée vers la paroi opposée du canal en même temps qu'un autre tourbillon se forme en raison du mouvement du FVG C. Ayant le même sens de rotation, ils s'apparient pour ne former plus qu'une seule entité, intensifiant de fait la valeur de vorticité et la taille de la structure tourbillonnaire à l'instant t_0+0,12 s.

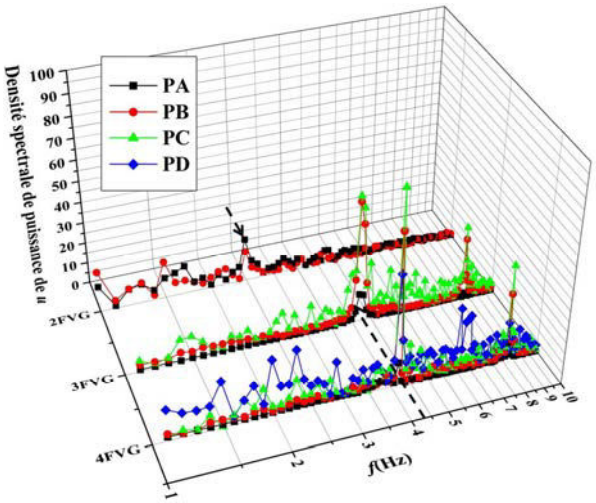

Figure 2: Densité spectrale de puissance de la vitesse longitudinale u dans le sillage des FVG pour les 3 configurations d'étude

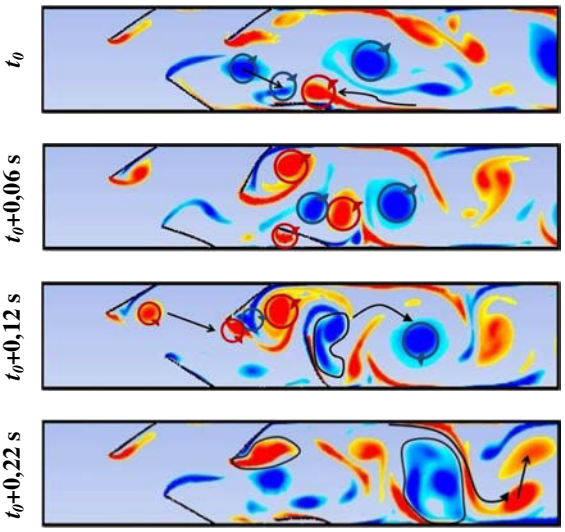

Figure 3: Visualisations instantanées du champ de vorticité pour la configuration 4FVG

L'observation de l'instationnarité de l'écoulement permet ainsi de mettre en évidence les formations et appariements des structures tourbillonnaires formées par les déplacements alternés des FVG. Les structures

tourbillonnaires produites interagissent à la fois dans la direction longitudinale de l'écoulement par leur convection forcée sous l'effet de l'écoulement, mais également verticalement par l'oscillation des perturbateurs. Il est également à noter que l'ajout successif de perturbateurs présente un double intérêt. En effet, il permet d'une part de produire de la vorticité dans l'écoulement qui intensifie les structures tourbillonnaires créées en amont et d'autre part, le déplacement du FVG joue un rôle bénéfique dans le mouvement du FVG amont puisqu'il produit des accélérations de l'écoulement dans des directions alternées et est à l'origine de forces de pression variables en intensité dans le temps qui permettent d'auto-entretenir le phénomène oscillatoire. L'analyse de phase des oscillations des perturbateurs montre d'ailleurs que les FVG situés sur une même paroi ont tendance à osciller en phase tandis que les FVG de la paroi opposée sont en opposition de phase. Même si cela ne fait pas l'objet de la présente étude, ces déphasages constatés peuvent potentiellement être exploités de manière intéressante pour exciter des structures flexibles de manière différente en faisant varier les tailles et les épaisseurs des FVG successifs.

Les observations réalisées mettent finalement en exergue l'intensification de la vorticité présente dans l'écoulement, ce qui présente un intérêt réel pour l'accroissement des transferts de chaleur qui fait l'objet de l'étude présentée dans la section suivante.

4.2. Analyse des performances thermiques

La *Figure 4* présente l'évolution temporelle de la température dans la configuration 4FVG. Les coordonnées spatiales sont adimensionnées par la hauteur du canal *H*, telles que :

$$X^* = \frac{x}{H} \quad \text{et} \quad Y^* = \frac{y}{H} \tag{9}$$

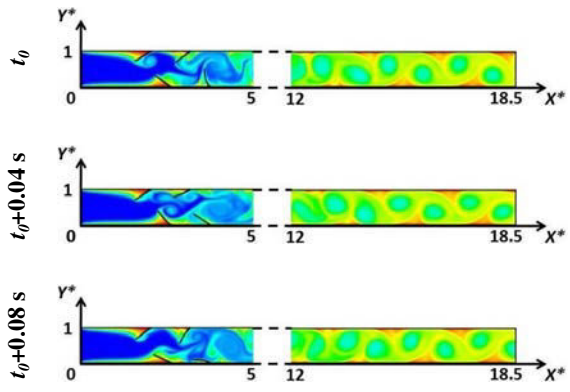

Figure 4: Champ instantanés de température pour la configuration 4FVG. Une partie du champ a été volontairement tronquée de façon à mettre en évidence les zones importantes de l'écoulement

Afin de quantifier le transfert de chaleur, un nombre de Nusselt local a été déterminé à partir de la moyenne temporelle et de la moyenne de température au niveau des parois haute et basse :

$$\overline{Nu}(x) = \frac{1}{t_2 - t_1} \int_{t_1}^{t_2} \frac{q_p^{"}(x,t) D_h}{k(T_p - T_d(x,t))} dt \tag{10}$$

où t_1 représente le pas de temps initiant le calcul statistique et à partir duquel l'écoulement a atteint un régime thermique établi (t_1=4 s), t_2 correspond au pas de temps final, $q_p^{"}$ au flux de chaleur pariétal moyen des parois haute et basse, T_d à la température débitante du fluide calculée pour chaque position x par :

$$T_d(x,t) = \frac{\int_0^H U(x,y,t) T(x,y,t) dy}{\int_0^H U(x,y,t) dy} \tag{11}$$

La *Figure 5* présente les valeurs du nombre de Nusselt local en fonction de la position longitudinale adimensionnée X^*. Le profil équivalent de $\overline{Nu}(x)$ dans le cas d'un canal lisse sans perturbateur a également été tracé. Les profils de $\overline{Nu}(x)$ indiquent un gain très sensible en termes de performance par rapport à un canal lisse. En déterminant la valeur moyennée suivant X^* (entre X^*=0 et X^*=18.5) correspondant à chaque cas d'étude, le gain observé est ainsi de 178% pour 2FVG, 278% pour 3FVG et 317% pour 4FVG. L'observation locale des valeurs de $\overline{Nu}(x)$ montre également un transfert de chaleur élevé à proximité des FVG. Il est à noter enfin que lorsque X^*>8, le transfert de chaleur présente des niveaux très similaires dans les configurations 3FVG et 4FVG.

L'évaluation des performances associées à l'ajout de FVG nécessite également de prendre en compte les pertes de charge engendrées. Le facteur de performance thermique η permet une évaluation de la performance globale. Il est défini à partir d'un nombre de Nusselt global et d'un coefficient de frottement caractérisant la perte de charge globale, au moyen de la relation [8] :

$$\eta = \left(\frac{Nu_{g,FVG}}{Nu_0} \right) \left(\frac{f_{FVG}}{f_0} \right)^{-1/3} \tag{12}$$

avec $Nu_{g,FVG}$ et Nu_0 les nombres de Nusselt globaux déterminés dans les configurations 2-3-4FVG et dans le canal lisse respectivement. La valeur du nombre de Nusselt global est déterminée à partir de la relation [9] :

$$Nu_g = \frac{\dot{m} c_p D_h}{2Lk} \frac{T_{d,sortie} - T_{d,entree}}{T_p - T_{moy}} \tag{13}$$

avec $\dot{m}$ le débit massique, L la longueur du canal, $T_{d,sortie}$ et $T_{d,entree}$ les températures débitantes en sortie et entrée de canal respectivement et

$T_{moy} = \left(T_{d,sortie} + T_{d,entree}\right)/2$. Les coefficients de frottement correspondants f_{FVG} et f_0 sont quant à eux déterminés par la relation :

$$f = \frac{2D_h}{4L}\frac{\Delta P}{\rho_f \overline{U}^2_{d,entree}} \qquad (14)$$

où ΔP représente la variation de pression moyennée temporellement entre l'entrée et la sortie du canal.

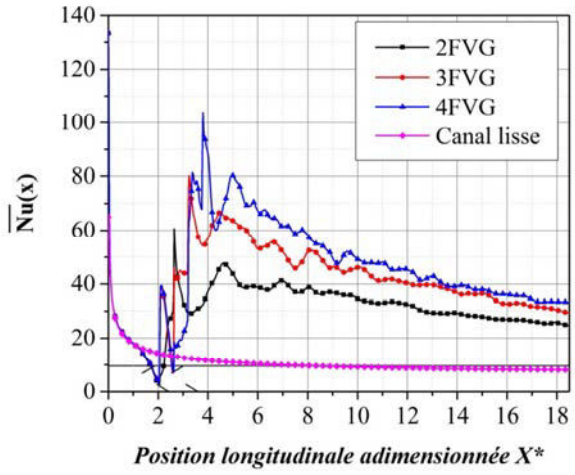

Figure 5: Evolution longitudinale du nombre de Nusselt local $\overline{Nu}(x)$

Le facteur de performance η vaut ainsi 1,33 pour la configuration à 2 FVG, 1,11 avec 3 FVG et 1.01 avec 4 FVG. Ces valeurs se traduisent par des gains de performance respectifs de 33%, 11% et 1% par rapport à la configuration de canal lisse. Ces valeurs décroissantes en fonction du nombre de FVG positionnés dans l'écoulement s'expliquent par l'augmentation de la perte de charge globale engendrée par l'effet de blocage de l'écoulement par la présence des FVG qui contrebalance l'augmentation du transferts de chaleur.

CONCLUSION

Cette étude présente une technique originale d'intensification des transferts de chaleur dans les écoulements laminaires. Le principe repose sur la mise en place de perturbateurs flexibles le long des parois d'une conduite dans le but de déstabiliser l'écoulement et les couches limites. L'interaction fluide-structure ayant lieu produit alors une mise en oscillation autoentretenue des éléments flexibles qui améliore le brassage de l'écoulement et l'efficacité de l'échange thermique convectif. En augmentant le nombre de perturbateurs positionnés dans l'écoulement, un régime fréquentiel dit "Lock-In" apparait et le sillage de l'écoulement oscille à la fréquence naturelle des éléments souples, ayant pour effet d'accroitre l'amplitude des déplacements des perturbateurs.

L'observation des nombres de Nusselt caractérisés localement permet de mettre en évidence l'intensification du transfert de chaleur en augmentant le nombre de perturbateurs souples. Pour autant, une analyse globale des performances des configurations étudiées souligne que les gains en termes de transfert de chaleur sont contrebalancés par l'augmentation de pertes de charge entre l'entrée et la sortie du canal.

Nos investigations actuelles amènent à penser que ce procédé d'amélioration des transferts de chaleur pourrait se montrer plus efficient à condition d'optimiser les dimensions des perturbateurs placés dans l'écoulement, leur forme, leur positionnement les uns par rapport aux autres ainsi que leurs propriétés mécaniques. Les phénomènes tridimensionnels de flexion-torsion et d'impacts sur la tridimensionnalité de l'écoulement seront en outre pris en compte dans nos prochaines études.

RÉFÉRENCES

[1] **FIEBIG,** M., Vortices, generators and heat transfer, *Chemical Engineering Research & Design,* vol. 76, pp. 108-123, (1998).

[2] **HABCHI,** C., **RUSSEIL,** S., **BOUGEARD,** D., **HARION,** J.-L., **LEMENAND,** T., et **DELLA VALLE,** D., Enhancing heat transfer in vortex generator-type multifunctional heat exchangers, *Applied Thermal Engineering,* vol. 38, pp. 14-25, (2012).

[3] **WANG,** Z.-D., **LAO,** Y.-J., **LI,** L.-J., et **CONG,** W.-C., Experiment on the characteristics of 3-D vortex ring behind a flexible oscillating caudal fin, *Journal of Hydrodynamics, Ser. B,* vol. 22, pp. 393-401, (2010).

[4] **KHANAFER,** K., **ALAMIRI,** A., et **POP,** I., Fluid–structure interaction analysis of flow and heat transfer characteristics around a flexible microcantilever in a fluidic cell, *International Journal of Heat and Mass Transfer,* vol. 53, pp. 1646-1653, (2010).

[5] **MIRZAEE,** H., **DADVAND,** A., **MIRZAEE,** I., et **SHABANI,** R., Heat transfer enhancement in microchannels using an elastic vortex generator, *Journal of Enhanced Heat Transfer,* vol. 19, (2012).

[6] ***ANSYS Academic Research****, user's guide*: ANSYS, Inc, (Release 15.0).

[7] **ALI,** S., **HABCHI,** C., **MENANTEAU,** S., **LEMENAND,** T., et **HARION,** J.-L., Heat transfer and mixing enhancement by free elastic flaps oscillation, *International Journal of Heat and Mass Transfer,* (2015).

[8] **PROMVONGE,** P. et **THIANPONG,** C., Thermal performance assessment of turbulent channel flows over different shaped ribs, *International Communications in Heat and Mass Transfer,* vol. 35, pp. 1327-1334, (2008).

[9] **SHAH,** R. K., Laminar flow friction and forced convection heat transfer in ducts of arbitrary geometry, *International Journal of Heat and Mass Transfer,* vol. 18, pp. 849-862, (1975).

Concept innovant d'échangeur/réacteur multifonctionnel par contrôle dynamique passif par générateurs de vorticité flexibles

Résumé :

Le but de cette étude est d'étudier l'utilisation d'interactions fluide-structure (FSI) pour améliorer le transfert de chaleur et les performances de mélange dans des échangeurs-réacteurs multifonctionnels, et d'évaluer des configurations pour lesquelles l'objectif est de produire et de maintenir un régime dynamique auto-entretenu d'oscillations des générateurs de tourbillons flexibles. Dans un premier temps, deux études numériques ont été réalisées pour des écoulements laminaires bidimensionnels. Les résultats montrent qu'un minimum de trois générateurs de tourbillons alternés est nécessaire pour produire une instabilité qui engendre les oscillations de larges amplitudes. L'ajout de deux promoteurs coplanaires en amont déstabilise l'écoulement en créant des forces périodiques agissant sur les générateurs de tourbillons en aval. Il en résulte une augmentation de la vitesse réduite qui impose un blocage en fréquence des oscillations des générateurs de tourbillons en aval. Dans cette configuration, des oscillations de larges amplitudes sont obtenues pour uniquement deux générateurs de tourbillons en aval. Les oscillations des générateurs de tourbillons produisent une vorticité intense qui a une incidence positive que le transfert de chaleur et sur le mélange. Dans un second temps, une configuration tridimensionnelle HEV incluant des générateurs de tourbillons trapézoïdaux flexibles orientés à 45° vers l'amont est étudiée par simulations numériques. Une analyse FFT réalisée sur les coefficients issus d'une analyse POD montre un pic fréquentiel correspondant aux formations et lâchers tourbillonnaires périodiques. Cette fréquence dominante correspond bien au mode propre d'oscillation des générateurs de tourbillons et engendre ainsi de larges amplitudes d'oscillations. De plus, une analyse de synergie est appliquée pour mettre en évidences les zones de fort et faible transferts corrélées aux positions des générateurs de tourbillons durant un cycle d'oscillation. Cette étude a permis de mettre en évidence plusieurs configurations permettant la mise en place d'un régime dynamique auto-entretenu grâce à des générateurs de tourbillons flexibles. La dynamique repose uniquement sur les interactions des forces fluides-solides, sans apport d'énergie externe, ce qui permet un gain d'efficacité et de compacité pour des échangeurs-réacteurs multifonctionnels.

Mots clés : Echangeurs-réacteurs multifonctionnels, Interaction Fluide-Structure, Transfert thermique, Mélange laminaire, Simulations numériques

Innovative concept of multifunctional heat exchanger/reactor by passive dynamic control using flexible vortex generators

Abstract :

The aim of this study is to investigate the use of fluid-structure interaction (FSI) to improve heat transfer and mixing performances in multi-functional heat exchangers/reactors, and to evaluate configuration designs where the main target is to produce and maintain self-sustained oscillations of flexible vortex generators. At first, two dimensional laminar flow studies are numerically investigated. The results show that a minimum of three alternating flaps is needed to produce an instability that leads to large displacement oscillations. However, the introduction of two co-planar flaps upstream destabilizes the flow by creating periodic forces that act on the alternating downstream flaps. Hence, this results in artificially increasing the reduced velocity that will induce the alternating flaps to be in a lock-in state. Thus in this case, large displacement amplitudes are created with two alternating flaps only. The free flaps oscillations produce vortices of higher strength which have a positive impact on heat transfer and mixing. Secondly, a three dimensional HEV configuration with flexible trapezoidal vortex generators inclined with an angle of 45° with respect to the wall and reversed opposite to the flow direction is numerically investigated. Fast Fourier Transformation is applied on the temporal variation of the Proper Orthogonal Decomposition (POD) coefficients which displays a dominant peak in the flow and corresponds to the vortices periodic formation and detachment. This dominant frequency synchronizes well with the structural oscillation frequency and the fundamental frequency of the tabs reaching a lock-in state and leading to large oscillation amplitudes. Moreover, the field synergy principle is applied to display areas of high and low heat transfer in conjunction with the FVG position during one cycle of oscillation. Finally, this study reveals several configuration designs for self-sustained oscillation of flexible vortex generators. The structural motion relies only on the fluid forces themselves without any external source of energy leading to more energy efficient and compact multi-functional heat exchangers/reactors.

Keywords : Multifunctional heat exchangers/reactors, Fluid–structure interaction, Heat transfer, Laminar mixing, Numerical simulation